Direct Detection and Self-coherent Detection Short-reach Optical Communication Systems for Data Center Networking

Zhenping Xing

Department of Electrical and Computer Engineering

McGill University

Montréal, Canada

April 2021

A thesis submitted to McGill University in partial fulfillment of the requirements for the degree of Doctor of Philosophy

Abstract

In this thesis, we aim at exploring the potentials and the limits of O-band intensity modulation direct detection (IM/DD) systems and C-band single sideband (SSB)/vestigial sideband (VSB) self-coherent detection systems for data center networking applications based on current technologies and advanced DSP algorithms.

For the O-band IM/DD system, we start from a 400 Gb/s 4-λ coarse wavelength division multiplexing (CWDM4) 4-level pulse amplitude modulation (PAM4) transmission system based on a commercial transmitter optical sub-assembly (TOSA). We experimentally show that by using faster-than-Nyquist (FTN) technologies, we can increase the total net rate to 600 Gb/s at 2 km and 10 km. We also propose a wavelength-interleaved four dimensional-PAM4-trellis coded modulation (4D-PAM4-TCM) scheme to improve the system's robustness against channel performance discrepancies caused by inter-channel component differences and the impacts of CD-chirp interactions. We experimentally show that the proposed scheme outperforms the conventional time-domain encoded 4D-PAM4-TCM scheme.

The SSB/VSB self-coherent detection system can be regarded as an upgrade of the IM/DD system, which slightly increases the hardware complexity and the DSP complexity to acquire CD compensation capability. In this thesis, we first focus on experimental studies of amplified VSB self-coherent systems using silicon photonic (SiPh) devices. We demonstrate 100 Gb/s PAM4 transmissions over 40-80 km using a digital-to-analog converter (DAC)-less transmitter based on a SiPh multi-electrode Mach Zehnder modulator (MZM) and a VSB receiver. We also propose a filter-response aware iterative Kramers Kronig (FA-iter-KK) algorithm to replace the conventional field reconstruction algorithms in a VSB system, which utilizes the frequency response of the optical filter to improve the accuracy of the field reconstruction process in the presence of the residual sideband. We further demonstrate a tunable power splitter based parallel path structure on the SiPh platform to control the carrier-to-signal power ratio (CSPR) in a VSB system.

In addition, we numerically study the transmission performance and the power consumption of IQ modulator based SSB systems and single MZM based VSB systems in unamplified loss

limited links over 40 km. We compare the best achievable performance of two CSPR control schemes, i.e. the bias tuning scheme and the parallel path structure based scheme, and we reveal that the choice of the CSPR control scheme depends on the swing of the driving voltage and the half-wave voltage of the modulator. We also compare the power consumption of different SSB/VSB self-coherent detections systems processed with different field reconstruction algorithms, including the FA-iter-KK algorithm we propose. We show that in an IQ modulator based SSB system, the iterative KK algorithm (with one iteration) is the most power efficient algorithm, but a VSB system processed with the FA-iter-KK algorithm (with one iteration) has the potential to achieve an even lower total system power consumption. We think this work can provide some guidance on practical implementations of SSB/VSB self-coherent detection systems.

Résumé

Dans cette thèse, nous explorons le potentiel et les limites des systèmes dans la bande O basés sur la modulation d'intensité/détection directe (IM/DD) et des systèmes à détection auto-cohérente à bande latérale unique (SSB)/bande latérale résiduelle (VSB) en bande C pour les applications de réseau de centres de données à partir de technologies actuelles et d'algorithmes DSP avancés.

Pour les systèmes IM/DD en bande O, nous partons d'un système de transmission à 4 longueurs d'onde multiplexées (CWDM4) à 400 Gb/s utilisant la modulation d'amplitude d'impulsion à 4 niveaux (PAM4) basé sur un sous-ensemble d'émetteur optique (TOSA) commercial. Nous montrons expérimentalement qu'en utilisant des technologies plus rapides que Nyquist (FTN), nous pouvons augmenter le débit net total à 600 Gb/s sur 2 km et 10 km. Nous proposons également un schéma de modulation codé en treillis PAM4 à quatre dimensions entrelacé en longueur d'onde (4D-PAM4-TCM) pour améliorer la robustesse du système par rapport aux écarts de performance des canaux causés par les différences de composants entre ceux-ci et les impacts des interactions entre la dispersion chromatique et les fréquences parasitiques (CD-chirp). Nous montrons expérimentalement que le schéma proposé surpasse le schéma 4D-PAM4-TCM codé dans le domaine temporel conventionnel.

Les systèmes à détection auto-cohérente SSB/VSB peuvent être considérés comme une version améliorée des systèmes IM/DD, augmentant légèrement la complexité matérielle et la complexité DSP pour acquérir la capacité de compensation CD. Dans cette thèse, nous nous concentrons d'abord sur des études expérimentales de systèmes auto-cohérents VSB amplifiés utilisant des dispositifs photoniques sur silicium (SiPh). Nous démontrons des transmissions PAM4 à 100 Gb/s sur 40-80 km à l'aide d'un émetteur sans convertisseur numérique-analogique (DAC) basé sur un modulateur Mach-Zehnder (MZM) multi-électrodes SiPh et un récepteur VSB. Nous proposons également un algorithme itératif Kramers Kronig (FA-iter-KK) à réponse de filtre connue pour remplacer les algorithmes de reconstruction de champ conventionnels dans un système VSB. Notre algorithme utilise la réponse en fréquence du filtre optique pour améliorer la précision du processus de reconstruction de champ en présence de la

bande latérale résiduelle. Nous démontrons en outre une structure de chemins parallèles basée sur un diviseur de puissance accordable sur la plate-forme SiPh pour contrôler le rapport de puissance porteuse/signal (CSPR) dans un système VSB.

En outre, nous étudions numériquement les performances en transmission et la consommation de puissance des systèmes SSB basés sur un modulateur IQ et des systèmes VSB basés sur un MZM unique dans des liens non amplifiés sur 40 km limités par les pertes. Nous comparons les meilleures performances réalisables de deux schémas de commande du CSPR, soit le schéma d'ajustement du point d'opération et le schéma basé sur la structure de chemins parallèles, et nous révélons que le choix du schéma de commande CSPR dépend de l'amplitude de la tension de commande et de la tension demi-onde du modulateur. Nous comparons également la consommation de puissance de différents systèmes à détection auto-cohérente SSB/VSB traités avec différents algorithmes de reconstruction de champ, y compris l'algorithme FA-iter-KK que nous proposons. Nous montrons que dans un système SSB basé sur un modulateur IQ, l'algorithme itératif KK (avec une itération) est l'algorithme le plus économe en énergie, mais un système VSB traité avec l'algorithme FA-iter-KK (avec une itération) a le potentiel d'atteindre une consommation électrique totale du système encore plus faible. Nous pensons que ce travail fournit des recommandations sur les implémentations pratiques des systèmes à détection auto-cohérente SSB/VSB.

Acknowledgements

First and foremost, I would like to express my deepest gratitude to my supervisor, Prof. David V. Plant, for giving me the opportunity to study in the Photonic Systems Group (PSG) at McGill University. It's a privilege to do experiments in such a well-equipped laboratory and work with world-class researchers. This thesis would not have been possible without Prof. Plant's kind guidance and continuous support along the way.

I would like to thank our collaborators from Ciena Corporation, especially Dr. Maurice O'Sullivan and Dr. Mohammad Pasandi, for their valuable suggestions on the research projects about the SSB/VSB self-coherent systems. I would also like to thank our collaborators from Lumentum Corporation, for providing us with their marvelous CWDM4 TOSA product, which is a key enabler of the research projects about the CWDM4 IM/DD systems.

I would like to thank Prof. Martin Rochette and Prof. Benoit Champagne for serving on my supervisory committee and providing me with important advices during each stage of my Ph.D. program.

During the past six years at McGill, I received great support from my current and previous colleagues at PSG. I would like to thank Dr. David Patel, Dr. Rui Li, Dr. Yun Wang, Dr. Alireza Samani, Dr. Eslam El-Fiky, Dr. Meng Qiu, Dr. Minh Thang Hoang, Dr. Mohamed Morsy-Osman, Dr. Mohammed Sowailem, Dr. Meng Xiang, Xueyang Li, Dr. Maxime Jacques, Dr. Md Ghulam Saber, Dr. Luhua Xu, Dr. Kuo Zhang, Dr. Sujie Fan, Michael Hui, Yannick D'Mello, Amar Kumar, Dr. Nicolas Abadia, Md Samiul Alam, Deng Mao, Jinsong Zhang, Oliver Carpentier, Heba Tamazin, Dr. Fangyuan Zhang, Dr. Xingyu Zhou, Dr. Zhuopeng Xiao, and Dr. Qunbi Zhuge, for their help in various research activities.

Finally, I would like to express my deepest love to my family, especially my father Tieniu Xing and my mother Junxia Ma. Thank you for standing behind me all the time. My life would not have been so amazing without your unconditional support.

My sincere gratitude,

Zhenping Xing

Associated Publications

The original contributions of the research works presented in this thesis resulted in the following 7 papers (3 journal papers and 4 conference papers). The contribution of the coauthors is stated for each paper below.

In addition, I have co-authored 30 journal papers and 17 conference papers, which are not directly related to this thesis, through the collaborations with my colleagues at McGill University.

Journal Articles Directly Related to This Thesis

1. **Z. Xing**, A. Samani, M. Xiang, E. El-Fiky, T. M. Hoang, D. Patel, R. Li, M. Qiu, M. G. Saber, M. Morsy-Osman, and D. V. Plant, "100 Gb/s PAM4 transmission system for datacenter interconnects using a SiP ME-MZM based DAC-less transmitter and a VSB self-coherent receiver," in Opt. Express, vol. 26, no. 18, pp. 23969-23979, Sep. 2018.

   I conceived the idea, conducted the experiment, and wrote the paper. A. Samani designed the modulator. E. El-Fiky helped me to build the experimental setup. The rest co-authors contributed in discussing the idea and editing the paper.

2. **Z. Xing**, M. Xiang, E. El-Fiky, X. Li, M. G. Saber, L. Xu, P. Koh, and D. V. Plant, "Experimental Demonstration of 600 Gb/s Net Rate PAM4 Transmissions Over 2 km and 10 km With a 4-λ CWDM TOSA," in Journal of Lightwave Technology, vol. 38, no. 11, pp. 2968-2975, June, 2020.

   I conceived the idea, conducted the experiment, and wrote the paper. M. Xiang taught me to write the code of THP. The rest co-authors contributed in discussing the idea and editing the paper.

3. **Z. Xing**, M. Xiang, X. Li, E. El-Fiky, M. G. Saber, L. Xu, P. Koh, and D. V. Plant, "Wavelength-Interleaved 4D-PAM4-TCM in a 4-λ × 100 Gb/s CWDM System," in IEEE Photonics Technology Letters, vol. 32, no. 13, pp. 755-758, July 2020.

   I conceived the idea, conducted the experiment, and wrote the paper. M. Xiang taught me to write the code of 4D-TCM. The rest co-authors contributed in discussing the idea and editing the paper.

Conference Proceedings Directly Related to This Thesis

4. **Z. Xing**, D. Patel, E. El-fiky, M. Xiang, R. Li, M. G. Saber, L. Xu, M. Hui, and D. V. Plant, "SiPh Self-coherent Transmitter Circuit with on-chip CSPR Control Capability based on a Tunable Power Splitter," in Optical Fiber Communication Conference (OFC), San Diego, 2019, paper Tu2H.3.

   I conceived the idea, conducted the experiment, and wrote the paper. D. Patel, E. El-fiky, R. Li helped me during the device design process. M. Hui helped to wire-bond the device for testing. The rest co-authors contributed in discussing the idea and editing the paper.

5. **Z. Xing**, M. Xiang, E. El-Fiky, X. Li, M. G. Saber, L. Xu, and D. V. Plant, "600G PAM4 transmission using a 4-lambda CWDM TOSA based on controlled-ISI pulse shaping and Tomlinson-Harashima precoding," 45th European Conference on Optical Communication (ECOC 2019), Dublin, Ireland, 2019, paper Tu.3.D.1.

   I conceived the idea, conducted the experiment, and wrote the paper. M. Xiang taught me to write the code of THP. The rest co-authors contributed in discussing the idea and editing the paper.

6. **Z. Xing**, X. Li, M. E. Mousa-Pasandi, M. O'Sullivan and D. V. Plant, "On computational complexities of KK algorithms with frequency-domain digital resampling", in the Adv. Photon. Congr. (IPR, NP, NOMA, PVLE, PSC, NETWORKS, SPPcom, SOF), 2020, paper SPTu1I.6.

   I conceived the idea, conducted the simulation, and wrote the paper. The co-authors contributed in discussing the idea and editing the paper.

7. **Z. Xing**, X. Li, M. E. Mousa-Pasandi, M. O'Sullivan and D. V. Plant, "Filter Response Aware Iterative KK Algorithm for VSB systems," 2020 European Conference on Optical Communications (ECOC), Brussels, Belgium, 2020, paper Th2D.8.

   I conceived the idea, conducted the simulation and the experiment, and wrote the paper. The co-authors contributed in discussing the idea and editing the paper.

List of Figures

Fig. 1.1 Mainstream technologies used in data center networks. 2
Fig. 1.2 Motivation of this thesis. 6
Fig. 2.1 Schematic of a modern optical communication system enabled by DSP and FEC....16
Fig. 2.2 Schematic of typical single wavelength IM/DD system. 18
Fig. 2.3 Small-signal frequency responses of CD in push-pull MZM based IM/DD systems with different wavelengths and at different transmission distances. 22
Fig. 2.4 Small-signal frequency responses of CD-chirp interactions in EML based IM/DD systems with different α values and transmission distances. 23
Fig. 2.5 Noise sources in an IM/DD system. 24
Fig. 2.6 (a) impulse responses and (b) frequency responses of RC filters with different roll-off factors.....31
Fig. 2.7 (a) impulse responses and (b) frequency responses of RRC filters with different roll-off factors. 32
Fig. 2.8 Frequency responses of normalized duobinary shaping filter and an RC shaping filter. 32
Fig. 2.9 Eye diagrams and time-domain symbol sequences of PAM2, duobinary PAM2, PAM4 and duobinary PAM4 signals.....33
Fig. 2.10 Tree diagram for Viterbi decoding of duobinary PAM4 signal. 35
Fig. 2.11 Precoding based and MLSE based methods for signal recovery in duobinary systems.....36
Fig. 2.12 Schematic of a typical linear FFE.....38
Fig. 2.13 Schematic of a typical FFE-DFE.....41
Fig. 2.14 Schematic of a typical THP encoder.....41
Fig. 2.15 (a) Training and (b) testing using THP. 42
Fig. 2.16 Histograms of original PAM4, extended PAM4 and THP encoded PAM4 signals. .43
Fig. 2.17 Illustration of data-flipping effect in THP-PAM4 systems.....44
Fig. 2.18 Normalized post filter responses (normalized to the maximum value) with different

α values. 46
Fig. 2.19 Gray coding of (a) PAM2 and (b) PAM4 signals. 48
Fig. 2.20 (a) Set partitioning of PAM4 amplitude levels, (b) Set partitioning of 4D constellation, and (c) 8-state 4D-PAM4-TCM encoder structure. 48
Fig. 2.21 Spectra of (a) a DSB signal and (b) an SSB signal. FT{x}: Fourier transform of x.51
Fig. 2.22 (a) Schematic and DSP stacks of an SSB self-coherent system, (b) operating principle of an SSB self-coherent system. 53
Fig. 2.23 (a) Schematic and DSP stacks of a VSB self-coherent system, (b) operating principle of a VSB self-coherent system. 55
Fig. 2.24 (a) Power responses of trapezoidal optical filters with different edge gradients, and (b) magnitude responses of VSB systems enabled by optical filters with different edge gradients. 69
Fig. 3.1 (a) Frequency responses of pulse shaping filters designed for 81 Gbaud signals, and (b) PSDs of 81 Gbaud signals in the digital domain before being loaded to DAC channels when processed with different transmitter DSP combinations. (©2020 IEEE) 76
Fig. 3.2 A simplified model of a typical IM/DD system. E/O and O/E represent electro-optical conversion and opto-electrical conversion, respectively. (©2020 IEEE) 77
Fig. 3.3 (a) Experimental setup and (b) DSP stacks of 600Gb/s CWDM FTN IM/DD transmission systems. TEC: thermoelectric cooler. (©2020 IEEE)....79
Fig. 3.4 BER performance of individual wavelength channels and the aggregated signal at BtB for 4×81 Gbaud PAM4 transmissions with different transmitter-side DSP combinations when processed with (a) FFE and (b) post filter + MLSE aided FFE at the receiver. (©2020 IEEE) 80
Fig. 3.5 BER performance of individual wavelength channels and the aggregated signal at BtB for 4×81 Gbaud controlled-ISI pulse shaped PAM4 transmissions when processed with different DSP combinations. (©2020 IEEE)....82
Fig. 3.6 (a) BER performance of 4×81 Gbaud THP aided and post filter + MLSE aided controlled-ISI pulse shaped PAM4 signals at BtB and 2 km, and (b) BERs of the

aggregated signal as functions of ROPs at 2 km for 4×81 Gbaud controlled-ISI pulse shaped PAM4 signal when processed with 41-tap linear FFE or 101-tap linear FFE. (©2020 IEEE) 84

Fig. 3.7 BER performance of 4×81 Gbaud controlled-ISI pulse shaped PAM4 signals using 41/101-tap FFE + post filter +MLSE in each channel at BtB and 10 km. (©2020 IEEE) 85

Fig. 3.8 BER as a function of symbol rate in each wavelength channel for post-filter + MLSE aided controlled-ISI pulse shaped PAM4 transmissions over 10 km, when processed with (a) 41-tap linear equalizer and (b) VE with kernel memory length of (41,11,3) at the receiver. (©2020 IEEE) 86

Fig. 3.9 4D symbol wavelength distribution procedures for (a) conventional 4D-PAM4-TCM and (b) wavelength-interleaved 4D-PAM4-TCM. (©2020 IEEE)..... 90

Fig. 3.10 Experimental setup and DSP blocks for 4×100 Gb/s CWDM 4D-PAM4-TCM links. (©2020 IEEE) 92

Fig. 3.11 Different component matching configurations in for 4×100 Gb/s CWDM 4D-PAM4-TCM systems. (©2020 IEEE) 93

Fig. 3.12 SNR-ROP and BER-ROP relations of individual wavelength channels at BtB with different component matching configurations in the conventional 4D-PAM4-TCM case. (©2020 IEEE) 94

Fig. 3.13 BERs as functions of ROP per channel at BtB with different component matching configurations and different modulation formats. (©2020 IEEE) 95

Fig. 3.14 Histograms and PSDs of noise in the best/worst channel at BtB with different ROP and the bad component matching configuration. (©2020 IEEE)..... 96

Fig. 3.15 Simulated BER performance of 64 Gbaud single-channel (conventional) 4D-PAM4-TCM systems at BtB with the existences of (a) flicker noise and (b) clock leakage. 97

Fig. 3.16 SNR-ROP and BER-ROP relations of individual wavelength channels after transmission over 10 km with different component matching configurations in the conventional 4D-PAM4-TCM case. (©2020 IEEE) 98

Fig. 3.17 BERs as functions of ROP per channel after transmission over 10 km with different component matching configurations and different modulation formats. (©2020 IEEE) 99

Fig. 3.18 (a) SNR-ROP and (b) BER-ROP relations of individual wavelength channels after transmission over 20 km with the “good” component matching configuration in the conventional 4D-PAM4-TCM case, and (c) BERs as functions of ROP per channel after transmission over 20 km with different modulation formats using the “good” component matching configuration. (©2020 IEEE).....100

Fig. 4.1 Schematic of the SiPh ME-MZM. [Reprinted] with permission from [35] © The Optical Society. 102

Fig. 4.2 (a) Experimental Setup, inset shows the spectrum of a 56 Gbaud signal before filtering, the OBPF response and the spectrum of a 56 Gbaud signal after filtering, and (b) receiver DSP blocks. [Adapted] with permission from [35] © The Optical Society. 104

Fig. 4.3 (a) BER of 56 Gbaud DAC-less PAM4 at BtB versus oversampling ratio when processed with the KK algorithm and a linear FFE, and (b) typical linear FFE taps converged for 56 Gbaud PAM4 at BtB, 80km without CDC and 80 km with CDC, where the KK algorithm is used to reconstruct the RSB signal in all these cases. [Adapted] with permission from [35] © The Optical Society. 107

Fig. 4.4 (a) BERs as functions of nonlinear kernel memory lengths with different DSP combinations for a 56 Gbaud PAM4 at B2B with a launch power of -3 dBm, (b)/(c) BERs as functions of nonlinear kernel memory lengths for a 56 Gbaud PAM4 at 80km with a launch power of 8 dBm when processed without/with frequency-domain CDC, and (d) transmission performance of 56 Gbaud PAM4 at 80 km with different DSP combinations. [Adapted] with permission from [35] © The Optical Society. 108

Fig. 4.5 (a) BERs as functions of symbol rate at B2B, 40 km and 80 km with 7 dBm ROP, and (b) Receiver sensitivity requirements for a 56 Gbaud PAM4 signal at 40 km and a 60 Gbaud PAM4 signal at 80 km, when processed with 1) the KK algorithm and a short-memory VE, 2) the KK algorithm, a frequency domain CDC block, and a short-memory

VE. [Adapted] with permission from [35] © The Optical Society. 111
Fig. 4.6 (a) Optical filter response and (b) Spectrum of the received VSB signal.(©2020 IEEE)..... 113
Fig. 4.7 Receiver DSP blocks for studies on different KK algorithms. (©2020 IEEE)..... 117
Fig. 4.8 Experimental results (a) effective SNR vs. number of iterations in iter-KK/FA-iter-KK algorithms and (b) BER vs ROP requirement of KK/FA-iter-KK algorithms. (©2020 IEEE)..... 118
Fig. 4.9 (a) schematic of the simulation setup, (b) frequency responses of trapezoidal filters with different edge gradients, (c) and (d) simulated BER-OSNR relations with different optical filters when processed with different KK algorithms. (©2020 IEEE)..... 120
Fig. 4.10 CSPR control methods in VSB self-coherent systems. (a) Tuning the bias point of the modulator, (b) digital carrier generation, and (c) the parallel path scheme with a fixed ratio power splitter and a VOA. [Adapted] with permission from [37] © The Optical Society. 122
Fig. 4.11 (a) schematic of tunable power splitter based parallel path structure for CSPR controlling, and (b) layout of CSPR controllable SiPh VSB self-coherent transmitter circuit. [Adapted] with permission from [37] © The Optical Society. 124
Fig. 4.12 (a) Transmitter DSP, (b) receiver DSP and (c) experimental setup for the demonstration of a 112 Gb/s 16QAM transmission over 80 km using the tunable power splitter based SiPh circuit. [Adapted] with permission from [37] © The Optical Society. 125
Fig. 4.13 (a) Relations between measured CSPRs and the DC voltages applied to the thermal phase shifter, (b) VSB spectra with different CSPRs, (c) definitions of filter response, LSB and RSB signals used in the FA-iter-KK algorithm when applied to a VSB system that suppresses the RSB spectrum and (d) BERs of 28 Gbaud 16QAM at 80 km as functions of CSPR values when processed with the FA-iter-KK algorithm with different number of iterations. [Adapted] with permission from [37] © The Optical Society. 127
Fig. 5.1 Link model of a loss limited IQ modulator based SSB self-coherent system in which

the CSPR is controlled through bias tuning. (a) The schematic of the system, (b) the transmission model and (c) the power budget model. 131

Fig. 5.2 Link model of a loss limited IQ modulator based SSB self-coherent system in which the CSPR is controlled through the tunable power splitter based parallel path structure. (a) The schematic of the system, (b) the transmission model and (c) the power budget model.....134

Fig. 5.3 (a) Transmitter and (b) receiver DSP stacks used in the link models shown in Figs. 5.1 and 5.2.....136

Fig. 5.4 Effective SNRs and the total optical loss of the transmitter circuit as functions of the CSPR when using different CSPR control schemes and a peak-to-peak driving voltage of (a) $0.5V\pi$ and (b) $V\pi$ in an IQ modulator based SSB system.....137

Fig. 5.5 (a) The achievable BERs at the optimum CSPR and (b) the optimum CSPR as functions of $Vpp/V\pi$ when using different CSPR control schemes in an IQ modulator based SSB system. 139

Fig. 5.6 (a) Frequency response of a commercialized optical filter, and (b) zoom-in of the region used for VSB filtering.....141

Fig. 5.7 Link model of a loss limited VSB self-coherent system in which the CSPR is controlled through bias tuning. (a) The schematic of the system, (b) the transmission model and (c) the power budget model.....142

Fig. 5.8 Link model of a loss limited VSB self-coherent system in which the CSPR is controlled through the tunable power splitter based parallel path structure. (a) The schematic of the system, (b) the transmission model and (c) the power budget model.143

Fig. 5.9 Transmitter and receiver DSP stacks used in the link models shown in Figs. 5.7 and 5.8.....144

Fig. 5.10 (a) The achievable BERs at the optimum CSPR and (b) the optimum CSPR as functions of $Vpp/V\pi$ when using different CSPR control schemes in a VSB system. 145

Fig. 5.11 Schematics of (a) the KK algorithm, and (b) the KK algorithm with digital

resampling blocks. 150
Fig. 5.12 Schematics of (a) the iter-KK algorithm, and (b) the ufKK algorithm. [Adapted] with permission from [38] © The Optical Society. 150
Fig. 5.13 Principles of time-domain implementations of (a) digital upsampling and (b) digital downsampling. [Adapted] with permission from [38] © The Optical Society. 150
Fig. 5.14 Principles of (a) time-domain digital resampling and (b) frequency-domain digital resampling with rational resampling ratio. [Adapted] with permission from [38] © The Optical Society. 151
Fig. 5.15 Principle of frequency-domain digital resampling (with rational resampling ratio) merged with frequency down-conversion and a digital filter. (a) Slice the input sequence into overlapping sections, (b) concatenate the processed and shortened sections to form the output sequence, and (c) frequency-domain processing of each section. 152
Fig. 5.16 An alternative implementation of the frequency-domain processing block after the KK-family algorithm, where the DFT is shared between two parallel processing blocks. 154
Fig. 5.17 Schematics of the frequency-domain processing blocks at the transmitters in (a) an IQ modulator based SSB self-coherent system and (b) a VSB self-coherent system. 155
Fig. 5.18 Principle of frequency-domain implementation of Hilbert transform. (a) Slice the input sequence into overlapping sections, (b) frequency-domain processing of every two sections, and (c) concatenate the processed and shortened sections to form the output sequence. 156
Fig. 5.19 Practical implementation of the KK algorithm and the following frequency-domain processing. 157
Fig. 5.20 Practical implementations of (a) the iter-KK algorithm with 1 iteration and the following frequency-domain processing, and (b) the ufKK algorithm and the following frequency-domain processing. 158
Fig. 5.21 (a) Transmitter and (b) receiver DSP stacks used in an IQ modulator based SSB system for the power consumption analysis. 159

Fig. 5.22 (a) Effective SNRs as functions of the ADC sampling rate, (b) BERs as functions of the overlapping sequence length used in the Hilbert transform, and (c) BERs as functions of the overlapping sequence length used in the receiver-side frequency-domain processing block after the KK-family algorithm, when applying different KK-family algorithms in a 100 Gb/s 40 km IQ modulator based loss limited SSB self-coherent system. 162

Fig. 5.23 (a) Practical implementations of the FA-iter-KK algorithm with 1 iteration and the following frequency-domain processing block, (b)-(d) principle of filter response aware frequency-domain processing in the FA-iter-KK algorithm, (b) slice the input sequence into overlapping sections, (c) frequency-domain processing of every two parallel sections, and (d) concatenate the processed and shortened sections to form the output sequence. 167

Fig. 5.24 (a) Transmitter and (b) receiver DSP stacks used in a VSB system for the power consumption analysis. 168

Fig. 5.25 (a) BERs as functions of the ADC sampling rate, when applying different KK-family algorithms in a 100 Gb/s 40 km loss limited VSB self-coherent system, (b) BER as a function of the overlapping sequence length used in the frequency-domain operation in the FA-iter-KK algorithm, and (c) BER as a function of the overlapping sequence length used in the receiver-side frequency-domain processing block after the FA-iter-KK algorithm, when applying the FA-iter-KK algorithm in a 100 Gb/s 40 km loss limited VSB self-coherent system. 169

Fig. 5.26 Power response of the optical filter seen by the signal with different laser frequency offsets, and (b) BERs as functions of laser frequency offset with different laser output power. 175

List of Tables

Table 2.1 FEC thresholds of certain codes recommended for optical communications 16

Table 2.2 Impacts of CD-chirp interactions on pulses 21

Table 2.3 Small-signal channel response in push-pull MZM and EML based IM/DD systems 22

Table 2.4 Comparison of a selected group of systems with digital CD compensation capabilities 57

Table 3.1 Received RMS voltage after PD-TIA (mV) (©2020 IEEE) 81

Table 5.1 Parameters used in the link models of the loss limited IQ modulator based SSB self-coherent systems 135

Table 5.2 Energy consumption per DSP operation 147

Table 5.3 Numbers of real multipliers and adders required per FFT block 148

Table 5.4 Rx DSP parameters used in an IQ modulator based SSB system 163

Table 5.5 Power consumption of the ADC channel and the KK-family algorithm related DSP blocks 164

Table 5.6 Rx DSP parameters used in a VSB system 171

Table 5.7 Parameters of the laser model 172

Table 5.8 Tx system parameters and DSP parameters used in different systems 173

Table 5.9 Comparison of power consumption of an IQ modulator based SSB system and a VSB system (Excluding common parts) 174

Table 5.10 Comparison of power consumption of an IQ modulator based SSB system and a VSB system considering the laser frequency drifting (Excluding common parts) 176

List of Acronyms

AC	Alternating Current
ADC	Analog-to-Digital Converter
ASE	Amplified Spontaneous Emission
AWG	Arbitrary Waveform Generator
AWGN	Additive Gaussian White Noise
BER	Bit Error Ratio
BPD	Balanced Photodetector
BPG	Binary Pattern Generator
BtB	Back to Back
CAP	Carrier-less Amplitude Phase Modulation
CD	Chromatic Dispersion
CDC	CD compensation
CMOS	Complementary Metal-Oxide-Semiconductor
CSPR	Carrier-to-Signal Power Ratio
CW	Continuous Wave
CWDM	Coarse Wavelength Division Multiplexing
DAC	Digital-to-Analog Converter
DBR	Distributed Bragg Reflector
DC	Direct Current
DFB	Distributed-Feedback Laser
DFE	Decision Feedback Equalization
DFT	Discrete Fourier Transform
DML	Directly Modulated Laser
DMT	Discrete Multi-tone
DP	Dual Polarization
DSB	Double Sideband
DSP	Digital Signal Processing

DWDM	Dense Wavelength Division Multiplexing
EAM	Electro-Absorption Modulator
EDFA	Erbium-Doped Fiber Amplifier
EEPN	Equalization Enhanced Phase Noise
EML	Electro-absorption Modulated Laser
FA-iter-KK	Filter response Aware Iterative KK (algorithm)
FEC	Forward Error Correction
FFE	Feed-Forward Equalization
FFT	Fast Fourier Transform
FIR	Finite Impulse Response
FSM	Finite-State Machine
FTN	Faster-Than-Nyquist
FWHM	Full Width Half Maximum
FWM	Four Wave Mixing
GbE	Gigabit Ethernet
GVD	Group Velocity Dispersion
HD-FEC	Hard Decision Forward Error Correction
IA	Implementation Agreement
IDFT	Inverse Discrete Fourier Transform
IIR	Infinite Impulse Response
IM/DD	Intensity Modulation Direct Detection
InP	Indium Phosphide
I/O	Input/Output
IQ	In-phase/Quadrature
ISI	Inter-Symbol Interference
iter-KK	Iterative KK (algorithm)
KK	Kramers-Kronig
LMS	Least Mean Square

LO	Local Oscillator
LP	Linear Polarized
LPF	Low Pass Filter
LSB	Left Sideband
LUT	Look-Up Table
ME-MZM	Multi-Electrode MZM
MLSE	Maximum Likelihood Sequence Estimation
MMF	Multimode Fiber
MMI	Multimode Interferometer
MOSFET	Metal-Oxide-Semiconductor Field-Effect Transistor
MSA	Multi-Source Agreement
MSE	Mean Square Error
MZI	Mach-Zehnder Interferometer
MZM	Mach-Zehnder Modulator
NEP	Noise Equivalent Power
NLS	Nonlinear Schrodinger (equation)
ODUk	Optical channel Data Unit-k
OIF	Optical Internetworking Forum
OPUk	Optical channel Payload Unit-k
OTUk	Optical channel Transport Unit-k
PAM	Pulse Amplitude Modulation
PAPR	Peak-to-Average Power Ratio
PD	Photodetector
PDFA	Praseodymium-Doped Fiber Amplifier
PDM	Polarization Division Multiplexing
PFA	Prime Factor Algorithm
PSD	Power Spectral Density
PSM	Parallel Single Mode

QAM	Quadrature Amplitude Modulation
QCSE	Quantum-Confined Stark Effect
QSFP-DD	Quad Small Formfactor Pluggable Double Density
RC	Raised-Cosine (filter)
RF	Radio Frequency
RIN	Relative Intensity Noise
RMS	Root-Mean-Square
ROM	Read-Only Memory
ROP	Received Optical Power
RRC	Root-Raised-Cosine (filter)
RS	Reed Solomon (error correction)
RSB	Right sideband
RTO	Real-Time Oscilloscope
SCM	Sub-Carrier Multiplexing
SD-FEC	Soft-Decision Forward Error Correction
SE	Spectral Efficiency
SiPh	Silicon Photonics
SMF	Single Mode Fiber
SNR	Signal to Noise Ratio
SOA	Semiconductor Optical Amplifer
SOI	Silicon-on-Insulator
SP	Single Polarization
SPM	Self-Phase Modulation
Sps	Sample(s) per symbol
SQNR	Signal-to-Quantization Noise Ratio
SSB	Single Sideband
SSBI	Signal-to-Signal Beating Interference
SSC	Spot-Size Converter

SSFT	Split-Step Fourier Transform
SVE	Simplified Volterra Equalizer
SVR	Stokes Vector Receiver
TCM	Trellis Coded Modulation
TEC	Thermoelectric Cooler
THP	Tomlinson Harashima Precoding
TOSA	Transmitter Optical Sub-Assembly
TIA	Transimpedance Amplifier
ufKK	Upsampling-free KK (algorithm)
VCSEL	Vertical Cavity Surface Emitting Laser
VE	Volterra Equalizer
VGC	Vertical Grating Couplers
VOA	Variable Optical Attenuator
VSB	Vestigial Sideband
XPM	Cross Phase Modulation
ZF	Zero-Forcing
1D	One-Dimensional
2D	Two-Dimensional
4D	Four-Dimensional

Contents

Abstract i

Résumé iii

Acknowledgements v

Associated Publications vi

List of Figures viii

List of Tables xvi

List of Acronyms xvii

Contents xxii

Chapter 1 Introduction 1

1.1 State-of-the-art 1

1.2 Motivation 6

1.3 Original contributions 10

1.4 Thesis organization 13

Chapter 2 Fundamentals of IM/DD and SSB/VSB self-coherent systems 15

2.1 Overview 15

2.2 FEC in optical communication systems 15

2.3 Fundamentals of IM/DD systems 17

2.3.1 System Structure 17

2.3.2 Transmission Impairments 18

2.3.2.1 Inter-symbol interference 18

2.3.2.2 Noise 24

2.3.2.3 Loss 26

2.3.2.4 Device and fiber nonlinearity 26
2.3.3 DSP blocks 29
2.3.3.1 Overview 29
2.3.3.2 Pulse shaping 29
2.3.3.3 Equalization for ISI compensation 36
2.3.3.4 FTN techniques 45
2.3.3.5 Bit-to-symbol/symbol-to-bit mapping 47
2.3.3.6 Timing recovery 50
2.4 Fundamentals of SSB/VSB self-coherent systems 51
2.4.1 System Structure 51
2.4.2 Transmission impairments and Digital Compensation Methods 61
2.4.2.1 Overview 61
2.4.2.2 Signal-signal beating interference 61
2.4.2.3 CD 67
2.4.2.4 Other impairments 70
Chapter 3 O-band CWDM4 IM/DD systems 73
3.1 Overview 73
3.2 600 Gb/s Net Rate PAM4 Transmissions enabled by FTN techniques 73
3.2.1 Motivation 73
3.2.2 Operation Principle 75
3.2.3 Experimental setup and DSP blocks 78
3.2.4 Experimental results 80
3.2.4.1 When Less-Heavy Pre-emphasis meets FTN 80
3.2.4.2 600 Gb/s net rate transmission over 2 km 83

3.2.4.3 Towards 600 Gb/s Transmissions over 10 km 84
3.2.5 Summary 86
3.3 Wavelength-interleaved 4D-PAM4-TCM in a CWDM4 System 87
3.3.1 Motivation 87
3.3.2 Wavelength-interleaved 4D-PAM4-TCM 89
3.3.3 Experimental setup and DSP blocks 91
3.3.4 Experimental results and discussions 92
3.3.4.1 Component-induced inter-channel performance difference 92
3.3.4.2 BtB transmission results 94
3.3.4.3 Error floor of 4D-PAM4-TCM in a non-AWGN channel 95
3.3.4.4 10/20 km transmission results 97
3.3.5 Summary 100
Chapter 4 Amplified VSB self-coherent systems 101
4.1 Overview 101
4.2 SiPh DAC-less PAM4 system with a VSB self-coherent receiver 101
4.2.1 Motivation 101
4.2.2 DAC-less PAM4 modulation with SiPh ME-MZM 102
4.2.3 Experimental setup and DSP blocks 104
4.2.4 Experimental results and discussions 106
4.2.5 Summary 112
4.3 Filter response aware iterative KK algorithm for VSB systems 112
4.3.1 Motivation 112
4.3.2 The FA-iter-KK algorithm 113
4.3.3 Experimental setup and results 116

4.3.4 Numerical analysis and discussions 119
4.3.5 Summary 121
4.4 SiPh parallel path transmitter circuit for on-chip CSPR control 121
4.4.1 Motivation 121
4.4.2 CSPR control with a tunable power splitter 123
4.4.3 Experimental setup and results 125
4.4.4 Summary 128
Chapter 5 Towards loss limited SSB/VSB systems 129
5.1 Overview 129
5.2 On CSPR control schemes in loss limited self-coherent systems 129
5.2.1 Motivation 129
5.2.2 Link models of loss limited IQ modulator based SSB systems 130
5.2.3 On CSPR control schemes in a loss limited IQ modulator based SSB system 136
5.2.4 Link models of loss limited VSB systems 141
5.2.5 On CSPR control schemes in a loss limited VSB system 144
5.2.6 Summary 145
5.3 On power consumption of KK-family algorithms 146
5.3.1 Motivation 146
5.3.2 Fundamental building blocks of DSP algorithms 147
5.3.3 Frequency-domain digital resampling vs. time-domain digital resampling 149
5.3.4 Frequency-domain implementation of Hilbert transform 155
5.3.5 Power consumption of KK-family algorithms in a loss limited IQ modulator based SSB system 157
5.3.6 Power consumption of FA-iter-KK algorithm in a loss limited VSB system 165

5.3.7 Summary and discussions 176

Chapter 6 Conclusion 179

6.1 Summary of presented work 179

6.2 Future work 181

Reference 184

Chapter 1 Introduction

1.1 State-of-the-art

Driven by insatiable demand for video, data, and cloud based services, as well as the emergence of new applications such as big data, Internet of things and edge computing, the global data center traffic is continuously growing [1]. In recent years, significant research and development efforts have been directed towards short-reach optical communication systems for data center networking [2].

So, what's special about optical links in data center networks?

Firstly, compared to traditional long-haul transmission links in core networks which typically cover several thousands of kilometers of single mode fiber (SMF), optical links in data center networks have much shorter transmission distances. Specifically, the intra-data center connections (connections within one building or between buildings on a campus) generally cover distances up to 10 km, and the inter-data center connections (connections between data centers) generally cover distances up to 120 km[1][3].

Secondly, in data center networks, optical transceivers are required to be in small form factor modules such as quad small form factor pluggable double density (QSFP-DD)[2], which present a challenge to both component and digital signal processing (DSP) suppliers in terms of compact component designs and low electrical power consumption.

Thirdly, optical communication links in data center networks are optimized for the lowest cost per bit rather than the best transmission performance, e.g. the longest reach or the highest

---

[1] The OIF 400-ZR implementation agreement (IA) defines a maximum reach of 120 km for complete coverage [4]. Typical inter-data center connections are much shorter (less than 80 km). To guard against natural disasters and power outages, data centers should be far away, but to have low latency communication between them, they shouldn't be too far away. There is a trade-off and the magic distance is 80 km (which is also the typical span length of an EDFA based system). That's why we hear about 80 km data center interconnects a lot [5].

[2] Although most technical specifications such as the 400G-FR4 specification from 100 G lambda MSA [6] and the 400-ZR IA from OIF [4] do not directly pose restrictions on the physical form factor, the form factor is important since it affects the port density and the rack size, which translate to the size of data centers [2].

spectral efficiency (SE). Hence, when we design an intra-data center or inter-data center link, we always need to take into consideration the hardware complexity as well as the computational complexities of the DSP algorithms[3], since both of them contribute to the total cost of the system.

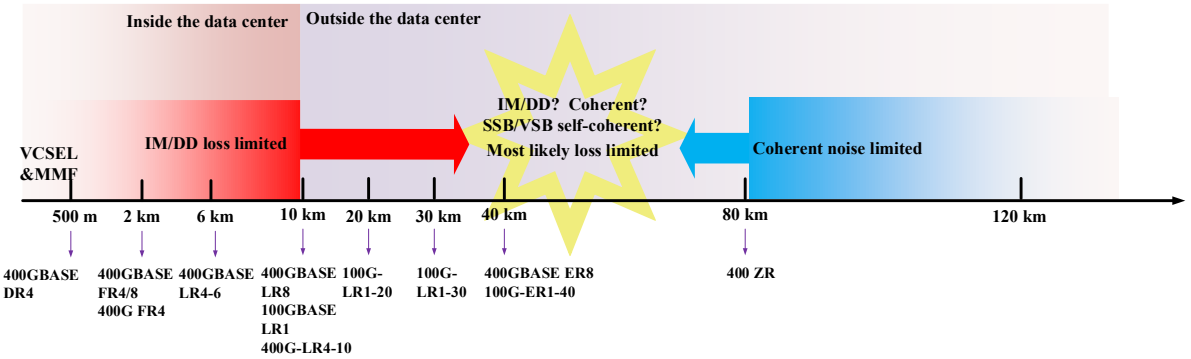

Fig. 1.1 Mainstream technologies used in data center networks.

Fig. 1.1 summarizes the mainstream optical communication technologies used in data center networks over different transmission distances. Currently, the server-to-server intra-data center connections below 500 m are dominated by vertical cavity surface emitting laser (VCSEL) transmitters and multimode fiber (MMF).

As the transmission distance scales to 500 m - 10 km, the inter-modal dispersion in the MMF becomes too severe, and the SMF becomes a default choice. In links below 10 km, intensity modulation direct detection (IM/DD) systems are much preferred than coherent systems[4], since the IM/DD systems are technologically simpler, more cost-effective, and intrinsically more compact. The main problem of an IM/DD system is that the achievable symbol rate is limited by the chromatic dispersion (CD)-induced power fading effect, which is difficult to be compensated for in the DSP. A simple method to work around this issue is to transmit the signals in the O-band (1260-1360 nm) instead of the C-band (1530-1565 nm), since the dispersion coefficient of the commonly used SMF-28 ultra fiber in the O-band is close to zero.

---

[3] The computational complexities of DSP algorithms affect the power consumption of the DSP chips, which then affects the operating expenditure of the system.

[4] In this thesis, for simplicity, we will use the terms “coherent/self-coherent detection system” and “coherent/self-coherent system” interchangeably.

However, the attenuation coefficient of the SMF-28 ultra fiber in the O-band is higher than that in the C-band[5][7]. Fortunately, the length scale of 500 m – 10 km is short enough such that optical amplification is still not required even if we use the O-band.

For links between 500m and 10 km, high-speed IM/DD transmissions have been demonstrated using different modulation formats, including 4-level pulse amplitude modulation (PAM4), discrete multi-tone (DMT) and carrier-less amplitude phase modulation (CAP)[9]-[13]. Among all these modulation formats, PAM4 has become the most widely adopted solution for 400 Gigabit Ethernet (GbE) applications. It has been selected in the IEEE 802.3bs-2017 standard, where 50 Gbaud PAM4 × 4 parallel single mode (PSM) fibers is used for the 500 m reach (400GBASE-DR4), and 25 Gbaud PAM4 × 8 wavelength division multiplexing (WDM) lanes at 800 GHz spacing is used for the 2 km (400GBASE-FR8) and 10 km reaches (400GBASE-LR8)[14]. In 2018, the 100 G Lambda Multi-Source Agreement (MSA) updated its 400G-FR4 technical specifications which also selected PAM4 as the modulation format, where 50 Gbaud PAM4 × 4 wavelengths on the 20 nm spacing coarse wavelength division multiplexing (CWDM) grid (i.e. 1271 nm, 1291 nm, 1311 nm and 1331 nm) is used for 2 km links [6]. To fully address the market requirements, the 100 G Lambda MSA has also announced release of a 400G-LR4-10 specification for 10 km links in Sept. 2020 [15], and the releases of 100G-LR1-20, 100G-ER1-30 and 100G-ER-40 specifications [16] in Nov. 2020 for 100 Gb/s single wavelength transmissions over 20 km, 30 km and 40 km reaches, respectively. In parallel, the IEEE 802.3cu 100 Gb/s and 400 Gb/s over SMF at 100 Gb/s per wavelength task force is working on standardization of 400GBASE-FR4/LR4-6 for 2 km/6 km links, which are also based on the 4-λ×100 Gb/s CWDM architecture, as well as standardization of 100 GBASE-LR1 for 10 km links which is based on 100 Gb/s/λ single wavelength operation [17].

As the transmission distance further increases, especially when it goes beyond 80 km, if we want to maintain a bit rate of 100 Gb/s/λ, O-band IM/DD transmission may not be a good choice, because:

1) At longer distance, the fiber loss in the O-band may lead to an extremely low received

[5] Corning's SMF-28 ultra fiber is compliant with ITU-T Recommendation G.652.D [8].

optical power (ROP) in a loss limited link, which will lead to an extremely low signal to noise ratio (SNR). Note that an O-band transmission system suffers from an additional fiber loss of at least 8 dB compared to a C-band transmission system at 80 km.

2) As the distance increases, the fiber loss increases, and optical amplification technologies may be acceptable in some cases (e.g. distance > 80 km). In the C-band, there exist mature optical amplification technologies, e.g. the erbium-doped fiber amplifier (EDFA), while its O-band equivalents either have worse noise figures (e.g. semiconductor optical amplifier (SOA)) or are more costly (e.g. praseodymium-doped fiber amplifier (PDFA)).
3) In a CWDM4 IM/DD system, the channel spacing is 20 nm. Even using O-band transmissions, as the distance increases, the accumulated CD in the edge channels may become severe especially when the symbol rate is high.
4) Since the CD is much weaker in the O-band, the phase-matching condition required by four wave mixing (FWM) is easier to be satisfied in the O-band [18]. Note that if we want to avoid optical amplifiers, we will have to increase the optical launch power for longer reaches. As a result, when the system is operating in the O-band, at longer distances, the FWM effect will be more severe and may significantly degrade the system's performance.

Hence, as the transmission distance keeps increasing, at some point, it could be beneficial to switch from the O-band to the C-band, since in the C-band, the SMF has lower loss, the optical amplifiers are more mature. The only problem is the CD, but the CD also helps to suppress the FWM. In fact, if we can get access to the complex-valued field information of the received waveform, the CD can be easily compensated for in the DSP. The most straightforward way to obtain the field information is to use a coherent system. In March 2020, the Optical Internetworking Forum (OIF) has published its implementation agreement (IA) for 400 ZR coherent optical interface [4], which proposes to use duo-polarization (DP) 16-ary quadrature amplitude modulation (16QAM), non-differential phase encoding/decoding, and a concatenated forward error correction (FEC) for 400 Gb/s per wavelength transmissions targeting the following two application scenarios:

1) 80-120 km amplified, point-to-point, dense WDM (DWDM) noise limited links with a

channel spacing of 75 GHz.

2) Unamplified, single wavelength loss limited links with shorter transmission distances (<80 km).

Nowadays (early 2021), it is fair to say that at least the inter-data center connections beyond 80 km are almost certain to be supported by DWDM C-band coherent systems such as the amplified version of the 400 ZR solution.

For shorter reaches, the 400 ZR IA proposes to use unamplified C-band coherent systems. Interestingly, the 400 ZR IA does not define a minimum reach in the unamplified case, which indicates that the coherent community has the ambition to further invade into the intra-data center market. Due to the developments of complementary metal-oxide-semiconductor (CMOS), integrated photonics and packaging technologies, the coherent transceivers are getting cheaper, smaller and more power efficient. Also, since the intra-data center traffic is ever-growing, loyal supporters of coherent technologies believe that, at some point, IM/DD systems just cannot support the required link throughput, and we will have to resort to the coherent solutions even inside the data center. It is possible that coherent systems may eventually dominate both the intra-data center and inter-data center connection markets, but as we will shortly see, the transition point has not arrived yet.

As of today, the release of the 400-ZR IA has not yet precluded the use of other solutions in unamplified links below 80 km. As we have mentioned, currently the intra-data center market (with reaches < 10 km) is still dominated by O-band IM/DD solutions (e.g. 400G/400GBASE-FR8/LR8/FR4/LR4). For reaches beyond 10 km and below 80 km, apart from the unamplified version of the 400 ZR solution, in addition to the 100G-LR1/ER1-20/30/40 MSA specifications mentioned previously, there also exists an IEEE 802.3 cn 400 GBASE-ER8 standard targeting reaches up to 40 km, which is based on an 8-λ ×50 Gb/s LAN-WDM (800 GHz spacing) O-band PAM4 IM/DD system [19]. But note that sticking to 4 wavelengths (or less) with a larger channel spacing would pose less challenges on the thermal stability and packaging requirement, hence there is also motivation to extend the reach of the 400G-LR4 solution (10 km). In addition, since the main challenge for a C-band IM/DD system at reaches beyond 10 km is the

CD induced power fading effect, one may consider upgrading an IM/DD system to a single sideband(SSB)/vestigial sideband(VSB) self-coherent system to incorporate digital CD compensation capability without resorting to a full coherent solution. Just like a coherent system, an SSB/VSB self-coherent system can compensate for the CD in the DSP since its receiver can retrieve the complex-valued field information of the detected waveform, but the hardware complexity of an SSB/VSB self-coherent system is only slightly higher than that of an IM/DD system, and much lower than that of a coherent system. It is still not clear which solution will win this market (reaches beyond 10 km and below 80 km). Most likely different technologies will just co-exist in the near future.

1.2 Motivation

Up to now we have described a big picture of the data center networking market. Fig. 1.2 shows the motivations of the research works that will be presented in this thesis. Our starting point is the IM/DD system, and in this thesis, we are going to upgrade the IM/DD system by adding new features to extend the its limit (either the speed or the reach). Note that in this thesis, the SSB/VSB self-coherent system is regarded as an upgrade of the IM/DD system, which incorporates both new DSP algorithms and extra hardware components.

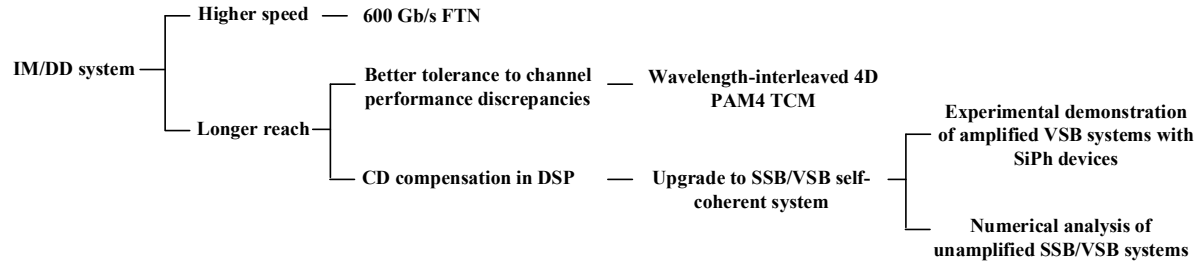

Fig. 1.2 Motivation of this thesis.

Firstly, there is motivation to further increase the throughputs of the current IM/DD solutions for intra-data center connections over 2-10 km since the intra-data center traffic is always growing. One of my research works that will be presented in this thesis is to use the faster-than-Nyquist (FTN) technology to improve the throughput of a 400Gb/s (net rate) O-band CWDM4 PAM4 IM/DD system over 2-10 km to 600 Gb/s (net rate) without upgrading the hardware.

Secondly, as we have said before, there is motivation to use IM/DD systems in links beyond 10 km while sticking to the CWDM4 structure, i.e. to extend the reach of the 400G-LR4 solution. Note that in a CWDM4 system, due to the component difference and the CD-chirp interaction induced power-fading effect, different wavelength channels will achieve different bit error ratios (BERs), which limits the overall transmission performance of the entire system. And since CD becomes more severe as the transmission distance increases, the channel performance discrepancies will increase at longer reaches. Another research work that will be presented in this thesis is to use the wavelength-interleaved four-dimensional trellis-coded modulation (4D-TCM) to improve the system's robustness against channel performance discrepancies in the CWDM4 architecture, and we found that this technique has the potential to increase the transmission distance of a 400Gb/s CWDM4 system to 20 km.

An alternative method to extend the reach of an IM/DD system is to enable CD compensation in the receiver DSP by upgrading an IM/DD system to an SSB/VSB self-coherent system, and once we obtain the CD compensation capability, we can transmit the signals in the C-band. In this thesis, I also studied the possibility of using C-band SSB/VSB self-coherent systems at reaches over 40-80 km. In general, there are two ways to generate an SSB/quasi-SSB signal:

1) use two digital-to-analog converter (DAC) channels to generate both the real part and the imaginary part of a complex-valued SSB signal, and then modulate the optical waveform using an In-phase and Quadrature (IQ) modulator (or other dual-drive modulator structures that can modulate a complex-valued waveform) [20]-[26],
2) use one DAC channel to generate a real-valued double sideband (DSB) signal and modulate it using a single-drive Mach Zehnder modulator (MZM), then use an optical filter to suppress half of the spectrum to generate a quasi-SSB signal [27]-[31].

The second scheme is often referred to as the VSB signal generation scheme in the literature [28]-[31], whose name stems from the fact that the unwanted sideband is usually not completely removed since the edge gradient of a practical optical filter cannot be infinitely large. From a research perspective, I am more interested in the VSB signal generation scheme, because:

1) The VSB scheme uses only one DAC channel at the transmitter, while the IQ modulator based scheme uses two DAC channels at the transmitter. The VSB scheme does require a sharp edge optical filter, but an optical filter is a passive device which does not consume power.
2) If the IQ imbalance can be neglected, the IQ modulator based SSB signal generation scheme can generate a rigorous SSB signal[6], while a VSB scheme can never generate a rigorous SSB signal due to the limited edge gradient of a practical optical filter. A key step in the receiver DSP of an SSB/VSB self-coherent system is to reconstruct the signal-signal-beating-interference-free (SSBI-free) field information of the received signal, and most of the existing algorithms are developed for rigorous SSB signals. In a sense, this is indeed a drawback of the VSB scheme, but it also indicates room for research. For instance, if we directly apply the existing algorithms to a VSB system, can the penalty be tolerated? And how can we modify the existing algorithms to better suit the quasi-SSB nature of the received signal in a VSB system?

Back in 2017-2019, when I was conducting most of my experimental works in this area, the OIF's 400-ZR IA was not published. At that time, there were still debates on which technology to use in the inter-data center connections, including both the unamplified loss limited case and the amplified noise limited case. Hence, most of my experimental works were focusing on VSB self-coherent systems targeting typical inter-data center connections over 80 km and did not preclude the use of EDFAs. Another reason to use EDFAs was that, I used silicon photonic (SiPh) devices in my experiments. I used vertical grating couplers (VGCs) as optical inputs and outputs (I/Os) of the SiPh chips to simplify the fiber alignment process, and the coupling loss of the VGCs has to be compensated for by EDFAs even in the back to back (BtB) configuration.

Now we know that at least for amplified links over 80-120 km, the SSB/VSB self-coherent system is not likely to be the path chosen by the industry in the end, the amplified DWDM

[6] The term "rigorous SSB" means that the unwanted sideband is completely removed. The IQ imbalance of a typical commercial IQ modulator is negligible [120].

version of the 400 ZR solution (i.e. a DP coherent solution) is likely to win this market. From the industry's perspective, actually there are only two directions, either using the IM/DD solution or using the coherent solution. At current stage, the SSB/VSB self-coherent system is still a toy of the academic research groups, which is still far from being commercialized. At reaches above 80 km, the optical amplifiers cannot be avoided anyway, hence we should use the C-band transmission to benefit from the maturity of the EDFA technology, then the coherent solution becomes the only commercially available option. The release of the 400 ZR IA indicates that, now the industry is ready to accept the cost of a full-coherent solution at reaches over 80 km-120 km. There is just no time for the SSB/VSB self-coherent system to grow into a competitor in this market.

The story is slightly different in loss limited links below 80 km, especially for reaches below 40 km. At these reaches, we don't need optical amplifiers, thus the O-band IM/DD system can still be used. The O-band IM/DD solutions and the C-band coherent solutions are likely to coexist in unamplified links over 10-80 km in the near future. The border between the "IM/DD realm" and the "coherent realm" is still to be determined. As long as there is competition, there could be a time window for alternative technologies to develop. If the SSB/VSB self-coherent systems still have chance, the chance lies in 100 Gb/s/λ (or beyond) loss limited unamplified links over 40 km. An O-band IM/DD systems may start to struggle at this rate and this distance because of the accumulated CD in the edge channels and the FWM issue when using the CWDM4 scheme, and an SSB/VSB self-coherent system provides an alternative solution to a full-coherent system which enables digital CD compensation and allows for C-band transmission.

Nevertheless, the experimental results obtained from the amplified VSB self-coherent systems over 80 km are still valuable, especially from a research point of view, since these results allow us to better understand the potentials and the limits of the VSB self-coherent system as an intermediate solution between the IM/DD system and the coherent system.

In addition, during the last year of my Ph.D. program (after the release of the 400 ZR IA), I numerically studied the transmission performance and the power consumption of unamplified

loss limited SSB/VSB self-coherent systems over 40 km, and this time, I considered both the IQ modulator based SSB system and the VSB system. I hope my analysis results can provide some guidance on practical implementations of SSB/VSB self-coherent systems.

1.3 Original contributions

This section summarizes the original contributions of this thesis.

O-band CWDM4 IM/DD systems

1) We propose to introduce a controlled amount of inter-symbol interference (ISI) during pulse shaping in a loss limited high symbol rate IM/DD system to increase the alternating current (AC) power of the received electrical signal after photo-detection and transimpedance amplification. The intentionally introduced ISI can then be mitigated using either the transmitter-side Tomlinson Harashima Precoding (THP) or the receiver-side feed forward equalization (FFE) aided with a 2-tap post filter and maximum likelihood sequence estimation (MLSE). Both methods allow us to achieve 4×81 Gbaud PAM4 ransmissions over 2 km with BERs below the hard decision FEC (HD-FEC) threshold of 3.8×10^{-3} using a commercial CWDM4-TOSA. We also demonstrate that by loading different symbol rates to different wavelength channels, we can further extend the reach to 10 km while maintaining an aggregated net rate beyond 600 Gb/s using the post filter + MLSE based ISI mitigation scheme. To the best of our knowledge, it was the highest reported transmission capacity by using PAM4 signaling in a CWDM4 IM/DD architecture for short-reach applications when this work was published [32],[33].
2) We propose to employ symbol-level wavelength-interleaving in conjunction with 4D-PAM4-TCM in the CWDM4 architecture to improve the system's robustness against channel performance discrepancies due to inter-channel component differences and the CD-chirp interactions. We experimentally prove that the proposed wavelength-interleaved 4D-PAM4-TCM scheme outperforms the conventional time-domain encoded 4D-PAM4-TCM scheme in a 400 Gb/s CWDM4 IM/DD transmission link over 0-20 km in terms of receiver sensitivity requirement at the KP4 FEC threshold of 2.26×10^{-4} when sizable channel performance discrepancies exist in such systems [34].

Amplified VSB self-coherent systems with SiPh devices

1) We propose and experimentally demonstrate for the first time a single wavelength 100 Gb/s DAC-less PAM4 modulation VSB self-coherent detection system over 40-80 km based on a SiPh multi-electrode MZM. The proposed system combines the hardware simplicity of a DAC-less intensity modulation transmitter and the CD compensation capability of a VSB self-coherent receiver. We systematically study the impacts of CD, SSBI, device nonlinearity and fiber nonlinearity on this system and the potential compensation methods [35].
2) In a VSB system, due to the limited edge gradient of the optical filter, the spectrum of the received signal is usually not strictly SSB. The under-filtered unwanted sideband could cause penalties to the conventional field reconstruction algorithms which are designed for rigorous SSB signals. To improve the field reconstruction accuracy in a VSB system, we propose a novel filter response aware iterative KK (FA-iter-KK) algorithm, which uses the frequency response information of the optical filter to facilitate the field reconstruction process. We experimentally verify that our proposed algorithm outperforms the conventional algorithms in a 100 Gb/s PAM4 system over 40-80 km, and we further show that this algorithm has the potential to relax the filter edge gradient requirement in a VSB system through numerical simulation [36].
3) An SSB/VSB self-coherent system requires a strong optical carrier to be inserted at the edge of the signal. In a practical system, the carrier-to-signal-power ratio (CSPR) needs to be carefully adjusted. In this thesis, we demonstrate a novel VSB self-coherent transmitter circuit with on-chip CSPR control capability on the SiPh platform. By using a parallel path structure, the demonstrated circuit enables CSPR control without the need to adjust the bias point of the modulator or sacrifice output levels of the DAC channels for digital carrier generation. In addition, we remove the need of a variable optical attenuator (VOA) in the parallel path structure by using an integrated tunable power splitter. We experimentally demonstrate a 100 Gb/s net rate 16QAM transmission over 80 km using this device [37].

Numerical analysis of unamplified SSB/VSB self-coherent systems

1) The parallel path structure based CSPR control scheme introduces more optical loss at the transmitter compared to the bias tuning based CSPR control scheme, which might be a problem in an unamplified loss limited system since it reduces the maximum achievable ROP. We build numerical models to simulate and compare the best achievable transmission performance of these two CSPR control methods when applied to a loss SSB/VSB self-coherent system over 40 km of SMF. We reveal that as long as we can achieve a large ratio of the peak-to-peak driving voltage to the modulator's half-wave voltage in the system, the parallel path structure based scheme can achieve better transmission performance than the bias tuning scheme even in a loss limited system.
2) A key step in the receiver DSP of an SSB/VSB self-coherent system is to reconstruct the complex-valued field information of the signal. If the received signal is a rigorous SSB signal, we can use the existing field reconstruction algorithms such as the Kramers Kronig (KK) algorithm, the iterative KK (iter-KK) algorithm and the upsampling-free KK (ufKK) algorithm, and if the received signal is not strictly SSB, we can use the FA-iter-KK algorithm proposed in this thesis. For simplicity, we will refer to these four algorithms as KK-family algorithms hereafter. The KK-family algorithms are often blamed for having high computational complexities, because these algorithms usually need to be implemented together with digital resampling blocks and require high sampling rates to accommodate the broadened spectra caused by nonlinear DSP operations. However, the current studies in the literature are mostly based on the assumption that the Hilbert transforms and the digital resampling blocks are implemented in the time domain using finite-impulse-response (FIR) filters, which actually overestimates the computational complexities the KK-family algorithms. In this thesis, we demonstrate how we can implement these blocks in the frequency domain to reduce the computational complexities of the KK-family algorithms [38]. We further estimate and compare the power consumption of all these four KK-family algorithms when applied to an SSB/VSB loss limited system over 40 km based on their computational complexities. We reveal that, in an IQ modulator based SSB system where the IQ imbalance can be neglected (i.e. a rigorous SSB system), the iter-KK algorithm with

1 iteration is the most power efficient option. In a VSB system, the FA-iter-KK algorithm is the only algorithm that can achieve a BER that is below the 6.7% overhead HD-FEC threshold. The power consumption of the FA-iter-KK algorithm with 1 iteration is slightly higher than that of the iter-KK algorithm with 1 iteration. But we also show that since a VSB system removes one DAC channel and one RF amplifier, and the transmitter DSP requires only the in-phase component at its output, a VSB system enabled by the FA-iter-KK algorithm with 1 iteration may still be more power efficient than an IQ modulator based SSB system enabled by the iterative KK algorithm with 1 iteration.

1.4 Thesis organization

The remainder of this thesis is organized as follows.

In Chapter 2, we provide the theoretical backgrounds of the IM/DD systems and the SSB/VSB self-coherent systems.

Chapter 3 presents our works on unamplified O-band CWDM4 IM/DD systems. Section Chapter 3 is an overview section. Section 3.2 presents our work on 600 Gb/s transmissions over 2 and 10 km enabled by the FTN technologies, which is based on our papers [32],[33]. Section 3.3 presents our work on the wavelength-interleaved 4D-PAM4-TCM scheme, which is based on our paper [34].

Chapter 4 presents our works on amplified C-band VSB systems based on SiPh devices. Section 4.1 is an overview section. Section 4.2 presents our work on 100 Gb/s DAC-less VSB-PAM4 transmission over 40-80 km with conventional field reconstruction algorithms, which is based on our paper [35]. Section 4.3 presents our work on the FA-iter-KK algorithm, which is based on our paper [36]. Section 4.4 presents our work on the SiPh parallel path structure with on-chip CSPR control capability, which is based on our paper [37].

In Chapter 5, we focus on numerical analysis results of unamplified C-band SSB/VSB self-coherent systems. Section 5.1 is an overview section. Section 5.2 describes the parameterized link models of loss limited SSB/VSB systems and compares the best achievable transmission performance of different CSPR control schemes using these link models. This work is was not published before. But the link models described in this section is the foundation of the work

presented in our paper [38] and section 5.3. Section 5.3 presents our work on the computational complexity/power consumption analysis of the KK-family algorithms. This section is an (tremendously) expanded and updated version of our conference paper [38].

Chapter 6 summarizes the key achievements of the works presented in the thesis. In addition, we point out some potential research directions in the future in this chapter.

Chapter 2 Fundamentals of IM/DD and SSB/VSB self-coherent systems

2.1 Overview

As we have mentioned in sections 1.1 and 1.2, we need low-cost short-reach optical communication systems to accommodate the ever-increasing data center traffic. Potential solutions include IM/DD systems, SSB/VSB self-coherent systems and coherent systems, and this thesis will focus on the first two solutions.

In order to focus more on our own contributions in the following chapters, I write this introductory chapter to review the fundamentals of the IM/DD systems and the SSB/VSB self-coherent systems. Readers who are familiar with modern short-reach optical communication technologies may skip this chapter, but they are always welcome to get back to refresh their memory whenever they encounter any confusing concepts or statements throughout this thesis.

2.2 FEC in optical communication systems

A modern optical communication system typically requires a BER of $< 10^{-15}$. To achieve such a low BER, we need FEC encoding before the transmitter-side DSP and FEC decoding after the receiver-side DSP as shown in Fig. 2.1. Directly estimating a post-FEC BER of around 10^{-15} is time consuming and resource demanding. In the development and optimization of modern optical communication systems, it is commonly accepted to separate the design and evaluation of the FEC code from the rest of the system, i.e. instead of measuring the post-FEC BER directly, we can measure the pre-FEC BER after the optical receiver and DSP but before FEC decoding, and then we will use the pre-FEC BER to predict the post-FEC BER performance of a certain FEC code[7] [39].

The pre-FEC BER required to achieve a target post-FEC BER is called the FEC threshold. Such FEC thresholds have been estimated for a variety of codes by dedicated FEC-decoding

[7] In the following chapters of this thesis, when we use the term “BER”, we are referring to the “pre-FEC BER” unless otherwise specified.

hardware, Monte-Carlo simulation data extrapolated to low post-FEC BERs, or analytic approximations, assuming a binary symmetric channel [39]. Table 2.1 summarizes the FEC thresholds of a selected group of codes considered in this thesis.

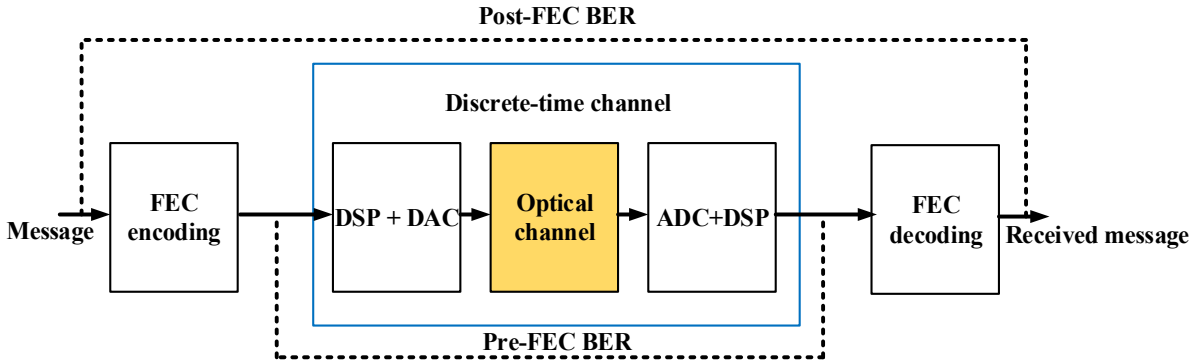

Fig. 2.1 Schematic of a modern optical communication system enabled by DSP and FEC.

Table 2.1 FEC thresholds of certain codes recommended for optical communications

Reference	Code type	Overhead	Post-FEC BER	FEC threshold
KP4 FEC [14][39]	Reed Solomon (RS) (544,514)	5.8%	1×10^{-15}	2.26×10^{-4}
HD-FEC [40][41]	Propretary "P-FEC"	6.7%	1×10^{-15}	3.8×10^{-3}
400-ZR SD-FEC [4]	Hamming(128,119)+ staircase (255, 239) "C-FEC"	14.8%	1×10^{-15}	1.25×10^{-2}

An important property of a FEC code is its coding rate. Assuming that we have a FEC code which encodes a k-bit stream into an n-bit stream, the coding rate $R = k/n$, and we have $0 < R < 1$, since a FEC code generally introduces redundancy to acquire error correction capability. Optical communications have historically preferred an equivalent notion of the coding rate: the overhead OH, which is defined as the ratio of the additional physical bit rate added by a system (or subsystem) to the physical bit rate entering the system (or subsystem). Based on this definition, the FEC overhead can be computed from the FEC coding rate as $OH = (1 - R)/R$. To achieve a net bit rate of X Gb/s using a FEC code with an overhead OH, we need a raw bit rate of $X(1 + OH)$ Gb/s.

In the literature, sometimes we see that a total bit rate of 112 Gb/s is required for 100 GbE applications considering the 6.7% FEC overhead [27]. This is because for Ethernet applications, in addition to the FEC overhead, people also need to consider the overheads of the optical channel payload unit-k (OPUk), the optical channel data unit-k (ODUk), and the optical channel transport unit-k (OTUk) [42]. Specifically, for 100GbE application, considering the

OPU4/ODU4/OTU4 overhead and an FEC overhead of 6.7%[8] and, we need a data rate of 112 Gb/s [43], hence if we consider the 400 ZR SD-FEC with an overhead of 14.8%, the required data rate is roughly $112(1+14.8\%)/(1+6.7\%) \approx 120$ Gb/s. But we have also seen papers in which the authors only consider the FEC overhead OH [24]. In that case, to achieve a net rate of 100 Gb/s, they need a raw rate of $100(1+OH)$ Gb/s. In this thesis, if the ratio of the total bit rate to the information bit rate equals to 1 plus the FEC overhead, then only the FEC overhead is considered. Otherwise, if the ratio of the total bit rate to the information bit rate is greater than 1 plus the FEC overhead, then both the FEC overhead and the OPUk/ODUk/OTUk overhead are considered.

2.3 Fundamentals of IM/DD systems

2.3.1 System Structure

The simplest optical communication system is an IM/DD system. To perform intensity modulation, one can either directly modulate the laser bias with the driving current or use a continuous wave (CW) laser followed by an external intensity modulator to decouple the light generation and the modulation mechanisms. Commonly used low-cost directly modulated lasers (DMLs) include distributed-feedback lasers (DFBs), distributed Bragg reflector (DBR) lasers, VCSELs and etc. As for the cases in which the lasers are externally modulated, two types of intensity modulators are often used: the electro-absorption modulator (EAM) and the MZM. The EAM and the laser diode are often integrated together on the same chip, such a device is called an electro-absorption modulated laser (EML). In general, DML and EML based solutions are cheaper and more compact than MZM based solutions. The benefit of using an MZM based solution is that, when the MZM is operated in the push-pull mode[9], chirp-free modulation can be achieved, i.e. one can modulate only the amplitude without changing the

[8] The OTUk frame structure include the FEC, the FEC in [42] is a RS(255,239) code, which has an overhead of 6.7%, hence we can assume that if we use the "P-FEC" [40][41] with the same overhead, the required data rate is the same.

[9] Push-pull operation means applying the RF signal X and its negation $\bar{X}$ to the two arms of the MZM. Note that push-pull operation does not necessarily require two driving signals. There also exist single-drive push-pull solutions which uses special electric designs to achieve on-chip generation of $\bar{X}$ from X [44].

phase. Thanks to the development of integrated photonics platforms, the sizes and the cost of MZM based solutions will keep decreasing, and using integrated MZMs in the IM/DD systems will be a future trend.

Fig. 2.2 shows the schematic of a typical single wavelength IM/DD system. Detailed descriptions of the DSP blocks will be provided in section 2.3.3. For now, we just focus on the hardware requirements. At the transmitter, a single wavelength IM/DD system requires only one DAC channel for radio frequency (RF) signal generation after applying transmitter-side DSPs. The generated signal is amplified by an RF amplifier (also known as an RF driver), and then applied to the intensity modulator (or the DML). At the receiver, a single wavelength IM/DD system requires only one single-ended PD to detect the signal. A transimpedance amplifier (TIA) can be used to amplify the received signal after photodetection. Then the amplified signal is sampled by an analog-to-digital convertor (ADC) channel before applying receiver-side DSPs.

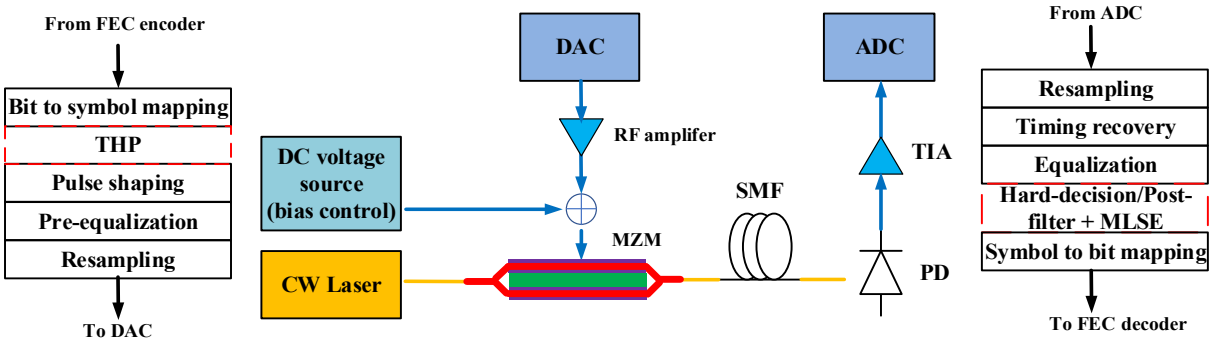

Fig. 2.2 Schematic of typical single wavelength IM/DD system.

For N-λ WDM operation, we need N of such single wavelength systems in parallel, each operating at a different wavelength, and we need to use a N-by-1 wavelength division multiplexer and a 1-by-N wavelength division demultiplexer to combine and separate different wavelength channels before and after the fiber.

2.3.2 Transmission Impairments

2.3.2.1 Inter-symbol interference

In a practical IM/DD system, the DAC, the RF amplifier, the intensity modulator/the DML, the PD, the TIA and the ADC have limited bandwidths. The frequency response of each component

imposes a low pass filter (LPF) on the signal, which broadens the optical pulses in the time domain and leads to inter-symbol interference (ISI). In an IM/DD system, the ISI caused by the bandwidth limitations of components exists even in the BtB configuration. Upon propagation, there is another source of ISI: the CD (and its interaction with the laser chirp).

CD can be understood as the frequency dependence of the refractive index $n(\omega)$, where ω represents the optical angular frequency. Mathematically, the CD in an SMF can be accounted for by expanding the mode-propagation constant β in a Taylor series about the pulse's center frequency ω_0:

$$\beta(\omega) = \beta_0 + \beta_1(\omega - \omega_0) + \frac{1}{2}\beta_2(\omega - \omega_0)^2 + \cdots \tag{2.1}$$

where the m^{th} order dispersion coefficient β_m is given by:

$$\beta_m = \left(\frac{d^m\beta}{d\omega^m}\right)_{\omega=\omega_0}, m = 0,1,2,\ldots \tag{2.2}$$

Specifically, β_1 and β_2 are related to the refractive index $n(\omega)$ through:

$$\beta_1 = \frac{1}{v_g} = \frac{n_g}{c} = \frac{1}{c}\left(n + \omega\frac{dn}{d\omega}\right) \tag{2.3}$$

$$\beta_2 = \frac{1}{c}\left(2\frac{dn}{d\omega} + \omega\frac{d^2n}{d\omega^2}\right) \tag{2.4}$$

where n_g and v_g are the group index and the group velocity, respectively. Note that the envelope of the optical pulse moves at the group velocity. β_2 characterizes the group velocity dispersion (GVD), thus is often referred to as the GVD coefficient in the literature. In optical communications, another widely used parameter to characterize the CD is the dispersion coefficient D, which is related to β_2 through:

$$D = \frac{d\beta_1}{d\lambda} = -\frac{2\pi c}{\lambda^2}\beta_2 \tag{2.5}$$

where λ is the wavelength of the light in the vacuum, and λ is uniquely linked to the angular frequency ω and the light speed in vacuum c through:

$$2\pi c = \lambda\omega \tag{2.6}$$

D is a function of λ or ω. For Corning SMF-28 ultra fiber, the dispersion coefficient $D(\lambda)$ can be approximated as:

$$D(\lambda) \approx \frac{S_0}{4}\left(\lambda - \frac{\lambda_D^4}{\lambda^3}\right)\text{ps/(nm}\cdot\text{km)}, \qquad \text{for } 1200\text{nm} \le \lambda \le 1600\text{nm} \tag{2.7}$$

where $S_0 = 0.092\ ps/(nm^2 \cdot \text{km})$ is the zero-dispersion slope, λ_D is the zero-dispersion wavelength, and we have $1302\ \text{nm} \leq \lambda_D \leq 1322\ nm$ [7]. According to Eq. 2.7, for any $\lambda > \lambda_D (\lambda < \lambda_D)$, we have $D > 0$ $(D < 0)$ and $\beta_2 < 0$ $(\beta_2 > 0)$.

Now we consider a series of optical pulses propagating in an SMF. Each pulse corresponds to a transmitted symbol. Due to the frequency dependence of the refractive index (i.e. the CD effect), in each pulse, different spectral components travel at different phase velocities. As a result, if there is no laser chirp, e.g. when an MZM is used in the push-pull mode for intensity modulation, the pulses will be broadened in the time domain, and each pulse will interfere with the pulses before and after itself, which leads to ISI.

If there is laser chirp, e.g. when a DML or an EML is used, the situation is more complicated. The laser chirp can be quantified via a parameter called the linewidth enhancement factor α [45],[46]. Given α, one can relate instantaneous frequency shift $\Delta f(t)$ to the optical modulation power $P(t)$ through:

$$\Delta f(t) = \frac{\alpha}{4\pi}\left(\frac{d\,[\ln P(t)]}{dt} + \kappa[P(t) - P_{bias}]\right) \tag{2.8}$$

The first and the second terms on the right-hand side of Eq. 2.8 are related to the transient chirp and the adiabatic chirp, respectively, where κ is the adiabatic chirp constant. If an EML is used, κ is close to zero, thus the system suffers only from the transient chirp, while a DML based system on the other hand, suffers from both the transient chirp and the adiabatic chirp. In the following chapters of this thesis, we will not study the DML based systems, thus we only consider the transient chirp hereafter.

The transient chirp term $\frac{\alpha}{4\pi}\frac{d\ln[P(t)]}{dt}$ depends on the logarithm of $P(t)$, which is a monotonically increasing function. At the rising (trailing) edge of a pulse, both $P(t)$ and $\ln[P(t)]$ increase (decrease) with time, thus the temporal derivative is positive (negative). Consequently, if α is positive, the transient chirp generates blue (red) shift in the pulse rising (trailing) edge, and if α is negative, the transient chirp generates red (blue) shift in the pulse rising (trailing) edge. Now we consider a wavelength channel with a negative β_2. A negative β_2 indicates that the group velocity increases as ω increases, i.e. the blue components travel faster than the red components. Therefore, if α is also negative, the trailing edge will travel

faster than the rising edge, and the pulse will be compressed when the propagation distance is short. However, as CD accumulates, the trailing edge will eventually overtake the rising edge and the pulse will be broadened again in the opposite direction. On the other hand, if α is positive, the rising edge travels faster than the trailing edge, and the pulse will always be broadened. One can easily generalize these conclusions to the positive β_2 cases[10]. The results are summarized in Table 2.2.

Table 2.2 Impacts of CD-chirp interactions on pulses

	$\alpha > 0$	$\alpha < 0$
$\beta_2 > 0$ $(D < 0)$	compress then broaden	broaden
$\beta_2 < 0$ $(D > 0)$	broaden	compress then broaden

Remember that the component bandwidth limitations also broaden the pulses in the time domain and would lead to ISI. Generally, to compensate for the ISI, one can use a linear feed forward equalizer (FFE) in DSP, as we will shortly see in section 2.3.3. The problem is that it will enhance the high-frequency noises. In the case where α and β_2 have opposite signs, the CD-chirp interaction always broadens the pulses. In other words, the CD-chirp interaction introduces more ISI to the system and increases the equalization enhanced noise after applying DSP, thus it degrades the BER performance. On the other hand, if α and β_2 have the same signs, the CD-chirp interaction first compresses the pulses when the accumulated CD is not too severe. In this case, the CD-chirp interaction partially compensates for the component-induced ISI that already exists in the system. As a result, the equalization enhanced noise is reduced, and the BER performance is improved. However, as the transmission distance increases, the CD-chirp interaction will eventually broaden the pulses again, which leads to more ISI and more equalization enhanced noise in the system, then the BER performance is degraded.

The above analysis helps us to qualitatively understand the impacts of CD and the CD-chirp interaction in an IM/DD system. Mathematically, the modulus of the small-signal transfer

[10] This is an explanation for readers who are more familiar with the linear chirp coefficient C defined in [18]. In [18], if C and β_2 have opposite signs, CD compresses the pulse. Note that in [18], if C is positive, ω increases with time in a pulse, i.e. the trailing edge has higher frequency than the rising edge, which is similar to the negative α case described in this thesis.

function of a dispersive IM/DD channel is given by:

$$H_{IM/DD}(\omega) = \left|\cos\left(-\frac{1}{2}\beta_2\omega^2 L\right) - \sin\left(-\frac{1}{2}\beta_2\omega^2 L\right) H_{IM\leftrightarrow PM}(\omega)\right| \tag{2.9}$$

where L is the transmission distance, ω is the angular frequency deviation from the central angular frequency of the laser, $H_{IM\leftrightarrow PM}(\omega)$ is the small-signal transfer function between phase and intensity modulations which characterizes the laser chirp. Table 2.3 summarize the $H_{IM\leftrightarrow PM}(\omega)$ and the resulted transfer function $H_{IM/DD}(\omega)$ in the push-pull MZM-based IM/DD system and the EML-based IM/DD system [46].

Table 2.3 Small-signal channel response in push-pull MZM and EML based IM/DD systems

Transmitter	$H_{IM\leftrightarrow PM}(\omega)$	$H_{IM/DD}(\omega)$
Push-pull MZM	0	$H_{MZM}(\omega) = \left\|\cos\left(-\frac{1}{2}\beta_2\omega^2 L\right)\right\|$
EML	α	$H_{EML}(\omega) = \left\|\sqrt{1+\alpha^2}\cos\left(-\frac{1}{2}\beta_2\omega^2 L + \tan^{-1}\alpha\right)\right\|$

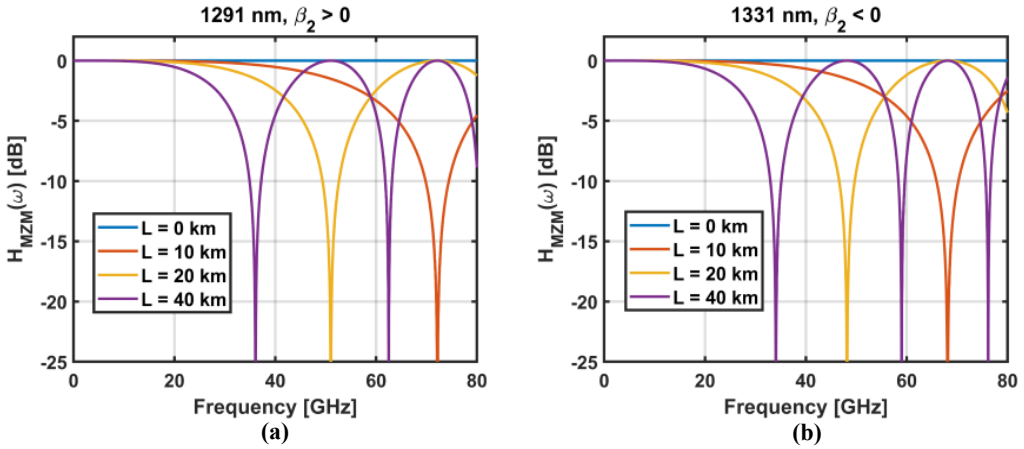

Fig. 2.3 Small-signal frequency responses of CD in push-pull MZM based IM/DD systems with different wavelengths and at different transmission distances.

Fig. 2.3 plots the small-signal frequency responses of CD in push-pull MZM based IM/DD systems with different wavelengths and at different transmission distances, where we assume $\lambda_D = 1310\ nm$. We observe frequency notches located at

$$f_{dip} = \frac{\omega_{dip}}{2\pi} = \sqrt{\frac{n+\frac{1}{2}}{2\pi|\beta_2|L}}, n = 0, 1, 2, \ldots \tag{2.10}$$

This phenomenon is known as the power fading effect, which is detrimental to the transmission performance, since the spectral information at those frequency notches will be lost and

equalizing the spectral components around frequency notches will result in significant equalization enhanced noise. Generally we only use the frequency regime before the first notch by limiting the symbol rate of the signal, then $H_{MZM}(\omega)$ can be regarded as an LPF, regardless of the sign of β_2. This LPF resulted from the accumulated CD will limit the channel bandwidth in a chirp-free IM/DD system, and will degrade the BER performance compared to the BtB case.

Similarly, we can plot the small-signal channel response of CD-chirp interactions in EML based IM/DD systems, as shown in Fig. 2.4. We observe that the linewidth enhancement factor α affects both the positions of the frequency notches and the heights of lobes. Interestingly, Fig. 2.4 indicates that the transient chirp can lead to some gain at specific frequency regions in the small-signal regime. This is because in a chirped system, both intensity and phase modulations exist. Upon propagation, the phase modulation can be transformed into intensity modulation and vice versa, which could evolve into an increase or decrease in the intensity modulation in some frequency spans.

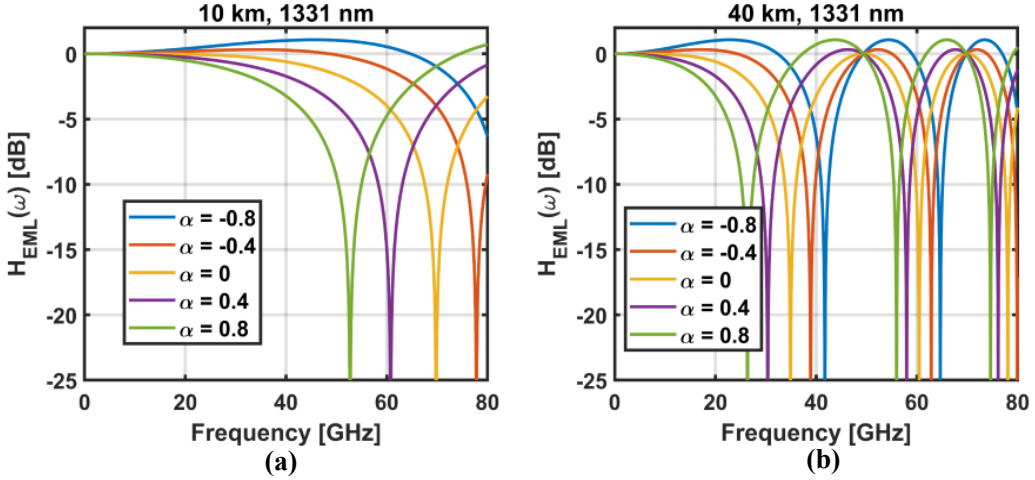

Fig. 2.4 Small-signal frequency responses of CD-chirp interactions in EML based IM/DD systems with different α values and transmission distances.

Again, we only look at the frequency regime before the first notch. If α and β_2 have the opposite signs, $H_{EML}(\omega)$ is always an LPF. It poses more burdens onto the digital equalizer, increases the equalization enhanced noise, and would degrade the BER performance. On the other hand, if α and β_2 have the same signs, $H_{EML}(\omega)$ becomes a peaking filter which

boosts the magnitude at a specified set of frequencies. In some cases, it is possible that this peaking filter could partially cancel the low-pass filtering effect due to the bandwidth limitation of components, thus the BER will be improved. In other cases, as CD accumulates, the superposition of $H_{EML}(\omega)$ and the component induced LPF leads to a more aggressive LPF, thus the BER performance is degraded.

2.3.2.2 Noise

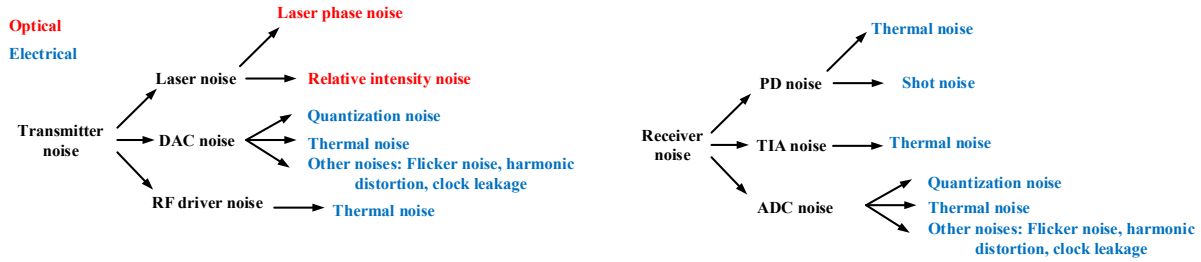

Fig. 2.5 Noise sources in an IM/DD system.

Fig. 2.5 summarizes the main sources of noises in a typical IM/DD system. Firstly, there is thermal noise from all electrical circuits, which is generated by the thermal agitation of the charge carriers (usually the electrons) inside an electrical conductor regardless of the applied voltage. Thermal noise can be approximated as additive Gaussian white noise (AWGN), whose one-sided power spectral density (PSD), or voltage variance (mean square) per hertz (Hz) of bandwidth is given by:

$$\overline{v_T^2} = 4k_B TR \tag{2.11}$$

where k_B is Boltzmann's constant in joules per kelvin, T is the temperature in kelvins, and R is the resistance in ohms.

In a PD, in addition to the thermal noise, there is also shot noise. Shot noise manifests the fact that an electric current consists of a stream of electrons generated at random times. The fluctuation of photocurrent due to shot noise can be modeled as a random process with Poisson statics, which is often approximated by Gaussian statics. The one-sided PSD of current fluctuation due to shot noise is given by:

$$\overline{I_s^2} = 2q(I_p + I_d) \tag{2.12}$$

where q is the electron charge, I_p and I_d are the average photocurrent and the dark current,

respectively. Eq. 2.12 shows that the PSD of shot noise (current noise) is constant, thus shot noise is also white.

In a practical system, since we use DAC and ADC channels with finite resolutions, there exists quantization noise. Quantization noise occurs whenever a continuous random variable is converted to a discrete one or a discrete random variable is converted to one with fever levels. The quantization noise can also be approximated as AWGN, and the signal-to-quantization-noise-ratio (SQNR) of a Q-bit ADC with a full-amplitude sine wave input is given by:

$$SQNR \approx 1.761 + 6.02Q\ dB \tag{2.13}$$

In modern metal-oxide-semiconductor field-effect transistor (MOSFET) devices like the DACs and the ADCs, there also exist other noise sources such as the harmonic distortions, the reference clock leakage, and the flicker noise (also known as 1/f noise) which mainly shows up at low frequencies.

Although a typical short-reach IM/DD system does not include an optical amplifier, there is still optical noise from the laser. The two major noise sources in a laser are 1) the phase noise and 2) the intensity noise. Laser phase noise follows a Wiener process, i.e. the result of the integral of a white Gaussian noise. Suppose the laser has a linewidth of Δv in Hz, the instantaneous frequency of the laser is a Gaussian variable with a variance given by:

$$\sigma_{PN}^2 = 2\pi\Delta v \tag{2.14}$$

Assuming that the phase noise results in a frequency modulation of $\exp\left(j\phi_{PN}(t)\right)$, the PSD of $\exp\left(j\phi_{PN}(t)\right)$ should follow a Lorentzian distribution [47] with a full-width at half-maximum of Δv. Although IM/DD system only detects the amplitude information, upon propagation, CD will convert frequency modulation to intensity modulation [46], thus the laser phase noise will also lead to intensity noise in an IM/DD system. Generally, the broader the laser linewidth is, the larger the resulted intensity noise will be.

The laser's intensity noise is related to the spontaneous emission in the laser cavity. Since the spontaneously emitted photons have random wavelengths, polarization, direction, and phase, they can coincide with the wavelength and the direction of the stimulate emitted photons and produce variation in the output intensity and frequency of the laser. The frequency variation

will lead to the laser phase noise, which has been addressed previously. To quantify the intensity noise of a laser, we usually use the relative intensity noise (RIN) value, which is defined as the ratio of the variance of the intensity noise to that of the squared average optical power. Assuming white noise, RIN is usually normalized to per 1-Hz bandwidth, and typical values range from -150 to -135 dBc/Hz.

2.3.2.3 Loss

Another important transmission impairment in the IM/DD system is the loss, which includes the excess loss of different components, the coupling loss at the fiber connectors, and the propagation loss due to the fiber attenuation. For Corning SMF-28 ultra fiber, the attenuation coefficient is ~0.03 dB/km in the O-band and ~0.02 dB/km in the C-band.

A typical short-reach IM/DD system does not include optical amplifiers (i.e. the system is loss limited), thus the ROP is determined by the laser output power and the total loss in the transmission link. Note that the ROP plays an important role in the achievable SNR at the receiver. If there is loss in the system, both the signal and the transmitter noise will be attenuated, but the power of the receiver noise is unaffected. By reducing the loss and increasing the ROP, we are indeed reducing the impact of the receiver noise on the system's performance until the system becomes limited by the transmitter noise.

2.3.2.4 Device and fiber nonlinearity

Up to now we assume that an IM/DD system is a linear system, i.e. the information will be linearly mapped from the electrical domain to the optical domain then back to the electrical domain, experience some ISI (linear filters), and corrupted with some additive noise. In the absence of noise, the end-to-end system response can be regarded as a single linear filter. This assumption is valid if the modulation is in the small-signal regime, the optical power launched into the fiber is not too high, and the transmission distance is not too long, so that the device and fiber nonlinearities can be neglected.

In a practical IM/DD system, there are three main sources of device nonlinearities: 1) the nonlinear transfer function of the modulators, 2) the saturations of the PDs and 3) the saturations of the RF amplifiers.

Remember that an IM/DD system detects the power of the signal, thus ideally, we should modulate the power of the signal. The power transfer function of an MZM is given by:

$$\frac{P_{out}}{P_{in}} = \frac{1}{2} + \frac{1}{2}\cos\big(\Delta\phi(t)\big) \tag{2.15}$$

where $\Delta\phi(t)$ is the phase difference between the two arms of the MZM. To achieve linear modulation, we need

$$\Delta\phi(t) = \frac{\pi}{2} + \eta s(t) \tag{2.16}$$

where $s(t)$ is the power-normalized target signal to be modulated and η is a scaling coefficient. Eq. 2.16 shows that if η is small enough, the output power of the MZM becomes linearly proportional to $s(t)$. The $\frac{\pi}{2}$ term in Eq. 2.16 denotes the bias point of the MZM, i.e. without modulation, the MZM should have a static phase difference of $\frac{\pi}{2}$ between the two arms, so that the MZM is biased at the middle point of the linear region of the power transfer function. However, as the driving voltage increases (as η increases), the small-signal modulation assumption is no longer valid, and the mapping from $s(t)$ to P_{out} becomes nonlinear since Eq. 2.15 is a nonlinear function.

The above analysis assumes that the mapping from the driving voltages to the phases in the MZM arms is linear. For MZMs based on Pockels effect such as the lithium niobate MZM, this assumption is valid. However, for MZMs fabricated on other platforms such as the Indium phosphide (InP) MZM based on the quantum-confined Stark effect (QCSE) [48] and the silicon MZM based on the plasma dispersion effect [49], this linear mapping assumption is only valid when the modulation is weak. In a practical system, the nonlinear mapping from driving voltages to the phase differences also contributes to the modulator nonlinearity.

Similarly, for the Franz-Keldysh effect based EMLs [50], we have the power transfer function:

$$\frac{P_{out}}{P_{in}} = \exp(-\alpha(t)L) \tag{2.17}$$

where L is the length of the EAM, and $\alpha(t)$ is the modulated absorption coefficient. Due to the nonlinear mapping from the driving voltage to $\alpha(t)$ and the nonlinear shape of Eq. 2.17, the linear modulation assumption is only valid when the swing of the driving voltage is small.

A PD converts an optical waveform to an electrical current. Generally, a linear relationship

exists between the incident optical power and the generated photocurrent. However, when the output photovoltage (the product of photocurrent and the load resistance) approaches the reverse bias voltage, the PD saturates, i.e. no additional photocurrent will output from the PD as the incident optical power increases. In other words, the mapping between the optical power to the photocurrent (or photovoltage) becomes nonlinear when the ROP is too high. Note that even if the averaged ROP is small, if the peak-to-average power ratio (PAPR) is high, the peak ROP may still exceeds the saturation threshold and lead to device nonlinearity.

In addition, a typical RF amplifier only delivers the gain up to a certain power level before it hits saturation. As the electrical power approaches the saturation level, the gain will be compressed, and the transfer function of the amplifier becomes nonlinear accordingly.

Another important source of nonlinear impairment in an optical communication system is the fiber nonlinearity. In silica fibers, only third order nonlinear effects exist [18]. The third order nonlinear effect (also known as the Kerr nonlinear effect) in an SMF is governed by the nonlinear Schrodinger (NLS) equation:

$$\frac{\partial A}{\partial z}+\frac{\alpha_{att}}{2}A+\beta_1\frac{\partial A}{\partial t}-\frac{j\beta_2}{2}\frac{\partial^2 A}{\partial t^2}=-j\gamma|A|^2A \tag{2.18}$$

where $A(z,t)$ is the electric field of the optical pulse, α_{att} is the attenuation coefficient of the fiber, and γ is the Kerr parameter. The time derivative terms account for the impacts of the group velocity mismatch induced walk-off effect and the GVD. The $-j\gamma|A|^2A$ term indicates that the Kerr nonlinear effect is indeed a perturbation of the refractive index response to the applied electric field $A(z,t)$, and the index change is proportional to $|A|^2$.

Eq. 2.18 models many nonlinear effects in a fiber, including self-phase modulation (SPM), cross phase modulation (XPM) and four wave mixing (FWM).

FWM can be understood as interactions between three wavelengths which produce a new wavelength. Suppose that the angular frequencies and the wave numbers correspond to those four wavelengths are $\omega_{1,2,3,4}$ and $k_{1,2,3,4}$, respectively, we have:

$$k_i=\frac{\omega_i n_i}{c}, i=1,2,3,4 \tag{2.19}$$

where n_i is the refractive index in each wavelength channel. FWM requires:

$$\omega_1 + \omega_2 = \omega_3 + \omega_4 \tag{2.20}$$

and

$$k_1 + k_2 = k_3 + k_4 \tag{2.21}$$

Eq. 2.21 is often referred to as the phase-matching condition in the literature.

In fact, SPM and XPM are just special cases of FWM, where we have:

$$\begin{cases} \omega_1 = \omega_2 = \omega_3 = \omega_4, & \text{for SPM} \\ \omega_1 = \omega_4, \omega_2 = \omega_3, & \text{for XPM} \end{cases} \tag{2.22}$$

Eq. 2.22 shows that in the SPM/XPM case, the phase-matching condition is satisfied automatically. Except for those special cases, in general, the phase-matching condition of FWM is difficult to be satisfied due to the accumulated CD especially when we transmit the signal in the C-band. However, if all the wavelengths are close to the zero-dispersion wavelength λ_D, the phase-matching condition can be satisfied more easily. FWM generates new and undesired signals of growing power with distance at frequencies that match those of existing signals in a fix-grid WDM system, thus it can severely degrade the performance of an O-band WDM systems. Consequently, when we design an O-band WDM system, we should confine the launch power and the transmission distances to avoid the onset of FWM.

2.3.3 DSP blocks

2.3.3.1 Overview

In this section, we will introduce several important DSP algorithms that are frequently used in typical IM/DD systems. We are not providing a thorough review of all the popular DSP algorithms in modern IM/DD systems. Instead, we only cover those algorithms that we used in our own experiments, as well as some other algorithms which we believe are beneficial to understand since they are closely related to the algorithms used the following chapters.

2.3.3.2 Pulse shaping

Transmitting a high symbol rate signal through a band-limited channel leads to ISI. Pulse shaping changes the waveform of the signal to limit its effective bandwidth, so that the ISI caused by the channel bandwidth limitation can be kept in control. There exist many different pulse shaping filters in the literature, among which we would like to focus on a special group of filters called Nyquist pulse shaping filters. As suggested by its name, a Nyquist pulse shaping

filter meets the Nyquist ISI criterion, i.e. the filter itself does not introduce ISI.

Theoretically, the best Nyquist pulse shaping filter is the sinc filter, which is a sinc function in the time domain and a rectangular function in the frequency domain. Eq. 2.23 and Eq. 2.24 show the impulse response and the frequency response of the sinc filter, respectively, where T is the symbol duration.

$$h(t) = \frac{1}{T} sinc\left(\frac{t}{T}\right), \qquad sinc(x) = \frac{\sin(\pi x)}{\pi x} \tag{2.23}$$

$$H(f) = \begin{cases} 0, |f| > \frac{1}{2T} \\ \frac{1}{2}, |f| = \frac{1}{2T} \\ 1, |f| < \frac{1}{2T} \end{cases} \tag{2.24}$$

The sinc filter is an ideal LPF since it perfectly passes (cuts) low (high) frequencies. Unfortunately, this filter can only be approximated in practice, since an ideal sinc filter is non-causal and requires infinite taps in the time domain.

A more commonly used Nyquist pulse shaping filter is the raised-cosine (RC) filter, the impulse response and frequency response of which are summarized as Eq. 2.25 and Eq. 2.26, where the parameter β is called the roll-off factor.

$$h(t) = \begin{cases} \frac{\pi}{4T} sinc\left(\frac{1}{2\beta}\right), t = \pm\frac{T}{2\beta} \\ \frac{1}{T}\text{sinc}\left(\frac{t}{T}\right)\frac{\cos\left(\frac{\pi\beta t}{T}\right)}{1-\left(\frac{2\beta t}{T}\right)^2}, otherwise \end{cases} \tag{2.25}$$

$$H(f) = \begin{cases} 0, |f| \geq \frac{1+\beta}{2T} \\ \frac{1}{2}\left[1+\cos\left(\frac{\pi T}{\beta}\left[|f| - \frac{1-\beta}{2T}\right]\right)\right], \frac{1-\beta}{2T} < |f| < \frac{1+\beta}{2T} \\ 1, |f| \leq \frac{1-\beta}{2T} \end{cases} \tag{2.26}$$

Fig. 2.6 plots the impulse responses and frequency responses of several RC filters with different roll-off factors.

In practical systems, due to the existences of white noise, people sometimes use two root-raised-cosine (RRC) filters at both the transmitter- and the receiver-side to perform matched

filtering, rather than use a single RC filter at the transmitter. The name of RRC filter stems from the fact that its frequency response is the square root of that of a RC filter. The combination of two RRC filters leads to an RC filter. The impulse response and frequency response of the RRC filter are given by Eqs. 2.27 and 2.28, respectively. Fig. 2.7 shows the impulse and frequency responses of RRC filters with different roll-off factors.

$$h(t) = \begin{cases} \frac{1}{T}\left(1+\beta\left(\frac{4}{\pi}-1\right)\right), t = 0 \\ \frac{\beta}{\sqrt{2}T}\left[\left(1+\frac{2}{\pi}\right)\sin\left(\frac{\pi}{4\beta}\right)+\left(1-\frac{2}{\pi}\right)\cos\left(\frac{\pi}{4\beta}\right)\right], t = \pm\frac{T}{4\beta} \\ \frac{1}{T}\frac{\operatorname{sinc}\left(\frac{t\pi}{T}(1-\beta)\right)+\frac{4\beta t}{T}\cos\left(\frac{\pi t}{T}(1+\beta)\right)}{\frac{\pi t}{T}\left[1-\left(\frac{4\beta t}{T}\right)^2\right]}, otherwise \end{cases} \quad (2.27)$$

$$H(f) = \begin{cases} 0, |f| \geq \frac{1+\beta}{2T} \\ \sqrt{\frac{1}{2}\left[1+\cos\left(\frac{\pi T}{\beta}\left[|f|-\frac{1-\beta}{2T}\right]\right)\right]}, \frac{1-\beta}{2T} < |f| < \frac{1+\beta}{2T} \\ 1, |f| \leq \frac{1-\beta}{2T} \end{cases} \quad (2.28)$$

Unlike an RC filter, the impulse response of a single RRC filter is not zero at the intervals of $\pm T$ unless $\beta = 0$, i.e. a single RRC filter does introduce ISI. Therefore, RRC filters have to be used in pairs, since the combination of two RRC filter results in an RC filter.

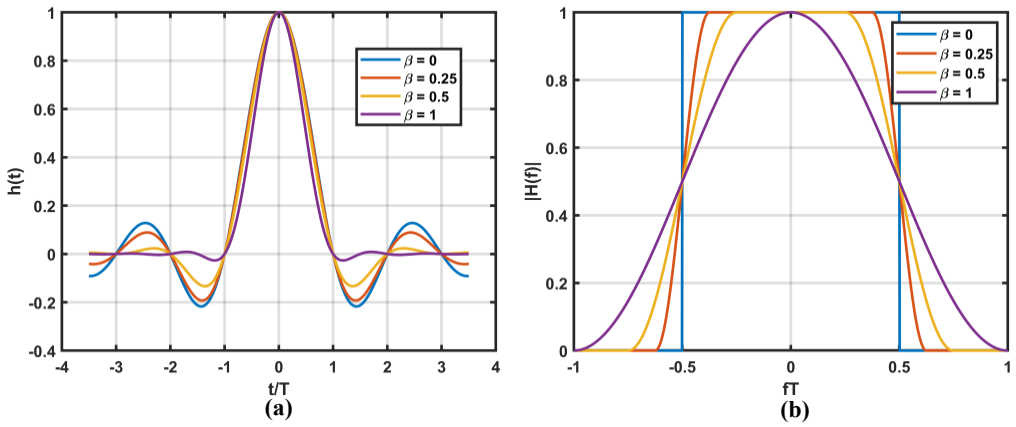

Fig. 2.6 (a) impulse responses and (b) frequency responses of RC filters with different roll-off factors.

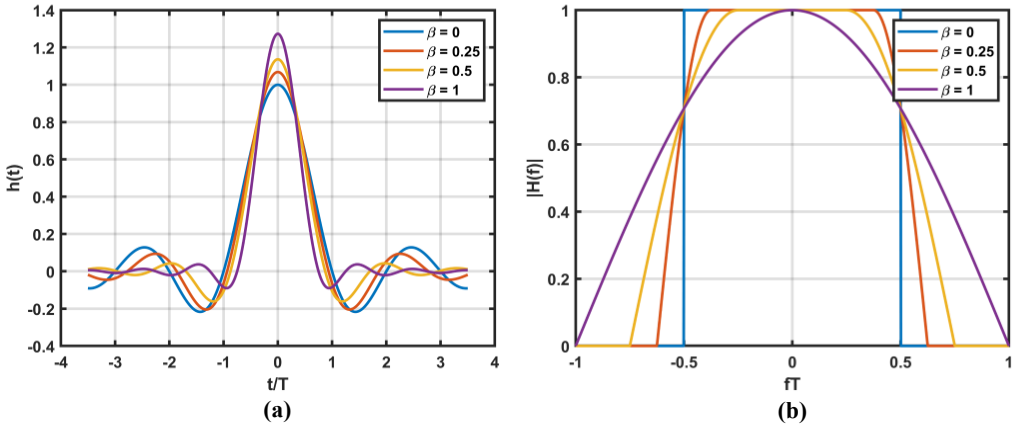

Fig. 2.7 (a) impulse responses and (b) frequency responses of RRC filters with different roll-off factors.

Before we move on to discuss about other DSP blocks, I would like to introduce another popular pulse shaping scheme called "duobinary shaping". Although we didn't use duobinary shaping directly in our experiments, we used FTN signaling, and as we will shortly see in section 2.3.3.4, duobinary shaping is a special case of FTN signaling.

The impulse response of duobinary shaping can be described as:

$$h(t) = \delta(t) + \delta(t - T) \tag{2.29}$$

Eq. 2.29 indicates that duobinary shaping can be easily implemented as a 2-tap FIR filter at 1 sample per symbol (Sps), as shown in Eq. 2.30.

$$y[n] = x[n] + x[n-1] \tag{2.30}$$

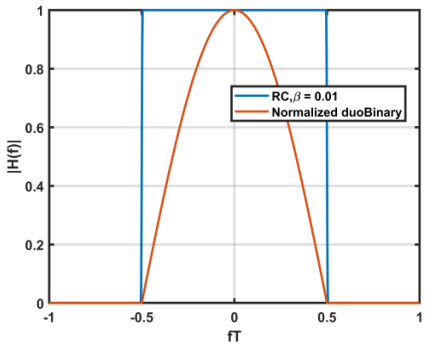

Fig. 2.8 Frequency responses of normalized duobinary shaping filter and an RC shaping filter.

The normalized frequency response of a duobinary shaping filter is plotted in Fig. 2.8. For comparison, the frequency response of an RC filter with a roll-off factor of 0.01 is also plotted in the same figure. As we can see, compared to RC pulse shaping, duobinary shaping concentrates more power to lower frequencies and reduces the 3 dB bandwidth of the signal,

which makes it more appealing in systems with extremely low bandwidths.

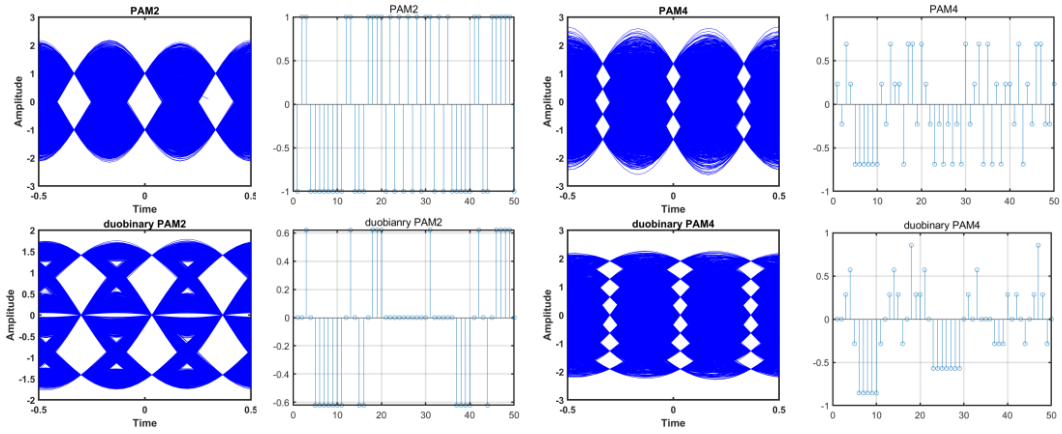

Fig. 2.9 Eye diagrams and time-domain symbol sequences of PAM2, duobinary PAM2, PAM4 and duobinary PAM4 signals.

The problem is that the duobinary shaping filter does not satisfy the Nyquist ISI criterion. In fact, it introduces severe ISI. Fig. 2.9 shows the eye diagrams and the time-domain symbol sequences of noiseless PAM2/PAM4 signals before/after duobinary shaping. No component bandwidth limitation is considered here, the only source of ISI is the duobinary shaping filter itself. We observe that a duobinary shaping filter transforms a PAM2/PAM4 signal into a PAM3/PAM7 signal. Fortunately, the ISI introduced by duobinary shaping rigorously follows Eq. 2.30. One can recover the original PAM2/PAM4 signal from the noise contaminated PAM3/PAM7 signal at the receiver using MLSE, since the ISI is known.

A detailed description of MLSE can be found in [51], here we use the duobinary PAM4 signal as an example to illustrate the process of MLSE using Viterbi algorithm. Suppose that the original PAM4 symbol sequence $I[k]$ has an alphabet of {-3,-1,1,3}, and we have $I[k] = 0$ for $k \leq 0$. The duobinary shaped sequence at the receiver can be described as $v[k] = I[k] + I[k-1] + \eta[k]$, where $\eta\,[k]$ is a sequence of statistically independent zero-mean Gaussian noise. Our purpose is to recover the sequence $I[k]$ from the received sequence $v[k]$. Since we know $I[0] = 0$, and both $I[1]$ and $I[2]$ have four possible values, we can compute 16 metrics

$$PM_1(I[2], I[1]) = \sum_{k=1}^{2} \left(v[k] - \sum_{j=0}^{1} I[k-j] \right)^2, \; I[1], I[2] = \pm 1, \pm 3 \qquad (2.31)$$

Some readers may have already realized that Eq. 2.31 is indeed the Euclidean distance between the noise contaminated received two-dimensional (2D) vector $(v[1], v[2])$ and a possible noiseless 2D vector $(I[0] + I[1], I[1] + I[2])$. Note that any subsequently received symbol $v[k], k > 2$ does not involve $I[1]$, thus at this point we may discard 12 of the 16 possible pairs $\{I[1], I[2]\}$, as is illustrated by the tree diagram shown in Fig. 2.10. Specifically, we discard 3 out of the 4 paths that terminate with a certain $I[2]$ value, and we save the most probable path. For example, for a path terminating with $I[2] = 3$, we choose the surviving path with the metric:

$$PM_1(I[2] = 3, I[1]) = \min_{I[1]} \left(\sum_{k=1}^{2} \left(v[k] - \sum_{j=0}^{1} I[k-j] \right)^2 \right), \qquad (2.32)$$

$$I[1] = \pm 1, \pm 3$$

This process will be repeated for each set of four paths terminating with $I[2] = \pm 1, \pm 3$. Only 4 paths and their corresponding metrics survive after receiving $v[1]$ and $v[2]$.

Then $v[3]$ arrives, the four surviving paths are extended as shown in Fig. 2.10 to yield 16 paths and 16 corresponding metrics given by

$$PM_2(I[3], I[2], I[1]) = PM_1(I[2], I[1]) + \left(v[3] - \sum_{j=0}^{1} I[3-j] \right)^2, \qquad (2.33)$$

$$I[3] = \pm 1, \pm 3$$

Again, of the four paths terminating with a certain $I[3]$ value, we only keep the most probable path. As a result, only four out of 16 paths survive at this stage. This procedure will then be repeated for each subsequently received $v[k]$ with $k > 3$.

The Viterbi algorithm described above maintains 4 surviving sequences. Upon reception of a new symbol $v[k]$, the 4 sequences are extended by one stage, and the corresponding 16 probabilities for the extended sequences are computed. These 16 sequences are subdivided into 4 groups corresponding to the 4 possible choices of $I[k]$, and the most probable sequence from each group is selected. The other 3 sequences are discarded, so that after this stage there is still only four surviving sequences. As we receive more symbols, the surviving sequences will

become longer and longer. It is impossible to store all the surviving sequences with ever increasing lengths. Instead, we make decisions after a fixed delay of q symbols. The value of q needs to be sufficiently large to ensure that all the four surviving sequences have identical symbols with a probability very close to 1 at the time q symbols ago, i.e., upon reception of $v[k]$, all four sequences have identical $I[k-q]$'s. From our experience, we found that for duobinary PAM4 signals, the performance loss is negligible when $q > 40$. Consequently, the surviving sequences can be truncated to the q most recent symbols, and only $4q$ symbols need to be stored. Note that only the surviving sequences are truncated, the metric associated with each sequence still contains information of all previously received symbols.

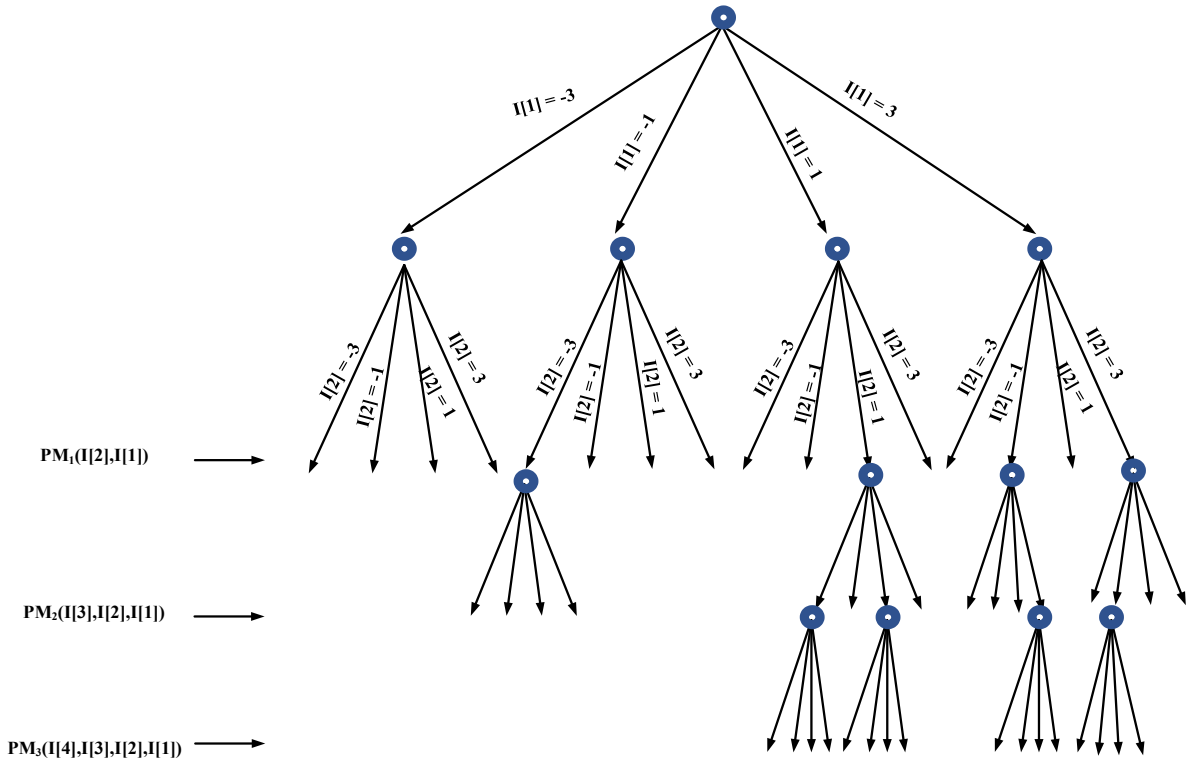

Fig. 2.10 Tree diagram for Viterbi decoding of duobinary PAM4 signal.

MLSE is one way to recover the original signal from the duobinary shaped signal. Another way is based on precoding. We still use duobinary PAM4 as an example to explain the process. The precoding procedure of a PAM4 signal can be implemented as following:

$$I_{enc}[k] = (I[k] - I_{enc}[k-1])\ mod\ 4 \tag{2.34}$$

where $I[k]$ and $I_{enc}[k]$ represent the original and encoded PAM4 signals, respectively. Note that here we assume that $I[k]$ has an alphabet of $\{0, 1, 2, 3\}$ instead of {-3,-1,1,3}. The

modulo operation in Eq. 2.34 simply adds multiples of 4 to $(I[k] - I_{enc}[k-1])$ to guarantee that $I_{enc}[k]$ is still a 4-level signal with the same alphabet, thus we can rewrite Eq. 2.34 into the following form

$$I_{enc}[k] = I[k] - I_{enc}[k-1] + 4d[k], d[k] \in Z \tag{2.35}$$

Then we apply the duobinary shaping filter to $I_{enc}[k]$ following Eq. 2.30:

$$\begin{aligned} v[k] = I_{enc}[k] + I_{enc}[k-1] &= I[k] - I_{enc}[k-1] + I_{enc}[k-1] + 4d \\ &= I[k] + 4d[k], d[k] \in Z \end{aligned} \tag{2.36}$$

We find that the duobinary shaped sequence is indeed the original PAM4 sequence plus 4 multiplies an integer, thus we can recover $I[k]$ from $v[k]$ by taking another modulo 4 operation at the receiver.

$$I[k] = (v[k])\ mod\ 4 \tag{2.37}$$

Conceptually, the receiver-side modulo 4 operation can be regarded as the inverse of both duobinary precoding and duobinary shaping, while the MLSE method only inverts the duobinary shaping step. Fig. 2.11 summarizes the difference between these two methods.

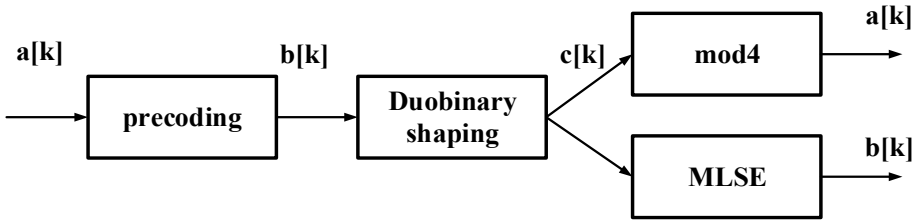

Fig. 2.11 Precoding based and MLSE based methods for signal recovery in duobinary systems.

2.3.3.3 Equalization for ISI compensation

Even if we use pulse shaping to limit the effective bandwidth of the signal, and we use a Nyquist pulse shaping filter which does not introduce ISI itself, in a typical IM/DD system, the transmitted signal still suffers from ISI due to the bandwidth limitations of components and the CD-induced power fading. Pulse shaping helps to control the ISI, but it cannot completely remove the ISI. To recover the ISI-free symbol sequence (to equalize the signal), one can use the MLSE technique. In section 2.3.3.2, we have introduced how to use MLSE to recover a duobinary shaped signal. In fact, the duobinary shaping process can also be regarded as a channel with ISI, whose channel response is given by Eq. 2.29. In that sense, when we use

MLSE to recover the signal, we are indeed equalizing that specific channel response.

Now we consider a more general case, where we have a channel with ISI that spans L+1 symbols. The MLSE criterion is equivalent to the problem of estimating the state of a finite-state machine (FSM), and the state at time interval k is given by:

$$S_k = (I[k-1], I[k-2], \dots, I[k-L]) \tag{2.38}$$

where we have $I[k] = 0$ for $k \leq 0$. Suppose the symbol has an alphabet with a size of M, the FSM has M^L states. In other words, the channel can be described by an M^L state trellis and we can use the Viterbi algorithm to determine the most probable path through the trellis. We begin with the samples $v[1], \dots, v[L+1]$, from which we can compute the M^{L+1} metrics

$$-\sum_{k=1}^{L+1} \ln P(v[k] \mid I[k], I[k-1], \dots, I[k-L]) \tag{2.39}$$

In AWGN channels, the metrics above can be replaced by the Euclidean-distance based metrics akin to Eq. 2.31. The M^{L+1} possible sequences of $I[L+1], I[L], \dots, I[1]$ can be subdivided into M^L groups corresponding to the M^L states $(I[L+1], I[L], \dots, I[2])$, i.e. the M sequences in each state differ in $I[1]$ and corresponds to the paths through the trellis that merge at a single node. In each state, we only keep the most probable sequence and assign the metric to the surviving sequence

$$\begin{aligned} PM_1(I[L+1]) &= PM_1(I[L+1], I[L], \dots I[2]) \\ &= \min_{I[1]} \left(-\sum_{k=1}^{L+1} \ln P(v[k] \mid I[k], I[k-1], \dots, I[k-L]) \right) \end{aligned} \tag{2.40}$$

Upon reception of $v[L+k], k \geq 2$, we compute M^{L+1} metrics for the M^{L+1} extended sequences based on the M^L metrics associated with the M^L surviving sequences as Eq. 2.41

$$\begin{aligned} PM_k(I[L+k]) &= PM_{k-1}(I[l+k-1]) \\ &+ \min_{I[k]}(-\ln P(v[L+k] \mid I[L+k], I[L+k \\ &- 1], \dots, I[k])) \end{aligned} \tag{2.41}$$

The M^{L+1} extended sequences are again subdivided into M^L groups, with each group containing M sequences that terminate in the same set of symbols $I[L+k], I[L+1-$

$1], \ldots, I[k+1]$ and differ in the symbol $I[k]$. We still only keep the most probable sequence in each group, so that we will be left again with M^L surviving sequences. Then this process can be repeated for the next received symbol.

MLSE is the optimum ISI compensation method in the sense that it minimizes the probability of a sequence error, the problem is that it has a computational complexity which grows exponentially with the channel memory length. The Viterbi algorithm computes M^{L+1} metrics for each new received symbol, which makes MLSE prohibitively expensive to implement, unless M and L are small (e.g. duobinary shaped PAM4 with M = 4 and L = 1).

An alternative suboptimal ISI compensation method which is widely used in practical systems is the linear feed forward equalizer (FFE), which can be expressed as

$$y[k] = \sum_{i=-N}^{N} w_i x[k-i] \tag{2.42}$$

where $x[k]$ and $y[k]$ represent the input and output samples at time interval *k,* respectively, and w_i represents the i^{th} tap coefficient. Fig. 2.12 shows the schematic of a 5-tap linear FFE. A linear FFE takes the form of an FIR filter, and its computational complexity is a linear function of the channel memory length.

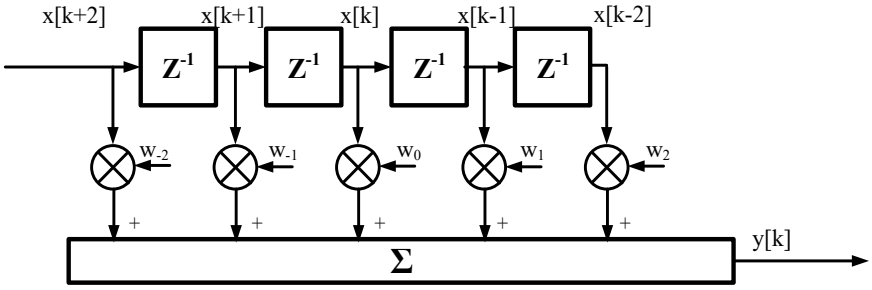

Fig. 2.12 Schematic of a typical linear FFE.

To minimize the ISI, we want the overall response of the pulse shaping filter, the channel response and the linear FFE filter to satisfy the Nyquist ISI criterion. Now we consider a linear channel, suppose we use an RC filter (or a pair of RRC filters) for pulse shaping, the complete elimination of the ISI requires the linear FFE filter to be the exact inverse of the channel frequency response. We call such a filter a "zero-forcing" (ZF) filter because it forces the residue ISI to zero, which is great if the channel is noise-less. However, if there is noise, a ZF

filter will significantly amplify the noise at frequencies where the channel response has small magnitude, since it attempts to completely invert the channel response. A more widely adopted criterion to design the required linear FFE filter is the mean square error (MSE) criterion, i.e. we adjust the tap coefficients to minimize the MSE of the signal

$$J = E\left|I[k] - \hat{I}[k]\right|^2 \tag{2.43}$$

where $I[k]$ is the symbol transmitted in the k^{th} signaling interval and $\hat{I}[k]$ is the estimate of that symbol at the output of the equalizer. By using the minimum MSE criterion, the optimized filter will not eliminate the ISI completely, instead, it minimizes the total power of the noise and the ISI. Note that even if we use the MSE criterion to determine the tap coefficients, the linear FFE still enhances noise after equalization. In practice, minimization of MSE can be implemented using adaptive algorithms such as the least mean square (LMS) algorithm [52].

Remember that we can split an RC filter to a pair of RRC filter, so that we can do half of the pulse shaping at the transmitter and leave the second half to be implemented at the receiver. We can also apply the same trick to the linear FFE filter discussed above. We can use a transmitter-side linear FFE filter to pre-compensate for a part of the ISI from the channel, and then use a receiver-side linear FFE filter to compensate for the rest part the ISI. The transmitter-side filter is also known as pre-emphasis [53] or pre-equalization [54] in the literature.

Before we move on, I would like to highlight three more things:

1) Although in Eq. 2.42 and Fig. 2.12 we only considered the linear terms, the FFE structure can actually be generalized to include nonlinear terms. For example, we can include higher-order terms in the Volterra series to form a Volterra equalizer (VE). Eq. 2.43 shows the formula of a 3$^{\text{rd}}$ order VE with kernel memory lengths of $(2N_1 + 1, 2N_2 + 1, 2N_3 + 1)$. Note that nonlinear FFEs can be used at both the transmitter and the receiver, and the tap coefficients can still be adaptively obtained (e.g. using the LMS algorithm).

$$y[k] = \sum_{i=-N_1}^{N_1} w_i x[k-i] + \sum_{i_2=-N_2}^{N_2} \sum_{i_1=-N_2}^{N_2} w_{i_1,i_2} x[k-i_1]x[k-i_2] + \sum_{i_3=-N_3}^{N_3} \sum_{i_2=-N_3}^{N_3} \sum_{i_1=-N_3}^{N_3} w_{i_1,i_2,i_3} x[k-i_1]x[k-i_2]\,x[k-i_3] \tag{2.44}$$

2) FFE can compensate for both the pre-cursor ISI (ISI caused by future samples on the current sample) and the post-cursor ISI (ISI caused by past samples on the current sample), which correspond to negative and positive i's in Eq. 2.42 (i_1, i_2, i_3's in Eq. 2.44), respectively.
3) FFE can operate at a sampling rate higher than 1 Sps. Compared to a T-spaced equalizer, a fractional spaced equalizer is less sensible to the choice of timing phase. Typically, people use $T/2$-spaced (operating at 2 Sps) FFE in practical systems.

Another popular ISI compensation method is the decision feedback equalizer (DFE), which can be expressed as Eq. 2.45.

$$\hat{y}[k] = x[k] - \sum_{i=1}^{N} h_i \hat{y}[k-i] \tag{2.45}$$

where $x[k]$ is the received sample at time instant k, and $\hat{y}[k]$ is the decision on the equalized symbol at time instant k. Eq. 2.45 is a feedback filter, which uses the decisions on previously detected symbols to remove the post-cursor ISI. In a practical system, both pre-cursor ISI and post-cursor ISI exist, thus a DFE is usually used together with an FFE. Specifically, we can replace the first term on the righthand-side of Eq. 2.45 with a linear FFE filter which only compensates for the pre-cursor ISI.

$$\hat{y}[k] = \sum_{i=-N_1}^{0} w_i x\left[k - \frac{i}{L}\right] - \sum_{i=1}^{N_2} h_i \hat{y}[k-i] \tag{2.46}$$

Note that the DFE part is typically operating at 1 Sps since it takes the decisions of symbols as inputs, but the FFE part can still be operating at L Sps ($L \geq 1$). Fig. 2.13 shows the schematic of an FFE-DFE structure with 3 feedforward taps and 2 feedback taps. The DFE part feeds hard decisions of the detected symbols back to its input, thus even if we only use linear taps, the FFE-DFE structure is still a nonlinear equalizer. In practical systems, the tap coefficients of

both the FFE part and the DFE part can be simultaneously obtained using the LMS algorithm. In general, FFE-DFE achieves better performance than FFE alone.

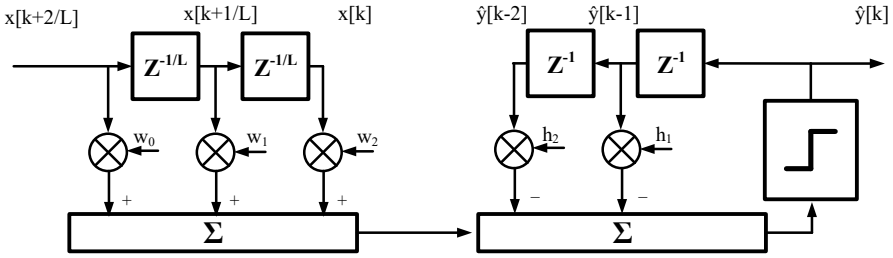

Fig. 2.13 Schematic of a typical FFE-DFE.

If FFE-DFE is used, the decision of the current symbol depends on the decisions of the previous symbols. In other words, if we have a decision error, it not only affects the detection of the current symbol, but also the detections of the future symbols, which is known as the "error propagation" problem. Error propagation would limit the performance of the DFE or the FFE-DFE especially when the SNR is low. To avoid error propagation, instead of using a DFE at the receiver, we can use Tomlinson-Harashima Precoding (THP) at the transmitter, which can be expressed as:

$$I_{THP}[k] = \left(I[k] - \sum_{i=1}^{N} h_i I_{THP}[k-i] \right) mod\ M \tag{2.47}$$

where $I[k]$ and $I_{THP}[k]$ represent the symbol sequences before and after THP encoding, respectively.

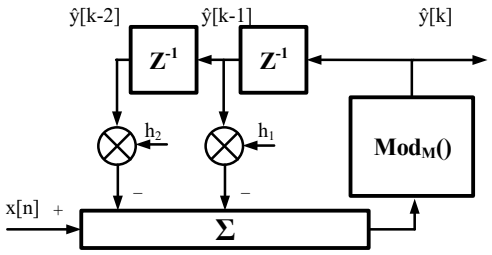

Fig. 2.14 Schematic of a typical THP encoder.

Fig. 2.14 shows the schematic of a 2-tap THP encoder. THP can be regarded as a transmitter-side version of DFE. It only compensates for the post-cursor ISI, thus it has to be used together with an FFE (or the combination of a transmitter-side FFE and a receiver-side FFE) which compensates for the pre-cursor ISI. The hard decision block in DFE is replaced by the modulo operation in THP. Since there is no decision, THP doesn't have decision errors, hence it doesn't

suffer from the error propagation problem.

Note that the modulo operation merely adds multiples of M to the output of THP, thus Eq. 2.47 can be linearized as

$$I_{THP}[k] = I[k] + Md[k] - \sum_{i=1}^{N} h_i I_{THP}[k-i], d[k] \in Z \tag{2.48}$$

$Md[k]$ is called the precoding sequence, which is unique, and is determined by the modulo operation to make sure that the output of THP is bounded within $[-M/2, M/2]$. If we regard $I[k] + Md[k]$ as the input, THP is indeed an infinite impulse response (IIR) filter. Remember that an FFE is a FIR filter, in the noiseless case, the combination of the IIR filter and the FIR filter (both are linear filters) can invert the channel frequency response.

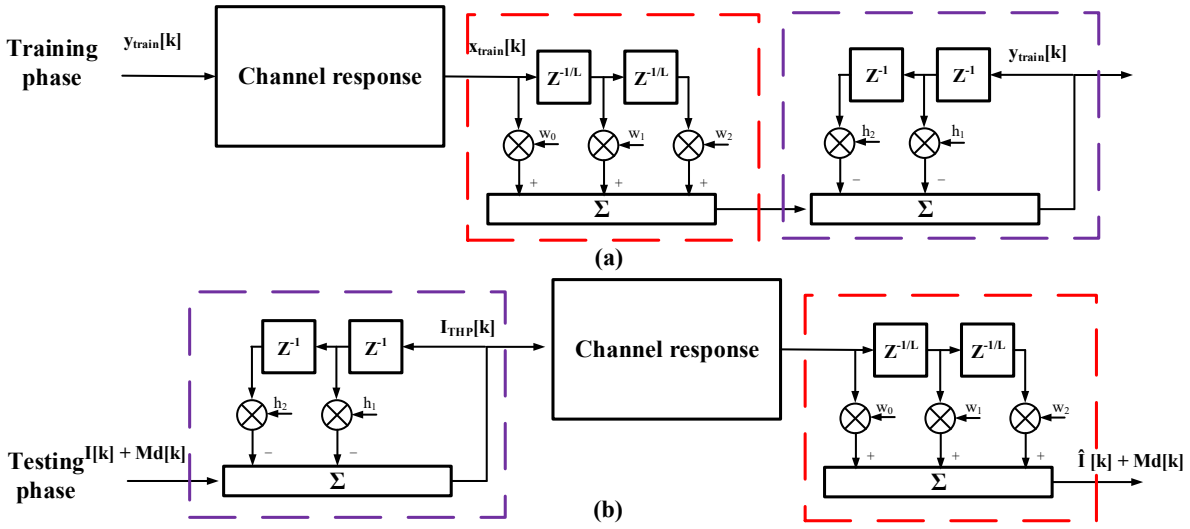

Fig. 2.15 (a) Training and (b) testing using THP.

To determine the THP tap coefficients in a practical system, we can use a training symbol assisted FFE-DFE structure at the receiver, obtain the tap coefficients using the LMS algorithm, then use the converged DFE tap coefficients as the THP tap coefficients. The trick is that in the training phase, we use training symbols instead of the hard decisions in the DFE to avoid error propagation. Since the training symbol assisted DFE is error-free and does not include the hard decision step, it can also be regarded as an IIR filter. Assuming that the channel response is linear and time invariant, we can change the order of the linear filters as shown in Fig. 2.15, that's why we can use the tap coefficients obtained from the training symbol assisted DFE as

the THP tap coefficients.

Keen readers may have realized that, in Fig. 2.15, the output of the FFE in the testing phase is the estimations of $I[k] + Md[k]$ rather than estimations of $I[k]$, thus before demodulation, we also need a receiver-side modulo(M) operation to remove the impact of the precoding sequence $Md[k]$

$$\hat{I}[k] = \left(\hat{I}[k] + Md[k]\right) mod\ M, d[k] \in Z \tag{2.49}$$

Fig. 2.16 shows the examples of the histograms of $I[k]$, $I[k] + Md[k]$, and $I_{THP}[k]$, where we consider a THP-PAM4 signal, and use the THP tap coefficients optimized for an experimental FTN-PAM4 system (details will be provided in Chapter 3, section 3.2). $I[k]$ is the original zero-mean PAM4 signal, which has an alphabet of $\{-3, -1, 1, 3\}$. Once the THP taps are determined, $d[k]$ will be uniquely determined by the modulo(M) operation. Here we choose M = 8, so that $I_{THP}[k]$ is confined to [-4,4].

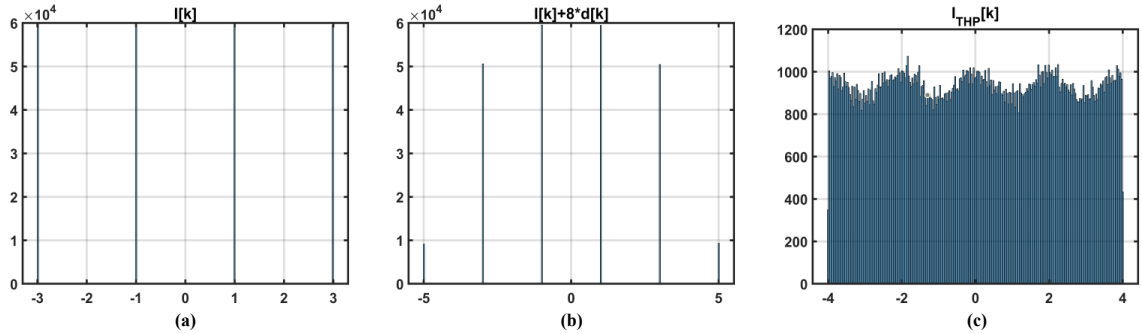

Fig. 2.16 Histograms of original PAM4, extended PAM4 and THP encoded PAM4 signals.

After THP encoding, $I_{THP}[k]$ no longer has distinct amplitude levels, i.e. $I_{THP}[k]$ can take any value between -4 and 4. $I[k] + Md[k], M = 8$ is a 6-level signal, which is often referred to as an extended PAM4 signal in the literature. Recall that in Fig. 2.15(b), the output of the receiver-side FFE is an estimation of $I[k] + Md[k]$ rather than an estimation of $I[k]$, which is why we need another modulo (M) operation after the receiver-side FFE. After applying modulo ($M = 8$) operation, all the ± 5 symbols turn into ∓ 3 symbols, and the 6-level extended PAM4 signal is transformed back to the original PAM4 signal.

Although THP does not have error propagation issue, it introduces a power penalty (a coding loss). The original PAM4 signal $I[k]$ shown in Fig. 2.16(a) has a PAPR of 2.55 dB, and the THP encoded PAM4 signal $I_{THP}[k]$ shown in Fig. 2.16(c) has a PAPR of 4.76 dB. Note that

the peak amplitude achievable in a specific system is determined by the output swing of the DAC channel and the gain of the RF amplifier, which is a fixed value (i.e. the system is peak power limited), thus a higher PAPR will lead to a lower average power of the signal. However, this does not mean that THP will introduce a power penalty of ~2.2 dB in the end, because in a practical system, after applying THP at 1 Sps, we will use pulse shaping and transmitter-side FFE, which also affect the PAPR of the signal. For instance, in Chapter 3, section 3.2 we will see that in our FTN-PAM4 experiment, THP introduces a power penalty of ~ 0.7 dB after applying pulse shaping and pre-emphasis. Nevertheless, in general, THP does reduce the average power of the signal. Therefore, the performance of THP-FFE is usually better than that of FFE-DFE since THP-FFE avoids error propagation, but it will be worse than that of the training symbol assisted FFE-DFE (an error propagation free FFE-DFE). But remember that the training symbol assisted FFE-DFE is just a trick to obtain the tap coefficients in the training phase, which cannot be applied in a practice in the testing phase, because the transmitted symbols are unknown at the receiver.

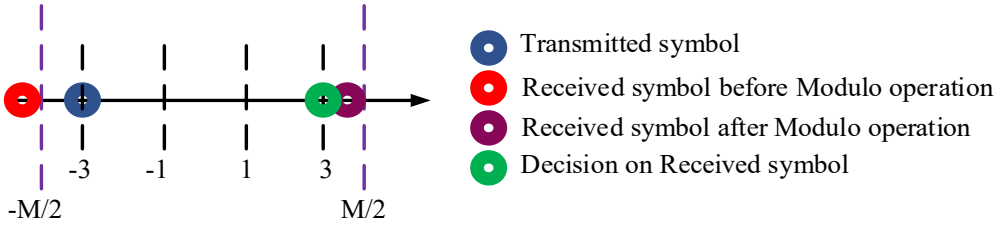

Fig. 2.17 Illustration of data-flipping effect in THP-PAM4 systems.

Another problem with THP is the so-called data flipping effect as illustrated in Fig. 2.17, where we still take a THP-PAM4 signal as an example. Since we use the modulo(M) operation at the receiver, all constellation points have two nearest neighbors, including the "-3" and "3" symbols, i.e. the constellation is indeed circular. Suppose we transmit a "-3" symbol, due to the existence of noise, the received symbol may appear to the left of the "-3" point on the constellation diagram. In a classic PAM4 system, this symbol will always be correctly identified as a "-3" symbol, since the "-3" symbol does not have a left neighbor. However, in a THP-PAM4 system, it is possible that the received symbol appears to the left of the boundary $-M/2$, thus will be mistakenly identified as a "3" symbol after modulo operation. Data-

flipping will lead to slightly higher symbol error rate, but it may be avoided if we choose a large enough M value. However, further increasing M will lead to higher PAPR after THP encoding (larger power penalty). In practice, M is chosen to be 8 for PAM4 signals to balance the data-flipping effect and the power penalty of THP.

2.3.3.4 FTN techniques

To avoid ISI in the system, we need the overall response of the transmitter filter, channel response and the receiver filter to be a linear filter that satisfy the Nyquist ISI criterion, e.g. an RC filter with a roll-off factor of β. Suppose the RC filter has a full width half maximum (FWHM) of B Hz, the maximum ISI-free symbol rate that can be transmitted in such a system with is B symbols per second (symbols/s). In the extreme case where $\beta = 0$, the RC filter becomes a B Hz brick-wall filter (i.e. a sinc filter) in the frequency domain. Therefore, the non-zero portion of the spectrum of an ISI-free signal with a symbol rate of B symbols/s has a single-sided bandwidth (bandwidth at baseband) of at least $B/2$ Hz.

However, this does not mean that we need $B/2$ Hz everywhere in the system, we just need the overall system response to meet the Nyquist ISI criterion. In practice, sometimes we need to transmit B symbols/s through a narrow channel with a single-sided bandwidth $< B/2$ Hz. For instance, the DAC channel or the ADC channel may have a sampling rate $< B/2$ Samples per second (Sa/s). To achieve that, we can use an aggressive pulse shaping filter to limit the bandwidth of the non-zero portion of the spectrum before transmission, and use the DSP algorithms discussed in section 2.3.3.3 to compensate for the ISI introduced by both the aggressive pulse shaping and the channel response. In the literature, people refer to this technique as faster-than-Nyquist (FTN) signaling [55],[56],[60]-[62], since it allows us to transmit a signal with a higher symbol rate (thus is faster) than the maximum ISI-free symbol rate determined by the Nyquist ISI criterion.

Based on the DSP algorithms used for ISI compensation, the FTN techniques can be subdivided into two groups 1) post filter + MLSE assisted FFE based FTN technique [55],[56] and 2) THP based FTN technique [57]-[62].

Suppose we transmit a signal with a symbol rate of B symbols/s, to minimize the ISI before

demodulation, the combined response of the transmitter and receiver filters should be the difference between a linear filter that meets the Nyquist ISI criterion, and the combined response of the aggressive pulse shaping filter and the channel response. In an FTN system, such difference can be extremely large, which will result in severe ISI. If we only use FFE at both the transmitter and the receiver to compensate for the ISI, the equalization enhanced noise will be troublesome. Fortunately, since the aggressive pulse shaping and the channel response are LPFs, the equalization enhanced noise is mainly at high frequencies, thus we can use a short-memory LPF such as a 2-tap post filter $1 + \alpha Z^{-1}$ to suppress the equalization enhanced noise, then use a M^1-state MLSE to invert that post filter. As shown in Fig. 2.18, by tuning the tap coefficient α, we can control the shape of the post filter to optimize the post-MLSE BER performance. Note that if $\alpha = 1$, the post filter becomes a duobinary shaping filter. In fact, the $\alpha = 1$ case is also referred to as receiver-side duobinary shaping in the literature [63].

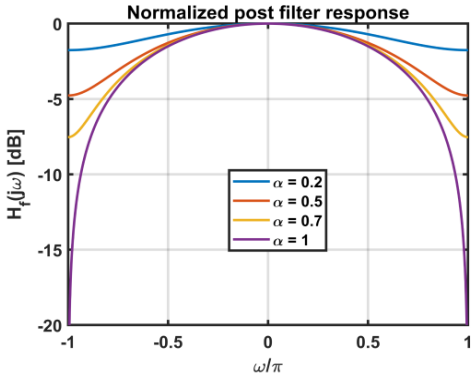

Fig. 2.18 Normalized post filter responses (normalized to the maximum value) with different α values.

Now we consider an FTN-PAM4 system, suppose that the optimal $\alpha = 1$, i.e. the FTN system is equivalent to a duobinary PAM4 system, the received signal can be directly equalized to a duobinary PAM4 (PAM7) sequence, which will not lead to severe noise enhancement, because the targeted 7-level sequence itself is not flat-top in the frequency domain. The original PAM4 sequence can be recovered by applying 4-state MLSE to the equalized 7-level sequence. Alternatively, the received signal can also be equalized to a flat-top PAM4 sequence, then a $1 + Z^{-1}$ post filter must be used to suppress the equalization enhanced noise, which will also shape the equalized PAM4 sequence into a PAM7 sequence, and then we can apply the 4-state MLSE. In other words, if we equalize the received sequence to a PAM7 sequence, the $1 + Z^{-1}$

post filter will be included in the converged FFE. In a more general case where the optimal $0 < \alpha < 1$, it is more convenient to use the second approach, i.e. equalizing the received signal to a PAM4 sequence, using a post filter + MLSE, and optimizing the α value.

In most FTN systems, a 2-tap post filter is good enough. However, if the equalization enhanced noise is too severe, one can increase the number of post filter taps and the memory length of MLSE to achieve a better BER at the cost of increasing the computational complexity.

Another kind of FTN technique is based on the THP-FFE structure. As we have mentioned in section 2.3.3.3, THP-FFE in general achieves better performance than FFE alone. Again, we take an FTN-PAM4 system as an example to explain the procedure. We need to first apply THP before the aggressive filtering at the transmitter, then we use an FFE at the receiver to equalize the received signal to the 6-level extended PAM4 sequence denoted in Fig. 2.16(b), followed by a modulo (8) operation to retrieve the original PAM4 signal. Some readers may have realized that this process is very similar to the process of precoding based duobinary PAM4 signaling, where we apply duobinary precoding before duobinary shaping at the transmitter, equalize the received signal to the 7-level duobinary PAM4 sequence (if equalization is required), then receive the uncoded PAM4 sequence through a modulo (4) operation. In fact, precoding based duobinary signaling can be regarded as a 1-tap THP with a fixed tap coefficient $h_1 = 1$. Note that in section 2.3.3.2, when we introduced the duobinary signaling, we assumed that the PAM4 signal has an alphabet of {0,1,2,3}, and we need a modulo(4) operation at the transmitter to make sure that the duobinary precoded sequence is confined within [0,3], thus the duobinary shaped PAM4 (the targeted sequence in receiver-side equalization) is a 7-level signal, while in section 2.3.3.3, when we introduced the THP, we assumed that the PAM4 signal has an alphabet of {-3,-1,1,3}, and we a modulo(8) operation to confine the THP-PAM4 signal to be within [-4,4], thus the extended PAM4 sequence (the targeted sequence in receiver-side equalization) is a 6-level signal.

2.3.3.5 Bit-to-symbol/symbol-to-bit mapping

All the previously introduced DSP algorithms are operated on the symbol level, but the FEC encoding and decoding are generally operated on the bit level. Therefore, we need a bit-to-

symbol mapping step at the beginning of the transmitter DSP, and a symbol-to-bit mapping step at the end of the receiver DSP. The bit-to-symbol and symbol-to-bit mappings are sometimes referred to as modulation and demodulation in the literature [51]. For traditional PAM2 and PAM4 signals, the bit-to-symbol and symbol-to-bit mappings can be implemented through Gray coding as shown in Fig. 2.19.

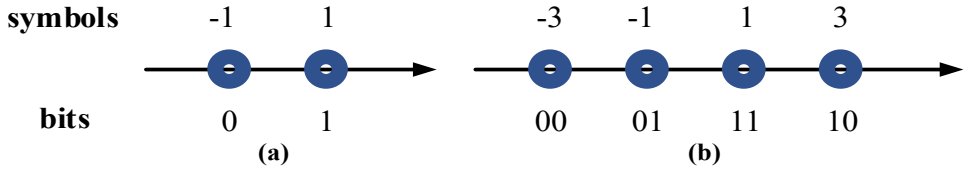

Fig. 2.19 Gray coding of (a) PAM2 and (b) PAM4 signals.

In this thesis, we also deal with another modulation format called 4D-TCM. TCM was first proposed by Ungerboeck as a technique to improve the error performance of synchronous data links since it increases the free Euclidean distance of the signal [64]. In recent years, 4D-PAMx-TCM has been intensively studied in short-reach IM/DD optical transmission systems [65]-[67]. Here we will take 8-state 4D-PAM4-TCM as an example to describe the encoding and decoding (i.e. bit-to-symbol mapping and symbol-to-bit mapping) processes.

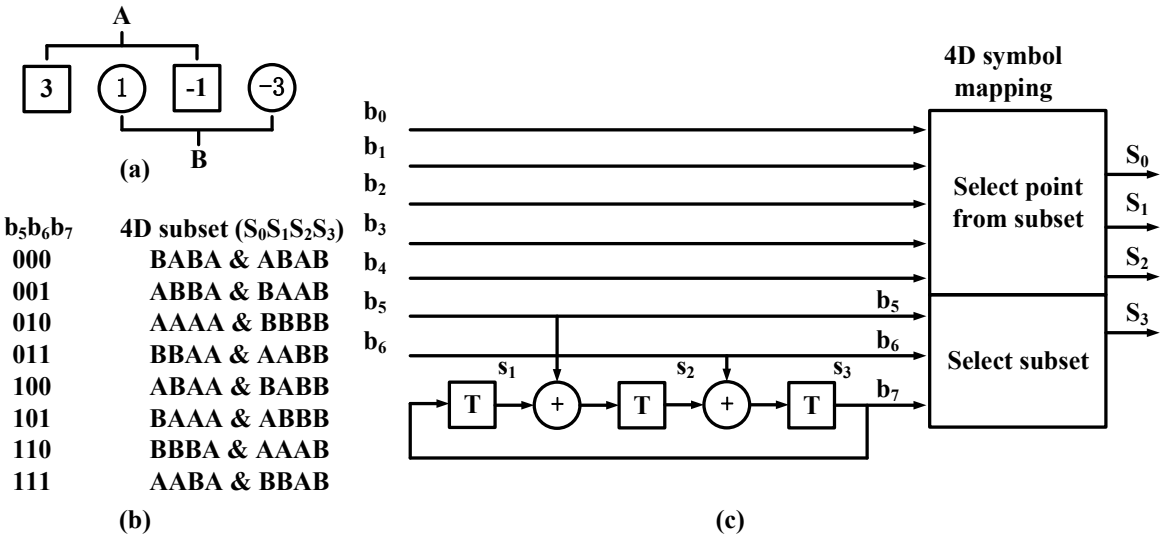

Fig. 2.20 (a) Set partitioning of PAM4 amplitude levels, (b) Set partitioning of 4D constellation, and (c) 8-state 4D-PAM4-TCM encoder structure.

Fig. 2.20 demonstrates the principle of an 8-state 4D-PAM4-TCM encoder. A 4D symbol is constructed from four independent 1D PAM4 symbols. Each PAM4 symbol corresponds to four possible amplitude levels, which are first partitioned into 2 groups as depicted in Fig. 2.20(a).

The 256-point ($4^4 = 256$) 4D constellation is then partitioned into 8 subsets as denoted in Fig. 2.20(b). Each subset contains 2×2^4=32 points and has a larger minimum Euclidean distance than that of the original 256-point constellation. One can map at most 8 bits to a 4D symbol. However, as shown in Fig. 2.20(c), 4D-PAM4-TCM uses a convolutional encoder to introduce 1-bit redundancy, thus only 7 out of the 8 bits can carry information (coding rate = 7/8). Specifically, 2 information bits are fed into the 8-state convolutional encoder (rate = 2/3) to generate 3 encoded bits, which are used to determine the choice of the subset, and the rest 5 information bits are directly mapped to the points in the chosen subset.

The convolutional encoder in Fig. 2.20(c) can be regarded as an FSM, and we have

$$\begin{aligned} s_1^{(i)} &= s_3^{(i-1)} \\ s_2^{(i)} &= \left(s_1^{(i-1)} + b_5^{(i)}\right) mod\ 2 \\ b_7^{(i)} &= s_3^{(i)} = \left(s_2^{(i-1)} + b_6^{(i)}\right) mod\ 2 \end{aligned} \tag{2.50}$$

Note that given a determined sequence of $(b_5^{(i)}, b_6^{(i)})$ and the initial state$\left(s_1^{(0)}, s_2^{(0)}, s_3^{(0)}\right) = (0,0,0)$, the state sequence $(s_1^{(i)}, s_2^{(i)}, s_3^{(i)})$ and the sequence of the choice of 4D constellation subset are also determined.

At the receiver, 4D-PAM4-TCM can be decoded using Viterbi algorithm. We maintain 8 surviving state trellises (8 surviving paths), each trellis ends with a different state $\left(s_1^{(i)}, s_2^{(i)}, s_3^{(i)}\right)_{(j)}, j = 0,1,\ldots,7$ and has a corresponding metric $PM_{(j)}^{(i)}$,. Upon reception of a new 4D symbol, we expand the existing trellises by one stage. According to Eq. 2.50, the end state of each surviving trellis can only transit to 4 possible states, and each possible state transition corresponds to a certain combination of $(b_5^{(i)}, b_6^{(i)}, b_7^{(i)})$, which is linked to a certain 4D constellation subset. For each possible 4D constellation subset $(S_0, S_1, S_2, S_3)_{(k)}, k = 0,1,\ldots,7$, we compute the minimum Euclidean distance between the received 4D symbol and the 4D constellation points in that subset $D_{(k)}$. Therefore, after expansion, we will have $8 \times 4 = 32$ new trellises, and each trellis has an updated metric $PM_{(j)}^{(i)} + D_{(k)}$. We then group these 32 trellises into 8 groups, and the 4 trellises in each group end with the same state. In

each group, we only keep the trellis with the minimum metric, thus we will end up again with 8 surviving trellises. Then the procedure described above is repeated for the each subsequently received 4D symbol.

The 8 surviving trellis will converge if we make decisions after a fixed delay of q 4D symbols (in our experiment that will be discussed in Chapter 3, we chose q = 500). After Viterbi decoding, we will obtain an estimated state sequence $(\hat{s}_1^{(i)}, \hat{s}_2^{(i)}, \hat{s}_3^{(i)})$, since we know the initial state$\left(s_1^{(0)}, s_2^{(0)}, s_3^{(0)}\right) = (0,0,0)$, we can estimate the sequence of $(b_5^{(i)}, b_6^{(i)}, b_7^{(i)})$ as follows:

$$\begin{aligned} \hat{b}_7^{(i)} &= \hat{s}_3^{(i)} \\ \hat{b}_6^{(i)} &= \left(\hat{s}_2^{(i-1)} + \hat{s}_3^{(i)}\right) mod\ 2 \\ \hat{b}_5^{(i)} &= \left(\hat{s}_1^{(i-1)} + \hat{s}_2^{(i)}\right) mod\ 2 \end{aligned} \tag{2.51}$$

For each received 4D symbol, once we get $(\hat{b}_5^{(i)}, \hat{b}_6^{(i)}, \hat{b}_7^{(i)})$, we know which 4D constellation subset was chosen for that 4D symbol, and $b_0^{(i)}$ to $b_4^{(i)}$ can be decoded accordingly by searching for the minimum Euclidean distance between the received 4D symbol and the 4D constellation points in that subset.

The encoding/decoding process described above can be easily extended to other modulation formats (such as 4D-PAM5-TCM) and other convolutional encoders (such as 16-state/32-state convolutional encoders). A more detailed description can be found in [65].

2.3.3.6 Timing recovery

Up to now we have reviewed all the DSP algorithms that we will encounter in Chapter 3. Before we end this section, we would like to briefly introduce one additional DSP block, the timing recovery block.

In a digital communication system, the output of the demodulator needs to be sampled periodically at the precise sampling time instants $mT + \tau$, where T is the symbol interval and τ is the time delay that accounts for the propagation time of the signal from the transmitter to the receiver. To perform that, we need to extract a clock signal at the receiver, such a process is called time recovery. There exist many classic timing recovery algorithms in the literature,

such as the algorithms proposed by Gardner [68], Godard [69], and Lee [70]. Although the conventional algorithms may fail for FTN signals which do not have frequency components beyond the Nyquist frequency ($1/2T$), there still exist some robust algorithms that are feasible for these signals [71]. In our experiment however, we use a trick to avoid timing recovery. Specifically, we share a 10 MHz clock reference between the transmitter and the receiver. Note that this is merely a trick that only works in the lab, in a practical system, the timing recovery block should not be omitted.

2.4 Fundamentals of SSB/VSB self-coherent systems

2.4.1 System Structure

Before we talk about the SSB/VSB self-coherent systems, let's first introduce the definitions of the terms "DSB" and "SSB". Fig. 2.21(a) shows a typical spectrum of a DSB signal. The term "DSB" reflects the fact that this signal contains both a right sideband (RSB) component $s_1(t)$ and a left sideband (LSB) component $s_2(t)$. In a general case, $s_1(t)$ and $s_2(t)$ can be two mutually independent complex-valued signals, hence the DSB signal $s_1(t) + s_2(t)$ is a complex-valued signal in the time domain, and its spectrum contains both the conjugate symmetric and conjugate antisymmetric components.

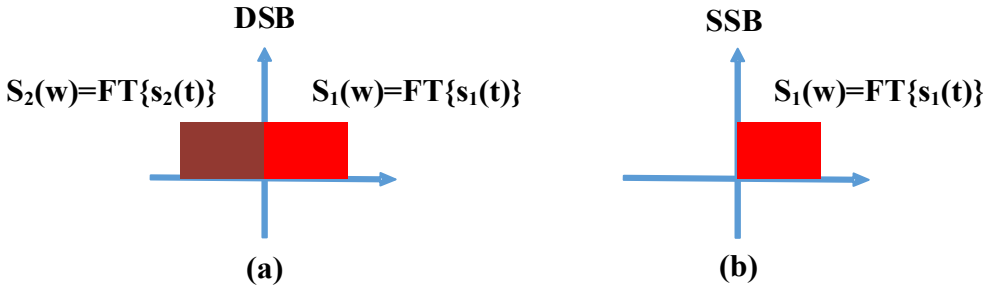

Fig. 2.21 Spectra of (a) a DSB signal and (b) an SSB signal. FT{x}: Fourier transform of x.

Then we consider a special case where we have

$$s_2(t) = s_1^*(t) \tag{2.52}$$

$s_1(t)$ and $s_2(t)$ can still be complex-valued signals, but now the DSB signal $s_1(t) + s_2(t)$ becomes a real-valued signal whose spectrum is conjugate symmetric, i.e.:

$$S_2(\omega) = S_1^*(-\omega) \tag{2.53}$$

where $S_1(\omega)$ and $S_2(\omega)$ represent the Fourier transforms of $s_1(t)$ and $s_2(t)$, respectively. In this case, both the RSB component $s_1(t)$ and the LSB component $s_2(t)$ contain all the information of the original DSB signal $s_1(t) + s_2(t)$. If we know one of them, we can easily derive the other using Eq. 2.52 or Eq. 2.53, and the DSB signal can be recovered by taking the real part of either $s_1(t)$ or $s_2(t)$, since we have:

$$s_1(t) + s_2(t) = s_1(t) + s_1^*(t) = 2Re\{s_1(t)\} = 2Re\{s_2(t)\} \tag{2.54}$$

We call a signal with a spectrum that contains only the RSB or the LSB component an SSB signal, an example is shown in Fig. 2.21(b).

Note that an IM/DD system receives a DSB signal, and the PD only detects the amplitude information of the received signal. If the accumulated CD is severe, the detected waveform will suffer from the power fading effect. The power fading effect is difficult to be compensated for in the receiver DSP (please refer to section 2.3.2.1). Therefore, in a high symbol rate IM/DD system, we usually need to limit the transmission distance to make sure that the first power fading induced frequency notch does not locate in the frequency range of our interest. In contrast, an SSB/VSB self-coherent system receives an SSB/quasi-SSB signal, and as we will shortly see in sections 2.4.2.2 and 2.4.2.3, it allows us to reconstruct the complex-valued optical field information (both the amplitude and the phase information) of the received signal in the DSP. The impact of CD on the optical field is a linear all-pass filter, which can be easily compensated for by applying an inverse filter in the DSP. Also note that an IM/DD system aims at transmitting a real-valued DSB signal, and based on our previous discussions, we know that transmitting only the RSB or the LSB of a real-valued DSB signal won't lead to loss of information. Therefore, switching from IM/DD solution to SSB/VSB self-coherent solution is a promising way to extend the reaches of high-speed optical transmission systems. In addition, since we can compensate for CD, the SSB/VSB self-coherent systems can be operated in the C-band to further benefit from the CD-suppressed FWM effects (please also refer to section 2.3.2.4) and the maturity of the optical amplification technologies (e.g. EDFA).

We will discuss more about the channel impairments in the SSB/VSB self-coherent systems and their compensation methods in sections 2.4.2. For now, let's first focus on the hardware

requirements.

Fig. 2.22(a) shows the schematic of a typical IQ modulator based SSB self-coherent system, as well as its transmitter and receiver DSP blocks, and Fig. 2.22(b) shows the operating principle of this system by illustrating the signal's spectra after major processing steps. Suppose we want to transmit the RSB of a baseband PAM signal (illustrated in the upper branch of Fig. 2.22(b)). In the transmitter DSP, we first generate a pulse shaped real-valued DSB PAM signal as we do in an IM/DD system, then we remove the LSB component in the digital domain, i.e. set half of the spectral bins to zeros. Since the RSB component is a complex-valued waveform in the time domain, we normally use two DAC channels, two RF drivers, and an IQ modulator to modulate this waveform. Note that by controlling both the real and the imaginary parts the waveform, if the IQ imbalance is negligible, ideally, we can generate a rigorous SSB signal using this scheme.

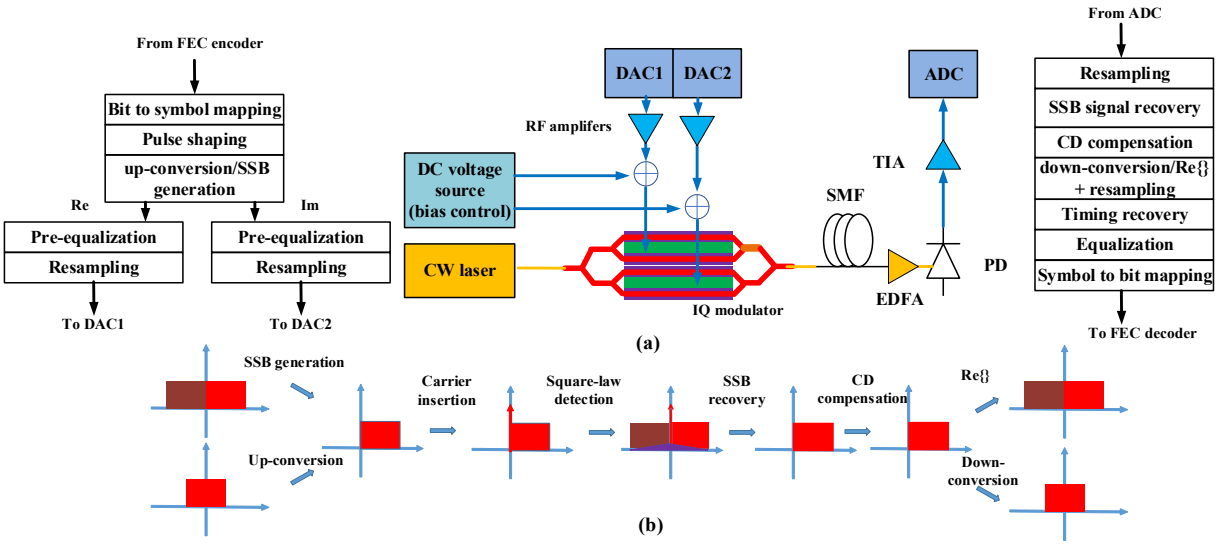

Fig. 2.22 (a) Schematic and DSP stacks of an SSB self-coherent system, (b) operating principle of an SSB self-coherent system.

An SSB self-coherent system requires a strong optical carrier to be inserted at the edge of the signal. A simple way to generate this carrier is to adjust the bias point of the IQ modulator to allow for some direct current (DC) leakage. Other popular carrier generation methods include digital carrier generation and parallel carrier path structure, we will discuss more about the pros and cons of these methods in Chapter 4 and Chapter 5. This inserted optical carrier serves as a clean phase reference without modulation, and the beating between the signal and the carrier helps us to retrieve the phase information of the signal. Functionally, this carrier is equivalent

to the local oscillator (LO) of a coherent system. The main difference is that, in a coherent system, the signal is generated from the transmitter-side laser, and the LO is generated from a separate receiver-side laser, but in an SSB self-coherent system, both the signal and the reference carrier are generated from the same laser at the transmitter. This is where the name "self-coherent system" stems from: the equivalent "LO" is a part of the transmitted waveform itself.

At the receiver side, we use only one single-ended PD and one ADC channel to detect the signal (just like an IM/DD system). If the aforementioned reference carrier is strong enough, we can reconstruct the complex-valued field information of the transmitted RSB waveform from the sampled photocurrent using DSP algorithms (please refer to section 2.4.2.2). Once we obtain the field information, we can apply digital CD compensation (please refer to section 2.4.2.3), and the real-valued DSB PAM signal can be obtained by taking the real part of the CD compensated RSB signal. The rest DSP blocks are the same as the DSP blocks of an IM/DD system.

Readers who are familiar with coherent systems may have realized that, an SSB self-coherent system is very similar to a heterodyne coherent system [72]. In a heterodyne coherent system, we also have an optical carrier inserted at the edge of a complex-valued signal, and we use a balanced photodetector (BPD) per polarization to detect the field information of the signal. In fact, from the receiver's perspective, an SSB self-coherent receiver can be regarded as a modified single-polarization (SP) heterodyne coherent detection receiver, where we replace the BPD with a single-ended photodetector (PD) and some novel SSB field recovery DSP algorithms, and we move the "LO" to the transmitter side.

As we have mentioned, an SSB self-coherent system can retrieve the complex-valued field information of an SSB signal at the receiver. Therefore, instead of transmitting the RSB component of a real-valued signal, e.g. a baseband PAM signal, we can also transmit a frequency up-converted complex-valued signal, e.g. a passband QAM signal, as shown in the bottom branch of Fig. 2.22(b). At the transmitter, we can first generate a pulse shaped QAM signal at baseband, then up-convert it in the frequency domain to make it an RSB signal. At the

receiver, after SSB field recovery and CD compensation, we can down-convert it back to the baseband and then apply standard baseband processing steps. If there is no guard band in the passband QAM transmission case, i.e. there is no frequency gap between the DC carrier and the edge of the QAM signal, assuming that we use the same RC/RRC roll-off factors for pulse shaping, to keep the spectral occupancy unchanged, the symbol rate of the passband QAM signal needs to be half of that of the baseband PAM signal. But also note that by transmitting a QAM signal, we have access to both the real and the imaginary dimensions of the signal, thus the SE can be doubled, and the total capacity can remain the same.

Compared to an IM/DD system depicted in Fig. 2.2, the SSB self-coherent system shown in Fig. 2.22(a) has the same hardware requirement at the receiver, but the transmitter is more complicated. It utilizes two DACs, two RF amplifiers and an IQ modulator, while an IM/DD system requires only one DAC, one RF amplifier and one single drive intensity modulator.

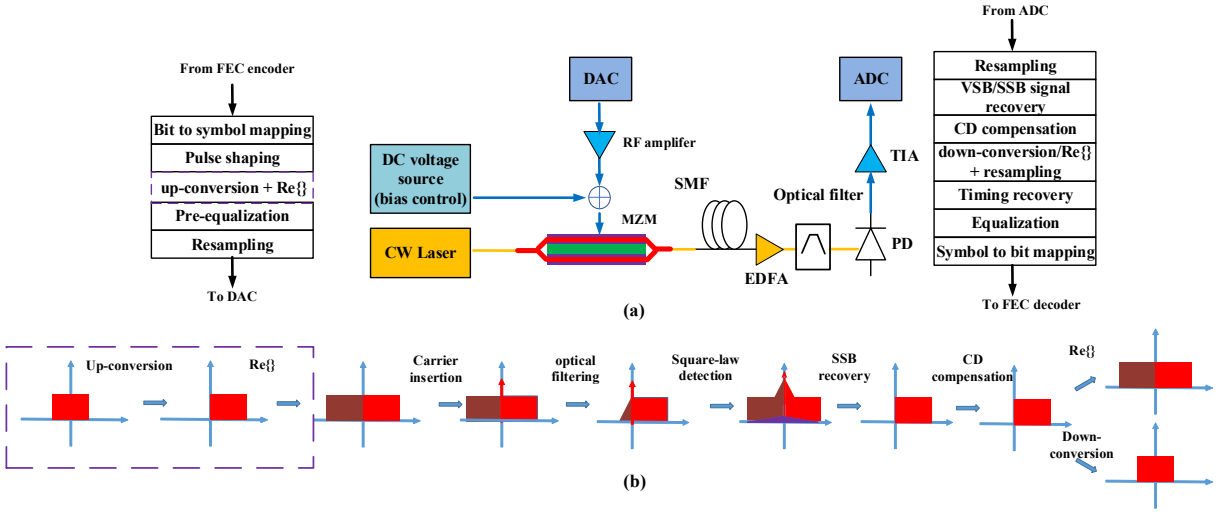

Fig. 2.23 (a) Schematic and DSP stacks of a VSB self-coherent system, (b) operating principle of a VSB self-coherent system.

Fig. 2.23(a) shows an alternative way to generate an SSB spectrum (more precisely, a quasi-SSB spectrum) with a simplified transmitter structure, where we first modulate a real-valued DSB signal using only one DAC, one RF amplifier and one single-drive push-pull MZM, and then use an optical filter to suppress half of the spectrum before photodetection. The filter can be inserted either before or after the fiber. Such an optical filter based system is often referred to as a VSB system in the literature [28]-[31]. The term “VSB” stems from the fact that the

unwanted sideband is usually under-suppressed due to the limited edge gradient of the optical filter. A VSB self-coherent system has almost the same hardware complexity as an IM/DD system. The only difference is that it requires an additional optical filter.

If the edge gradient of the optical filter is large enough, the power of the residual unwanted sideband will be much weaker than the power of the targeted sideband, i.e. the filtered signal is quasi-SSB. If so, we can treat this quasi-SSB signal as a rigorous SSB signal in the receiver DSP, i.e. we can apply the SSB field reconstruction algorithms that are designed for rigorous SSB signals directly to the quasi-SSB signal to retrieve the field information. Unfortunately, the residual unwanted sideband will cause penalties to these algorithms, hence a VSB self-coherent system generally achieves worse transmission performance than an IQ modulator based SSB self-coherent system. But a VSB self-coherent system can still achieve better transmission performance than an IM/DD system, especially when the accumulated CD is severe, because it allows for field reconstruction and enables digital CD compensation. As long as we use an optical filter in the system, the unwanted sideband will be suppressed to some extent. Even if the residual unwanted sideband leads to sizable power fading effect in the system, the power fading issue of a VSB system will not be as severe as that of an IM/DD system, hence the equalization induced noise enhancement in a VSB self-coherent system will also be weaker than that of an IM/DD system (please refer to section 2.4.2.3 for more discussions).

Just like an IQ modulator based SSB self-coherent system, a VSB self-coherent system can also transmit a passband QAM signal. Since we only use one DAC channel at the transmitter, instead of modulating the complex-valued frequency up-converted QAM signal as we do in an IQ modulator based system, we only modulate its real part in a VSB system, as shown in the dashed box in Fig. 2.23(b). Note that the complex conjugate of an RSB signal is an LSB signal, which does not overlap with the original RSB signal in the frequency domain. Therefore, taking the real part of an RSB signal in the transmitter DSP does not lead to loss of information. In fact, in a VSB self-coherent system, transmitting a passband QAM signal instead of a baseband PAM signal is beneficial, since it allows us to insert a guard band between the reference carrier

and the edge of the signal, which can relax the filter edge gradient requirement (at the cost of slightly reducing the SE).

Table 2.4 Comparison of a selected group of systems with digital CD compensation capabilities

	DAC	ADC	OE/EO Devices	Passive Devices	Max Capacity
SP SSB (Fig. 2.22(a))	2x @B	1x @B	1x SP-IQM (2x MZM) 1x PD	None	MB/2
SP VSB (Fig. 2.23(a))	1x @B	1x @B	1x MZM 1x PD	1x Optical filter	MB/2
SP Twin-SSB [73]-[75]	2x @B	2x @B	1x SP-IQM (2x MZM) 2x PD	2x Optical filter	MB
DP SVR-SSB Digital carrier generation [76],[77]	4x @B/2	4x @B	1x DP-IQM (4x MZM) 2x PD+ 2x BPD (6x PD)	1x SP Hybrid 1x PBS 2x 80/20 splitter	MB
DP SVR-SSB ESE Maximized [78]	4x @B	4x @B	1x DP-IQM (4x MZM) 2x PD+ 2x BPD (6x PD)	1x SP Hybrid 1x PBS 2x 80/20 splitter	3MB/2
DP SSB-orthogonal offset carriers (digital carrier generation) [79]	4x @B/2	2x @B	1x DP-IQM (4x MZM) 2x PD	2x Optical filter 1x 50/50 splitter	MB
DP homodyne coherent [72]	4x @B	4x @B	1x DP-IQM (4x MZM) 4x BPD (8x PD)	1x DP Hybrid (2x SP Hybrid) 1x PBS, 1x PMS	2MB

B is the sampling rate in Sa/s, M is the size of modulation alphabet per real dimension, e.g. M = 2 for PAM4, and M = 4 for 16QAM. SP: single polarization. DP: dual polarization. PBS: polarization beam splitter.

Up to now, we have introduced the basic structures of the IQ modulator based SSB self-coherent system and the VSB self-coherent system. Before we discuss about the transmission impairments and the associated impairment mitigation methods in these two systems, we would like to provide a brief review of other interesting variations of SSB/VSB self-coherent system structures that have attracted attentions in recent years.

The hardware requirements and maximum achievable capacities of a selected group of

SSB/VSB self-coherent system structures are summarized in Table 2.4, where the first two rows correspond to the IQ modulator based SSB self-coherent system and the VSB self-coherent system, respectively.

Note that in an IQ modulator based SSB self-coherent system, we need two DAC channels, each with a sampling rate of B Sa/s, to generate a complex-valued SSB signal that occupies a bandwidth of $B/2$ Hz. This is actually a waste of DAC resources, since two DAC channels at B Sa/s can generate a complex-valued DSB signal that covers a bandwidth of B Hz. To make full use of DACs' sampling rates, the twin SSB scheme was proposed [73]-[75]. A twin-SSB self-coherent system has the same transmitter-side hardware requirements as that of an IQ modulator based SSB self-coherent system, but it simultaneously modulates two independent SSB signals (both LSB and RSB) instead of one SSB signal, with each SSB signal occupying a bandwidth of $B/2$ Hz. At the receiver side, since a twin SSB self-coherent system transmits a DSB spectrum, we need two VSB self-coherent receivers to detect the field of the LSB and the RSB signals separately, which requires two optical filters, two PDs and two ADC channels. To some extent, a twin SSB system can be regarded as two parallel VSB systems that are multiplexed together in a smart way.

The IQ modulator based SSB self-coherent system, the VSB self-coherent system and the twin-SSB self-coherent system introduced above are all SP systems. To further improve the SE, one may need polarization division multiplexing (PDM). However, implementing PDM in a self-coherent system is not that straightforward. In a self-coherent system, the reference carrier is generated at the transmitter. Suppose we have two carriers of the same power at the same frequency on both polarization states, the combination of the X-Polarization (X-Pol) and Y-Polarization (Y-Pol) carriers is indeed a 45-degree linear polarized (LP) carrier. Upon propagation, the polarization state of this LP carrier will be rotated. In the extreme case, at the receiver side, this LP carrier may have no projection on one polarization state, such that the field information on this polarization state can never be reconstructed. To solve this problem, several DP SSB self-coherent schemes which involve the use of the stokes vector receivers (SVRs) have been proposed. For instance, [76],[77] proposed a scheme that uses the SVR to

de-rotate the polarization state of the received signal at the beginning of the receiver DSP stack, so that both X-Pol and Y-Pol have a strong reference carrier to enable the SSB field reconstruction process. The authors also proposed to digitally generate the reference carrier from the DACs and let the modulators to be biased rigorously at the null point (i.e. no DC leakage is allowed). This way, the carrier doesn't have to be located at 0 Hz, and we can use DAC channels with sampling rates of $B/2$ Sa/s to generate $B/2$ Hz SSB signals. But note that digital carrier generation requires the DAC channels to have higher resolutions in order to maintain the quality of the signal, thus it does not necessarily save DAC resources and DAC power consumption. In a typical SSB self-coherent system, the CSPR is ~10 dB. Hence when we use the digital carrier generation scheme, we are using the DAC to generate not only the signal, but also a carrier whose amplitude is $\sim\sqrt{10}$ times stronger than that of the signal. If we want to use the same number of output levels to generate the signal, we will have to use a DAC with higher resolution to generate both the signal and the carrier. In addition, the DP SVR-SSB structure proposed in [76],[77] uses four B Sa/s ADC channels to detect two $B/2$ Hz complex-valued SSB signals, which is a waste of ADC resources. Remember that in an SP self-coherent system, we just need one B Sa/s ADC channel to detect one $B/2$ Hz complex-valued SSB signal. To maximize the electrical SE[11] in the SVR based DP SSB self-coherent solutions, later in [78], the authors showed that the complex-valued SSB signal on one polarization state can actually be replaced by a complex-valued DSB signal, and the field information of both X pol and Y pol can still be reconstructed. In this structure, the reference carrier is better to be inserted at 0 Hz, thus the authors did not use the digital carrier generation scheme.

An alternative method to implement PDM in an SSB self-coherent system is to put the X-Pol carrier and the Y-Pol carrier at the opposite sides of the signal, thus digital carrier generation or additional transmitter-side lasers have to be used [79].Without loss of generality, let's assume that the X-Pol carrier is inserted at the left side of the signal, and the Y-Pol carrier is inserted

[11] Defined as Capacity divided by the one-sided bandwidth of the ADC [78]

at the right side of the signal. At the receiver, the transmitted waveform (whose polarization state has been rotated) will be evenly split into two paths. In each path, an optical filter will be used to suppress one of the carriers before photodetection. If the right-side (left-side) carrier is sufficiently suppressed, the PD will see an RSB (LSB) spectrum, and the remaining left-side (right-side) carrier only beats with the signal of the same polarization state. The intra- and inter-polarization signal-signal-beating-interference (SSBI) can be mitigated through an iterative DSP algorithm proposed in [79], and polarization demultiplexing can be achieved accordingly. Note that in this structure, the power splitter and the two optical filters need to be polarization insensitive.

For comparison, we also show the hardware requirements and the maximum achievable capacity of a standard DP coherent system in the last row of Table 2.4. The SSB/VSB self-coherent system can be regarded as an intermediate solution between the SP IM/DD system and the DP coherent system. By upgrading from the SP IM/DD system to the DP coherent system, one could achieve: 1) digital CD compensation capability and 2) higher fiber capacity through PDM. If we just need the CD compensation capability to extend the reach, then all the variations shown in Table 2.4 satisfy the needs. In other words, we can actually stick to the SP self-coherent solutions. If we also want to push for higher capacity, we will have to use DP solutions. However, as we have discussed previously, the self-coherent system is not an ideal platform for PDM implementation, since the reference carrier is inserted at the transmitter, and it makes polarization demultiplexing challenging. The existing PDM self-coherent solutions in the literature are not that attractive in terms of hardware complexity. The hardware requirement of an SVR based DP self-coherent system is very close to that of a DP coherent system (especially the requirements of the DAC channels and the ADC channels), but its maximum achievable capacity is only $3/4$ of that of a DP coherent system. The orthogonal offset carrier based PDM scheme seems to be more promising, but it requires digital carrier generation or additional lasers at the transmitter. Remember that digital carrier generation requires DACs with higher resolutions, and additional lasers would also result in additional cost, power consumption and packaging challenges.

Therefore, my personal bias is that a self-coherent system with a transmitter-side inserted reference carrier is just not designed for DP operations. If we do need DP operation at some point, we should directly upgrade to the coherent system, since an "LO" based PDM solution is much more elegant and efficient. In this thesis, I will focus on the SP SSB/VSB self-coherent systems, as these two schemes make minimal changes to the hardware requirements of an IM/DD system, but enables digital CD compensation.

2.4.2 Transmission impairments and Digital Compensation Methods

2.4.2.1 Overview

As we have discussed in the previous section, an SSB/VSB self-coherent system[12] can be regarded as an upgrade of an IM/DD system. Most of the transmissions impairments in an IM/DD system also exist in an SSB/VSB self-coherent system. Moreover, by comparing Fig. 2.22 or Fig. 2.23 with Fig. 2.2, we observe that many DSP blocks introduced in section 2.3.3 are also used in an SSB/VSB self-coherent system. Therefore, to avoid redundant materials, this section will focus on the unique transmission impairments of an SP SSB/VSB self-coherent system and the additional DSP blocks that are required to mitigate those impairments. At the end of this section, we will briefly mention the common transmission impairments and DSP blocks that exist in both IM/DD and SSB/VSB self-coherent systems, and we will point the readers to the corresponding topics in section 2.3.

2.4.2.2 Signal-signal beating interference

Let's start with the signal-signal beating interference (SSBI) issue in a rigorous SSB system. Without loss of generality, we can assume that the PD receives a rigorous RSB signal $s(t)$ and a constant-value DC carrier C. After square-law detection [80], the photocurrent $I(t)$ can be expressed as:

$$\begin{aligned} I(t) = R|C + s(t)|^2 &= R[C + s(t)][C + s^*(t)] \\ &= R[C^2 + Cs(t) + Cs^*(t) + s(t)s^*(t)] \end{aligned} \tag{2.55}$$

where R is a scaling factor related to the responsivity of the PD and the ROP. Here we assume

[12] Unless otherwise specified, in the remainder of this thesis, by "SSB/VSB self-coherent system" we are referring to "SP SSB/VSB self-coherent system".

that C is a real number. The absolute phase of the DC carrier doesn't matter since it is just a phase reference, and what really matters is the phase difference between $s(t)$ and C.

Also, since we can normalize the power of $I(t)$, we can drop the scaling factor R and focus on the terms inside the square brackets in Eq. 2.55. The first term is a carrier-carrier beating term, which is a constant component at 0 Hz. It can be easily removed by subtracting the mean from the signal. The second term and the third term are linearly proportional to $s(t)$ and its complex conjugate $s^*(t)$, respectively, which are the carrier-signal beating terms. The fourth term is the product of the signal $s(t)$ and its complex conjugate $s^*(t)$, i.e. the SSBI.

Our target is to reconstruct the complex-valued signal $s(t)$. If $s(t)$ is a rigorous RSB signal, then $s^*(t)$ is a rigorous LSB signal, then the second term and the third term do not overlap with each other in the frequency domain. If the CSPR is extremely large, i.e. $C^2 \gg |s(t)|^2$, the second term and the third term will be much stronger than the fourth term, hence the impact of the fourth term can be ignored, and we can recover $s(t)$ from the photocurrent $I(t)$ using the following steps:

a. Subtract the mean to remove the DC (0 Hz) term and normalize the power

b. Use a digital filter to remove the LSB components.

In the remainder of this thesis, we will refer to this procedure as the SSB filtering algorithm.

Unfortunately, in a practical system, the CSPR cannot be arbitrarily large, and the SSBI may not be negligible. If we use the SSB filtering algorithm to recover $s(t)$, we will obtain a mixture of the targeted SSB signal and the positive-frequency components of the SSBI term. Therefore, in practice, we need to use more advanced SSB field recovery algorithms to mitigate the impact of SSBI, e.g. the "Kramers Kronig (KK)-family" algorithms.

Now we introduce the principles of the KK-family algorithms that we will encounter frequently in Chapter 4 and Chapter 5. Consider a complex-valued signal $s(t) = s_r(t) + js_i(t)$, where $s_r(t)$ and $s_i(t)$ are the real and imaginary parts of $s(t)$, respectively. If $s(t)$ is a rigorous RSB signal, $s_r(t)$ and $s_i(t)$ are related through the KK relation:

$$s_i(t) = IFT\{j \cdot sgn(\omega) FT\{s_r(t)\}\}, \qquad sgn(\omega) = \begin{cases} -1, \omega < 0 \\ 0, \omega = 0 \\ 1, \omega > 0 \end{cases} \tag{2.56}$$

where $FT\{\}$ and $IFT\{\}$ represent the Fourier transform and the inverse Fourier transform, respectively. The operation described by the righthand side of Eq. 2.56 is also known as the Hilbert transform of $s_r(t)$ [80]. Eq. 2.56 can be easily proved using the properties of Fourier/inverse Fourier transforms and the fact that $s(t)$ is a rigorous RSB signal.

Now we define a new signal $u(t) = 1 + s(t) = |1 + s(t)| \exp[j\phi(t)]$, and consider a function $U(t) = \ln\{u(t)\} = \ln|u(t)| + j\phi(t) = U_r(t) + jU_i(t)$, where $U_r(t)$ and $U_i(t)$ are the real and imaginary parts of $U(t)$. If we add a condition $1 > |s(t)|$ for all t, $U(t)$ can be expanded as:

$$U(t) = \ln\{1 + s(t)\} = \sum_{n=1}^{\infty} (-1)^{n+1} \frac{s^n(t)}{n} \tag{2.57}$$

Remember that $s(t)$ is a rigorous RSB signal, thus the spectrum of $s^n(t)$ is the nth autoconvolution of an RSB spectrum, which is zero for all $\omega < 0$. Therefore, $U(t)$ is also an RSB signal, and $U_r(t)$ and $U_i(t)$ are also related through the KK relation.

Readers may have already realized that $u(t)$ is indeed a combination of a rigorous RSB signal $s(t)$ and a carrier at 0 Hz, which is exactly the waveform received by the PD in a rigorous SSB self-coherent system. If we can obtain the field information of $u(t)$, we can easily obtain the field information of $s(t)$ by removing the DC component. Remember that the PD detects the square of the amplitude of the received waveform

$$I(t) \propto |u(t)|^2 \tag{2.58}$$

Hence, we can recover the field information of $s(t)$ from $I(t)$ as follows:

a. Take the square root of $I(t)$ to obtain $|u(t)|$.

b. Take the logarithm of $|u(t)|$ to obtain $U_r(t) = \ln|u(t)|$.

c. Get the phase information of $u(t)$ through the KK relation $\phi(t) = U_i(t) = IFT\{j \cdot sgn(\omega) FT\{U_r(t)\}\}$.

d. Recover the field information of $u(t) = |u(t)| \exp[j\phi(t)]$.

e. Recover the field information of $s(t)$ by removing the DC component from $u(t)$.

The algorithm described above is the most well-known KK-family algorithm: the KK algorithm, which includes a logarithm function. In the remainder of this thesis, when we use the term “the KK algorithm”, we are referring to this log-based KK algorithm.

Taking the logarithm of a signal will broaden its spectrum, hence we need digital upsampling

and downsampling before and after the KK algorithm to accommodate the broadened spectrum [20]. To bypass resampling, several variations of the KK algorithm have been proposed. Here we introduce two of them: 1) the iterative KK (iter-KK) algorithm [80] and 2) the upsampling-free KK (ufKK) algorithm [81],[82].

Note that Eq. 2.55 can be transformed into the following form:

$$I(t) = |C + s(t)|^2 = C^2 + 2Cs_r(t) + s_r^2(t) + s_i^2(t) \tag{2.59}$$

where we drop the scaling factor R since we can normalize the power of $I(t)$ before applying further processing. Eq. 2.59 can then be transformed into Eq. 2.60:

$$s_r(t) = \sqrt{\left|I(t) - s_i^2(t)\right|} - C \tag{2.60}$$

Eq. 2.60 allows us to compute $s_r(t)$ from $s_i(t)$. Remember that we also have the KK relation, i.e. we can also compute $s_i(t)$ from $s_r(t)$ using Eq. 2.56. Hence the iter-KK algorithm can be implemented as follows:

a. Start by assuming $s_i(t) = 0$, use Eq. 2.60 to obtain an initial estimation of $s_r(t)$.

b. Substitute the current estimation of $s_r(t)$ into Eq. 2.56 to obtain a better estimation of $s_i(t)$.

c. Substitute the current estimation of $s_i(t)$ into Eq. 2.60 to obtain a better estimation of $s_r(t)$.

d. Use step b and step c iteratively until the estimations of $s_r(t)$ and $s_i(t)$ are stable.

e. Recover $s(t) = s_r(t) + js_i(t)$.

It has been proved that, as the number of iteration increases, the performance of the iter-KK algorithm converges to that of the KK algorithm in a rigorous SSB self-coherent system, but the iter-KK algorithm does not require upsampling at the receiver since it avoids the logarithm operation [80].

In [82], the authors proposed an alternative variation of the KK algorithm which also bypasses the logarithm operation, the ufKK algorithm. In fact, the iter-KK algorithm is also free from upsampling. Here we simply follow the naming convention of [82], i.e. in this thesis, whenever we use the term “ufKK”, we are referring to the algorithm proposed in [82].

The ufKK algorithm approximates the KK algorithm. Remember that the photocurrent $I(t)$ in a rigorous SSB system can be expressed as Eq. 2.59, thus the square root of $I(t)$ can be approximated to the second order binomial expansion as:

$$\begin{aligned}\sqrt{I(t)} &= C\sqrt{1+\frac{2s_r(t)}{C}+\frac{s_r^2(t)+s_i^2(t)}{C^2}} \\ &= C+s_r(t)+\frac{s_i^2(t)}{2C}+O(C^{-2})\end{aligned} \tag{2.61}$$

where $O(\cdot)$ denotes the order of approximation. Assuming that the CSPR is large, i.e. $C \gg |s_r(t)|$, the phase of the signal can be approximated as

$$\phi(t) = \tan^{-1}\frac{s_i(t)}{C+s_r(t)} = \frac{s_i(t)}{C}+O(C^{-2}) \tag{2.62}$$

According the KK algorithm, we also have

$$\begin{aligned}\phi(t) = U_i(t) &= IFT\{j\cdot sgn(\omega)FT\{U_r(t)\}\} \\ &= IFT\left\{j\cdot sgn(\omega)FT\left\{\log\sqrt{I(t)}\right\}\right\}\end{aligned} \tag{2.63}$$

Note that by using the second-order Taylor's expansion at $\sqrt{I(t)} = C$, $\ln\sqrt{I(t)}$ can be express as:

$$\begin{aligned}\ln\sqrt{I(t)} &= \ln\left\{C\left[\left(\frac{\sqrt{I(t)}}{C}-1\right)+1\right]\right\} \\ &= 2\frac{\sqrt{I(t)}}{C}-\frac{1}{2}\frac{I(t)}{C^2}+\ln C-\frac{3}{2}+O(C^{-3})\end{aligned} \tag{2.64}$$

The third and the fourth constant terms in Eq. 2.64 are DC terms, which can be ignored since they can be removed by the subsequent Hilbert transform. By combining Eq 2.61 to Eq. 2.64, we can recover the real part of the optical field $C+s_r(t)$ using Eq. 2.65:

$$\begin{aligned}C+s_r(t) &\cong \sqrt{I(t)}-\frac{s_i^2(t)}{2C} = \sqrt{I(t)}-\frac{C}{2}\left(\frac{s_i(t)}{C}\right)^2 \\ &\cong \sqrt{I(t)} \\ &\quad -\frac{C}{2}\left(IFT\left\{j\cdot sgn(\omega)FT\left\{2\frac{\sqrt{I(t)}}{C}-\frac{1}{2}\frac{I(t)}{C^2}\right\}\right\}\right)^2\end{aligned} \tag{2.65}$$

Now we have derived all the mathematical foundations of the ufKK algorithm, which can be described as follows:

a. Take the mean of the photocurrent $I(t)$ to estimate C.

b. Take the square root of $I(t)$.

c. Use Eq. 2.65 to obtain $s_r(t)$.

d. Use Eq. 2.56 (the KK relation) to obtain $s_i(t)$ from $s_r(t)$.

e. Recover $s(t) = s_r(t) + js_i(t)$.

All the KK-family algorithms we have introduced above are based on the following two assumptions:

1) The CSPR is relatively large, i.e. $C \gg |s(t)|$

2) $s(t)$ is a rigorous SSB signal.

In a VSB system however, the second condition may not be satisfied. Suppose we use the optical filter to suppress the LSB components, the PD would receive a DC carrier C, the RSB signal $s_1(t)$, and an under-filtered LSB signal $s_2^*(t)$. Note that in this thesis we define $s_2(t)$ to be the complex conjugate of the residual LSB signal for the convenience of derivation, such that both $s_1(t)$ and $s_2(t)$ are RSB signals. The photocurrent in a VSB system should be expressed as:

$$\begin{aligned} I(t) &= R|C + s_1(t) + s_2^*(t)|^2 \\ &= R[C^2 + Cs_1(t) + Cs_2(t) + Cs_2^*(t) + Cs_1^*(t) \\ &\quad + s_1(t)s_1^*(t) + s_1(t)s_2(t) + s_1^*(t)s_2^*(t) + s_2(t)s_2^*(t)] \end{aligned} \tag{2.66}$$

Again, there is the carrier-carrier beating term at DC, the carrier-signal beating terms, and the SSBI terms. The carrier-signal beating terms are the useful terms since they are linearly proportional to $s_1(t)$, $s_2(t)$ and their complex conjugates. Now let's consider a case where the PD detects a rigorous RSB signal $s_1(t) + s_2(t)$, then the photocurrent becomes:

$$\begin{aligned} I'(t) &= R|C + s_1(t) + s_2(t)|^2 \\ &= R[C^2 + Cs_1(t) + Cs_2(t) + Cs_2^*(t) + Cs_1^*(t) \\ &\quad + s_1(t)s_1^*(t) + s_1(t)s_2^*(t) + s_1^*(t)s_2(t) + s_2(t)s_2^*(t)] \end{aligned} \tag{2.67}$$

Interestingly, if the CSPR is extremely large, the SSBI terms can be ignored, then $I'(t)$ and $I(t)$ become identical. Remember that the KK-family algorithms introduced in this section assume that the PD detects a rigorous SSB signal. If we apply one of these algorithms directly

in a VSB system, we will end up with an estimation of $s_1(t) + s_2(t)$. This is not too bad. As we will shortly see in section 2.4.2.3, both $s_1(t)$ and $s_2(t)$ are related to the RSB component $s_0(t)$ of the transmitter-side signal $s_0(t) + s_0^*(t)$, and $s_1(t) + s_2(t)$ can be obtained by applying a linear filter to the $s_0(t)$, thus we can actually recover $s_0(t)$ from $s_1(t) + s_2(t)$ by applying an inverse filter through time/frequency-domain equalizations.

The problem is that if the SSBI terms cannot be neglected, the difference between the SSBI terms in Eq. 2.66 and the SSBI terms in Eq. 2.67 would degrade the accuracy of the estimated RSB signal when using the KK-family algorithms described in this section. As a result, a VSB system generally achieves worse performance than a rigorous SSB system if we simply use the existing KK-family algorithms, thus there is motivation to develop a new algorithm specifically for the VSB systems. In this thesis, we propose a filter response aware iterative KK (FA-iter-KK) algorithm, which can be regarded as a generalization of the iter-KK algorithm introduced in this section, but it is directly based on Eq. 2.66 instead of Eq. 2.55 or Eq. 2.67. The principle and the test results of this algorithm will be presented in Chapter 4, section 4.3.

2.4.2.3 CD

The key motivation to upgrade an IM/DD system to an SSB/VSB self-coherent system is to acquire digital CD compensation capability. Note that the impact of CD on the optical field is an all pass filter, which can be described as

$$FT\{s(t)\} = FT\{s_0(t)\} \exp\left(\frac{1}{2} j\beta_2 \omega^2 L\right) \tag{2.68}$$

where $s_0(t)$ represents the optical field of the signal at the transmitter, $s(t)$ is the optical field of the signal at the receiver, L is the transmission distance, and FT{} denotes Fourier transform.

If $s_0(t)$ is a rigorous RSB signal, so is $s(t)$. Hence in a rigorous SSB system, we can first retrieve the complex-valued field information of $s(t)$ using the algorithms described in subsection 2.4.2.2, and then apply an inverse filter to $s(t)$ to compensate for the CD.

$$FT\{s_0(t)\} = FT\{s(t)\} \exp\left(-\frac{1}{2} j\beta_2 \omega^2 L\right) \tag{2.69}$$

In a VSB system however, the situation is more complicated. As we have discussed in section 2.4.2.2, the estimation of $s(t)$ itself is not that accurate if we use the SSB field reconstruction

algorithms developed for rigorous SSB systems in a VSB system.

In addition, the residual sideband could lead to power fading effect in a VSB system. Remember that in a VSB system where the residual LSB signal $s_2^*(t)$ cannot be neglected, the SSB field reconstruction algorithms introduced in section 2.4.2.2 estimates the field information of $s_1(t) + s_2(t)$. Now we define the transmitter side DSB signal as $s_0(t) + s_0^*(t)$, where $s_0(t)$ is the RSB component. Given the frequency response of the optical filter $H_F(\omega)$, $s_1(t)$ and $s_2^*(t)$ are related to $s_0(t)$ and $s_0^*(t)$ through the following equations:

$$FT\{s_1(t)\} = FT\{s_0(t)\}H_F(\omega)\exp\left(\frac{1}{2}j\beta_2\omega^2 L\right) \tag{2.70}$$

$$FT\{s_2^*(t)\} = FT\{s_0^*(t)\}H_F(\omega)\exp\left(\frac{1}{2}j\beta_2\omega^2 L\right) \tag{2.71}$$

Using the properties of the Fourier transform, Eq. 2.71 can then be transformed into:

$$FT\{s_2(t)\} = FT\{s_0(t)\}H_F^*(-\omega)\exp\left(-\frac{1}{2}j\beta_2\omega^2 L\right) \tag{2.72}$$

By combining Eq. 2.70 and Eq. 2.72, we have:

$$\begin{aligned} &FT\{s_1(t) + s_2(t)\} \\ &\quad = FT\{s_0(t)\}\left[H_F(\omega)\exp\left(\frac{1}{2}j\beta_2\omega^2 L\right)\right. \\ &\quad \left. + H_F^*(-\omega)\exp\left(-\frac{1}{2}j\beta_2\omega^2 L\right)\right] \end{aligned} \tag{2.73}$$

If we have an extremely sharp optical filter which removes all the LSB components, i.e. $H_F(\omega)$ is an ideal RSB filter, then $s_2(t)$ vanishes, and Eq. 2.73 degenerates to Eq. 2.70. In this case, the VSB system becomes a rigorous SSB system, and if we only look at the RSB components, we find that the system simply applies an all-pass filter $\exp\left(\frac{1}{2}j\beta_2\omega^2 L\right)$ to the signal. In another extreme case, where we don't use any optical filter, i.e. $H_F(\omega)$ is an all-pass filter, then the system becomes an IM/DD system. In this case, the terms inside the square brackets of Eq. 2.73 turn into $2\cos(\frac{1}{2}\beta_2\omega^2 L)$. If we drop the scaling factor 2 and take the magnitude only, this is exactly the small-signal channel response of a chirp-free IM/DD system (please refer to Table 2.3). Again, we only care about the RSB components of the signal. Since this is an IM/DD system, the transmitted RSB spectrum will suffer from the power fading effect.

In a more general case, $H_F(\omega)$ is neither an ideal RSB filter nor an all-pass filter. An example

is shown in Fig. 2.24, where we consider C-band transmission at 1550 nm over 40 km of SMF, and we assume that $H_F(\omega)$ is a trapezoidal function on a logarithmic scale.

Fig. 2.24 shows that the power fading effect does exist in a VSB system, as we can see frequency notches in the system's magnitude response. But unlike an IM/DD system, the spectral information at these frequency notches is not completely lost, i.e. the power fading effect in a VSB system is weaker than that in an IM/DD system. Generally, the sharper the optical filter is, the weaker the power fading effect will be. We also observe that the power difference between the LSB components and the RSB components has an impact on the depths of the notches. The larger the power difference is, the smaller the depth will be. Consequently, in a VSB system, the power fading effect is more severe in the low frequency regime than in the high frequency regime.

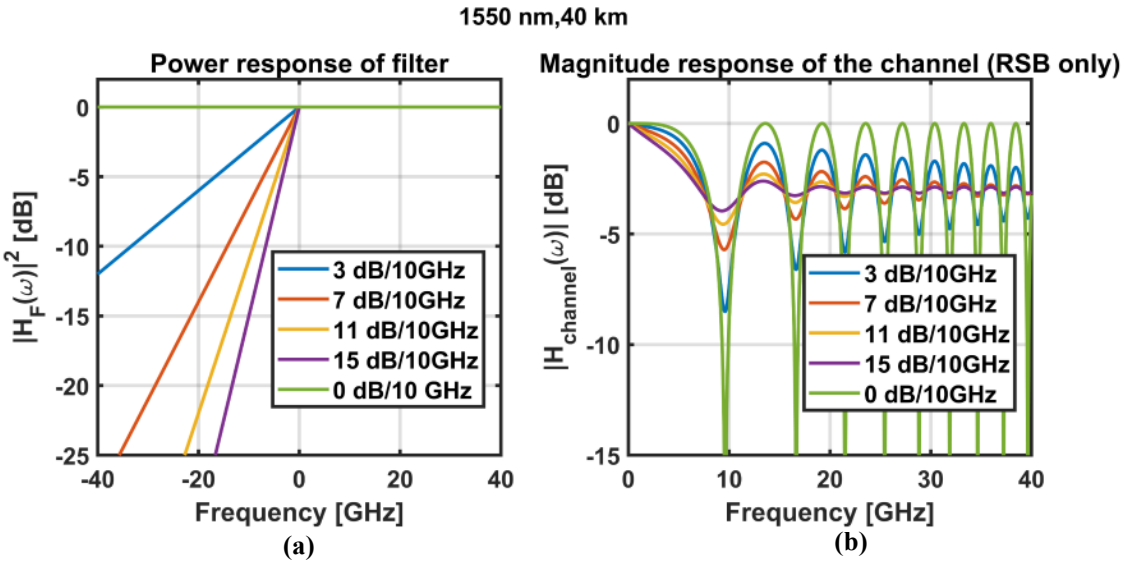

Fig. 2.24 (a) Power responses of trapezoidal optical filters with different edge gradients, and (b) magnitude responses of VSB systems enabled by optical filters with different edge gradients.

In a practical VSB system, although $s_2(t)$ cannot be totally neglected, it is much weaker than $s_1(t)$. If we obtain a relatively accurate estimation of $s_1(t) + s_2(t)$, we can simply apply an all-pass filter $\exp\left(-\frac{1}{2}j\beta_2\omega^2 L\right)$ to combat the CD. By doing so, we can still get a decent estimation of $s_0(t)$, because this filter compensates for the CD effect on $s_1(t)$, which is the dominant term in $s_1(t) + s_2(t)$. However, an all-pass filter cannot flatten the frequency-domain ripples, and the ripples usually need to be compensated for by a time-domain equalizer,

e.g. an FFE[13]. As a result, the equalization enhanced noise will be more severe in a VSB system than in a rigorous SSB system, which degrades the performance of a VSB system.

In this thesis, for simplicity, we only consider VSB self-coherent systems which use push-pull MZMs at the transmitter-side. Therefore, we didn't include the impact of laser chirp in the above analysis. The chirp of DMLs/EMLs could introduce additional phase modulations. Implementing a DML/EML based VSB system requires additional modifications of the receiver DSP, which is beyond the scope of this thesis. If the readers are interested in this topic, please refer to [29],[31] for more information.

2.4.2.4 Other impairments

In this section, I will quickly go through other typical transmission impairments in an SSB/VSB self-coherent system.

Bandwidth limitations of devices: Just like an IM/DD system, the bandwidth limitations of the DAC(s), the ADC, the modulator, the RF amplifier, the PD and the TIA also lead to ISI in an SSB/VSB self-coherent system. Hence in an SSB/VSB self-coherent system, in addition to the CD compensation block, we also need pulse-shaping (section 2.3.3.2) and time-domain equalizers (section 2.3.3.3) to limit the signal's bandwidth and combat the ISI.

Noises: Since an SSB/VSB self-coherent system allows us to compensate for dispersion in DSP, it can be operated in the C-band and benefit from the maturity of EDFA technology to further extend the reach. Therefore, in addition to the noise sources introduced in section 2.3.3.2, an amplified SSB/VSB self-coherent system could also suffer from the amplified spontaneous emission (ASE) noise from the EDFAs.

In addition, we should pay more attention to the impact of the laser phase noise. In an SSB/VSB self-coherent system, the receiver detects the both the amplitude and the phase information of the signal. Since the reference carrier and the signal are from the same laser, they experience the same amount of phase noise (and frequency drifting), hence after carrier-signal beating, the

[13] In this case, the time equalizer is indeed compensating for the difference between the all-pass filter $\exp\left(-\frac{1}{2}j\beta_2\omega^2 L\right)$ and the real system response.

phase noise (and frequency drifting) experienced by the carrier and the signal would cancel each other. Therefore, unlike a coherent system which incorporates a separate laser as the LO, a self-coherent system does not need frequency offset compensation or carrier phase recovery blocks in the receiver DSP. But this does not mean that the laser linewidth can be arbitrarily large in SSB/VSB self-coherent systems. It has been proved that the equalization enhanced phase noise (EEPN) and the phase to amplitude noise still exist in SSB/VSB self-coherent systems, which also scale with the laser linewidth [83].

Loss: If EDFAs are used, the SSB/VSB self-coherent system will become a noise limited system, since the EDFAs can boost the optical power, and optimal ROP can always be achieved. On the other hand, there is still motivation to exclude the use of EDFAs even in C-band transmissions especially for short transmission distances (e.g. < 80 km). An unamplified SSB/VSB self-coherent system is a loss limited system, and as we have discussed in section 2.3.2.3, the loss will limit the achievable ROP in such systems, which then affects the transmission performance.

Device and fiber nonlinearities: Just like an IM/DD system, in an SSB/VSB self-coherent system, there also exist device nonlinearities originated from the PD and the RF amplifiers. The situation with the modulator induced device nonlinearity is slightly more complicated. Note that an SSB/VSB self-coherent system detects the field information of the signal (rather than the intensity information), hence to minimize the modulator induced device nonlinearity, ideally each MZM should be biased at the middle point of the linear regime of its field transfer function (rather than its power transfer function) [98]. The field transfer function of an MZM is given by:

$$\frac{E_{out}(t)}{E_{in}(t)} = \cos\left(\frac{\phi_2(t) - \phi_1(t)}{2}\right)\exp(j\frac{\phi_2(t) + \phi_1(t)}{2}) \tag{2.74}$$

where $\phi_{1,2}(t)$ represent the phase modulations on the two arms of the MZM. Eq. 2.74 shows that, to achieve linear modulation, the MZM (or the children MZMs in the IQ modulator) needs to be biased at the null point. But note that an SSB/VSB self-coherent system also requires a strong optical carrier to be inserted at the edge of the (quasi-)SSB signal. The simplest way to do so is to off-bias the modulator to allow for some DC leakage, which will lead to increased

modulator induced device nonlinearity. To decouple the carrier generation and the device nonlinearity, one option is to bias the modulator at null point, and then use a parallel optical path to generate the carrier. We will discuss more about this option in Chapter 4 and Chapter 5. Moreover, the SSBI can also be regarded as a special kind of device nonlinearity, which is originated from the square-law detection of the PD. In fact, as we will see in Chapter 4, one alternative way to deal with the SSBI is to leave it untreated during the SSB field reconstruction process (e.g. using the SSB filtering algorithm), and then use a nonlinear equalizer (e.q. a 2^{nd} order VE) to compensate for the ISI, the SSBI, and the device nonlinearity originated from other sources simultaneously.

As for the fiber nonlinearity (Kerr effect), since the SSB/VSB self-coherent systems are normally operated in the C-band, the FWM can be suppressed by the accumulated CD. But SPM and XPM still exist in these systems. Remember that the strength of Kerr nonlinearity is proportional to the cubic of the magnitude of the signal (Eq. 2.18). Therefore, in a noise limited SSB/VSB self-coherent system (with EDFAs), the launch power (i.e. the optical power launched into the fiber) should be optimized to achieve the best transmission performance. On the other hand, in a loss limited SSB/VSB self-coherent system (without EDFAs), the launch power is directly determined by the laser output power and the total loss of the transmitter, which are then related to the ROP requirement and the loss budget of the system. In other words, in a loss limited SSB/VSB self-coherent system, optimization of the launch power is deeply coupled with optimizations of other system parameters such as the ROP, the modulator's driving voltage, the CSPR and etc.

Chapter 3 O-band CWDM4 IM/DD systems

3.1 Overview

In this chapter, we will demonstrate two novel methods to improve the transmission performance of CWDM4 PAM4 systems based on advanced DSP algorithms. Specifically, in section 3.2, we propose to intentionally introduce a controlled amount of ISI in the transmitter-side DSP to increase the AC power at the receiver, then we use FTN techniques to compensate for the ISI. We achieve 600 Gb/s net rate transmission over 0-10 km using the proposed scheme considering the 6.7% overhead hard decision FEC [32],[33]. In section 3.3, we propose to combine a symbol-level wavelength-interleaver with a 4D-PAM4-TCM encoder to improve the system's robustness against channel performance discrepancies. We experimentally proved that the proposed wavelength-interleaved 4D-PAM4-TCM system outperforms the conventional 4D-PAM4-TCM system in terms of receiver sensitivity requirement at the KP4 FEC threshold in a 4×100Gb/s link over 0-20 km when sizable channel performance discrepancies exist in such systems [34].

3.2 600 Gb/s Net Rate PAM4 Transmissions enabled by FTN techniques

3.2.1 Motivation

To increase the throughput of a CWDM system without increasing the number of wavelengths, one needs to use either a higher-order modulation format or a higher symbol rate, which leads to a more stringent requirement for either the SNR or the overall system bandwidth. Both paths require better components.

Alternatively, the burdens on the hardware can be relieved at the expense of using more advanced DSP techniques, such as FTN techniques. FTN techniques allow for transmissions of high symbol rate signals through channels with limited bandwidth, at the cost of introducing ISI to the signal. Since the ISI is severe, conventional FFE or DFE based ISI compensation methods would suffer from noise enhancement issue and error propagation issue respectively,

thus are insufficient for ISI mitigation in FTN systems, which leads to two different branches of FTN techniques. For the FFE based method, a 2-tap post filter $1 + \alpha Z^{-1}$ can be applied to suppress the equalization-enhanced noise, and then the signal can be recovered using MLSE [55],[56]. For the DFE based method, THP has been proposed as a transmitter-side version of DFE, so that the error propagation problem can be avoided [57]-[62]. A detailed introduction of these two branches of FTN techniques has been provided in Chapter 2, section 2.3.3.2-2.3.3.4.

The key idea of FTN technique is to introduce a certain amount of ISI through an aggressive low pass filter (LPF), so that the bandwidth requirement of the signal is reduced, and then to mitigate the ISI using advanced DSP algorithms such as poster-filter + MLSE or THP. The LPF can be achieved by either utilizing the analog bandwidth of a component [56] or digitally implementing an RC pulse shaping filter with a small roll-off factor to mimic a brick-wall response [60]-[62]. A brick-wall digital filter is preferred when the system has a strict bandwidth limitation. Such strict bandwidth limitation may arise from the limited converter sampling rate as in [60], or the bandwidth limitation of a certain test equipment as in [61],[62]. In this work however, we look at the FTN technologies from a different perspective. We aim at increasing the AC power of the received signal instead of packing more data into a limited frequency range. In our experimental setup, the system bandwidth (after pre-emphasis) and the sampling rate of the converters are large enough to support Nyquist pulse shaping of signals with target symbol rates. We also use a digital RC pulse shaping filter to introduce a controlled amount of ISI, but instead of sticking to a brick-wall response, we jointly optimize the FWHM and the roll-off factor of the filter. As we will shortly see in section 3.2.2, the optimized controlled-ISI pulse shaping filter does not reduce the signal's bandwidth of non-zero portion of the spectrum when compared to a Nyquist pulse shaped signal. However, it reduces the PAPR of the signal when used together with a pre-emphasis filter, and it changes the power distribution of the signal in the frequency domain, which leads to higher electrical AC power after photo-detection and transimpedance amplification at the receiver. As a result, the BER performance can be improved accordingly once the introduced ISI is properly mitigated using

THP or receiver-side FFE aided with post-filter + MLSE.

The remainder of section 3.2 is organized as follows. We explain the operational principle in section 3.2.2, where we compare the controlled-ISI pulse shaping with the classic Nyquist pulse shaping, especially focusing on their impacts on the AC power of the signal. The experimental setup and the DSP blocks are described in section 3.2.3. The experimental results are presented in section 3.2.4. We first demonstrate and compare controlled-ISI pulse shaped 600 Gb/s PAM4 transmission results at BtB and 2 km, when processed with THP and post filter + MLSE aided FFE, respectively. Then we explore the limit of our system at 10 km by sweeping the symbol rate in each wavelength channel and using Volterra equalizer (VE) to mitigate the nonlinear impairments. Finally, we conclude this work in section 3.2.5.

3.2.2 Operation Principle

The impulse response of a generalized RC filter can be described as Eq. 3.1.

$$h(t) = h(nT_s) = \frac{1}{T_p} \frac{\operatorname{sinc}\left(\frac{nT_s}{T_p}\right) \cos\left(\frac{n\pi\beta T_s}{T_p}\right)}{1 - \left(2\beta \frac{nT_s}{T_p}\right)^2} \tag{3.1}$$

where β is the roll-off factor, T_s and T_p represent the target symbol duration and the symbol duration considered in pulse shaping, respectively. The FWHM of the frequency response is $1/T_p$, and a pulse shaped signal requires a bandwidth (defined as the width of non-zero portion of the signal's spectrum) of $(1+\beta)/T_P$. If T_p equals to T_s, then Eq. 3.1 represents the impulse response of a classic Nyquist pulse shaping filter, which does not introduce ISI, regardless of the choice of β. If $T_p > T_s$ however, the pulse shaping filter inevitably introduces ISI to the signal, and the amount of ISI is affected by both the T_p/T_s ratio and the β value. In this work, these two parameters are jointly optimized to control the amount of introduced ISI, therefore in the rest part of this section, we refer to the $T_p > T_s$ case as controlled-ISI pulse shaping.

Fig. 3.1(a) shows the frequency responses of a Nyquist pulse shaping filter and an optimized controlled-ISI pulse shaping filter. Both filters are designed for an 81 Gbaud signal ($1/T_s = 81$ GHz). The Nyquist pulse shaping filter aims at minimizing the signal bandwidth, and it is implemented as an RC filter with a FWHM of $1/T_p = 81$ GHz and a roll-off factor of $\beta =$

0.01. The controlled-ISI pulse shaping filter is optimized for the best BER performance at BtB, when THP and a pre-emphasis filter that flattens the frequency responses of cascaded devices up to the RF amplifier are used at the transmitter. It is implemented as an RC filter with $1/T_p = 71$ GHz and $\beta = 0.3$.

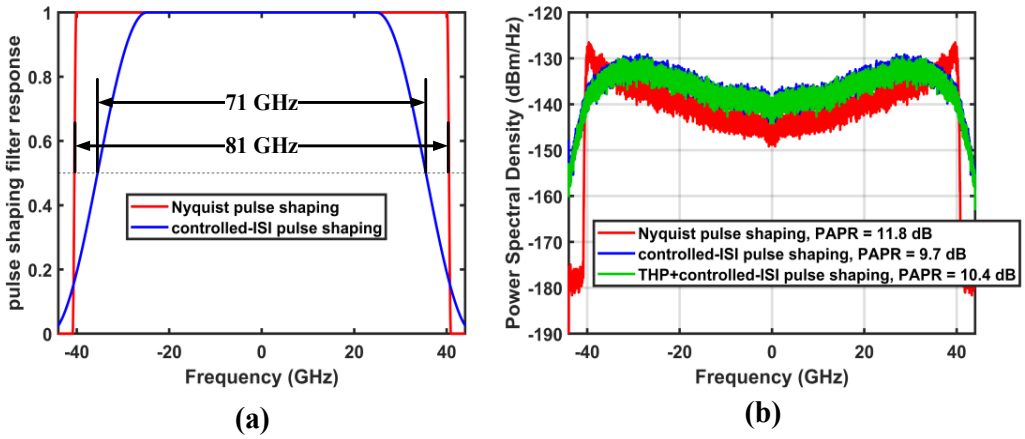

Fig. 3.1 (a) Frequency responses of pulse shaping filters designed for 81 Gbaud signals, and (b) PSDs of 81 Gbaud signals in the digital domain before being loaded to DAC channels when processed with different transmitter DSP combinations. (©2020 IEEE)

Note that the Nyquist pulse shaped signal requires a bandwidth of (1+0.01)×81 = 81.81 GHz, while the controlled-ISI pulse shaped signal requires a bandwidth of (1+0.3)×71 = 92.3 GHz. The controlled-ISI pulse shaped signal is further truncated to be within [-44 GHz, 44GHz] by an anti-aliasing filter during the resampling process, since our DAC has a limited sampling rate of 88 Gsa/s. Nevertheless, the bandwidth of non-zero portion of the signal's spectrum required by the controlled-ISI pulse shaped signal is still larger than that of the Nyquist pulse shaped signal. Fig. 3.1(b) shows the PSDs of 81 Gbaud PAM4 signals processed with 1) Nyquist pulse shaping, 2) controlled-ISI pulse shaping, and 3) THP + controlled-ISI pulse shaping. The PAPR corresponds to each curve is denoted in the legend. After applying THP (if used) and pulse shaping, the signals are pre-emphasized and quantized to 8 bits before PSD and PAPR computations. A full description of DSP blocks will be provided in section 3.2.3. Fig. 3.1(b) shows that, by using controlled-ISI pulse shaping, we can reduce the PAPR of the signal and concentrate more power at lower frequencies after applying transmitter-side DSP. As a result, the electrical AC power of the received signal after photo-detection and transimpedance

amplification is increased, as we will shortly see.

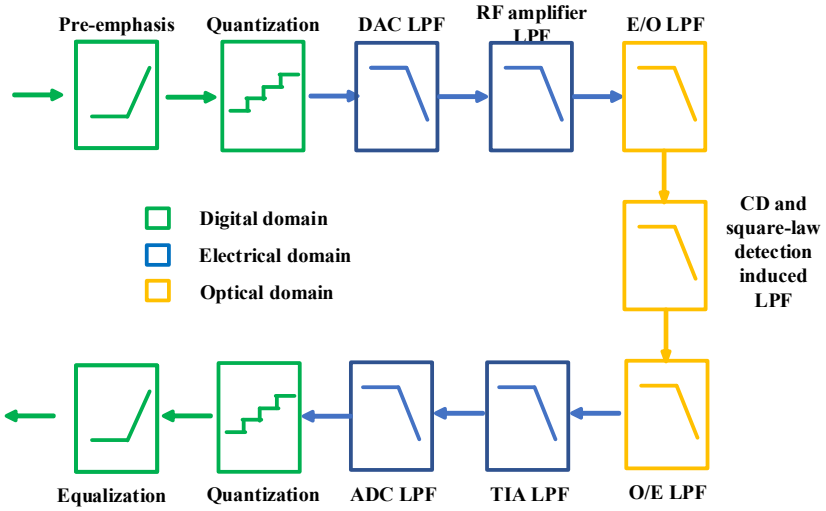

Fig. 3.2 A simplified model of a typical IM/DD system. E/O and O/E represent electro-optical conversion and opto-electrical conversion, respectively. (©2020 IEEE)

Fig. 3.2 depicts a linear and noise-less model of a typical IM/DD system. Generally, both transmitter-side pre-emphasis and receiver-side equalization are required to compensate for the ISI caused by the bandwidth limitations of the devices and the CD induced power fading effect. Unlike receiver-side equalization, pre-emphasis does not enhance noise from the channels, but it increases the PAPR of the signal in the digital domain. When quantized to the same number of amplitude levels, since the peak power is fixed, a lower PAPR leads to a higher average signal power in the digital domain. After digital waveform generation, the signal is first mapped to the electrical domain by a DAC channel, then amplified by an RF amplifier, mapped to the optical domain through modulation, transmitted through a dispersive channel, mapped back to the electrical domain through photo-detection, amplified again by a TIA and finally mapped back to the digital domain by an ADC channel. During this process, the signal sees multiple LPFs as shown in Fig. 3.2. The high frequency components of the signal experiences more attenuation (or less gain in the cases of the RF amplifiers and the TIAs) than the low frequency components. Therefore, a signal with power concentrated at lower frequencies will experience less loss through those LPFs. Note that in a loss limited system, there is no optical amplifier, and we assume that each RF amplifier or TIA provides a fixed gain regardless of the input power (no saturation occurs). The AC power of the received signal is mainly determined by the

average power in the digital domain at the transmitter and the frequency-dependent loss introduced by those LPFs. Since controlled-ISI pulse shaping reduces the PAPR of the signal and concentrates more power at lower frequencies in our system, it could increase the electrical AC power at the receiver.

Note that pulse-shaping and pre-emphasis can be implemented in the frequency domain in one step as a single digital filter. The superposition of the optimized controlled-ISI pulse shaping filter and the pre-emphasis filter in this work is indeed a less-heavy pre-emphasis filter designed for a Nyquist pulse shaped signal with a roll-off factor of 71*(1+0.3)/81-1 = 0.14. By doing less-heavy pre-emphasis (introducing more ISI at the transmitter), we pose more burdens onto the receiver-side equalization, which leads to increased equalization-enhanced noise. Therefore, in this work we propose to combine controlled-ISI pulse shaping with 1) THP to mitigate the introduced ISI so that the burdens on receiver-side FFE is relieved, or 2) a post-filter to suppress the receiver-side-FFE-enhanced noise, then use MLSE to retrieve the signal. THP can be regarded as DFE based pre-equalization at the transmitter. As we can see from the green curve in Fig. 3.1(b), unlike FFE based pre-emphasis, THP does not significantly change the PSD distribution, but it does introduce a power penalty and slightly increases the PAPR. The post filter and MLSE are implemented at the receiver, thus do not affect the PAPR or the PSD distribution at the transmitter. In other words, by using controlled-ISI pulse shaping, we aim at replacing a portion of the transmitter-side pre-emphasis with THP or receiver-side FFE aided with post-filter + MLSE to increase the received AC power without increasing equalization enhanced noise, so that the received SNR is increased, and the BER performance can be improved accordingly.

3.2.3 Experimental setup and DSP blocks

The experimental setup and the DSP blocks are shown in Fig. 3.3(a) and Fig. 3.3(b), respectively. We use four 88 Gsa/s 8-bit DAC channels from the same arbitrary waveform generator (AWG) and four SHF s804b RF amplifiers with 22 dB gain to simultaneously drive the four O-band EMLs inside the CWDM-TOSA. The optical output of the TOSA is launched into 0 to 10 km of SMF. Then we use a VOA to control ROP. At the receiver side, a commercial

CWDM demultiplexer (DeMux) is used to separate the four channels. We didn't have access to four high speed ADC channels by the time we did the experiment, thus we used a Picometrix PT-28E photodiode with TIA (PD-TIA) and a 160 Gsa/s 8-bit ADC channel from a Keysight real-time oscilloscope (RTO) to detect the four wavelength channels one by one. No optical amplifier is used in this experiment.

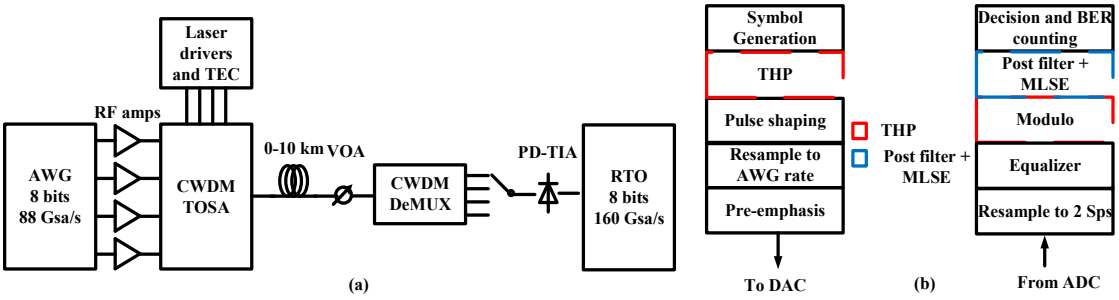

Fig. 3.3 (a) Experimental setup and (b) DSP stacks of 600Gb/s CWDM FTN IM/DD transmission systems. TEC: thermoelectric cooler. (©2020 IEEE)

The transmitter and receiver DSPs are performed off-line using Matlab. At the transmitter, for each wavelength channel, after PAM4 symbol generation, if THP is used, it is implemented at 1 Sps before pulse shaping. We use 50-tap THP in this work, and the tap coefficients are obtained from a training symbol aided DFE at the receiver as we did in Fig. 2.15. Then the signal is pulse shaped, resampled to the AWG sampling rate, and pre-emphasized by a 75-tap linear FFE. The pre-emphasis filter flattens the combined frequency responses of 1) the DAC channels and the RF amplifiers, or 2) the DAC channels, the RF amplifiers and the EMLs. At the receiver, the signal of each wavelength channel is first resampled to 2 Sps, then equalized by either a linear FFE or a 3rd -order VE. If THP is used at the transmitter, a modulo operation is also required at the receiver. Alternatively, in the post filter + MLSE case, a 2-tap post filter with a Z-domain response of $1+\alpha Z^{-1}$ is applied after equalization to suppress the FFE enhanced noise, where α needs to be optimized for each combination of wavelength, distance and symbol rate, and then the PAM4 sequence is recovered through a 4-state MLSE based on Viterbi algorithm (section 2.3.3.3). Finally, the PAM4 sequence is decoded back to a bit stream and the pre-FEC BER can be computed accordingly.

3.2.4 Experimental results

3.2.4.1 When Less-Heavy Pre-emphasis meets FTN

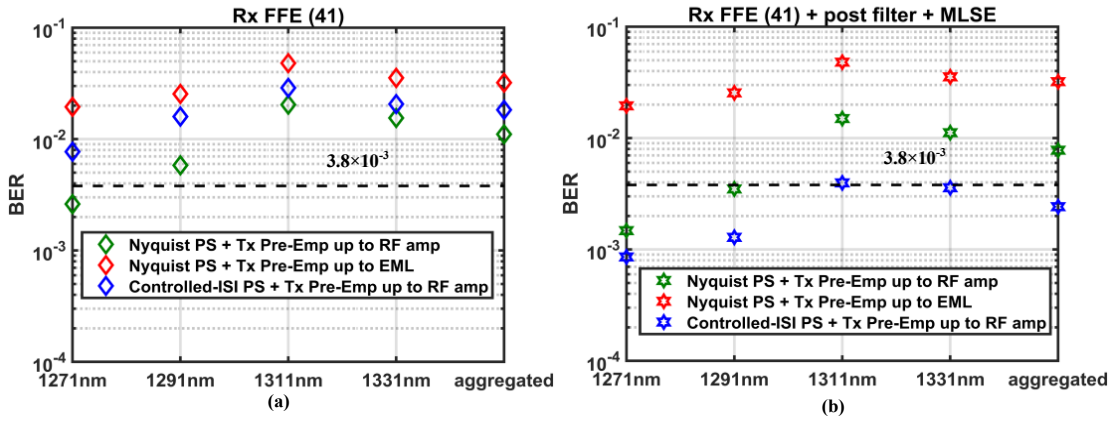

Fig. 3.4 BER performance of individual wavelength channels and the aggregated signal at BtB for 4×81 Gbaud PAM4 transmissions with different transmitter-side DSP combinations when processed with (a) FFE and (b) post filter + MLSE aided FFE at the receiver. (©2020 IEEE)

Fig. 3.4(a) shows the BtB BER performance of individual wavelength channels and the aggregated signal (BER averaged over all channels) with different transmitter-side DSP combinations, when a 41-tap linear FFE is applied in each channel at the receiver. Specifically, we compare the following three cases: 1) Nyquist pulse shaped PAM4 signals with pre-emphasis up to the EMLs, 2) Nyquist pulse shaped PAM4 signals with pre-emphasis up to the RF amplifiers, and 3) controlled-ISI pulse shaped PAM4 signals with pre-emphasis up to the RF amplifiers. According to the Fig. 3.3, case 2 does less heavy pre-emphasis than case 1, and according to section 3.2.3, case 3 does less heavy pre-emphasis than case 2. The symbol rate and the ROP of each wavelength channel in all cases are 81 Gbaud and -3 dBm, respectively. The BER performance discrepancies should be attributed to 1) component differences at the transmitter, which includes the differences of bandwidth limitations of DAC channels, RF amplifiers and EMLs, the differences of thermal/flicker/laser noises from the transmitter, the differences of modulation efficiencies of EMLs and etc., and 2) the wavelength dependence of the PD's responsivity. Note that ROP includes both DC and AC components. In our system, the DC power is much stronger than the AC power, but only the AC power is the useful part since the signals are zero-mean in the digital domain. Table 3.1 lists the received root-mean-square

(RMS) voltages (measured after PD-TIA) as a measure of the received AC power in all four wavelength channels when using different DSP combinations.

Table 3.1 Received RMS voltage after PD-TIA (mV) (©2020 IEEE)

Wavelength (nm)	1271	1291	1311	1331
Nyquist pulse shaped PAM4 w/ pre-Emp up to EML	20.7	21.5	14.2	15.7
Nyquist pulse shaped PAM4 w/ pre-Emp up to RF amp	30	35.2	21.9	23.8
Controlled-ISI shaped PAM4 w/ pre-Emp up to RF amp	51.4	59.8	39.8	44
Controlled-ISI shaped PAM4 w/ THP + pre-Emp up to RF amp	48.7	56.9	37.8	42.8

Measured at BtB with -3 dBm ROP in each wavelength channel

Fig. 3.4(a) shows that if only FFE is used at the receiver, there is a trade-off between the achievable received AC power and the FFE enhanced noise. We observe that pre-emphasizing up to the RF amplifiers (case 2) provides better BER performance than pre-emphasizing up to the EMLs (case 1), since a less-heavy pre-emphasis filter would lead to higher received RMS voltages. However, further increasing the amount of ISI at the transmitter through controlled-ISI pulse shaping (case 3) leads to worse BER performance, as the penalty of increased FFE enhanced noise cancels the gain of increased received AC power.

We then investigate the potential to suppress the equalization enhanced noise using post-filter + MLSE in each case, and the results are shown in Fig. 3.4(b). Interestingly, when using Nyquist pulse shaping with pre-emphasis up to the EMLs (case 1, red points in Fig. 3.4(b)), the optimized α values for all wavelength channels are 0's, and applying post filter + MLSE does not improve the performance, which indicates that the bandwidth limitation is mainly originated from the transmitter side, and the receiver FFE enhanced noise is weak in this case. However, applying post filter + MLSE does improve the BERs in case 2 and case 3, as we can see from the green points and the blue points in Fig. 3.5(b). Unfortunately, in our system, even with the help of post filter + MLSE, Nyquist pulse shaping with pre-emphasis up to the RF amplifiers cannot support a 4×81 Gbaud PAM4 transmission even at BtB considering 6.7% overhead HD-FEC (with a pre-FEC BER threshold of 3.8×10^{-3}). On the other hand, we found

that by using post filter + MLSE, controlled-ISI pulse shaping with pre-emphasis up to the RF amplifiers outperforms Nyquist pulse shaping with the same pre-emphasis filter, since controlled-ISI pulse shaping further improves the received AC power, and the penalty of FFE enhanced noise can be sufficiently mitigated by post filter + MLSE.

Alternatively, the FFE noise enhancement issue can also be mitigated by applying THP at the transmitter, so that the ISI burdens posed onto the receiver side is relieved. From Table 3.1 we observe that there is a power penalty caused by using THP, as we have discussed in section 3.2.2. Nevertheless, the power penalty of THP does not cancel the AC power gain of controlled-ISI pulse shaping. Fig. 3.5 shows the BtB BER performance of 4×81 Gbaud controlled-ISI pulse shaped PAM4 signals when processed with 1) THP, 2) poster + MLSE and 3) THP + poster + MLSE. We found that post filter + MLSE based method provides slightly better performance than THP based method, since THP has a power penalty which leads to a slightly worse received SNR.

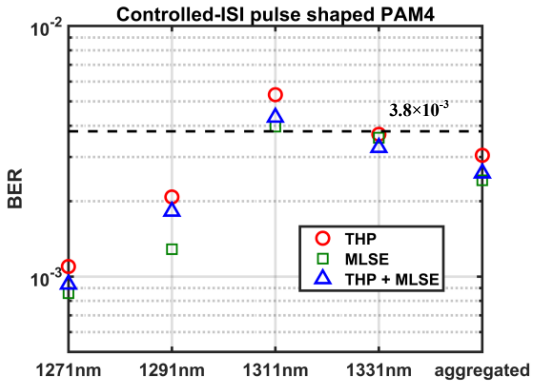

Fig. 3.5 BER performance of individual wavelength channels and the aggregated signal at BtB for 4×81 Gbaud controlled-ISI pulse shaped PAM4 transmissions when processed with different DSP combinations. (©2020 IEEE)

Applying THP and post filter + MLSE at the same time does not improve the performance when compared to the post filter + MLSE only case. From our experience, if THP is applied, the optimized α values of the post filters are close to 0's, which indicates that THP has almost completely removed the post-cursor ISI in the system, the impact of receiver FFE enhanced noise is negligible, and post-filter + MLSE becomes redundant. On the other hand, if we can accept the relatively high computational complexity of MLSE, we should avoid using THP so

that we won't suffer from the power penalty.

In short:

1) Doing less pre-emphasis does help. Therefore, if we only use FFE at the receiver, we should pre-emphasize up to the RF amplifiers rather than to the EMLs.
2) Further reducing the amount of pre-emphasis (controlled-ISI pulse shaping) can further improve the performance if the FFE enhanced noise is mitigated using FTN techniques (post filter + MLSE or THP).
3) Post-filter + MLSE provides better performance than THP.

3.2.4.2 600 Gb/s net rate transmission over 2 km

Next, we demonstrate the transmission results of 4×81 Gbaud controlled-ISI pulse shaped PAM4 signals over 2 km with -3 dBm ROP in each channel. We still use 41-tap linear FFEs at the receiver. The results are shown in Fig. 3.6(a). The red and the green markers correspond to the THP based and post filter + MLSE based controlled-ISI pulse shaping cases, respectively. Interestingly, in the 1271 nm and 1291 nm channels, transmissions over 2 km improve the BER performance compared to the BtB cases. Since these two channels have negative dispersion coefficients (positive GVD coefficients), according to Table 2.1, the EMLs in the TOSA must have positive linewidth enhancement factors, and the CD-chirp interaction compresses the pulses in the time domain in these two channels. This is further proved by the fact that in the 1331 nm channel, transmission over 2 km degrades the BER performance, as the 1331 nm channel has positive dispersion coefficient (negative GVD coefficient), and the CD-chirp interaction broadens the pulses. Although the 1311 nm channel and the 1331 nm channel have worse performance compared to the rest two channels, the BERs of the aggregated signals (the averaged BER across all wavelength channels) at BtB and 2 km are below the 6.7% overhead HD-FEC threshold of 3.8×10^{-3} in both THP and post-filter + MLSE aided controlled-ISI pulse shaping cases, which means that we can achieve a net rate of 81×4×2/106.7% = 607.3 Gb/s for transmissions up to 2 km with only a 41-tap linear FFE in each channel, as long as the HD-FEC is designed to be bit-interleaved over all the wavelength channels.

We also note that after 2 km of SMF, both THP based and post filter + MLSE based methods

achieve similar BERs. This is more apparent in the BER versus ROP curves shown in Fig. 3.6(b), where the gap between the red curve and the green curve is small. We would like to highlight that, in this demonstration, we use 41-tap linear FFEs at the receiver because we want to minimize the number of adaptive taps while maintaining an average BER that is below the FEC threshold at 2 km. Further increasing the number of taps to 101 has almost no impact on the THP-aided case as shown in Fig. 3.6(b), since we have already used sufficient transmitter THP taps to remove the post-cursor ISI, and 41 T/2-spaced receiver FFE taps are enough to mitigate the residue ISI. In the post filter + MLSE aided case however, both pre-cursor and post-cursor ISIs need to be compensated for by the receiver FFE (or more precisely, the ISI excluding the part that has been handled by pre-emphasis), then the post filter and MLSE are used to suppress the equalization enhanced noise. Fig. 3.6(b) shows that we are still undercompensating for the ISI by using just 41 receiver taps. By further increasing the number of taps to 101, we can achieve a receiver sensitivity gain of 1 dB in the post filter + MLSE case at the 6.7% overhead FEC threshold.

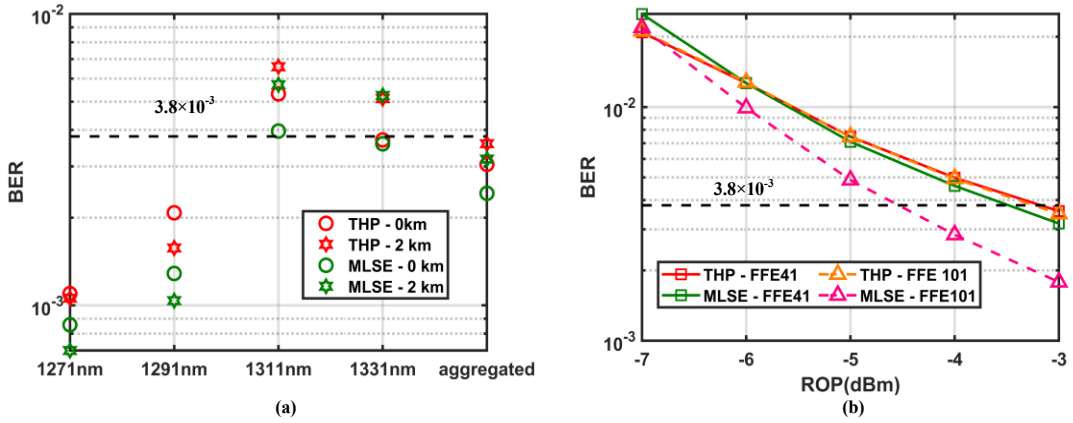

Fig. 3.6 (a) BER performance of 4×81 Gbaud THP aided and post filter + MLSE aided controlled-ISI pulse shaped PAM4 signals at BtB and 2 km, and (b) BERs of the aggregated signal as functions of ROPs at 2 km for 4×81 Gbaud controlled-ISI pulse shaped PAM4 signal when processed with 41-tap linear FFE or 101-tap linear FFE. (©2020 IEEE)

3.2.4.3 Towards 600 Gb/s Transmissions over 10 km

Next, we try to extend the reach to 10 km. Here we only consider the case with controlled-ISI pulse shaping + post filter + MLSE, since this combination provides the best performance. Fig. 3.7 compares the transmission performance of 4×81 Gbaud signals at BtB and 10 km with -3

dBm ROP in each channel. The number of FFE taps used are denoted in the legend. As we can see, after 10 km of SMF, the transmitted signal still benefits from the pulse compression effect due to the CD-chirp interaction in the 1291 nm channel. However, in the 1271 nm channel, the BER performance is degraded after 10 km of transmission, since this channel is more dispersive than the 1291 nm channel, and the CD-chirp interaction starts to broaden the pulses. The pulse-broadening issue is even more severe in the 1331 nm channel, which becomes the worst channel after transmitting over 10 km of fiber.

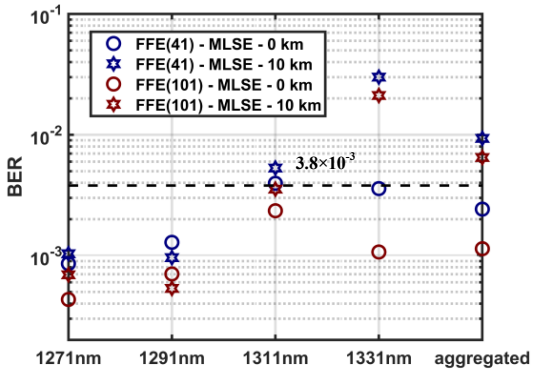

Fig. 3.7 BER performance of 4×81 Gbaud controlled-ISI pulse shaped PAM4 signals using 41/101-tap FFE + post filter +MLSE in each channel at BtB and 10 km. (©2020 IEEE)

The average BER at 10 km is above the 6.7% overhead HD-FEC threshold, even if we use 101-tap FFEs to sufficiently mitigate the ISI, which indicates that sharing of FEC gain across different channels through bit-interleaving cannot support 10 km transmission in our system. However, we observe that even with only 41-tap FFEs at the receiver, the BERs of the 1271 nm and the 1291 nm channels are still way below the FEC threshold. Therefore, it might be beneficial to relieve some burdens from the "bad" channels and add these burdens to the "good" channels.

To explore the limit of our system, we sweep the symbol rate in each wavelength channel with a fixed ROP of -3 dBm. Fig. 3.8(a) shows the results when only 41-tap linear FFE is used at the receiver. We observe that by loading 85 Gbaud, 85 Gbaud, 79 Gbaud and 72 Gbaud to the 1271 nm, 1291 nm, 1311 nm and 1331 nm channels respectively, we can achieve a BER below 3.8×10^{-3} in each channel, and the aggregated net rate excluding the FEC overhead is (85+85+79+72)*2/106.7% = 601.69 Gb/s. Since the signal with increased AC power (RMS

voltage) may suffer from EML/TIA nonlinearities, we also tried to improve the performance by replacing the linear equalizers with VEs, and the results are shown in Fig. 3.8(b). With the help of 3rd order (41,11,3) VEs, the symbol rates in each channel can be increased to 86 Gbaud, 85 Gbaud, 81 Gbaud and 73 Gbaud, respectively, which corresponds to a net rate of (86+85+81+73)*2/106.7% = 609.18 Gb/s. The gain is marginal, which indicates that the nonlinear impairments is not severe in this system.

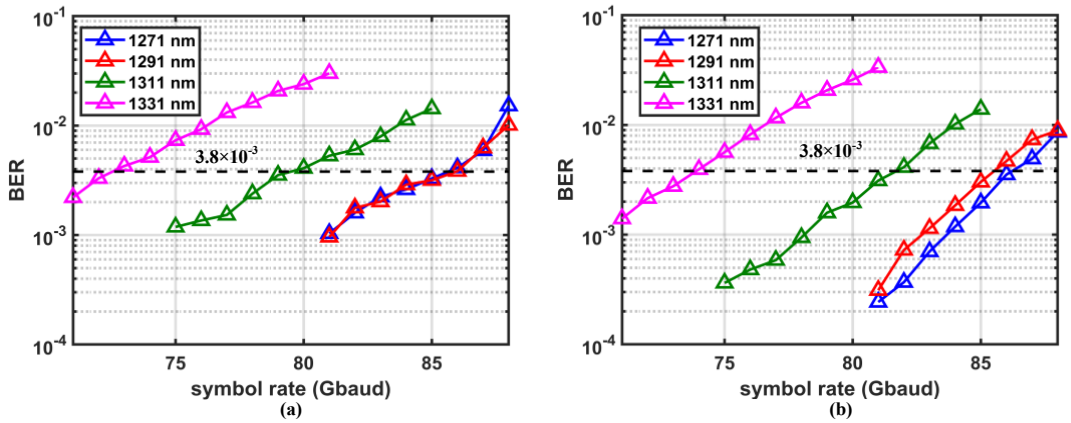

Fig. 3.8 BER as a function of symbol rate in each wavelength channel for post-filter + MLSE aided controlled-ISI pulse shaped PAM4 transmissions over 10 km, when processed with (a) 41-tap linear equalizer and (b) VE with kernel memory length of (41,11,3) at the receiver. (©2020 IEEE)

3.2.5 Summary

By introducing a certain amount of ISI at the transmitter, we can increase the AC power of the received signal in the electrical domain after photo-detection and transimpedance amplification, and the received SNR is improved accordingly. The introduced ISI can be compensated for using FTN techniques, i.e. 1) receiver-side FFE aided with post-filter + MLSE or 2) transmitter-side THP. Both methods enable 4 × 81 Gbaud PAM4 (net rate 605.6 Gb/s) transmission over 2 km with a BER below the HD-FEC threshold of 3.8×10^{-3}. We also demonstrate that by loading different symbol rates to different wavelength channels, we can further extend the reach to 10 km while maintaining an aggregated net rate of 600 Gb/s using post filter + MLSE based ISI mitigation method. To the best of our knowledge, by the time this work was published, it was the highest reported transmission capacity using PAM4 signaling in a 4-λ CWDM IM/DD architecture for short-reach applications.

3.3 Wavelength-interleaved 4D-PAM4-TCM in a CWDM4 System

3.3.1 Motivation

In a typical multi-wavelength IM/DD system, different wavelength channels achieve different transmission performance (BERs) due to 1) inter-channel component differences and 2) the CD-chirp interactions. Suppose we transmit the same bitrate in each wavelength channel, instead of looking at the BER of individual channels, in many cases we only need to make sure that the average BER is below the HD-FEC threshold. The assumption here is that the HD-FEC is designed to be bitwise interleaved across all different wavelength channels, thus the average BER represents of the BER of the aggregated signal if we look at all the channels as a single super-channel.

Now let's consider an extreme case where the BER of one channel is significantly worse than the BERs of the other channels (e.g. worse by more than an order of magnitude). The average BER will be clamped to the BER of the worst performing channel divided by the number of channels, regardless of how well the remaining channels perform. An example was shown in Fig. 3.7, where the average BER performance of the entire system was mainly limited by the performance of the 1331 nm channel (i.e. average BER roughly equals to BER of the 1331 nm channel divided by 4). This channel accidentally uses the worst components among four channels, and experiences severe pulse-broadening after transmission over 10 km introduced by the interaction between positive CD (positive dispersion coefficient)and positive chirp (positive linewidth enhancement factor, please refer to section 2.3.2.1 for more information). As a result, the system cannot support transmission of 4×81 Gbaud PAM4 signals over 10 km with the 6.7% overhead HD-FEC due to the poor performance of the 1331 nm channel. Although here we use a CWDM4 FTN-PAM4 system as an example, such extreme cases also occur in other multi-wavelength IM/DD systems, regardless of the number of wavelength channels or the choice of the modulation format. Generally, if the transmission performance of different wavelength channels are averaged through bitwise interleaving, and if we use an HD-FEC, the pre-FEC BER of the aggregated signal will more affected by the pre-FEC BERs of

the “bad” channels than the pre-FEC BERs of the “good” channels, especially when the inter-channel pre-FEC BER gaps are large, which then limits the post-FEC BER performance of the aggregated signal.

One workaround is to load different symbol rates onto different wavelength channels to minimize the inter-channel BER gaps as we did in section 3.2.4.3, i.e. let each channel transmit the highest symbol rate to achieve a BER that is just below the HD-FEC threshold. We would like to point out that using different symbol rates in different wavelength channels may require each channel to run its DSP at a different clock rate, which leads to extra implementation cost. Alternatively, one can fix the symbol rate but vary the SEs in different wavelength channels through time domain hybrid modulation [84] or probabilistic constellation shaping [85], i.e. let each channel transmit a signal with the highest SE at a fixed symbol rate that achieves a BER just below the HD-FEC threshold. Similar technique has been widely used in sub-carrier multiplexing (SCM)/DMT systems, which is often referred to as “bit/entropy loading”. We can simply treat the four wavelength channels as a single super channel with colored channel responses and apply the bit/entropy loading technique. No matter which technique we use, we merely transmit more(less) data through channels with higher(lower) SNRs by customizing the symbol rates or SEs in different channels. But note that reallocating the burdens onto different channels requires prior knowledge of the link, i.e. knowledge about the relative performance of each component, the transmission distance, the zero-dispersion wavelength of a specific fiber, the wavelength drift of each laser and etc. Unfortunately, such information may not always be available during the design phase of the transceivers.

In this work, we show that in a special kind of multi-wavelength system, i.e. a CWDM4 4D-PAMx-TCM system, we can directly improve the system’s robustness against potential channel performance differences induced by component differences and CD-chirp interactions, without any prior knowledge of the link. 4D-PAMx-TCM has attracted attention in recent years in short-reach IM/DD optical transmission systems as a method to improve the SNR performance [65]-[67]. Conventional 4D-PAMx-TCM uses four consecutive time-domain one-dimensional (1D) symbols to construct a 4D symbol. Therefore, in the CWDM4 architecture, each wavelength

channel will be encoded and decoded independently. In this work, we propose to implement a symbol-level wavelength-interleaver in conjunction with a 4D-PAMx-TCM encoder, i.e. each 4D symbol consists of four 1D symbols from four different wavelength channels, so that the four channels can be jointly encoded and decoded. In the remainder of this section, we refer to this scheme as wavelength-interleaved 4D-PAMx-TCM. For simplicity, we only consider the 8-state 4D-PAM4-TCM to demonstrate the idea. We experimentally prove that the proposed wavelength-interleaved 4D-PAM4-TCM scheme outperforms the conventional time-domain encoded 4D-PAM4-TCM scheme in 4-λ × 100 Gb/s CWDM IM/DD links over 0-20 km when there exist sizable channel performance discrepancies in such systems.

The remainder of section 3.3 is organized as follows. In section 3.3.2, we describe the operating principle of wavelength-interleaved 4D-PAM4-TCM. Then we describe the experimental setup and DSP blocks in section 3.3.3. The experimental results are discussed in section 3.3.4. Finally, we conclude this work in section 3.3.5.

3.3.2 Wavelength-interleaved 4D-PAM4-TCM

The 8-state 4D-PAM4-TCM encoder is implemented following the method described in Chapter 2, section 2.3.3.5. The encoded 4D symbols are then distributed to four wavelength channels. The wavelength distribution procedures for conventional and wavelength-interleaved 4D-PAM4-TCMs are shown in Fig. 3.9(a) and Fig. 3.9(b), respectively, where $S_i(T)$ denotes the i^{th} 1D symbol used to construct the 4D symbol at the time interval T. Conventional time-domain encoded 4D-PAM4-TCM distributes a 4D symbol to four consecutive 1D symbols of the same wavelength. Each wavelength channel is encoded/decoded independently, thus both the intra-4D-symbol correlation (i.e. correlation between 1D symbols that constructs a 4D symbol introduced through set-partitioning) and the time-domain-correlations (i.e. correlations between 4D symbols at different time intervals introduced by the convolutional encoder) are within the same wavelength. Alternatively, in this work, we propose to implement symbol-wise wavelength-interleaving in conjunction with 4D-PAM4-TCM, i.e. each 4D symbol consists of four 1D symbols from four distinct wavelengths at the same time interval, so that the four wavelength channels are jointly encoded and decoded. In this case, the intra-4D-symbol

correlations are distributed to different wavelength channels, and the time-domain-correlation is still continuous as time goes by, if we regard the four wavelength channels as a single super channel.

At the receiver side, the 4D symbols are first reconstructed by reversing the wavelength distribution procedure described above, and then decoded using the Viterbi algorithm. Wavelength-interleaved 4D-PAM4-TCM enables sharing of noise-induced Euclidean distance penalties between "good" channels and "bad" channels during TCM decoding (i.e. determination of each 4D symbol relies on 1D space information from all different wavelength channels). In other words, it allows us to perform a symbol-level averaging over four wavelengths, which could improve the system's robustness against channel performance discrepancies compared to the bit-level averaging process in the conventional 4D-PAM4-TCM case, as we will observe in section 3.3.4.

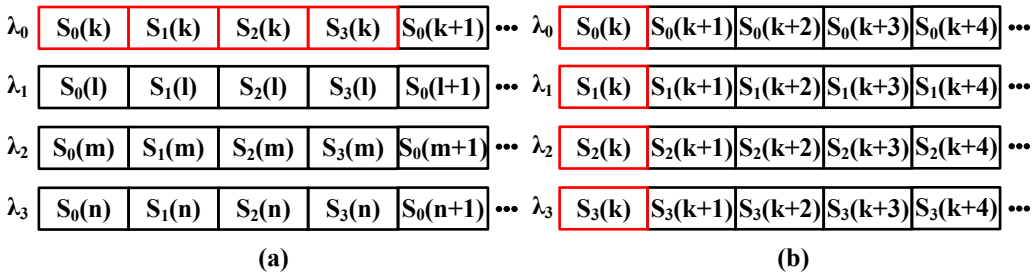

Fig. 3.9 4D symbol wavelength distribution procedures for (a) conventional 4D-PAM4-TCM and (b) wavelength-interleaved 4D-PAM4-TCM. (©2020 IEEE)

Some readers may have realized that wavelength-interleaved 4D-PAM4-TCM requires inter-channel synchronization. We would like to point out that, in a practical system, inter-channel synchronization only needs to be implemented at 1 Sps right before TCM decoding, since all DSP blocks before TCM decoding do not require information from other channels. In addition, a conventional 4D-PAM4-TCM system also requires inter-channel synchronization before HD-FEC decoding if the FEC is bitwise interleaved across four channels. The additional computational complexities required by inter-channel synchronization should be the same in both a wavelength-interleaved 4D-PAM4-TCM system and a conventional 4D-PAM4-TCM system with FEC gain shared across all the four wavelength channels.

3.3.3 Experimental setup and DSP blocks

To experimentally compare the performance of conventional 4D-PAM4-TCM and wavelength-interleaved 4D-PAM4-TCM, we use the experimental setup and DSP blocks shown in Fig. 3.10. Compared to Fig. 3.3(a), the transmitter (i.e. AWG, RF amplifiers and the TOSA) and the CWDM DeMux are the same. The main difference is at the receiver side. By the time we did this experiment, we didn't have access to four PT-28E high bandwidth PD-TIAs and four 160Gsa/s real-edge RTO channels (each channel has a brick-wall bandwidth limitation of 66 GHz). But 4D-PAM4-TCM requires joint encoding/decoding across all four wavelength channels, thus it is more convenient to detect the four channels simultaneously rather than detect them one by one as we did in section 3.2.3. Therefore, we decided to use four Picometrix PT-40D PD-TIAs (with similar 3 dB bandwidths but much lower 6 dB bandwidths compared to PT-28E PD-TIAs), followed by four 80 Gsa/s 8-bit RTO channels (each channel has a brick-wall bandwidth limitation of 33 GHz) at the receiver to demonstrate the idea at a lower speed. Although we reduce the symbol rate compared to section 3.2.3, we compare the systems' performance at a more stringent FEC threshold (i.e. the KP4-FEC threshold of 2.26×10^{-4} instead of the "P-FEC" threshold of 3.8×10^{-3}), and try to extend the reach to explore the limit of the system. No optical amplifier is used for 0-10 km transmissions, and a praseodymium-doped fiber amplifier (PDFA) is used for 20 km transmissions to compensate for the fiber loss[14]. A VOA is used in each wavelength channel to control the ROP for receiver sensitivity studies. We target 112 Gb/s per wavelength transmissions, which corresponds to 64 Gbaud/λ 4D-PAM4-TCM since it has a coding rate of 7/8. We also transmit 56 Gbaud/λ traditional PAM4 signals (with the same capacity) in our system for comparison. RC pulse shaping filters with roll-off factors of 0.03 and 0.1 are used for 64 Gbaud and 56 Gbaud signals, respectively. While a small roll-off factor leads to a relatively high PAPR, it prevents severe filtering of the signal due to the limited RTO bandwidth, since each RTO channel has a brick-wall bandwidth limit

[14] Due to device aging, the output power of the EMLs was reduced when we conducted this experiment, hence we have to use a PDFA to cover 20 km, but my colleagues once proved that this TOSA could provide higher power, which is sufficient to achieve the ROP required in this work even at 20 km. The TOSA we used was merely a prototype. A well-packaged product for commercial applications should have a much longer lifetime.

of 33 GHz. In this experiment, we don't use FTN techniques as we did in section 3.2. Pre-emphasis is performed at the AWG sampling rate (88 Gsa/s) to compensate for the frequency responses of cascaded devices up to the RF amplifiers. At the receiver, after resampling and synchronization, a 41-tap FFE is implemented at 2 Sps in each channel before TCM decoding to sufficiently compensate for ISI.

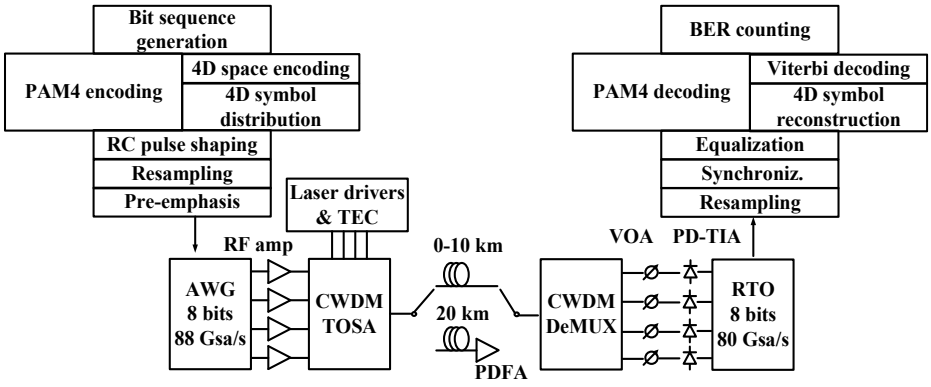

Fig. 3.10 Experimental setup and DSP blocks for 4×100 Gb/s CWDM 4D-PAM4-TCM links. (©2020 IEEE)

In this experiment we used training symbol (a portion of the transmitted sequence) to assist the convergence of FFE taps in the LMS algorithm before switching to decision directed mode, thus we implement synchronization between the transmitter-side and receiver-side sequences at 2 Sps before equalization. Note that this way the inter-channel synchronization is automatically achieved since the transmitter-side sequences in different wavelength channels are synchronized. However, as we mentioned in section 3.3.2, if we use blind adaptive equalization algorithms that makes use only of the receiver-side sequences, inter-channel synchronization at the receiver only needs to be implemented before TCM decoding at 1 Sps.

3.3.4 Experimental results and discussions

3.3.4.1 Component-induced inter-channel performance difference

To better understand the inter-channel component differences in our system, we first measured the BtB pre-FEC BER performance of 64 Gbaud traditional PAM4 signals with different combinations of transmitter/receiver components. Since all RF amplifiers / PD-TIAs used in this experiment have similar performance, we always group a certain RF amplifier/PD-TIA together with a certain DAC channel (AWG channel)/ADC channel (RTO channel). For

confidentiality reasons, I cannot show the original measurement results of this part in this thesis. But for the purpose of presenting the benefits of the wavelength-interleaved 4D-PAM4-TCM scheme, it is sufficient to only mention the following observations. In our system, we have:

1) DAC 3 + RF amplifier 3 > DAC 1 + RF amplifier 1 > DAC 2+ RF amplifier 2 > DAC 4+ RF amplifier 4,
2) EML 2 > EML 1 > EML 4 > EML 3,
3) and PD-TIA 2+ADC 2 > PD-TIA 1+ADC 1 > PD-TIA 4+ ADC 4 > PD-TIA 3+ADC 3,

where "A" > "B" represents "A" achieves better BER performance than "B".

Fig. 3.11 shows two component matching configurations considered in this experiment. The blue lines demonstrate a "bad" matching configuration where the best DAC, EML, and ADC are grouped in one channel, and the worst DAC, EML, and ADC are grouped in another channel. This configuration represents the worst case that could happen if we blindly match up DACs, EMLs and ADCs in the system. It is possible to minimize the component-induced channel performance differences through proper rearrangement of components (e.g. grouping a "bad" DAC and a "bad" EML with a "good" ADC). The red lines in Fig. 3.11 shows an example of such a "good" matching configuration. Note that if component differences exist, searching for a "good" component matching configuration in a practical transmission link can be difficult, since it requires prior knowledge of components at both the transmitter and the receiver. On the other hand, component differences may be reduced through improvements in the fabrication and packaging processes, thus there is motivation to separate the impacts of component differences and the CD-chirp interactions. In this work, we use the aforementioned "good" matching configuration to emulate the case where the component-induced inter-channel BER performance discrepancies are insignificant.

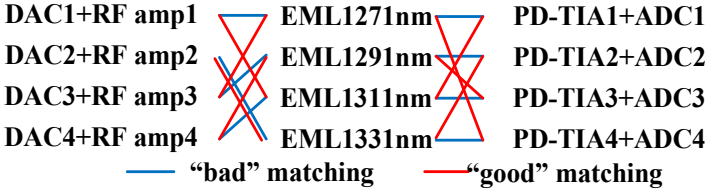

Fig. 3.11 Different component matching configurations in for 4×100 Gb/s CWDM 4D-PAM4-TCM systems. (©2020 IEEE)

3.3.4.2 BtB transmission results

We first compare the transmission performance of conventional and wavelength-interleaved 4D-PAM4-TCMs with different component matching configurations at BtB. The results are shown in Fig. 3.12 and Fig. 3.13, where SNRs are measured after equalization, and the BERs are measured after TCM decoding (but before HD-FEC decoding).

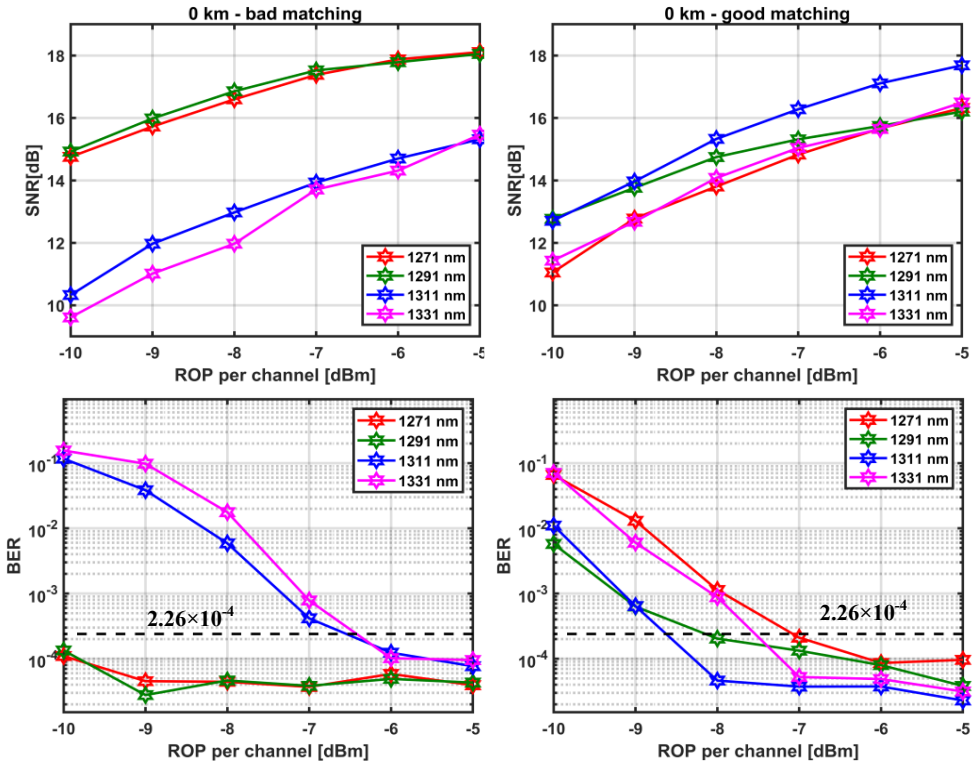

Fig. 3.12 SNR-ROP and BER-ROP relations of individual wavelength channels at BtB with different component matching configurations in the conventional 4D-PAM4-TCM case. (©2020 IEEE)

Since all four channels have the same bitrates, the average BER represents the BER of the aggregated signal, which determines the post-FEC BER performance of the entire system assuming the HD-FEC is bitwise interleaved across all channels.

As we can see from Fig. 3.12, in the conventional 4D-PAM4-TCM case, the SNR difference between the best channel and the worst channel can be as large as ~4 dB when using a “bad” component matching configuration, and the average BER performance is predominantly influenced by the worst channel. Wavelength-interleaved 4D-PAM4-TCM however, is based on a symbol-wise interleaver before TCM decoding, which allows for sharing of the Euclidean distance penalties between the “good” channels and the “bad” channels during the Viterbi

decoding process (introduced in section 2.3.3.5). From Fig. 3.13 we observe that the wavelength-interleaved 4D-PAM4-TCM system achieves a receiver sensitivity gain of 0.6 dB compared to the conventional 4D-PAM4-TCM system at the KP4 FEC threshold of 2.26×10^{-4}. On the other hand, if we use the "good" component matching configuration, the SNR difference between the best and the worst channel is reduced to < 2 dB, and the receiver sensitivity gain of the wavelength-interleaved 4D-PAM4-TCM system is reduced to ~0.3 dB.

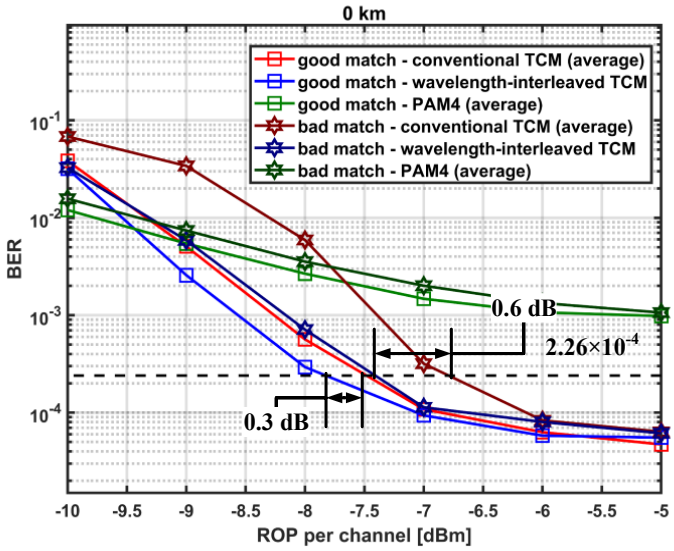

Fig. 3.13 BERs as functions of ROP per channel at BtB with different component matching configurations and different modulation formats. (©2020 IEEE)

3.3.4.3 Error floor of 4D-PAM4-TCM in a non-AWGN channel

Interestingly, from Fig. 3.12 and Fig. 3.13 we observe that once the BER approaches ~5×10^{-5}, 4D-PAM4-TCM cannot further improve the BER performance when we increase the ROP even if the SNR keeps increasing, as if there is an error floor, thus the average BERs of both conventional and wavelength-interleaved 4D-PAM4-TCM systems converge at high ROP regardless of the choice of the component matching configuration. Here we provide a possible explanation for this error floor phenomenon.

Note that 4D-PAM4-TCM is originally designed for AWGN channels [64]. Fig. 3.14 shows the histograms and the PSDs of the BtB noise in the best/worst channel with different ROP in our system when using the bad component matching configuration. As we can see, the noise in our system is generally Gaussian, and is not white since there exist clock leakage from the AWG

channels, flicker noise (1/f noise) which dominates at low frequency, and noise enhancement effect originated from receiver-side equalization. Since we use devices with large bandwidths in our system, the impact of equalization enhanced noise is relatively weak, i.e. the “colored” noise components are mainly originated from the flicker noise and the clock leakage. Both the flicker noise and clock leakage in our system are mainly coming from the transmitter, therefore, at the receiver, the “colored” noise components can actually be regarded as a part of the received signal, and the receiver itself would add more white noise such as the thermal noise from the PD-TIAs and the ADC channels. When the ROP is low, the “colored” noise components (especially the flicker noise) is overshadowed by the white noise added by the receiver. Therefore, in the low ROP region, BER steadily decreases as the SNR increases. On the other hand, when the ROP is high, the “colored” noise components become dominant (because it is a part of the received signal), the channels can no longer be regarded as AWGN channels, and the gain achieved by 4D-PAM4-TCM is very limited, which leads to the aforementioned error floor phenomenon.

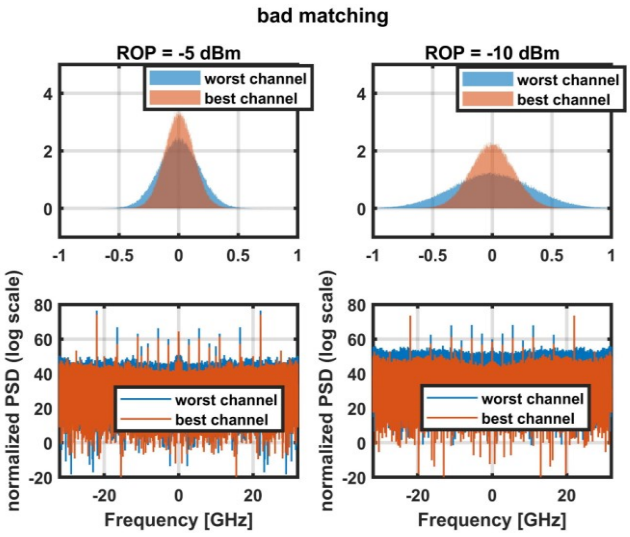

Fig. 3.14 Histograms and PSDs of noise in the best/worst channel at BtB with different ROP and the bad component matching configuration. (©2020 IEEE)

To verify our hypothesis, we numerically study the impacts of flicker noise and clock leakage in a single wavelength conventional 4D-PAM4-TCM system, and the results are shown in Fig. 3.15. We don’t consider any device bandwidth limitations or CD-chirp interactions in this simulation, and each data point is obtained through averaging over 20 independent simulations

(BER averaged over 20 independent simulations). When we vary the SNR, we only vary the power of AWGN components, i.e. we always keep the power of flicker noise/clock leakage unchanged since they are part of the signal. Note that when there exists flicker noise or clock leakage, we also slightly reduce the AWGN power to keep the same SNR as the pure AWGN case. Readers may remember that in Fig. 3.14, even at low ROP, the clock leakage cannot be fully buried in the white noise, however Fig. 3.15 shows that clock leakage has almost no impact on the 4D-PAM4-TCM system. On the other hand, we find that the existence of flicker noise does lead to an error floor when SNR is high (when white noise is no longer dominant).

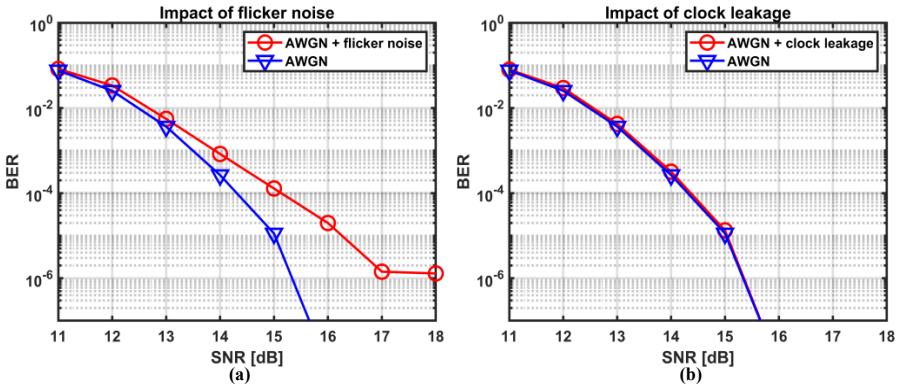

Fig. 3.15 Simulated BER performance of 64 Gbaud single-channel (conventional) 4D-PAM4-TCM systems at BtB with the existences of (a) flicker noise and (b) clock leakage.

We would like to highlight that, although 4D-PAM4-TCM cannot achieve its maximum possible gain in our experiment since the channels are not rigorously AWGN, we still observe gaps between the BER vs. ROP curves associated with the conventional and wavelength-interleaved 4D-PAM4-TCM schemes at the KP4 FEC threshold in Fig. 3.13, since the error floor only occurs when the BER is well below 2.26×10^{-4}.

3.3.4.4 10/20 km transmission results

Next, we compare the performance of conventional and wavelength-interleaved 4D-PAM4-TCM systems after transmissions over 10 km. The results are shown in Fig. 3.16 and Fig. 3.17. As we have mentioned in section 3.2.4.2, the linewidth enhancement factors of EMLs are positive in our system. According to Table 2.2, at short transmission distances, the interaction between the positive chirp (positive line width enhancement factor) and the positive/negative dispersion (positive/negative dispersion coefficient) will broaden/compress the pulse, which

will increase/decrease the equalization enhanced noise, and degrade/improve the BER performance. Not surprisingly, from Fig. 3.12 and Fig. 3.16 we observe that after transmission over 10 km of SMF, the CD-chirp interaction significantly decreases the SNR (degrade the BER performance) in the 1331 nm channel with positive dispersion coefficient, and slightly increases the SNRs (improve the BER performance) in the 1271/1291 nm channels with negative dispersion coefficients.

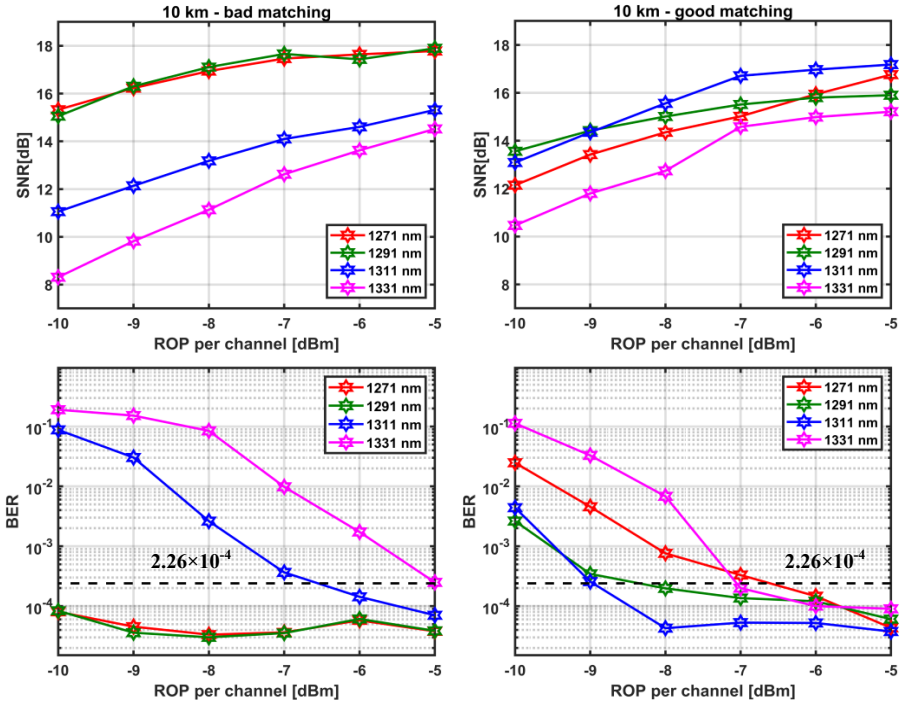

Fig. 3.16 SNR-ROP and BER-ROP relations of individual wavelength channels after transmission over 10 km with different component matching configurations in the conventional 4D-PAM4-TCM case. (©2020 IEEE)

Since the SNR difference between the best channel and the worst channel increases after transmission over 10 km of SMF, the receiver sensitivity gains of the wavelength-interleaved 4D-PAM4-TCM at the KP4 FEC threshold are increased to 1.4 dB and 0.5 dB, when using the "bad" and "good" component matching configurations, respectively. Fig. 3.16 shows that if we use the "good" component matching configuration, even after 10 km of SMF, the SNR difference between the best channel and the worst channel is not significant, and wavelength-interleaved 4D-PAM4-TCM only achieves limited receiver sensitivity gain at the KP4 FEC threshold. Suppose that the component difference can be sufficiently mitigated in the future by

improving the fabrication and packaging processes, i.e. the component-induced channel performance discrepancies can be completed eliminated, we can anticipate that the gain of wavelength-interleaved 4D-PAM4-TCM will be further reduced. Does that mean wavelength-interleaved 4D-PAM4-TCM is useless in a system without component difference? Not necessarily. In fact, as we further increase the transmission distance, the impacts of CD-chirp interactions will become more and more severe, and eventually lead to significant inter-channel performance discrepancies.

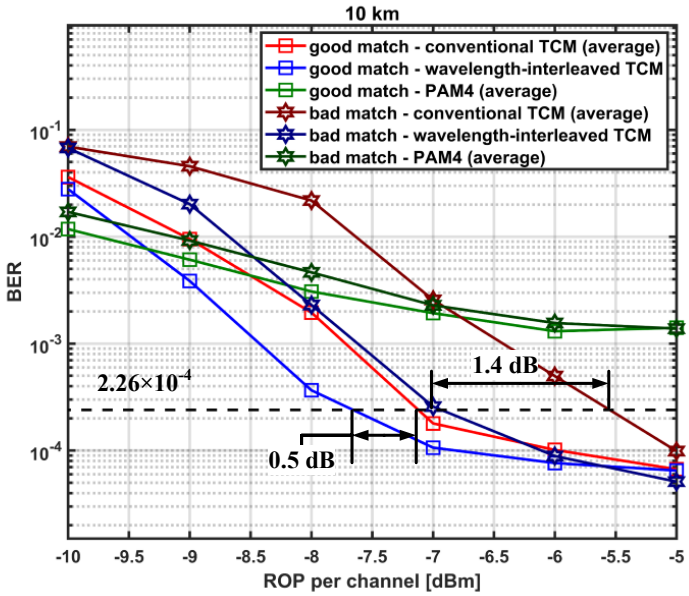

Fig. 3.17 BERs as functions of ROP per channel after transmission over 10 km with different component matching configurations and different modulation formats. (©2020 IEEE)

To prove that, we extend the reach to 20 km in our experiment. This time we only consider the "good" component matching configuration (to emulate the case where the component-induced channel performance difference is sufficiently suppressed), and the results are shown in Fig. 3.18. Remember that we use a PDFA for the 20 km transmission experiment, thus all wavelength channels suffer from additional SNR penalties introduced by the PDFA.

By comparing Fig. 3.16 and Fig. 3.18, we observe that after transmission over 20 km, the CD-chirp interactions further increase the SNR difference between the best and the worst channels to ~4 dB. As a result, the receiver sensitivity gain achieved by wavelength-interleaved 4D-PAM4-TCM at the KP4 FEC threshold is increased to 1.2 dB, which is no longer trivial. In

other words, if we have an unamplified (loss limited) system without component difference, given a fixed laser output power in each channel, the wavelength-interleaved 4D-PAM4-TCM scheme proposed in this work can be used to extend the reach of the system.

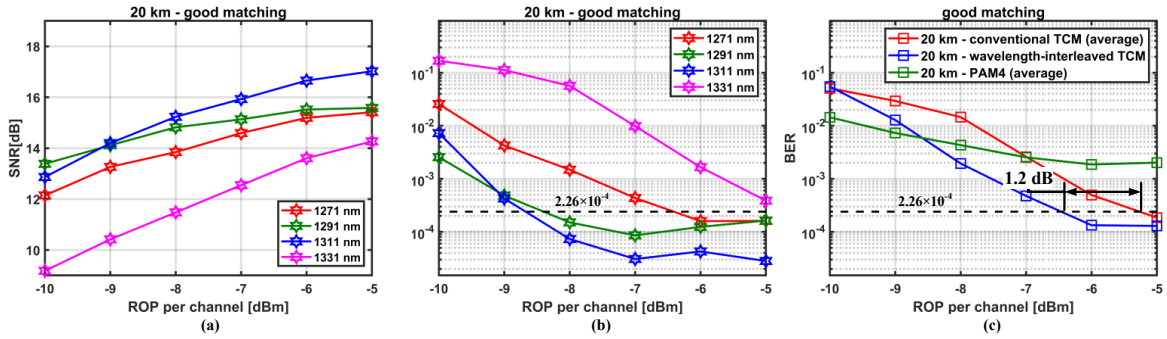

Fig. 3.18 (a) SNR-ROP and (b) BER-ROP relations of individual wavelength channels after transmission over 20 km with the "good" component matching configuration in the conventional 4D-PAM4-TCM case, and (c) BERs as functions of ROP per channel after transmission over 20 km with different modulation formats using the "good" component matching configuration. (©2020 IEEE)

3.3.5 Summary

We propose to employ a symbol-wise wavelength-interleaver in conjunction with 4D-PAM4-TCM in the 4-λ CWDM architecture to improve system robustness against channel performance discrepancies due to component differences and CD-chirp interactions. We experimentally prove that the proposed wavelength-interleaved 4D-PAM4-TCM system outperforms the conventional 4D-PAM4-TCM system in a 4-λ×100 Gb/s CWDM4 IM/DD transmission link over 0-20 km in terms of receiver sensitivity required at the KP4 FEC threshold, when sizable inter-channel BER gaps exist in such systems.

Chapter 4 Amplified VSB self-coherent systems

4.1 Overview

In this chapter, we will present our experimental works on 100 Gb/s VSB self-coherent systems over 40-80 km of fiber. We systematically studied the linear and nonlinear impairments in a VSB-PAM4 link based on a SiPh multi-electrode MZM [35], and the results will be presented in section 4.2. We also proposed a novel filter-response aware iterative Kramers Kronig (FA-iter-KK) algorithm to improve the accuracy of the field reconstruction process in the presence of a under-filtered residual sideband in the VSB systems [36], which will be described in section 4.3. In addition, we designed a SiPh transmitter circuit which decouples the control of CSPR and the control of modulator bias point in SSB/VSB self-coherent systems [37]. The circuit design and the experimental results will be demonstrated in section 4.4.

4.2 SiPh DAC-less PAM4 system with a VSB self-coherent receiver

4.2.1 Motivation

Multi-drive modulator based DAC-less transmitter has gained interests in the community as a low-complexity multi-level signal generator which does not require high-resolution DAC channels [86],[87]. Multi-drive modulators have been realized on a variety of material platforms including Lithium Niobate [86],[87], Indium Phosphide (InP) [88] and Silicon Photonics (SiPh) [89]-[95]. Specifically, DAC-less PAM4 generation using the SiPh multi-drive modulators have been intensively studied in the academia recently. By using a multi-electrode MZM (ME-MZM) [91], a ring assisted MZM [92], a dual-drive Michelson interferometric modulator [93], a dual-parallel Mach-Zehnder modulators [94], or a cascaded micro-ring modulators [95], one can multiplex two PAM2 signals generated from two binary pattern generator (BPG) channels in the optical domain to obtain a PAM4 signal. In [91], a 100 Gb/s DAC-less and DSP-free PAM4 transmission over 1 km of SMF based on SiPh ME-MZM was reported.

A DAC-less PAM4 system is a DSB IM/DD system. As we have mentioned in Chapter 2, section 2.3.2.1, the accumulated CD and square law detection lead to power fading effect in DSB IM/DD systems, which prohibits the applications of IM/DD systems in the inter-data center links that typically covers 40-80 km of SMF [96]. One possible way to extend the reach of an IM/DD system is to upgrade it to an SSB/VSB self-coherent system, as we have described in Chapter 2, section 2.4. An SSB/VSB self-coherent allows us to apply CD compensation in the receiver DSP, and it does not significantly increase the hardware complexity compared to an IM/DD system. And specifically, for a DAC-less PAM4 system, since no DAC channels are used at the transmitter, the VSB scheme is more suitable as it does not require transmitter DSP for SSB generation.

In this work, to the best of our knowledge, by the time this work was published, we experimentally demonstrated for the first time a DAC-less, single ADC solution for single wavelength single polarization 100 Gb/s transmission over 40-80 km of dispersion uncompensated link using a SiPh ME-MZM and a VSB self-coherent receiver [35]. We report a 112 Gb/s PAM4 transmission over 40 km of SMF with a BER below the 6.7% overhead HD-FEC threshold of 3.8×10^{-3}, and a 120 Gb/s PAM4 transmission over 80 km of SMF with a BER below the 14.8% overhead SD-FEC threshold of 1.25×10^{-2}, without any transmitter DSPs.

4.2.2 DAC-less PAM4 modulation with SiPh ME-MZM

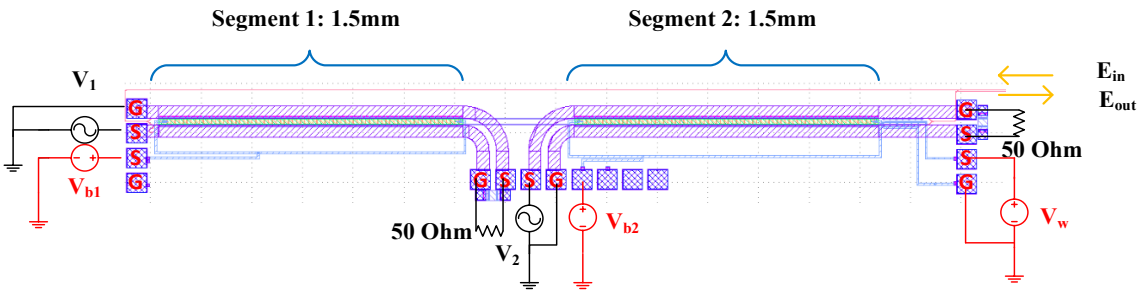

Fig. 4.1 Schematic of the SiPh ME-MZM. [Reprinted] with permission from [35] © The Optical Society.

The schematic of the SiPh ME-MZM used in this experiment for DAC-less PAM4 generation is shown in Fig. 4.1, where V_i and $V_{b,i}$ (i = 1 or 2) are the AC driving signals and DC bias voltages applied to the two phase shifting segments, V_w is a DC voltage applied to the thermal phase shifter to adjust the default phase difference between the two arms of the MZM, E_{in}

and E_{out} represent the optical input and output, respectively. The device was fabricated on a silicon-on-insulator (SOI) wafer with a 220-nm thick silicon layer and a 2-μm thick buried oxide layer, through a multi-project wafer run at Advanced Micro Foundry in Singapore. It consists of two series push-pull phase shifting segments with identical lengths of 1.5 mm. Both segments have the same lateral p-n junction structures as the phase shifters of the previously reported MZMs from our group [97]. In this work, we use two short phase shifters to increase the electro-optic (E/O) bandwidth of the device, instead of using a 1.5-mm long segment and another 3-mm long segment as my colleagues did in [97], since shorter segments have lower microwave losses. The 3 dB E/O bandwidth of a 1.5-mm long segment is greater than 45 GHz. To obtain a PAM4 signal, two independent time-aligned binary signals with the same symbol rates are used to drive the two phase shifting segments simultaneously. Both segments are driven in the push-pull mode, hence the chirp induced during modulation is negligible. The two segments have the same V_π's. If there is no device nonlinearity, the swing of one driving signal should be twice the swing of the other driving signal. In this experiment however, the two driving voltages are adjusted to be 6 V_{pp} and 2.3 V_{pp} respectively to generate four PAM4 levels that are spaced as equally as possible, where the level spacings are measured from the eye diagrams obtained after applying the receiver DSPs.

There are two main sources of device nonlinearities in this ME-MZM based transmitter. Firstly, the phase does not vary linearly with the driving voltage when using a SiPh phase shifter. Secondly, the amplitude change is not linearly proportional to the phase shift due to the choice of the bias point. As we have discussed in Chapter 2, section 2.4.2.2, an SSB/VSB self-coherent system detects the field information of the received signal, hence ideally the modulator should be biased at the null point, which is in the middle of the linear region of the field transfer function [98]. However, we also need a strong DC carrier, thus we need to bias the modulator above the null point. We would like to point out that neither of these two sources of device nonlinearity is unique to the SiPh ME-MZM based DAC-less transmitter, since the first issue is inevitable in any system that consists of a SiPh phase shifter, and the second issue is shared by all the SSB/VSB self-coherent systems that adjust the MZM's bias point to control the CSPR.

Note that if the modulator's device nonlinearities are solely originated from the phase shifters, the four amplitude levels after detection will be unevenly spaced but still symmetrically distributed, which can be easily compensated for by adjusting the swings of the two driving voltages to pre-distort the PAM4 signal in the electric domain [91]. However, in this system, the combination of the phase-shifter nonlinearity and the choice of bias point will result in four unevenly spaced and asymmetrically distributed PAM4 levels, thus adjusting the V_{pp}'s does alleviate but cannot completely solve this issue. To further mitigate the modulator's device nonlinearities, advanced receiver DSP is required, as we will see in sections 4.2.3 and 4.2.4.

4.2.3 Experimental setup and DSP blocks

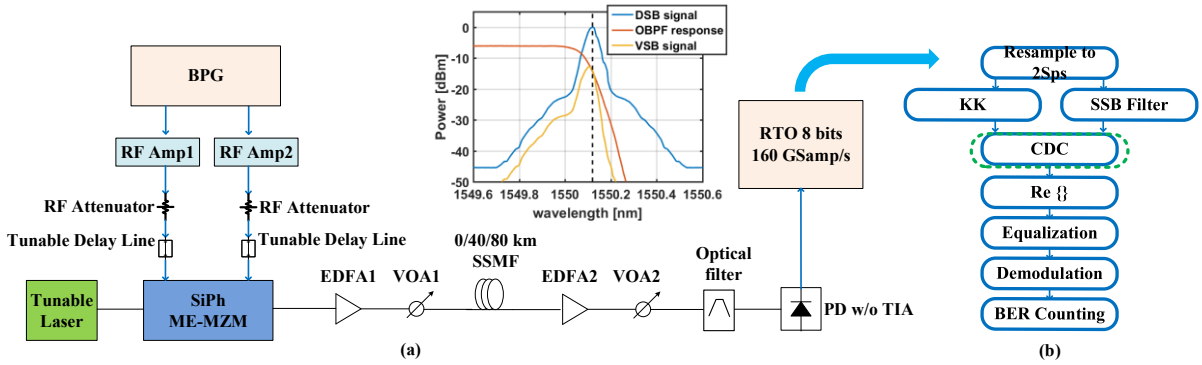

Fig. 4.2 (a) Experimental Setup, inset shows the spectrum of a 56 Gbaud signal before filtering, the OBPF response and the spectrum of a 56 Gbaud signal after filtering, and (b) receiver DSP blocks. [Adapted] with permission from [35] © The Optical Society.

The schematic of the experimental setup and the receiver DSP blocks are shown in Fig. 4.2. Two independent binary signals are first generated from two channels of a BPG, and then applied to the SiPh ME-MZM. Matched cables and tunable delay lines are used to ensure that the two binary signals are properly aligned in the time domain. A 15.5 dBm tunable laser operating at 1550.1 nm is used as the light source. The SiPh chip has 18 dB fiber-to-fiber insertion loss, including 11 dB loss from the VGC pairs, 4 dB loss from the modulator when biased at the maximum point and 3 dB loss from the routing waveguide. The optical filter serves as both the VSB filter and the out of band ASE noise filter, which has 6 dB insertion loss. In this work, we use the VSB filter to keep the RSB and suppress the LSB. Two EDFAs and two VOAs are used to 1) compensate for the loss and 2) control the launch power and the ROP separately. After VSB filtering, the optical signal is detected by a PD without TIA, then

digitized by a 160 GSa/s ADC(RTO) channel and processed offline. The frequency response of the optical filter is shown in the inset of Fig. 4.2(a).

In the experiment, we jointly optimize the modulator's bias point and the peak-to-peak values of the two driving voltages to achieve the best performance at BtB. The CSPR corresponding to a 56 Gbaud signal at the optimized point is 11.4 dB.

In the receiver DSP, the complex-valued field information of the RSB signal is first reconstructed using either the KK algorithm or the SSB filtering algorithm (please refer to Chapter 2, section 2.4.2.2 for more information). If a frequency-domain CD compensation (CDC) block is used, it is added right after the RSB field reconstruction block, i.e. it only compensates for the CD experienced by the RSB part of the signal. Then the PAM4 signal is obtained by taking the real part of the RSB signal. After that, a linear/nonlinear time-domain equalizer is applied to compensate for the residue ISI and the nonlinear impairments. Note that if the frequency-domain CDC block is not used, the time-domain equalizer will also compensate for the CD induced ISI. In this work we consider two kinds of nonlinear equalizers: 1) a 2nd order Volterra equalizer (VE), and 2) a simplified 2nd order Volterra equalizer (SVE), which can be expressed as Eqs. 4.1 and 4.2, respectively.

$$y[k] = \sum_{i=-N_1}^{N_1} w_{1,i} x[k-i] + \sum_{i_2=-N_2}^{N_2} \sum_{i_1=-N_2}^{N_2} w_{2,i_1,i_2} x[k-i_1]x[k-i_2] \tag{4.1}$$

$$y[k] = \sum_{i=-N_1}^{N_1} w_{1,i} x[k-i] + \sum_{i=-N_2}^{N_2} w_{2,i} x^2[k-i_1] \tag{4.2}$$

Eq. 4.2 is merely a simplified version of Eq. 4.1 which limits the 2nd order terms to the self-squared terms. Including nonlinear terms in the FFE allows us to mitigate the nonlinear transmission impairments including the device and the fiber nonlinearities. Note that VE and SVE can also mitigate the SSBI issue in an SSB/VSB self-coherent system, especially if no other SSBI mitigation methods such as the KK-family algorithms are applied [24],[27]. Assuming that the SSBI is the only source of nonlinear impairment, the transmitter-side and receiver-side signals are related through a linear filter. Remember that the SSBI is the beating product of the receiver-side signal and its complex conjugate, but the VE/SVE tries to recover

the transmitter-side signal, hence to estimate and invert the impact of SSBI in the VE/SVE based method, ideally we need all the 2nd order terms in Eq. 4.1 to effectively describe the interaction between the ISI induced by the linear filter and the square-law detection. Unfortunately, the computational complexity of a full VE is very high. Although we only consider the 1st order and the 2nd order terms in this work, a VE with kernel memory lengths of $(2N_1+1,\ 2N_2+1)$ still requires $2N_1+1$ linear taps and $(N_2+1)(2N_2+1)$ nonlinear taps. Generally, the more severe the ISI is, the longer the required kernel memory lengths will be, thus there is a trade-off between the performance and the computational complexity. Also note that in the absence of pulse shaping, the signal generated in a DAC-less scheme generally occupies a wider bandwidth than an RC shaped signal of the same symbol rate with a small roll-off factor. Therefore, compared to a system with pulse shaping, our system intrinsically experiences more ISI originated from both the CD and the device bandwidth limitations, thus it requires even longer kernel memory lengths. The SVE on the other hand, can limit the number of nonlinear taps to L_2, but this is achieved at the cost of compromising the performance, as we will shortly see from the experimental results in section 4.2.4.

All the receiver DSP blocks before the demodulation step are operated at 2 Sps. After equalization, the data stream is downsampled to 1 Sps for the demodulation and BER counting steps.

4.2.4 Experimental results and discussions

It has been reported that typically the KK algorithm needs to be operated at more than 3 Sps in a passband 16QAM SSB system, since the KK algorithm contains nonlinear operations which broaden the signal's spectrum [20]. But note that in this work we are processing a baseband PAM4 signal. Consider a passband 16QAM signal without any guard band that occupies the same bandwidth as the RSB part of a baseband PAM4 signal, the symbol rate of the passband 16QAM signal should be half of that of the baseband PAM4 signal. In other words, 2 Sps in our system is equivalent to 4 Sps in a passband 16QAM system with the same bandwidth requirement. As we can see from the oversampling ratio – BER relation in Fig. 4.3(a), further increasing the oversampling ratio will not improve the performance.

Fig. 4.3(b) shows the number of linear FFE taps required to compensate for the ISI of a 56 Gbaud PAM4 signal without digital pulse shaping after 0/80 km of SMF, where we use the KK algorithm to suppress the SSBI and use a time-domain equalizer which only contains the first order terms in Eq. 4.1. The tap coefficients are obtained using the LMS algorithm. We find that in the BtB case, $N_1 = 25$ is required to compensate for the ISI caused by the bandwidth limitations of the devices, which corresponds to $2N_1 + 1 = 51$ $T/2$-spaced taps, where T represents the symbol duration. After transmission over 80 km of fiber, $N_1 = 50$ should be used due to the CD induced pulse broadening. However, if we apply frequency-domain CDC before the time domain equalizer in the 80 km transmission case, N_1 can be reduced to 25. In the following analysis, for a 56 Gbaud signal, we will keep using $N_1 = 50$ and $N_1 = 25$ in cases where frequency-domain CDC is and is not applied, respectively.

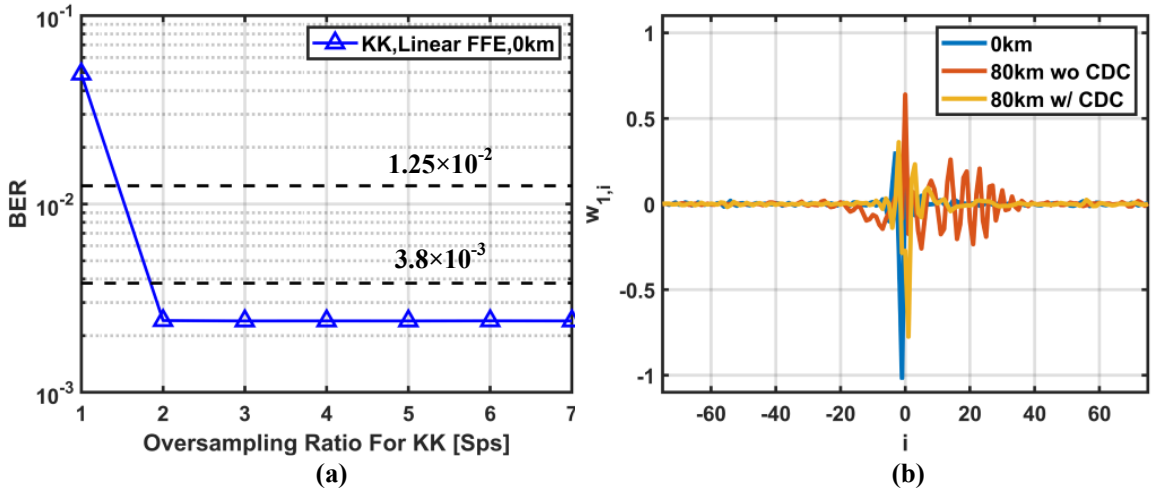

Fig. 4.3 (a) BER of 56 Gbaud DAC-less PAM4 at BtB versus oversampling ratio when processed with the KK algorithm and a linear FFE, and (b) typical linear FFE taps converged for 56 Gbaud PAM4 at BtB, 80km without CDC and 80 km with CDC, where the KK algorithm is used to reconstruct the RSB signal in all these cases. [Adapted] with permission from [35] © The Optical Society.

Next, we study the impacts of nonlinear impairments on the system performance, including the SSBI, the modulator's device nonlinearity and the fiber nonlinearity. Fig. 4.4(a)-4.4(c) show the relations between the BER and the 2nd order kernel memory lengths $2N_2 + 1$ of a 56 Gbaud PAM4 signal when processed with different combinations of receiver DSPs at different transmission distances.

As we can see from the BtB results, when the KK algorithm is not applied, both the VE and

the SVE can achieve better BER performance than the linear FFE, since both the VE and the SVE can combat the SSBI. However, if the KK algorithm is applied, the SVE no longer improves the BER performance, since the KK algorithm can sufficiently suppress the SSBI in our system, but the VE can still improve the BER performance. In fact, the VE always achieves better performance than the SVE. We attribute this phenomenon to the fact that our system also suffers from MZM induced device nonlinearity (note that the fiber nonlinearity is negligible in the BtB case), which can only be partially compensated for by adjusting the Vpp's of the two driving signals. The remaining device nonlinearity can be effectively mitigated by the VE, but not the SVE, as we can tell from Fig. 4.4(a). Moreover, we find that in the BtB case, the SSB filtering algorithm outperforms the KK algorithm, even when we only use a linear FFE at the receiver, which indicates that the residue LSB component resulting from the imperfect filtering does degrade the performance of the KK algorithm in our system.

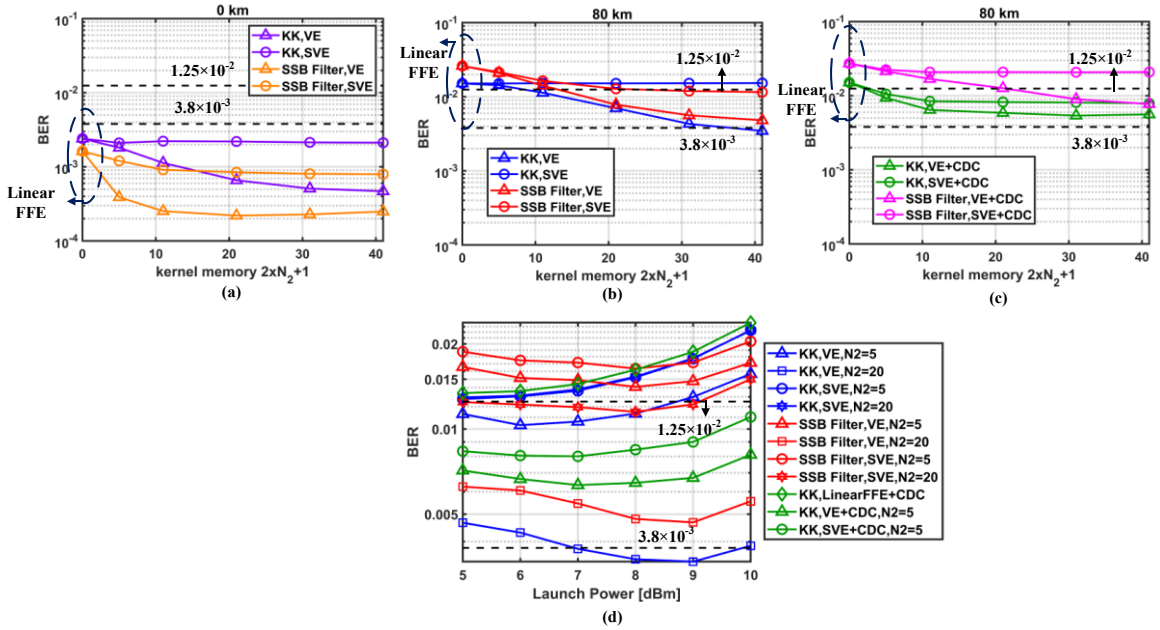

Fig. 4.4 (a) BERs as functions of nonlinear kernel memory lengths with different DSP combinations for a 56 Gbaud PAM4 at B2B with a launch power of -3 dBm, (b)/(c) BERs as functions of nonlinear kernel memory lengths for a 56 Gbaud PAM4 at 80km with a launch power of 8 dBm when processed without/with frequency-domain CDC, and (d) transmission performance of 56 Gbaud PAM4 at 80 km with different DSP combinations. [Adapted] with permission from [35] © The Optical Society.

On the other hand, after transmission over 80 km, the system also suffers from the fiber nonlinearity due to the relatively high launch power. Note that the launch power in this system

includes the power of a strong carrier which is roughly 10 times stronger than the signal. As we can see from the BER versus launch power curves in Fig. 4.4(d), if we increase the nonlinear kernel memory length of the VE, the optimum launch power allowed by the system can be increased, which indicates that a VE can improve the system's tolerance to the fiber nonlinearity. On the other hand, increasing the nonlinear kernel memory length of the SVE does not change the optimum launch power. Therefore, we can conclude that an SVE alone cannot mitigate the fiber nonlinearity in our system.

In addition, we observe that after 80 km of fiber, when the kernel memory length is short, the KK algorithm starts to show advantages over the SSB filtering algorithm, as we can see from Fig. 4.4(b). This is because when CD kicks in, the system suffers from severe ISI. Compared to the BtB case, a longer nonlinear kernel memory length is required in the 80 km case to effectively characterize the impact of the SSBI. If we only use the SSB filtering algorithm to reconstruct the RSB, and we use insufficient nonlinear kernel memory length in the VE/SVE, the penalty caused by the under-compensated SSBI will outweigh the penalty caused by the residue LSB when we the KK algorithm. As we increase the kernel memory length, in the SVE case, the SSB filtering algorithm will outperform the KK algorithm again, since both the SVE with enough kernel memory and the KK algorithm can effectively suppress the SSBI, but neither of them can mitigate other kinds of nonlinear impairments, and the KK algorithm suffers from additional penalty caused by the residual LSB. However, in the VE case, as we increase the kernel memory length, the KK algorithm always shows better performance than the SSB filtering algorithm at 80 km. We think this is because the VE can also mitigate the fiber nonlinearity (which is the major difference between the 80 km case and the BtB case). By adding a KK block to suppress the SSBI, we are relieving the burdens on the VE, thus the VE can mitigate the fiber nonlinearity more effectively, and the gain of that could prevail over the penalty suffered by the KK algorithm caused by the residue LSB.

Fig. 4.4(b) also shows that 56 Gbaud PAM4 transmission over 80 km with a BER below the 6.7% overhead HD-FEC threshold of 3.8×10^{-3} is achievable with the KK algorithm and a VE with a 2nd order nonlinear kernel memory length of 41 (N_2 = 20). However, the number of 2nd

order adaptive taps increases dramatically as the kernel memory length N_2 increases (# of taps = $(N_2 + 1)(2N_2 + 1)$), which makes this VE less preferable in practice. Directly limiting the kernel memory length of the VE will significantly degrade the performance at 80 km, because all the nonlinear impairments are deeply coupled with severe ISI after fiber transmission. Note that the ISI at 80 km is mainly originated from the CD. What if we insert a frequency-domain CDC block before the time-domain equalization to reduce the ISI first, and then reduce the kernel memory length of the VE/SVE?

After applying the CDC, a VE with a short kernel memory length should be able to effectively compensate for the MZM induced device nonlinearity just like the BtB case, since the MZM induced device nonlinearity is introduced at the transmitter before the dispersive fiber. However, the SSBI is introduced after the fiber, thus ideally it should be handled before the CDC. As we can see from the red curves in Fig. 4.4(b) and the magenta curves in Fig. 4.4(c), applying the CDC directly to a SSBI contaminated signal (i.e. when the KK algorithm is not used) in fact degrades the BER performance. The fiber nonlinearity is introduced in the fiber together with CD, thus applying CDC before the nonlinear equalization does help to reduce the required memory length, although this 2-step approximation also leads to a performance penalty. By comparing the blue curves in Fig. 4.4(b) and the green curves in Fig. 4.4(c), we find that when SSBI is suppressed by the KK algorithm, applying CDC improves the BER performance in both the VE and the SVE cases if the kernel memory is less than 20. But adding the CDC block also limits the best performance that can be achieved with longer kernel memory length in both cases. Interestingly, we also find that when combined with the KK algorithm and the CDC block, the SVE can also mitigate fiber nonlinearity to some extent. As we can see from Fig. 4.4(d), at 80 km, if both the KK algorithm and the CDC are used, by switching from linear FFE to SVE, the optimum launch power can be increased, but if CDC is not enabled, increasing the 2nd order kernel memory length of the SVE does not increase the optimum launch power.

To balance the performance and the computational complexity, in the following analysis, we use the KK algorithm to suppress the SSBI, a frequency domain CDC block to reduce the

required nonlinear kernel memory length, and a memory-limited VE ($N_2 = 5$, $2N_2 + 1 = 11$, which corresponds to 66 nonlinear taps) to mitigate the remaining linear and nonlinear ISIs.

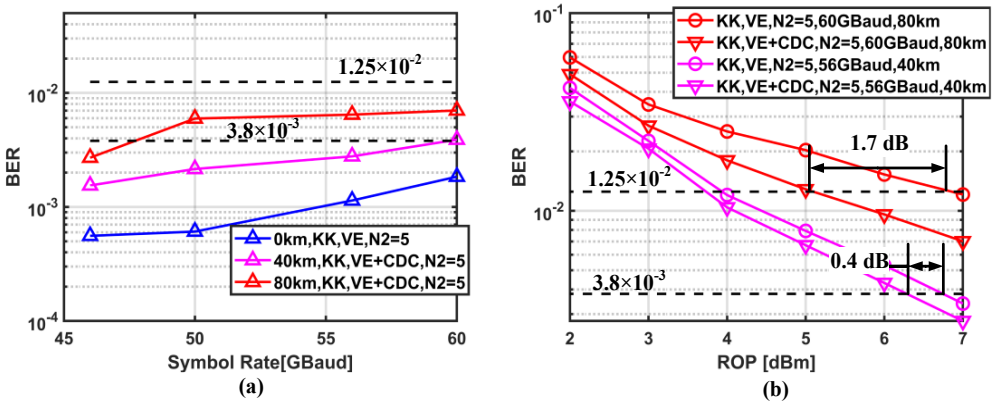

Fig. 4.5 (a) BERs as functions of symbol rate at B2B, 40 km and 80 km with 7 dBm ROP, and (b) Receiver sensitivity requirements for a 56 Gbaud PAM4 signal at 40 km and a 60 Gbaud PAM4 signal at 80 km, when processed with 1) the KK algorithm and a short-memory VE, 2) the KK algorithm, a frequency domain CDC block, and a short-memory VE. [Adapted] with permission from [35] © The Optical Society.

To explore the capacity limit of this DAC-less VSB self-coherent system, we sweep the symbol rate at BtB, 40 km and 80 km with an ROP of 7 dBm. The memory length of the linear kernel and the launch power are re-optimized for different baud rates and distances, while the nonlinear kernel memory length is fixed at 11. The results are shown in Fig. 4.5(a). As we can see, for links up to 40 km, we can use the HD-FEC with 6.7% overhead to achieve a net rate of 100 Gb/s. Specifically, we report a 112 Gb/s transmission over 40 km of SMF with a BER below the 6.7% overhead HD-FEC threshold of 3.8×10^{-3}. For longer distances, the HD-FEC seems to be insufficient (at least the with the current choice of DSPs, but we will show how to improve the performance by using new DSP algorithms in section 4.3), and we need the SD-FEC with higher overhead to achieve a net rate of 100 Gb/s, and here we report a 120 Gb/s transmission over 80 km of SMF with a BER below the 14.8 % overhead SD-FEC threshold of 1.25×10^{-2}.

Then we study the receiver sensitivity requirements with and without the CDC block at different transmission distances. Fig. 4.5(b) plots the BER performance as functions of the ROP. We observe that at 40 km, for a 56 Gbaud signal, by applying the frequency-domain CDC before the VE, only 0.4 dB receiver sensitivity gain can be achieved at the HD-FEC threshold,

and the gain at the SD-FEC threshold is negligible. However, at 80 km, for a 60 Gbaud signal, we can achieve a sensitivity gain of 1.7 dB at the SD-FEC threshold. Based on our previous discussions, the CDC block becomes helpful when there is interaction between a significant amount of ISI and the nonlinear impairments which makes a memory limited VE insufficient to characterize and mitigate the nonlinear impairments. Compared to the 40 km case, both the ISI and the fiber nonlinearity are more severe after 80 km of fiber, and that explains why the CDC block achieves better sensitivity gain at 80 km.

4.2.5 Summary

In this work, we experimentally demonstrate a high-speed single wavelength DAC-less VSB PAM4 transmission system for short-reach applications by combining a SiPh ME-MZM based DAC-less PAM4 transmitter with a VSB self-coherent receiver. The effects of the CD, the SSBI, the modulator and the fiber nonlinearities, as well as their mitigation methods have been comprehensively studied. Specifically, the KK algorithm, a frequency domain CDC block and a memory limited time domain VE have been used in the receiver DSP to suppress the SSBI, relax the requirement of the nonlinear kernel memory length, and compensate for the linear and nonlinear ISIs, respectively. We report a 112 Gb/s transmission over 40 km below the HD-FEC threshold with an overhead of 6.7%, and a 120 Gb/s transmission over 80 km below the SD-FEC threshold with an overhead of 14.8%.

4.3 Filter response aware iterative KK algorithm for VSB systems

4.3.1 Motivation

As we mentioned several times in this thesis, a VSB self-coherent system can be regarded as an upgrade of an IM/DD system which merely adds an optical filter between the transmitter and the receiver. If the edge of the optical filter is sharp enough, we can retrieve the field information of the received quasi-SSB signal using the KK-family algorithms introduced in Chapter 2, section 2.4.2.2, and then apply dispersion compensation in DSP to extend the transmission distance. The problem is that most of the existing KK-family algorithms assume that the PD receives a rigorous SSB signal, which is not strictly true in a VSB system. In most

cases, the optical filter has a limited edge gradient (i.e. the filter is not sharp enough), hence the unwanted sideband cannot be completely removed, and the residual unwanted sideband will degrade the performance of these conventional KK-family algorithms. Therefore, there is motivation to develop a new field reconstruction algorithm specifically for the VSB system, which does not assume that the residual unwanted sideband is negligible. In this work, we propose a filter response aware iterative KK algorithm (FA-iter-KK) for this purpose. The FA-iter-KK algorithm can be regarded as an upgrade of the iter-KK algorithm introduced in Chapter 2, section 2.4.2.2. Specifically, it utilizes the optical filter response information in each iteration to improve the accuracy of the estimated field when the unwanted sideband is insufficiently suppressed.

To test the performance of this algorithm, we reuse the experimental setup presented in section 4.2, and we prove that the FA-iter-KK algorithm outperforms the KK and the iter-KK algorithms in our system for the parameters of this study. We also numerically investigate the FA-iter-KK algorithm's potential to relax the optical filter edge gradient requirement in a VSB-PAM4 system.

4.3.2 The FA-iter-KK algorithm

Fig. 4.6 depicts the the optical filter response and the spectrum of the received signal in a typical VSB system. Without loss of generality, we assume that the optical filter suppresses the LSB spectrum. The received signal includes three parts: a strong DC carrier c, the targeted RSB $s_1(t)$ and the residual LSB $s_2^*(t)$. Here we define $s_2(t)$ as the complex conjugate of the residual LSB for the convenience of derviation, so that $s_1(t)$ and $s_2(t)$ are RSB signals.

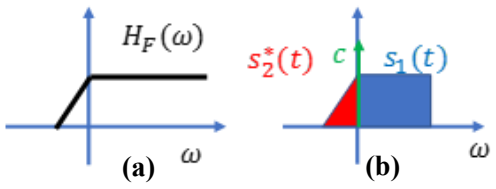

Fig. 4.6 (a) Optical filter response and (b) Spectrum of the received VSB signal.(©2020 IEEE)

After square-law detection and an ADC, the sampled photocurrent can be expressed as

$$\begin{aligned} I[n] &= (C + s_1[n] + s_2^*[n])(C + s_1^*[n] + s_2[n]) \\ &= \{C + Re(s_1[n]) + Re(s_2[n])\}^2 \\ &+ \{Im(s_1[n]) - Im(s_2[n])\}^2 \end{aligned} \tag{4.3}$$

where $s_i[n], i = 1,2$ represents the sampled version of $s_i(t)$. Then we define the RSB part of the signal before transmission and optical filtering as $s_0(t)$, which results in $s_0[n]$ after sampling, and we have

$$s_1[n] = IDFT\{DFT\{s_0[n]\}H_{CD}(j\omega_k)H_F(j\omega_k)\} \tag{4.4}$$

$$s_1[n] = IDFT\{DFT\{s_0[n]\}H_{CD}(j\omega_k)H_F(j\omega_k)\} \tag{4.5}$$

where $DFT\{\}$ and $IDFT\{\}$ represent the discrete Fourier transform (DFT) and the inverse discrete Fourier transform (IDFT), respectively. $H_{CD}(j\omega_k)$ and $H_F(j\omega_k)$ are the frequency responses of the CD effect and the optical filter, where $\omega_k = 2\pi k/N, k = 0,1, \dots, N-1$, and N is the size of the DFT/IDFT. Note that $H_F(j\omega_k)$ can be obtained through measurement, and $H_{CD}(j\omega_k) = \exp\left(-\frac{1}{2}j\beta_2\omega_k^2 L\right)$, where β_2 and L are the GVD coefficient and the transmission distance, respectively. Next, we define:

$$b[n] = Re(s_1[n]) + Re(s_2[n]) \tag{4.6}$$

Obviously, $b[n]$ is a real-valued signal, which can be computed from Eq. 4.3:

$$b[n] = \sqrt{I[n] - \{Im(s_1[n]) - Im(s_2[n])\}^2} - C \tag{4.7}$$

Also, based on Eqs. 4.4 and 4.5, we have:

$$s_1[n] = IDFT\left\{2\frac{DFT\{b[n]\}H_{RSB}(j\omega_k)H_{CD}(j\omega_k)H_F(j\omega_k)}{H_{CD}(j\omega_k)H_F(j\omega_k) + H_{CD}^*(-j\omega_k)H_F^*(-j\omega_k)}\right\} \tag{4.8}$$

$$s_2[n] = IDFT\left\{2\frac{DFT\{b[n]\}H_{RSB}(j\omega_k)H_{CD}^*(-j\omega_k)H_F^*(-j\omega_k)}{H_{CD}(j\omega_k)H_F(j\omega_k) + H_{CD}^*(-j\omega_k)H_F^*(-j\omega_k)}\right\} \tag{4.9}$$

where $H_{RSB}(j\omega)$ is a digital RSB filter which keeps all the positive frequency components and sets zeros to all the negative frequency components, i.e.:

$$H_{RSB}(j\omega_k) = \begin{cases} 1, \omega_k > 0 \\ 0, \omega_k \le 0 \end{cases} \tag{4.10}$$

Then we define:

$$H_1(j\omega_k) = \frac{H_{RSB}(j\omega_k)H_{CD}(j\omega)H_F(j\omega)}{H_{CD}(j\omega_k)H_F(j\omega_k) + H_{CD}^*(-j\omega_k)H_F^*(-j\omega_k)} \tag{4.11}$$

$$H_2(j\omega_k) = \frac{H_{RSB}(j\omega_k)H_{CD}^*(-j\omega_k)H_F^*(-j\omega_k)}{H_{CD}(j\omega_k)H_F(j\omega_k) + H_{CD}^*(-j\omega_k)H_F^*(-j\omega_k)} \tag{4.12}$$

Based on Eqs. 4.8-4.12, the imaginary parts of $s_1[n]$ and $s_2[n]$ are given by:

$$Im\{s_1[n]\} = IDFT\{DFT\{b[n]\}\{-jH_1(j\omega_k) + jH_1^*(-j\omega_k)\}\} \tag{4.13}$$

$$Im\{s_2[n]\} = IDFT\{DFT\{b[n]\}\{-jH_2(j\omega_k) + jH_2^*(-j\omega_k)\}\} \tag{4.14}$$

Note that the derivations of Eqs. 4.13 and 4.14 utilizes the fact that $b[n]$ is a real signal, thus its spectrum is Hermitian symmetric. Eqs 4.7, 4.13 and 4.14 are the mathematical foundations of the proposed FA-iter-KK algorithm. Specifically, to obtain an accurate estimation of $b[n]$, we can do the following:

a. Start by assuming $Im\{s_1[n]\} = Im\{s_2[n]\} = 0$, use Eq. 4.7 to obtain an initial estimation of $b[n]$.

b. Use Eqs. 4.13 and 4.14 to estimate $Im\{s_1[n]\}$ and $Im\{s_2[n]\}$ from $b[n]$.

c. Use Eq. 4.7 again to update the estimation of $b[n]$ using the $Im\{s_1[n]\}$ and $Im\{s_2[n]\}$ values obtained from step b.

d. Repeat steps b-c iteratively to improve the accuracy until the results converge.

The FA-iter-KK algorithm can be regarded as a generalization of the iter-KK algorithm (please refer to Chapter 2, section 2.4.2.2). Suppose that we have an extremely sharp optical filter with a frequency response $H_F(j\omega) = H_{RSB}(j\omega)$, then $s_2[n]$ vanishes (thus Eq. 4.14 no longer exists), and Eq. 4.7 degenerates to Eq. 2.60, which allows us to estimate $Re\{s_1[n]\}$ from the photocurrent $I[n]$ and a given $Im\{s_1[n]\}$ value. In the meantime, we have $H_1(j\omega_k) = H_{RSB}(j\omega_k)$, hence Eq. 4.13 degenerates to Eq. 2.56, which says we can estimate $Im\{s_1[n]\}$ from a given $Re\{s_1[n]\}$ value through a Hilbert transform (the KK relation). Remember that the main idea behind the iter-KK algorithm is to use Eqs. 2.60 and 2.56 iteratively to approach accurate estimations of $Re\{s_1[n]\}$ and $Im\{s_1[n]\}$. In the FA-iter-KK algorithm, we inherit this idea, and replace Eqs. 2.56 and 2.60 with their generalized forms Eqs. 4.7, 4.13 and 4.14, since in a practical VSB system, the optical filter has a frequency response $H_F(j\omega_k) \neq H_{RSB}(j\omega_k)$, and the impact of $s_2[n]$ should not be neglected. Strictly speaking, the FA-iter-KK algorithm does not really include a KK relation based step. But note that Eqs. 4.13 and 4.14 can be regarded as the generalized KK relation, and the basic idea of this algorithm is inherited from the iter-KK algorithm, thus we think it is still appropriate to say that the proposed algorithm is a generalized iter-KK algorithm that is aware of the optical filter response, and it also belongs to the KK-family.

The FA-iter-KK algorithm seem complicated at first glance. But note that both Eqs. 4.13 and 4.14 merely apply a linear filter to a real-valued signal $b[n]$, and the outputs of these two

equations are also real-valued signals. Frequency-domain linear filtering can be implemented using the overlap-and-save algorithm [52]. The weighting coefficients of the filters can be computed offline and pre-stored, since they only depend on the fiber parameters (the length L and β_2) and the filter design (the shape of its spectral response).

Once we obtain a relatively accurate estimation of $b[n]$, we can recover the transmitter side RSB signal $s_0[n]$ through:

$$s_0[n] = IDFT\left\{\frac{DFT\{b[n]\}H_{RSB}(j\omega_k)}{H_{CD}(j\omega_k)H_F(j\omega_k) + H_{CD}^*(-j\omega_k)H_F^*(-j\omega_k)}\right\} \tag{4.15}$$

Eq. 4.15 is a generalization of the CD compensation step which considers the fact that the residual wanted sideband could lead to power fading effect in a VSB system (please refer to Chapter 2, section 2.4.2.3), hence the generalized CD function that needs to be inverted is no longer an all-pass filter. Again, assuming that the optical filter is extremely sharp, i.e. $H_F(j\omega_k) = H_{RSB}(j\omega_k)$, Eq. 4.15 degenerates to the classic CD compensation (Eq. 2.69) of the RSB signal $s_1[n] + s_2[n]$. Note that a CD compensation step is always required regardless of the choice of the field reconstruction algorithm. Both the classic CD compensation (Eq. 2.69) and Eq. 4.15 apply a linear filter to $b[n]$, which can be implemented using the overlap-and-save algorithm. Hence, using Eq. 4.15 instead of Eq. 2.69 generally improves the transmission performance, but does not increase the computational complexity.

The derivation presented in this section ignores the device bandwidth limitations. Theorectically, in Eqs. 4.4 and 4.5, we should replace $H_{CD}(j\omega_k)H_F(j\omega_k)$ with the end-to-end channel response that includes the frequency responses of all the components in the link. In practice, we can assume that we have a $s_0[n]$ tainted with ISI (induced by the bandwidth limitations of the devices). Hence, we can first recover the ISI contaminated $s_0[n]$ with the FA-iter-KK algorithm, and then apply an FFE to mitigate the ISI.

4.3.3 Experimental setup and results

To experimentally show that our proposed FA-iter-KK algorithm can outperform the KK algorithm and the iter-KK algorithm in a VSB system, we reuse the experimental setup shown in Fig. 4.2(a). Just a highlight of some important system parameters, we use a two BPG channels to generate two 56 Gbaud PAM2 signals, and then use a SiPh ME-MZM to optically

combine them into a PAM4 signal. The power of the DC carrier is tuned by controlling the bias point of the modulator. After transmission over 40-80 km of fiber, we use an optical filter with an edge gradient of ~15 dB/10 GHz at the receiver as a VSB filter. The VSB signal is detected by a 50 GHz PD (without TIA) and then sampled by a 160 Gsa/s RTO channel. Since this is a DAC-less system, we only have DSP at the receiver.

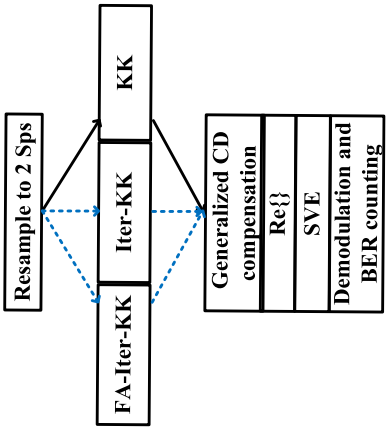

Fig. 4.7 Receiver DSP blocks for studies on different KK algorithms. (©2020 IEEE)

The offline DSP blocks used in this work are shown in Fig. 4.7. Compared to Fig. 4.2(b), we made the following changes: 1) in addition to the case where we use the KK algorithm to reconstruction the field information of the SSBI-free signal, we also consider the cases where we use the iter-KK/FA-iter-KK algorithms, 2) no matter which field reconstruction algorithm we use, we always implement the generalized CD compensation (Eq. 4.15) instead of the classic CD compensation (Eq. 2.69), and 3) we only consider the SVE (Eq. 4.2) this time for time-domain equalization, and we always use 41 linear taps and 5 nonlinear taps (2^{nd} order kernel memory length = 5) regardless of the transmission distance or the choice of the field reconstruction algorithm.

We first sweep the number of iterations in the iter-KK and the FA-iter-KK algorithms. The results are shown in Fig. 4.8(a). We also show the performance of the KK algorithm as dashed lines in Fig. 4.8(a) for comparison. The 0-iteration point corresponds to the case where we use the initial guess of $b[n] = \sqrt{I[n]} - c$ directly as the input of the generalized CD compensation block. We observe that both the KK algorithm and the iter-KK algorithm achieve a modest effective SNR improvement compared to the 0-iteration case, since the residual LSB

degrades the performance of these two algorithms, even though we have already used a sharp optical filter in this system. Here the effective SNR is the SNR measured after applying the receiver DSP, which is defined as:

$$SNR_{eff} = \frac{\sum_{i=1}^{M} P_X(x_i)|\mu_i|^2}{\sum_{i=1}^{M} P_X(x_i)\sigma^2} \tag{4.16}$$

where M is the size of the alphabet of the tranmistted symbols, μ_i and σ_i^2 are the emprical mean and the variance of the received symbols that belong to the (transmitter-side) input symbol x_i and $P_X(x_i)$ is its probability of occurance. In this work, we consider a uniform PAM4 signal, hence we have $M = 4$ and $P_X(x_i) = 1/4$ for all i. Note that the effective SNR value includes all distortions between the input and the output of the channel, e.g. the penalty of DSP algorithms, the undercompenstated ISI, and the undercompensated nonlinear impariments.

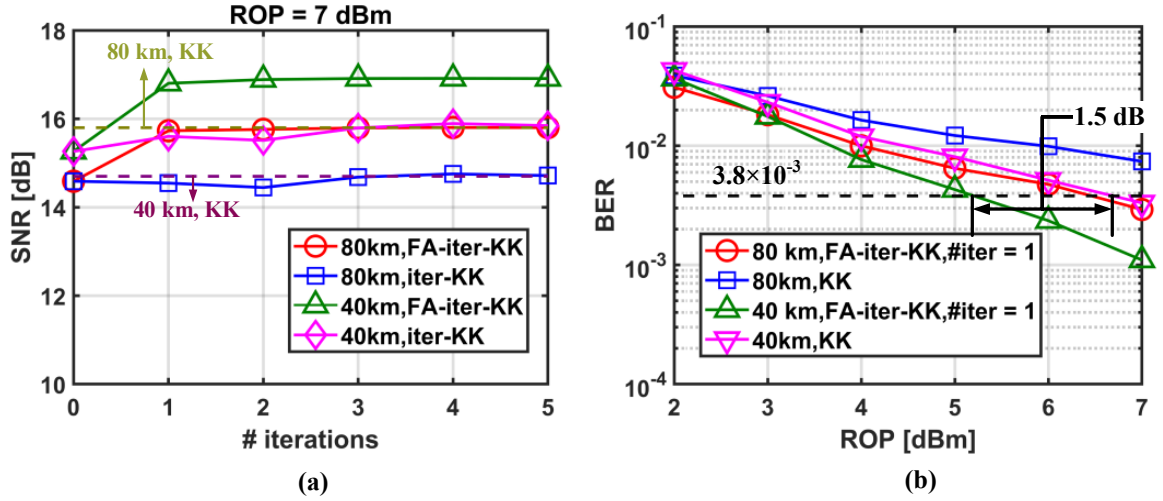

Fig. 4.8 Experimental results (a) effective SNR vs. number of iterations in iter-KK/FA-iter-KK algorithms and (b) BER vs ROP requirement of KK/FA-iter-KK algorithms. (©2020 IEEE)

On the other hand, the FA-iter-KK algorithm requires just 1 iteration to achieve apparent effective SNR improvement. We also observe that the performance of the iter-KK algorithm will converge to that of the KK algorithm as the number of iteration increases, even in the presense of the residual LSB, hence in the following analysis, we will only compare the FA-iter-KK algorithm and the KK algorithm.

Fig. 4.8(b) shows the BERs as functions of the ROP when using 1) the FA-iter-KK algorithm

with 1 iteration and 2) the KK algorithm. Firstly, we observe that even when using the KK algorithm, the BER performance reported here are better than the results reported in section 4.2.5. But we use a simpler time-domain equalizer in this work, which should degrade the BER performance. The performance improvement should be attributed to the fact that we use the generalized CD compensation (Eq. 4.2) to replace the conventional CD compensation (Eq. 2.69) in this experiment. The generalized CD compensation also compensates for the power fading effect induced by the residual LSB, which allows us to relieve some burdens from the time-domain equalizer. Secondly, we observe that by using the FA-iter-KK algorithm instead of the KK algorithm, we can further improve the BER performance. Specifically, at 40 km, the FA-iter-KK algorithm achieves a receiver sensitivity gain of 1.5 dB with respect to the KK algorithm at the HD-FEC threshold of 3.8×10^{-3} with an overhead of 6.7%, and at 80 km, only the FA-iter-KK algorithm can achieve 112 Gb/s transmission with a BER below the HD-FEC threshold.

4.3.4 Numerical analysis and discussions

The above experiment results show that the FA-iter-KK algorithm can improve the BER performance compared to the KK algorithm when applied to the same system. That makes us think if it is possible to maintain certain BER performance using a less sharp optical filter by applying the FA-iter-KK algorithm.

Since we cannot tune the edge gradient of the optical filter used in our experiment, we decide to numerically study this possibility. Fig. 4.9(a) shows the simulation setup. In this simulation, we use a simple link model which includes an RC filter for pulse shaping (to make sure that the signal has limited bandwidth), the AWGN source, the CD effect, the optical filter, the square-law detection and the receiver DSP. The impacts of the component bandwidth limitations, the device nonlinearity and the fiber nonlinearity are not considered. The optical filter is inserted at the recevier, hence it suppresses both the unwanted sideband and the AWGN from the transmitter and the channel. In this simplified model, we assume that the optical filter response has a trapezoidal shape in the semi-logarithmic scale, i.e. its frequency response is flat-top in the passband, and the filter edge is a straight line on the log-linear plot. The power

responses of several filters with different edge gradients are shown in Fig. 4.9(b).

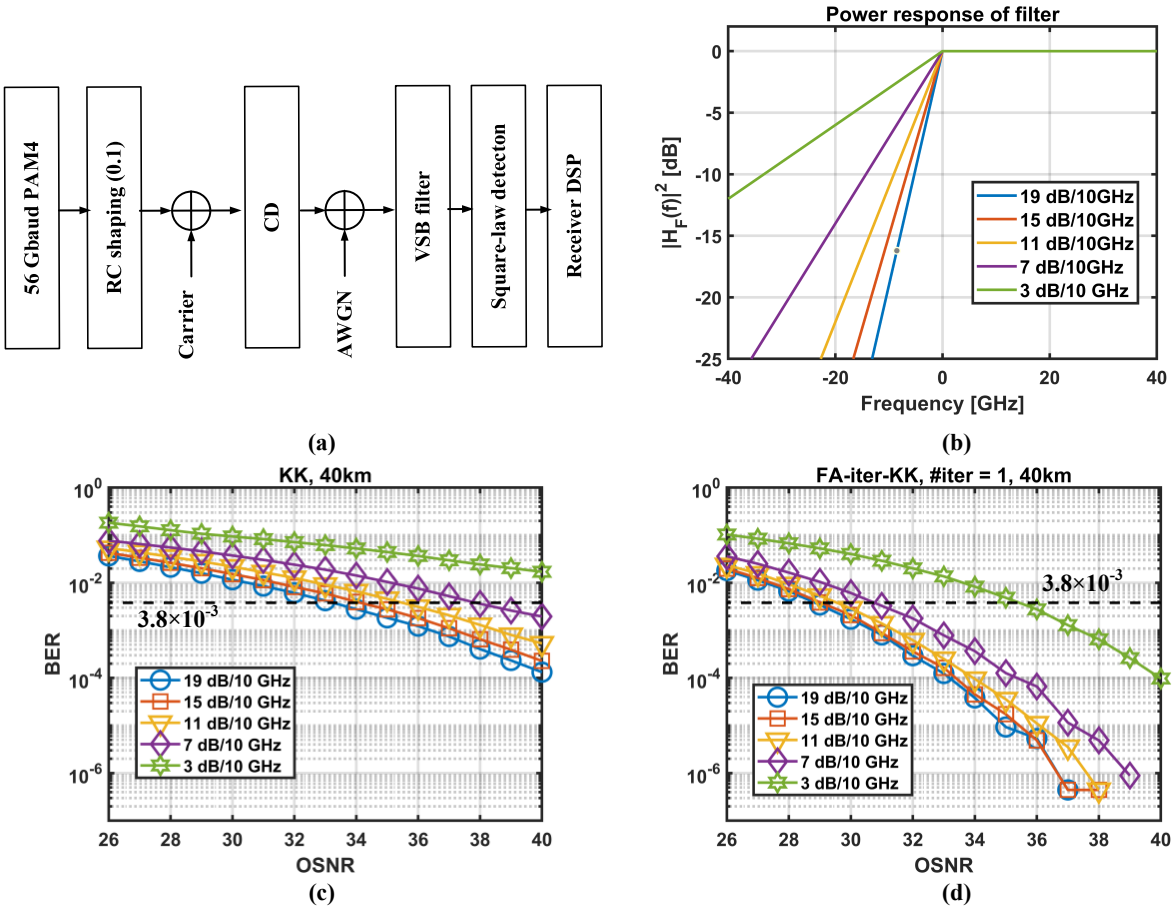

Fig. 4.9 (a) schematic of the simulation setup, (b) frequency responses of trapezoidal filters with different edge gradients, (c) and (d) simulated BER-OSNR relations with different optical filters when processed with different KK algorithms. (©2020 IEEE)

In this study, we assume that there are EDFAs in the system, hence the PD always receives the optimum ROP, and the system is noise-limited. Therefore, in this simulation, we didn't consider the impact of the insertion loss (the loss at the passband) of the filter, but note that if the system is loss-limited, the filter's insertion loss does affect the transmisson performance, as we will see in Chapter 5, section 5.2.4.

Fig. 4.9(c) and Fig. 4.9(d) show the simulated BER performance after transmission over 40 km of fiber when using 1) the FA-iter-KK algorithm with 1 iteration and 2) the KK algorithm at the receiver. Note that here the OSNR value includes the carrier power as a part of the signal power, and the CSPR is optimized for each pair of optical filter edge gradient and OSNR value. We observe that with similar OSNR, the FA-iter-KK algorithm requires a less sharp optical

filter to achieve the same BER as the KK algorithm. For example, with an OSNR of 36 dB, the KK algorithm requires a 11 dB/10 GHz optical filter to achieve a BER of 3.8×10^{-3}, while the FA-iter-KK algorithm only requires a 3 dB/10 GHz filter to achieve comparable performance. When the OSNR is reduced to 32 dB, the KK algorithm can no longer achieve a BER below 3.8×10^{-3} even using a sharp filter with an edge gradient of 19 dB/10 GHz, while the FA-iter-KK algorithm requires a 7 dB/10 GHz filter to achieve the HD-FEC threshold BER.

4.3.5 Summary

In this work, we propose an FA-iter-KK algorithm which utilizes the optical filter response information to improve the accuracy of field reconstruction process in a VSB system. We experimentally prove that the FA-iter-KK algorithms outperforms the KK and the iter-KK algorithms in a 56 Gbaud VSB-PAM4 system over 40-80 km when the residual LSB is not negligible, and we numerically show that the FA-iter-KK can reduce the optical filter edge gradient requirement of a VSB system.

4.4 SiPh parallel path transmitter circuit for on-chip CSPR control

4.4.1 Motivation

An SSB/VSB self-coherent system requires the transmitter to insert an optical carrier at the edge of the signal to serve as the phase reference. In practice, the CSPR should be optimized. According to Chapter 2, section 2.4.2.2, the KK-family algorithms requires a relatively large CSPR to reconstruct the field information of the SSB/quasi-SSB signal. The CSPR cannot be too small, since a small CSPR will cause penalties to these algorithms and degrade the BER performance. The CSPR cannot be too large either. Note that in a self-coherent system, the OSNR is defined as the ratio of the total power of the carrier and the signal to the power of the noise in 0.1 nm optical bandwidth, because the carrier is generated from the transmitter-side laser and is transmitted through all the EDFAs (if there is any). However, it is the carrier-less SNR, i.e. the ratio of the signal power to the noise power, that affects the BER performance. Consider a noise limited system, where the ROP (the total power of the carrier and the signal at the receiver side) is clamped to its optimum value by the EDFAs. Given a fixed OSNR, the

total power of the noise is also fixed. Increasing the CSPR means increasing the carrier power and reducing the signal power, which will reduce the carrier-less SNR. In other words, if the CSPR is sufficiently large such that the accuracy of the field reconstruction process is no longer the predominant limiting factor of the transmission performance, further increasing the CSPR will degrade the achievable BER performance.

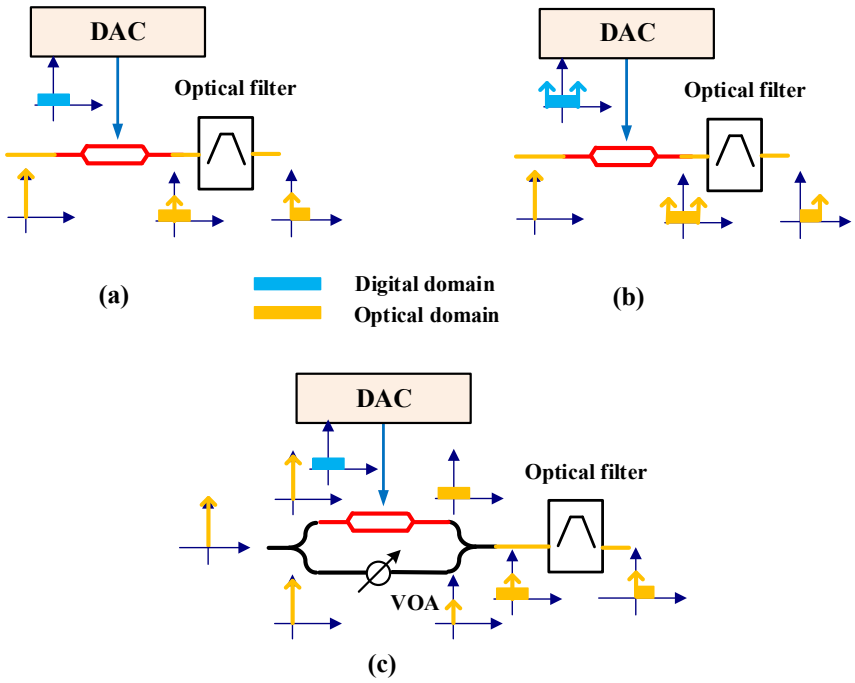

Fig. 4.10 CSPR control methods in VSB self-coherent systems. (a) Tuning the bias point of the modulator, (b) digital carrier generation, and (c) the parallel path scheme with a fixed ratio power splitter and a VOA. [Adapted] with permission from [37] © The Optical Society.

Therefore, in a practical SSB/VSB self-coherent system, the CSPR needs to be optimized, hence it is beneficial to have some sort of CSPR tunability. Fig. 4.10 summarizes the mainstream CSPR control methods, where we take a VSB self-coherent system as an example to demonstrate the idea. The simplest scheme is to tune the bias point of the modulator to control the strength of the DC leakage as shown in Fig. 4.10(a), where the DC leakage serves as the carrier [20]. However, tuning the bias point far away from the null point (the middle point of the linear region of the MZM's field transfer function) will enhance the device nonlinearity, which could degrade the transmission performance. The digital carrier generation scheme depicted in Fig. 4.10(b) provides a solution that decouples the CSPR control and the device nonlinearity issue, in which the modulator is biased strictly at the null point and the

carrier is digitally generated at the outer edge of the signal (because the DAC channel(s) cannot generate DC component) [76]. The CSPR can be easily controlled in DSP in this scheme. However, digital carrier generation requires the DAC channel(s) to have higher resolutions and larger bandwidths, since the carrier is typically much stronger than the signal (CSPR > 10dB), thus only a small portion of the DAC output levels can actually be used to generate the actual signal part. Fig. 4.10(c) shows the third method, where the optical carrier is introduced through a carrier path parallel to the signal path [75]. In this scheme, the MZM is biased at the null point, and all the output levels of the DAC channel(s) can be used for signal generation. The CSPR is controlled through a VOA embedded in either the carrier path or the signal path.

In this work, we implement a parallel path structure based transmitter circuit on the SiPh platform to acquire on-chip CSPR control capability in a VSB self-coherent system. In addition, we propose to use an integrated tunable power splitter in the circuit to remove the VOA in the conventional parallel path structure. We report a 112 Gb/s passband 16QAM transmission over 80 km using our device with a BER below the 6.7% overhead hard-decision forward error correction threshold of 3.8×10^{-3}.

4.4.2 CSPR control with a tunable power splitter

The use of a VOA in Fig. 4.10(c) is not power-efficient since it wastes some optical power on the attenuator. In this work, we propose to use a modified parallel path structure as shown in Fig. 4.11(a). The 50/50 power splitter at the input of the parallel path structure is replaced by a tunable power splitter. By adjusting the splitting ratio of the tunable power splitter, we can control the portion of the optical power launched into the carrier path, and the remaining optical power is launched into the signal path, hence the CSPR can be controlled without using a VOA in any of the paths.

A tunable splitter can be implemented as a Mach-Zehnder interferometer (MZI) with a thermal phase shifter embedded in one of its arms. The tunable power splitter, the MZM and the carrier path (a plain waveguide) can be integrated on the SiPh platform to reduce the cost and the footprint as shown in Fig. 4.11(b). Note that in an SP self-coherent system, it is necessary to align the polarization states of the carrier and the signal, which further motivates the on-chip

implementation since the integrated components are inherently polarization maintaining due to the strong birefringence of the SiPh waveguides [49].

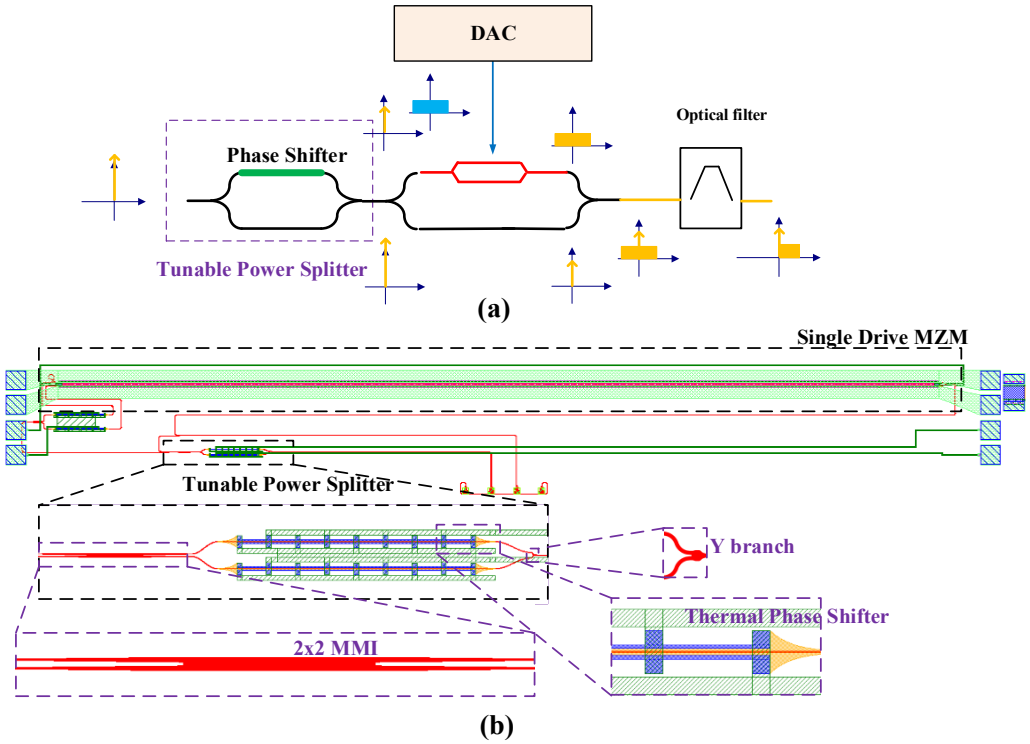

Fig. 4.11 (a) schematic of tunable power splitter based parallel path structure for CSPR controlling, and (b) layout of CSPR controllable SiPh VSB self-coherent transmitter circuit. [Adapted] with permission from [37] © The Optical Society.

The SiPh transmitter circuit was fabricated in a multi-project-wafer run at Advanced Micro Foundry on a silicon-on-insulator wafer with a 2-μm buried oxide. A Y branch [99] and a 2×2 multimode interferometer (MMI) [100] were used as the input and the output of the tunable power splitter respectively for broadband operation. A thermal phase shifter was implemented as a 245 μm long heavily N doped rib waveguide, which can be regarded as a heating resistor when applied with a DC voltage. The heavily N doped waveguide has slightly higher loss then the undoped waveguide (~0.75 dB/mm instead of ~0.2 dB/mm), therefore we embedded two identical phase shifters in both arms of the MZI to eliminate the loss difference, though we only apply voltage to one of them to adjust the splitting ratio. A VSB self-coherent transmitter only requires a single-drive MZM since the SSB spectrum will be obtained through optical filtering at the receiver. In this work we used a single-drive push-pull MZM for chirp-free modulation. The P++ region width of the MZM was 12.6 μm, and the PN junctions were

divided into 49 μm segments with 1 μm intrinsic spaces, the rest design parameters are the same as the parameters used in [9].

Although in this work we use a VSB system as an example to demonstrate the concept, the proposed tunable power splitter based parallel path structure (and so as the other CSPR control methods depicted in Fig. 4.11) can also be used in other SSB self-coherent system structures, as long as the laser is modulated externally. All we need to do is to replace the MZM in Fig. 4.11(a)-(b) with a different modulator, for instance, an IQ modulator biased at the null point.

4.4.3 Experimental setup and results

We test the fabricated SiPh transmitter circuit with a VSB self-coherent receiver which consists of a commercial optical filter with an edge gradient of ~15 dB/10 GHz and a DC-coupled single-ended PD without TIA. The DSP blocks and the experimental setup are shown in Fig. 4.12.

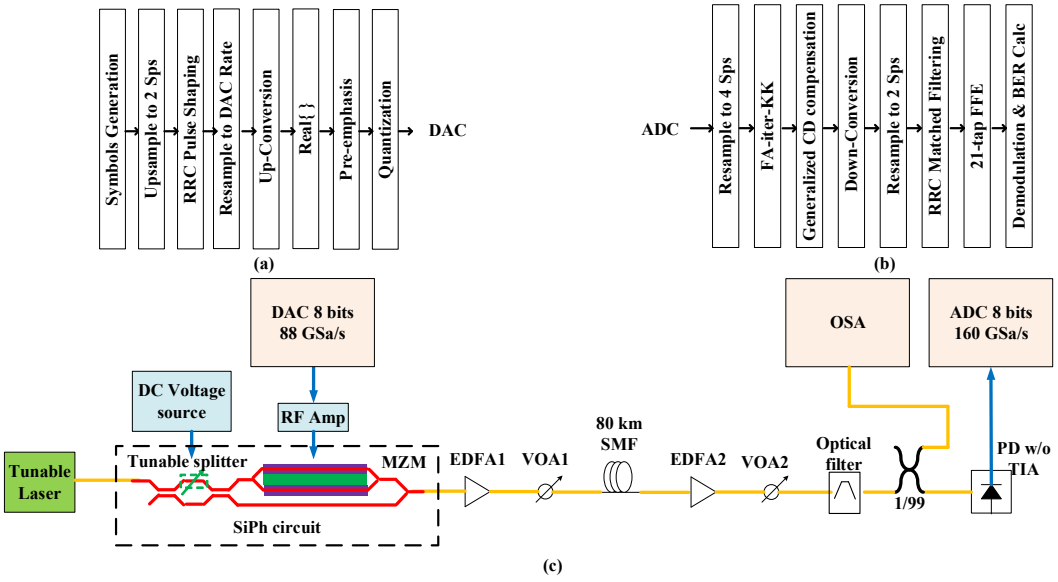

Fig. 4.12 (a) Transmitter DSP, (b) receiver DSP and (c) experimental setup for the demonstration of a 112 Gb/s 16QAM transmission over 80 km using the tunable power splitter based SiPh circuit. [Adapted] with permission from [37] © The Optical Society.

This time, we transmit a passband 16QAM signal instead of a baseband PAM4 signal as we did in section 4.2, since in this experiment we use an 8-bit DAC channel rather than a DAC-less transmitter for signal generation, and the passband 16QAM scheme allows us to insert a guard band (optimized to be 3 GHz) between the DC carrier and the edge of the signal, so that

the unwanted sideband can be further suppressed.

The offline transmitter DSP includes baseband 16QAM symbol generation, resampling from 1 Sps to 2 Sps, RRC pulse shaping with a roll-off factor of 0.1 at 2 Sps , resampling from 2 Sps to the DAC's sampling rate, frequency up-conversion, real waveform generation (taking the real part of the frequency up-converted RSB signal), pre-emphasis (a 71-tap transmitter-side FFE operating at the DAC's sampling rate that flattens the combined frequency responses of the DAC and the RF amplifer) and quantization (quantize the signal to 8-bit). The processed data sequence is then uploaded to an 8-bit DAC channel operating at 88 GSa/s to generate the analog RF waveform. The output of the DAC is amplified to ~ 3 V peak-to-peak by an RF amplifier before being applied to the SiPh chip using a ground-signal-signal-ground (GSSG) probe. The MZM is terminated by a 50 Ohm resistor using another GSSG probe. A DC voltage V_H is applied to the thermal phase shifter in the tunable power splitter through an unused probe tip to control the splitting ratio. In this experiment, the bias point of the MZM is controlled by selecting appropriate operating wavelength since the length of the two MZM arms are designed to be imbalanced. A 15.5 dBm tunable laser is used as the light source, and the wavelength is adjusted to be at 1548.72 nm so that the MZM is biased at the null point.

The output of the SiPh circuit transmits over 80 km of SMF before being detected by the VSB receiver. We use EDFA/VOA pairs before and after the fiber to control the launched power and the received power separately. A high resolution OSA is used to monitor the spectrum before PD detection. The signal detected by the PD is digitized by an 8-bit RTO channel (which serves as the ADC channel) operating at 160 Gsa/s. Then the offline receiver DSP is applied, which includes resampling from the RTO sampling rate to 4 Sps, the FA-iter-KK algorithm, the generalized CD compensation (please also refer to section 4.3 for more information), frequency down-conversion, resampling from 4Sps to 2Sps, RRC matched filtering, a 21 tap $T/2$ spaced linear FFE, and the 16QAM demodulation.

By controlling the DC voltage V_H, we can control the splitting ratio of the tunable power splitter, which then determines the CSPR. Fig. 4.13a) shows the relation between the measured CSPRs and the V_H values, and Fig. 4.13(b) shows the received VSB spectra with several

different CSPR values. The signal's spectra are not flat-top since the transmitter-side pre-emphasis filter only compensates for the frequency responses of the DAC channel and the RF amplifier. The bandwidth limitations of the RF cables, the probes and the modulator are left to be treated in the receiver-side FFE.

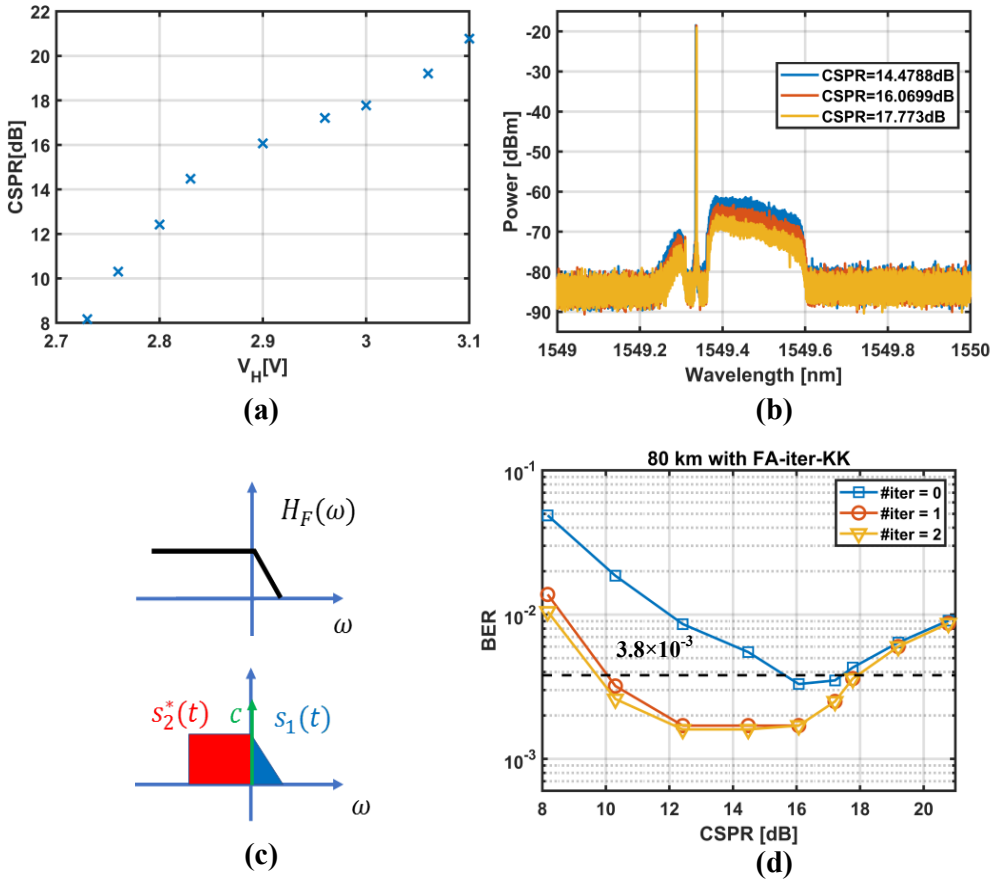

Fig. 4.13 (a) Relations between measured CSPRs and the DC voltages applied to the thermal phase shifter, (b) VSB spectra with different CSPRs, (c) definitions of filter response, LSB and RSB signals used in the FA-iter-KK algorithm when applied to a VSB system that suppresses the RSB spectrum and (d) BERs of 28 Gbaud 16QAM at 80 km as functions of CSPR values when processed with the FA-iter-KK algorithm with different number of iterations. [Adapted] with permission from [37] © The Optical Society.

Keen readers may have noticed from Fig. 4.13(b), that, in this experiment, the optical filter suppresses the RSB spectrum rather than the LSB spectrum, which is different from the situation described in section 4.3. But note that if we use the definitions of $H_F(\omega)$, $s_2^*(t)$ and $s_1(t)$ shown in Fig. 4.13(c), then Eqs. 4.3-4.15 still hold, which means the FA-iter-KK algorithm and the generalized CD compensation block can be used directly in this experiment without modifications.

Fig. 4.13(d) shows the BER performance of 28 Gbaud 16QAM transmissions over 80 km as functions CSPR values. The launched power and the ROP are optimized to 8 dBm and 7 dBm, respectively. As we have explained in section 4.3, if we use 0 iteration in the FA-iter-KK algorithm, we directly use the initial guess $Re\{s_1[n]\} + Re\{s_2[n]\} = \sqrt{I[n]} - C$ as the input of the generalized CD compensation block.

Fig. 4.13(d) shows that, compared to the 0-iteration case, adding 1 iteration in the FA-iter-KK algorithm reduces the optimal CSPR value and significantly improves the best achievable BER performance. But further increasing the number of iterations only achieves marginal performance improvement. By using only 1 iteration, when the CSPR is in the range of 12-16 dB, a BER of 1.7×10^{-3} can be achieved, which is below the HD-FEC threshold of 3.8×10^{-3} with an overhead of 6.7%. We also observe that, for small CSPR values, there is a relatively large gap between the curves related to the 0-iteration and the 1-iteration cases, because the performance of the self-coherent system is mainly limited by the SSBI when the CSPR is small, and using 1 iteration to improve the estimation accuracy of $Re\{s_1[n]\} + Re\{s_2[n]\}$ can efficiently mitigate the impact of the SSBI. On the other hand, when the CSPR is large, all the three curves in Fig. 4.13(d) converge. This is because as we increase the CSPR, we launch more light into the carrier path, hence the signal power is inevitably reduced. As a result, the carrier-less SNR is reduced, and the system is predominantly limited by the noise rather than the SSBI, thus the BER performance improvement achieved by the FA-iter-KK algorithm becomes marginal. Our observations further confirm that the CSPR needs to be optimized in practical systems for specific link conditions and DSP choices.

4.4.4 Summary

In this work, we demonstrate a SiPh VSB self-coherent transmitter circuit with on-chip CSPR control capability. The tunable power splitter based solution removes the need of a VOA from a conventional parallel carrier path scheme, which enables CSPR tuning without adjusting the modulator's bias point or sacrificing the DAC's output levels for digital carrier generation. By carefully adjusting the CSPR using our device, we achieve a 112 Gb/s 16QAM transmission over 80 km at a BER below the 6.7% overhead HD-FEC threshold.

Chapter 5 Towards loss limited SSB/VSB systems

5.1 Overview

As we have mentioned in Chapter 1, section 1.2, the future of the SSB/VSB self-coherent system lies in loss limited links over 40 km. To better understand the potentials and the limits of unamplified SSB and VSB self-coherent systems when implemented in practice, we build parameterized numerical models to estimate the transmission performance and the power consumption of such systems. Specially, in this chapter, we will focus on the following two topics:

1) which CSPR control method should we use in a loss limited SSB/VSB system?
2) which KK-family algorithm should we use in a loss limited SSB/VSB system considering the trade-off between the achievable performance and the system's power consumption?

The results will be presented in sections 5.2 and 5.3, respectively.

5.2 On CSPR control schemes in loss limited self-coherent systems

5.2.1 Motivation

In Chapter 4, section 4.4, we have introduced a tunable power splitter based parallel path structure to control the CSPR in an SSB/VSB self-coherent system, and we said that this scheme can reduce the modulator's device nonlinearity since it decouples the control of the CSPR and the control of the modulator's bias point.

One thing we didn't say in section 4.4 is that, even though we can use a tunable coupler to avoid wasting optical power at the VOA, the parallel path structure based scheme still has higher optical loss at the transmitter compared to the bias tuning scheme. This is because in the parallel path structure, we need a 50/50 coupler to combine the outputs of the carrier path and the signal path. After modulation, the carrier and the signal do not overlap with each other in the frequency domain. As a result, the 50/50 coupler at the output of the parallel path structure will introduce 3 dB loss to both the carrier and the signal. Moreover, the parallel path structure

adds some extra components including three 50/50 couplers (three MMIs), a thermal phase shifting section, and a plain waveguide (which serves as the carrier path), and these components also have their own excess losses.

As we have mentioned in section 1.2, ever since the release of the 400 ZR IA [4], the amplified version of the 400 ZR solution is going dominate the inter-data center connection market over 80-120 km, and the future of the SSB/VSB self-coherent systems lies in unamplified loss limited links with shorter reaches (e.g. 40 km). The additional optical loss at the transmitter may not be a problem in a noise limited system, since the EDFA (operating in the constant output power mode) can compensate for the loss (hence the optimum ROP can always be achieved). But it is a problem in a loss limited system, since the higher optical loss at the transmitter will reduce the achievable ROP, which will degrade the transmission performance. A question then arises: is the parallel path structure based scheme really better than the bias tuning scheme in a loss limited system? In this section, we are going to answer this question through numerical simulations, and this time we will consider both the IQ modulator based SSB system and the VSB system.

5.2.2 Link models of loss limited IQ modulator based SSB systems

Fig. 5.1 illustrates the link model of a loss limited IQ modulator based SSB self-coherent system, in which the CSPR is controlled by tuning the bias point of the modulator. The link model consists of two parts:

1) a transmission model which tracks the complex-valued time-domain waveform and the SNR at the input and output of each component, as shown in Fig. 5.1(b),
2) an optical power budget model which tracks the optical power at the input and output of each component, as shown in Fig. 5.1(c).

These two parts are mutually coupled. As we can see from Fig. 5.1(b) and 5.1(c), the transmission model requires the launch power and the ROP from the optical power budget model to determine the fiber nonlinearity and the impact of the receiver noise, and the optical power budget model requires the field information of the output signals of the MZMs from the transmission model to determine the modulation loss and compute the launch power.

Now we take a deeper look at the transmission model. Except for the laser phase noise, all the other noise sources are modelled as AWGN sources. The laser phase noise is modelled as a Wiener process (please refer to section 2.3.2.2 for more information).

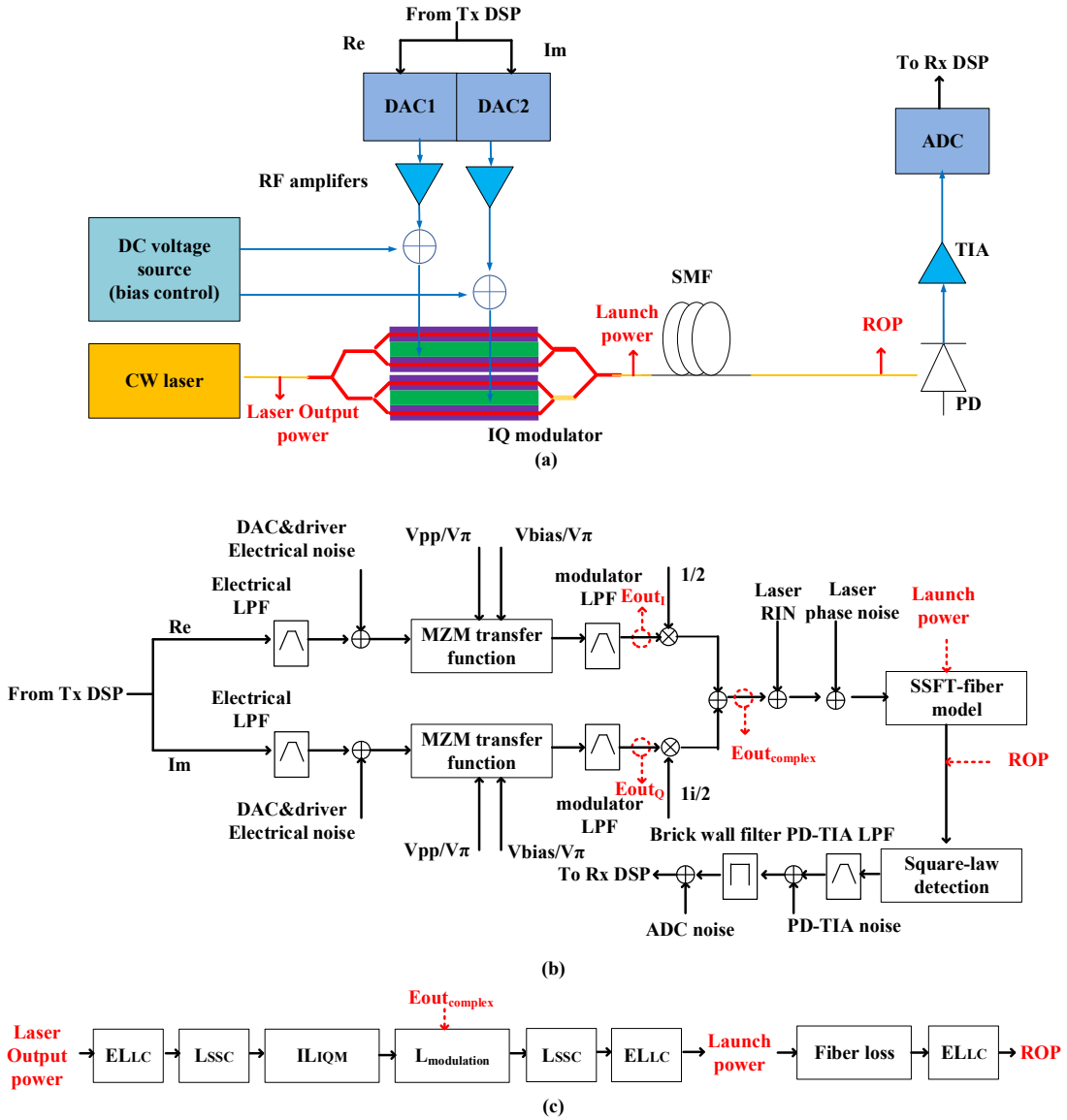

Fig. 5.1 Link model of a loss limited IQ modulator based SSB self-coherent system in which the CSPR is controlled through bias tuning. (a) The schematic of the system, (b) the transmission model and (c) the power budget model.

Each low-pass filter (LPF) is modelled as a super-Gaussian function, whose amplitude response is given by:

$$H_{LPF}(f) = \exp\left(-\frac{\ln 2}{2}\left(\frac{f}{B}\right)^{2d}\right) \tag{5.1}$$

where B is the 3 dB bandwidth, and d is the order of the function. Note that here d does

not need to be an integer. By simultaneously adjusting B and d, we can use Eq. 5.1 to approximate almost all the frequency responses of the electrical/electro-optical/opto-electrical devices considered in this work. One exception is the ADC channel, whose frequency response is modelled as a brick-wall filter, because the frequency response of the ADC channel in our lab (the RTO channel) is almost flat-top up to its cut-off frequency, and the signal above the cut-off frequency is attenuated by more than 30 dB.

In this model, we treat the cascade of a DAC channel and a RF amplifier as an integrated part (hereafter known as an "RF chain"), which is modelled as a single LPF followed by a single AWGN source.

The IQ modulator consists of two child-MZMs, a phase shifter, and two 50/50 couplers at the input and the output of the parent interferometer. We assume that the phase difference between the in-phase branch and the quadrature branch is strictly $\pi/2$, and the two child-MZMs are identical, which are driven by two RF signals with the same peak-to-peak voltages. The MZM's transfer function is modelled as a sinusoid function. The optical field at the output of the child-MZM in the in-phase branch or the quadrature branch can be expressed as:

$$E_{outI,Q}(t) = \sin\left(\frac{\pi}{2}\left(\frac{V_{inI,Q}(t)}{\max\left(\left|V_{inI,Q}(t)\right|\right)}\frac{V_{pp}}{2V_{\pi}} + \frac{V_{bias}}{V_{\pi}}\right)\right) \tag{5.2}$$

where $V_{inI,Q}(t)$ is a real-valued driving voltage signal generated from the RF chain, V_{pp} is the peak to peak driving voltage, V_{bias} is a DC voltage that is used to control the bias point of the MZM, and V_{π} is the half-wave voltage of the MZM. We assume that the MZM uses the single-drive push-pull structure [44], i.e. with a single driving input, each arm of the MZM is driven with half of the bus voltage in a push-pull fashion, hence we don't need to include the modulation-induced chirp term in Eq. 5.2. For each combination of $(V_{pp}/V_{\pi}, V_{bias}/V_{\pi})$, we can estimate the modulation loss of the IQ modulator using the following equation:

$$L_{modulation} = -20\log_{10}\left(\left|\frac{1}{2}E_{outI}(t) + \frac{i}{2}E_{outQ}(t)\right|\right)\ [dB] \tag{5.3}$$

where $E_{outI}(t)$ and $E_{outQ}(t)$ are the optical fields at the outputs of the two child-MZMs in the in-phase branch and the quadrature branch, which are computed using Eq. 5.2. Note that Eq. 5.3 has already considered the optical loss caused by the quadrature combination process

in the IQ modulator's parent interferometer. The estimated modulation loss is then used in the optical power budget to compute the total optical loss of the transmitter and the launch power, as we can see in Fig. 5.1(c).

Next, we add the laser intensity noise and phase noise. Then the optical waveform is launched into the fiber, which is modelled using the split-step-Fourier-transform (SSFT) method [18]. After the fiber, the receiver-side optical waveform is detected by a PD-TIA. The PD-TIA model consists of a square-law detection block, an LPF, and an AWGN source. Then we use a brick-wall filter and another AWGN source to emulate the frequency response and the noise of the ADC channel. Note that if the noise is added at the transmitter, it will be attenuated together with the carrier and the signal by the losses of the fiber and the link components, but if the noise is added at the receiver, it will not be attenuated. Therefore, in a loss limited system, when we add the receiver-side noises (the PD-TIA noise and the ADC noise in this case) in the transmission model, we cannot directly set the SNR values as we do with the transmitter-side noise sources. Instead, we need to set the absolute value of the noise power. For instance, in this model, we set the noise equivalent power (NEP) of the PD-TIA, which determines the RMS voltage of the PD-TIA noise given the responsivity of the PD and the transimpedance gain of the TIA. Then we use the ROP estimated from the optical power budget model to compute the signal power in the electrical domain, and the electrical SNR can be computed accordingly.

To incorporate the parallel path structure in the IQ modulator based SSB self-coherent system, we need to modify the link model shown in Fig. 5.1 into the model shown in Fig. 5.2. The differences between these two models are highlighted in purple.

Note that here we assume that the length of the carrier path can be properly designed to match the delays introduced by the two paths in the parallel path structure, hence we can first generate the combination of an electrical noise contaminated modulated signal and a clean optical carrier, and then add the laser intensity noise and the laser phase noise as shown in Fig. 5.2(b). When the parallel path structure is used, the modulator is always biased at the null point. To add the carrier in the transmission model, we need to know the CSPR, which needs to be computed

using the optical power budget model as shown in Fig. 5.2(c).

In this work, we assume that the parallel path structure (or the IQ modulator in the bias tuning case) is implemented on the InP platform (and we will explain why we don't consider the SiPh platform later in section 5.2.3). Table 5.1 lists all the system parameters that are used in the link models shown in Fig. 5.1 and Fig. 5.2.

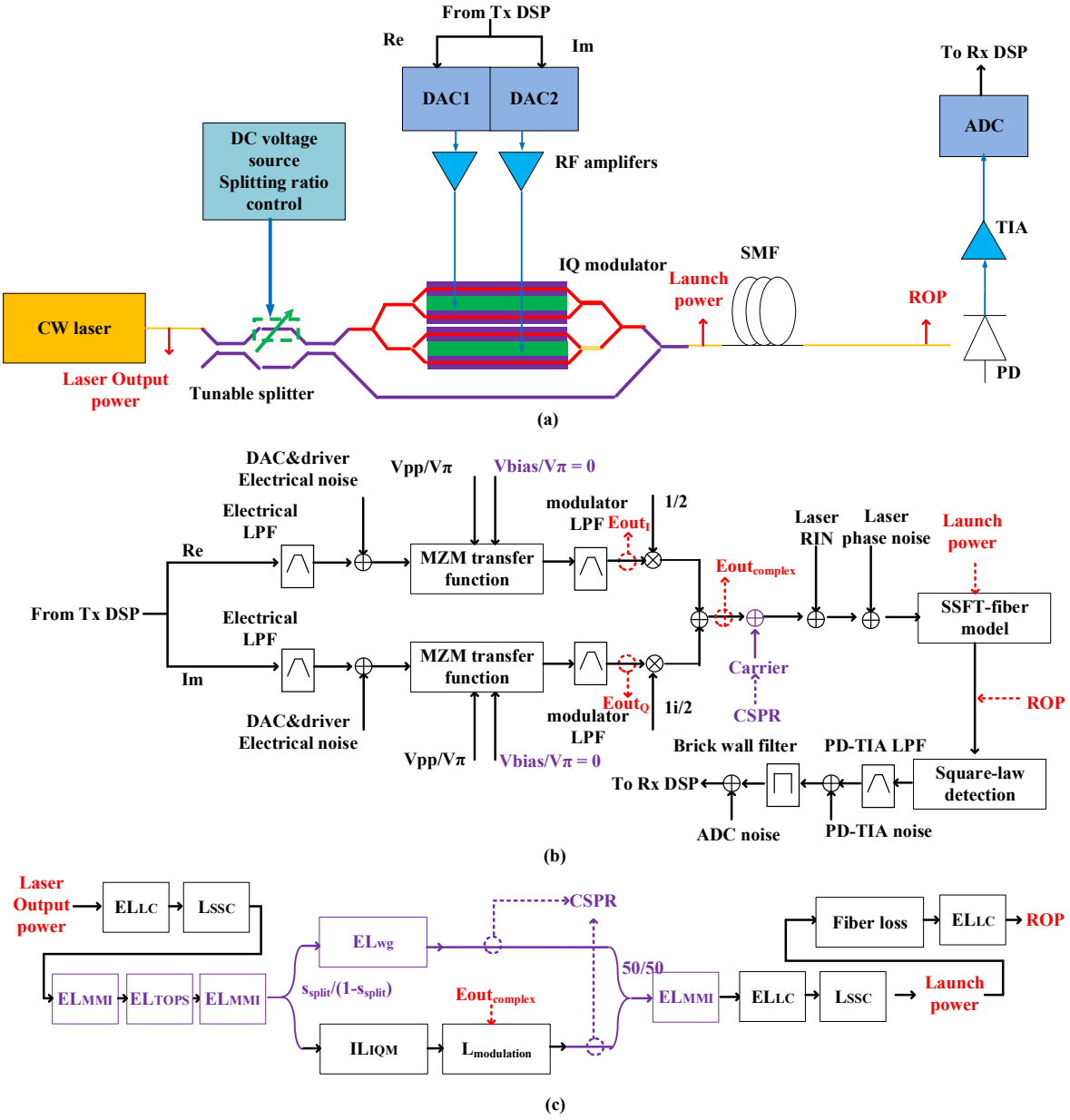

Fig. 5.2 Link model of a loss limited IQ modulator based SSB self-coherent system in which the CSPR is controlled through the tunable power splitter based parallel path structure. (a) The schematic of the system, (b) the transmission model and (c) the power budget model.

Table 5.1 Parameters used in the link models of the loss limited IQ modulator based SSB self-coherent systems

Block	Symbol	Comment	Value
RF chain (DAC and RF amplifier) [a]	B_{RF}	3 dB bandwidth of the super-Gaussian LPF	12 GHz
	d_{RF}	Order of super-Gaussian filter LPF	0.6
	SNR_{RF}	Signal to noise ratio of the RF chain	30 dB
	R_{DAC}	Sampling rate of the DAC	64 GSa/s
IQ modulator [101]	B_{MZM}	3 dB bandwidth of the super-Gaussian LPF	44 GHz
	d_{MZM}	Order of super-Gaussian filter LPF	6
	IL_{IQM}	Insertion loss of the IQ modulator [b]	6 dB
	L_{SSC}	Total loss of the spot-size converter (SSC): the sum of the coupling loss and the excess loss of the SSC [102]	2 dB/facet
	V_{bias}/V_{π}	V_{bias}/V_{π} ratio to control the MZM's bias point	To be optimized
	V_{pp}/V_{π}	V_{pp}/V_{π} ratio to control the depth of modulation	To be varied
Tunable coupler [103]	s_{split}	Splitting ratio of the input coupler in the parallel path structure [c]	To be varied
	EL_{MMI}	Excess loss of the MMI	0.5 dB
	EL_{wg}	Excess loss of the carrier path (plain waveguide)	0.1 dB
	EL_{TOPS}	Excess loss of the thermal-optic phase shifting section (<1 mm)	0.2 dB
Laser	P_{las}	Output optical power of the laser	16 dBm
	Δv_{las}	Laser linewidth [4]	1 MHz
	RIN_{las}	Relative intensity noise of the laser [4]	-140 dBc/Hz
	λ_{las}	Central wavelength of the laser [d]	1550 nm
Connector [104]	IL_{LC}	Insertion loss of the LC type fiber connector	0.3 dB/connector
SMF-28 ultra Fiber [7]	$\lambda_{D,SMF}$	Zero-dispersion wavelength [d]	1310 nm
	$S_{0,SMF}$	Zero-dispersion slope [d]	0.089 ps/(nm^2·km)
	α_{SMF}	Attenuation coefficient of SMF in the C-band	0.2 dB/km
	$D_{MFD,SMF}$	Mode-field diameter of the SMF [e]	10.4 μm
	$n_{2,SMF}$	Nonlinear index of the fiber [e]	2.6e-20 m^2/W
	L_{SMF}	Length of the fiber	40 km
	N_{SSFT}	Number of blocks used in the SSFT method	4
PD-TIA [105]	B_{Rx}	3 dB bandwidth of the super-Gaussian LPF	37 GHz
	d_{Rx}	Order of super-Gaussian filter LPF	2.3
	CG_{Rx}	Conversion gain of the PD-TIA	724 V/W
	NEP	Noise equivalent power of the PD-TIA	3.4 μW
ADC [a]	B_{ADC}	Cut-off frequency of the ADC channel	32 GHz
	$S_{noise,ADC}$	Power spectral density of the noise from the ADC	-149.5 dBm/Hz
	R_{ADC}	Sampling rate of the ADC channel	64 GSa/s

[a] Values estimated based on our lab experience.

[b] Estimated by subtracting the total loss of two SSCs from the fiber-to-fiber insertion loss of the IQ modulator module (at 1550 nm). The fiber-to-fiber insertion loss is measured when all the MZI structures (including the parent interferometer) are biased at the maximum transmission point.

[c] Defined as the power launched into the carrier path divided by the power launched into the signal path

[d] Dispersion coefficient is calculated using Eq. 2.7 (section 2.3.2.1).

[e] Effective nonlinear coefficient is calculated using $\gamma_{SMF} = \frac{8}{9}\frac{2\pi}{\lambda_{las}}\frac{n_{2,SMF}}{A_{eff,SMF}}$, and $A_{eff,SMF} = \frac{1}{4}\pi D_{MFD,SMF}^2$ [18].

5.2.3 On CSPR control schemes in a loss limited IQ modulator based SSB system

Now we have the link models of two loss limited IQ modulator based SSB self-coherent systems which use two different CSPR control schemes, i.e. the bias tuning scheme and the parallel path structure based scheme. In this section, we are going to compare the best achievable transmission performance of these two systems.

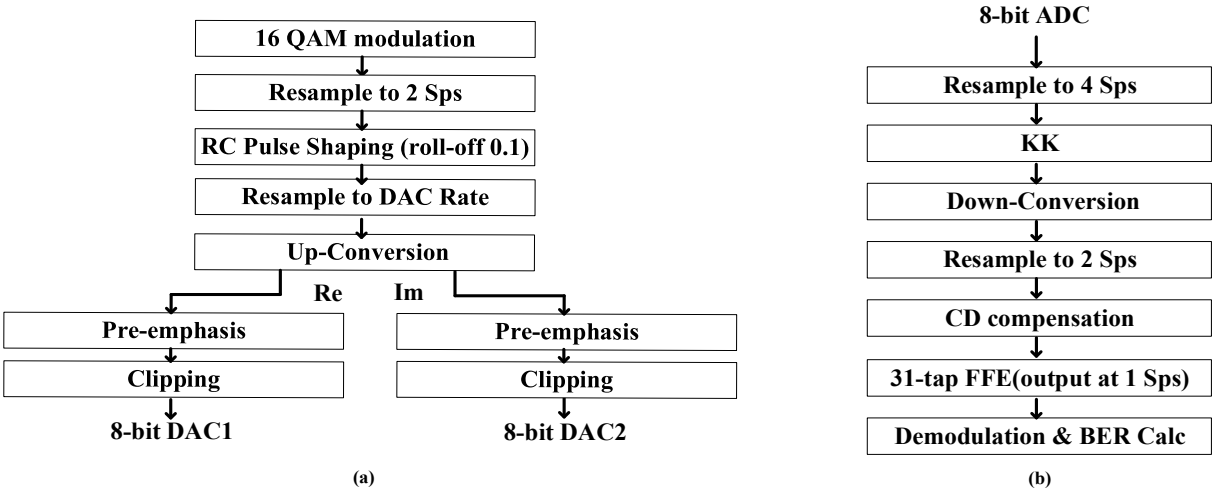

Fig. 5.3 (a) Transmitter and (b) receiver DSP stacks used in the link models shown in Figs. 5.1 and 5.2.

In each system, we transmit a 28 Gbaud passband 16QAM signal (which corresponds to a net rate of 112 Gb/s) with a guard band of 0.6 GHz[15] over 40 km of SMF. We use the same DSP stacks in both systems. The DSP stacks are shown in Fig. 5.3. The pre-emphasis in the transmitter DSP is a 51-tap FFE that flattens the overall frequency response of the DAC channel and the RF amplifier, and the rest part of the ISI is handled in the receiver DSP. In this work, we are only interested in the impacts of the choice of the CSPR control scheme on the

[15] For now, please just accept this value. We will explain why we choose this value in section 5.3.5.

achievable transmission performance, hence we use sufficiently large sampling rate (4 Sps) for the KK algorithm in the receiver DSP to make sure that the sampling rate does not limit the performance.

We first consider two special cases, where we have 1) $V_{pp}/V_{\pi} = 0.5$, and 2) $V_{pp}/V_{\pi} = 1$. Fig. 5.4 plots the effective SNRs (defined in Eq. 5.3) and the total optical loss of the transmitter circuit (which includes the modulation loss, the insertion loss of the modulator, the additional loss introduced by the parallel path structure, the insertion loss of the two SSCs and the coupling loss at the two SSCs) as functions of the CSPR in these two cases when using different CSPR control schemes in the system.

The red curves in Fig. 5.4 show that, given a fixed V_{pp}/V_{π}, if we increase the CSPR, we can decrease the transmitter's optical loss regardless of the choice of the CSPR control scheme. Likewise, given a fixed CSPR, if we increase V_{pp}/V_{π}, we can also decrease the transmitter's optical loss regardless of the choice of the CSPR control scheme. Keep in mind that in a loss limited system, since the laser's output power is fixed, a higher transmitter loss will always lead to a lower ROP.

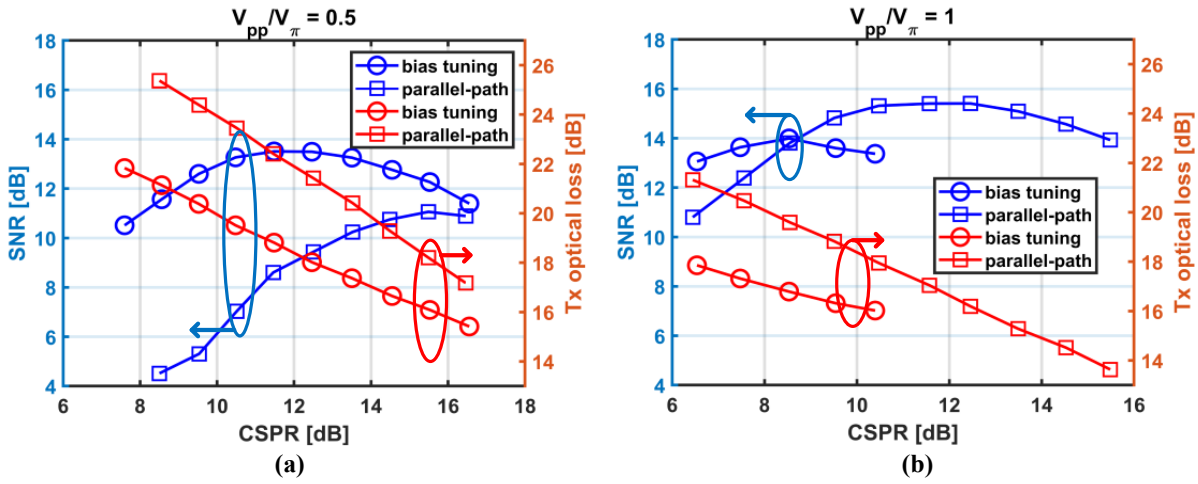

Fig. 5.4 Effective SNRs and the total optical loss of the transmitter circuit as functions of the CSPR when using different CSPR control schemes and a peak-to-peak driving voltage of (a) $0.5V_{\pi}$ and (b) V_{π} in an IQ modulator based SSB system.

Now we study the $V_{pp}/V_{\pi} = 0.5$ case. As we can see from Fig. 5.4(a), when we use the bias tuning scheme, the optimum CSPR is ~12 dB, and the corresponding total loss of the transmitter circuit is ~18 dB. We also confirm that introducing the parallel path structure does

increase the optical loss at the transmitter. When we switch from the bias tuning scheme to the parallel path structure based scheme, the transmitter loss at the CSPR of 12 dB is increased to 22 dB. Note that the power of the receiver-side noise in our model is independent of the ROP, and according to the square-law detection rule, the power of the electrical-domain signal after photodetection is proportional to the beating of the carrier and the signal. If the total power of the carrier and the signal (i.e. the ROP) is fixed, then increasing the CSPR will reduce this beating term. However, as we increase the CSPR, the ROP is also increased. Therefore, increasing the CSPR within a certain range may increase the ratio of the receiver-side electrical signal power to the receiver-side noise power, hence may improve the transmission performance. That's why the optimum CSPR in the parallel path structure based system is increased to ~15.5 dB, which corresponds to a transmitter loss of ~18 dB. But the CSPR cannot be too large either. As we keep increasing the CSPR and the ROP, at some point, when the ROP is sufficiently large, the impact of the receiver-side noise on the transmission performance becomes weak, and the impact of the transmitter-side noise becomes dominant. In this case, further increasing the ROP may not improve the overall SNR, since increasing the CSPR would also decrease the signal to laser intensity noise ratio[16]. Therefore, there is always an optimum CSPR no matter which CSPR control scheme we use, and the higher optical loss of the parallel path structure based scheme leads to a larger optimum CSPR. We find that if we have $V_{pp}/V_{\pi} = 0.5$, the best achievable effective SNR (at the optimum CSPR) of the parallel path structure based scheme is lower than that of the bias tuning scheme.

What about the $V_{pp}/V_{\pi} = 1$ case? In this case, when we use the bias tuning scheme, although the transmitter loss is reduced compared to the $V_{pp}/V_{\pi} = 0.5$ case, the maximum effective SNR achieved at the optimum CSPR is not increased. This is because when the V_{pp}/V_{π} is larger, the modulation depth is larger. In addition, if we want to achieve the same CSPR, we need to move the bias point further away from the linear regime of the MZM's transfer function.

[16] Because both the carrier and the signal suffer from the laser intensity noise, increasing the CSPR means increasing power launched into the carrier path and reducing the power launched into the signal path, thus the signal power is reduced, but the laser intensity noise power is increased (since the carrier path experiences less loss than the signal path).

As a result, the device nonlinearity from the modulator is significantly increased, which cancels the gain that can be achieved by increasing the ROP. Note that normally we need to guarantee that $V_{bias} + V_{pp}/2 \leq V_{\pi}$, otherwise Eq. 5.2 is no longer a monotonic function of the input signal $V_{inI,Q}(t)$. Consequently, there is an additional constraint on the tunable range of the CSPR in the bias tuning scheme when V_{pp}/V_{π} is large. Specifically, in this case, we have $V_{pp}/V_{\pi} = 1$, hence V_{bias}/V_{π} should not be greater than 0.5, and the CSPR should not exceeds 10.4 dB. On the other hand, if we use the parallel path structure based scheme, as we increase V_{pp}/V_{π} from 0.5 to 1, the system can benefit from the reduced transmitter's optical loss, but the device nonlinearity is not significantly increased, since the modulator is always biased at the null point. As a result, the optimum CSPR value is reduced from 15.5 dB to 11.5 dB, and the maximum achievable effective SNR (at the optimum CSPR) of the parallel path structure based scheme is lower than that of the bias tuning scheme.

In short, when $V_{pp}/V_{\pi} = 0.5$, the bias tuning scheme is better than the parallel path structure based scheme, but when $V_{pp}/V_{\pi} = 1$, the parallel path structure based scheme is better than the bias tuning scheme. In other words, there must be a cross point, at which the two CSPR control schemes achieve similar performance.

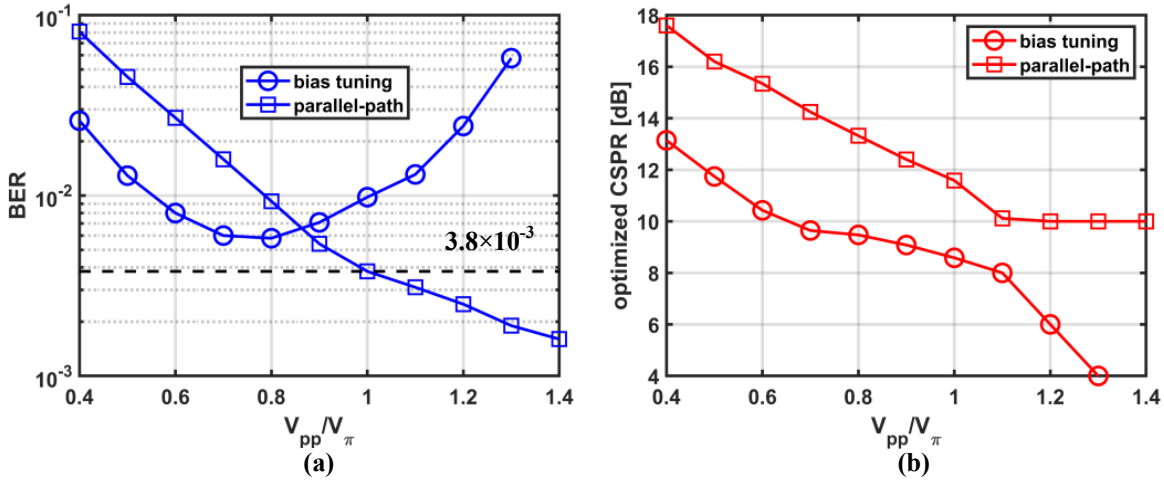

Fig. 5.5 (a) The achievable BERs at the optimum CSPR and (b) the optimum CSPR as functions of V_{pp}/V_{π} when using different CSPR control schemes in an IQ modulator based SSB system.

Fig. 5.5(a) plots the best BERs that can be achieved at the optimum CSPR when using different CSPR control schemes as functions of V_{pp}/V_{π}, and Fig. 5.5(b) plots the optimum CSPRs

against V_{pp}/V_{π}. The sudden decrease of the optimum CSPR in the bias tuning case is because we enforce $V_{pp}/2 + V_{bias} \leq V_{\pi}$ to guarantee that the MZM's transfer function is monotonic, which limits the maximum achievable CSPR.

As we can see from Fig. 5.5, the bias tuning scheme achieves its best performance when $V_{pp}/V_{\pi} = 0.7$. On the other hand, if we use the parallel path structure based scheme, as we increase V_{pp}/V_{π} from 0.4 to 1.3, the best achievable BER is always decreasing. The cross point occurs at V_{pp}/V_{π} = 0.85, i.e. when V_{pp}/V_{π}>0.85, the parallel path structure based scheme starts to outperforms the bias tuning scheme in our system. We also note that, as long as the maximum achievable V_{pp}/V_{π} is larger than 1[17], by simultaneously optimizing V_{pp}/V_{π} and CSPR, the best achievable BER (over the tunable range of $V_{pp}/V_{\pi} \in$(0.4,1.4)) of the parallel path structure based scheme is lower than that of the bias tuning scheme. In other words, in order to achieve the best transmission performance in a loss limited IQ modulator based SSB self-coherent system with the systems parameters listed in Table 5.1, if the maximum achievable V_{pp}/V_{π} is less than 1, we should use the parallel path structure based scheme, otherwise we should use the bias tuning scheme.

Based on our lab experience, when we use an RF chain with the specifications shown in Table 5.1, after applying the transmitter DSP as shown in Fig. 5.3(a), the maximum achievable V_{pp} is around 2.5 V [106]. A typical InP IQ modulator with an insertion loss of ~6 dB (excluding the coupling loss and the excess loss of the SSCs) and a 3dB electro-optical bandwidth of >40 GHz has a V_{π} of 1.3 – 2 V [107]-[109]. Therefore, if we use the InP platform at the transmitter, a $V_{pp}/V_{\pi} > 1$ is achievable, and based on our discussions above, we should use the parallel path structure based CSPR control scheme.

On the other hand, a state-of-the-art SiPh IQ modulator with a similar 3 dB electro-optical bandwidth (~37 GHz) and an insertion loss (excluding the coupling loss and the excess loss of the edge couplers) of 5.6 dB has a V_{π} of 6.3 V [110]. When using the RF chains considered in

[17] The maximum achievable V_{pp} means the V_{pp} achieved when the DAC is the used up to its maximum swing and the RF amplifier is operating with its maximum gain. Note that we can easily reduce the V_{pp} from its maximum value by 1) reducing the gain of the RF amplifier, 2) adding RF attenuators or 3) using less DAC levels.

this model, the maximum achievable V_{pp}/V_{π} is ~0.4. As we can see in Fig. 5.5, if $V_{pp}/V_{\pi} = 0.4$, neither of the two CSPR control schemes can achieve a BER that is below the 6.7 % overhead HD-FEC threshold of 3.8×10^{-3} in our system, and further reducing V_{pp}/V_{π} will only degrade the BER peformance. Hence, we don't consider the SiPh platform in this system.

5.2.4 Link models of loss limited VSB systems

Similarly, we can repeat the analysis above in a VSB self-coherent system. Again, we start with the link models. By switching from an IQ modulator based SSB system to a VSB system, we should modify the link models shown in Fig. 5.1 and Fig. 5.2 into the models shown in Fig. 5.7 and Fig. 5.8, respectively. The modified parts are highlighted in green.

Firstly, the two RF chains and the IQ modulator are replaced by a single RF chain and a single MZM. But the specifications of the RF chain and the MZM are not changed. The MZM used in Fig. 5.1(Fig. 5.2) is identical to a child-MZM of the IQ modulator used in Fig. 5.7(Fig. 5.8), and the insertion loss of the MZM is estimated by subtracting the total excess loss of two MMIs from the insertion loss of the IQ modulator, i.e. $IL_{MZM} = IL_{IQM} - 2EL_{MMI}$, because now we can remove the parent interferometer structure in the IQ modulator. The modulation loss is now estimated as:

$$L_{modulation} = -20\log_{10}(|E_{out}(t)|)\ [dB] \tag{5.4}$$

where $E_{out}(t)$ is the optical field at the output of the MZM computed from Eq. 5.2.

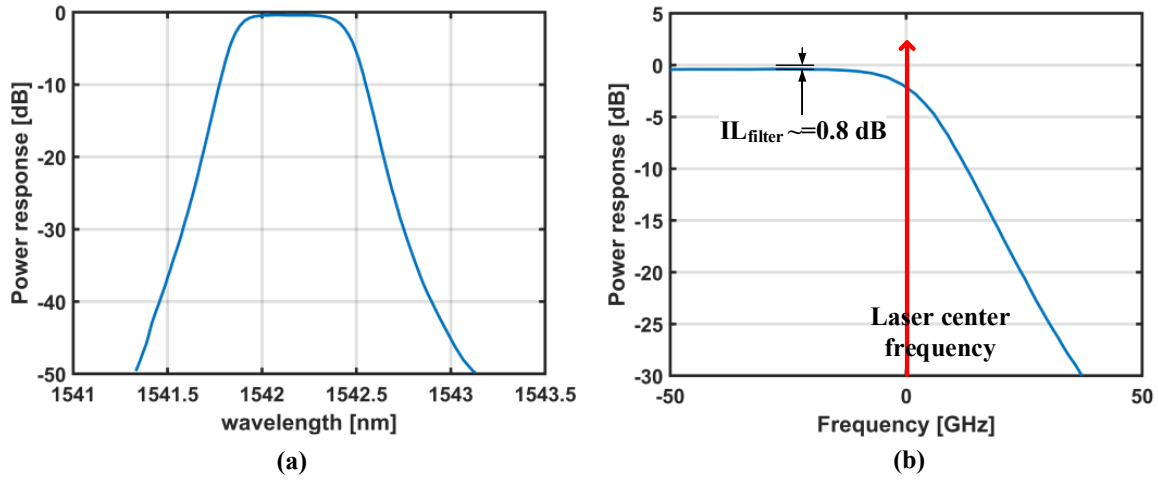

Fig. 5.6 (a) Frequency response of a commercialized optical filter, and (b) zoom-in of the region used for VSB filtering.

Secondly, an optical filter is inserted before the PD-TIA. In this work, we consider using a commercial product from Lumentum [111], whose frequency response is shown in Fig. 5.6. This filter has an insertion loss of around 0.8 dB in the passband (excluding the loss of the fiber connectors), the flat-top passband is wider than 32 GHz, and the sharper edge has an edge gradient of around 8 dB/10 GHz.

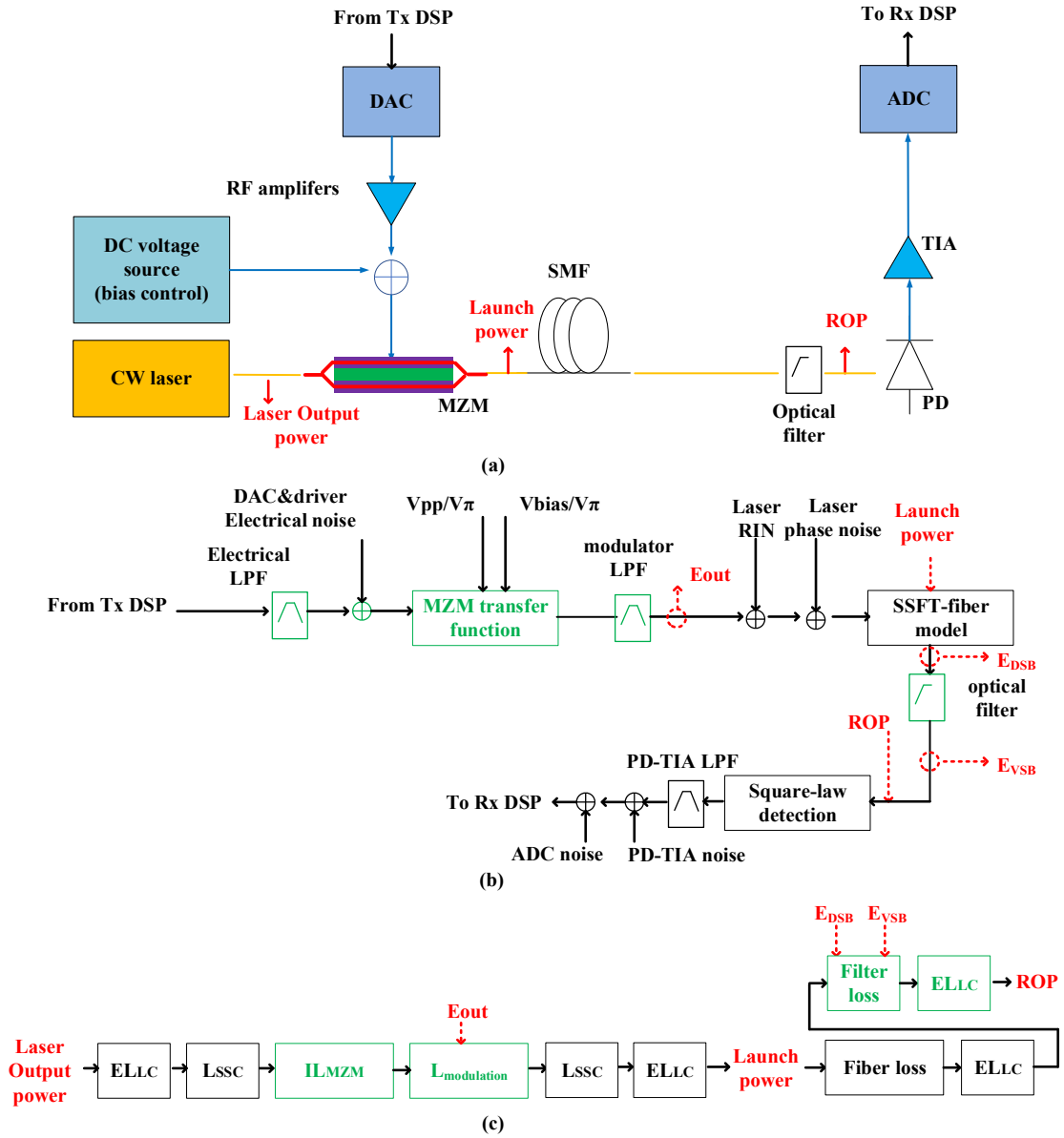

Fig. 5.7 Link model of a loss limited VSB self-coherent system in which the CSPR is controlled through bias tuning. (a) The schematic of the system, (b) the transmission model and (c) the power budget model.

We note that the filter has a round corner at the start of the edge slope, i.e. the gradient at the start of the edge slope is less than 8 dB/10 GHz. Hence in practice, we need to properly adjust the center wavelength(frequency) of the laser as shown in Fig. 5.6(b), such that the sideband

to be suppressed sees a relatively sharp filter response, but the carrier and the sideband to be kept don't experience a large optical loss.

Since the loss introduced by the optical filter is frequency dependent, it is estimated by subtracting the power of the VSB signal after the filter from the power of the DSB signal before the filter using the transmission model (Fig. 5.7(b) or Fig. 5.8(b)). The insertion loss of the optical filter has already been included in the filter response, but note that the use of an optical filter also adds an extra fiber connector to the system, hence in the power budget model, we need to add the excess loss of this additional LC connector.

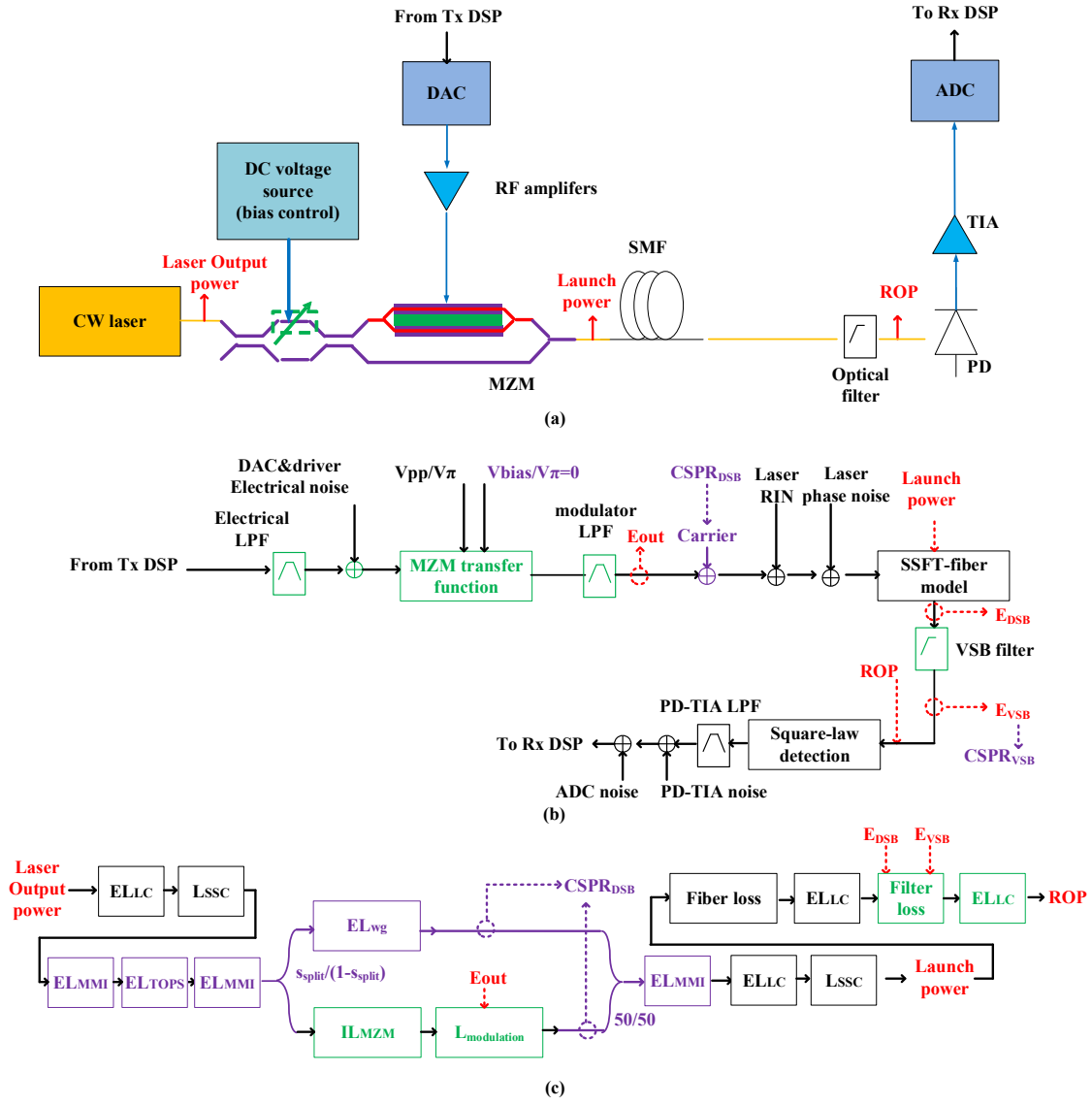

Fig. 5.8 Link model of a loss limited VSB self-coherent system in which the CSPR is controlled through the tunable power splitter based parallel path structure. (a) The schematic of the system, (b) the transmission model and (c) the power budget model.

The transmitter now generates a DSB signal since it uses only one RF chain and one MZM. Consequently, if the parallel path structure is used, the splitting ratio of the tunable coupler now determines the carrier to DSB signal power ratio ($CSPR_{DSB}$). $CSPR_{DSB}$ can still be used to determine the carrier power in the transmission model, but note that the counterpart of the CSPR in the IQ modulator based system should be the carrier to VSB signal power ratio ($CSPR_{VSB}$), which needs to be computed after the optical filter in the transmission model.

5.2.5 On CSPR control schemes in a loss limited VSB system

Now we can compare the transmission performance of two loss limited VSB systems with different CSPR control schemes using the link models shown in Fig. 5.7 and Fig. 5.8. In this study, we still consider a 28 Gbaud passband 16QAM signal with a guard band of 0.6 GHz and a fiber length of 40 km. The DSP stacks are shown in Fig. 5.9.

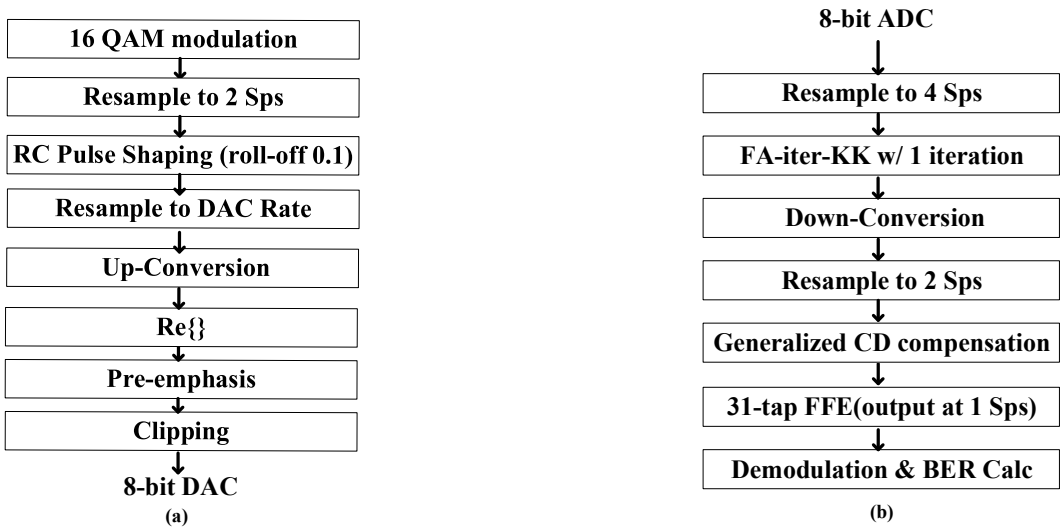

Fig. 5.9 Transmitter and receiver DSP stacks used in the link models shown in Figs. 5.7 and 5.8.

There is only one DAC channel in a VSB system, hence in the transmitter DSP, we only keep the real part of the complex waveform at the output of the up-conversion block. The optical filter has a limited edge gradient, hence in the receiver DSP, as we did in section 4.3, we use the FA-iter-KK algorithm with 1 iteration and the generalized CD compensation algorithm to replace the KK algorithm and the conventional CD compensation algorithm.

Fig. 5.10(a) plots the achievable BERs at the optimum CSPR as functions of V_{pp}/V_{π} when using different CSPR control schemes in a VSB system, and Fig. 5.10(b) plots the optimum

CSPRs versus V_{pp}/V_{π}. Again, in the bias tuning scheme, we add the constraint $V_{pp}/2 + V_{bias} \leq V_{\pi}$ to make sure that the MZM's transfer function is a monotonic function of the input voltage signal, which limits the maximum achievable CSPR and results in a sudden decrease of the optimum CSPR in Fig. 5.10(b) when $V_{pp}/V_{\pi} > 1.1$.

Similar to what we have observed in an IQ modulator based SSB system in section 5.2.3, in a VSB system, when V_{pp}/V_{π} is small, the bias tuning scheme achieves better transmission performance than the parallel path structure based scheme, but when V_{pp}/V_{π} is larger than 0.95, the parallel path structure base scheme is better than the bias tuning scheme.

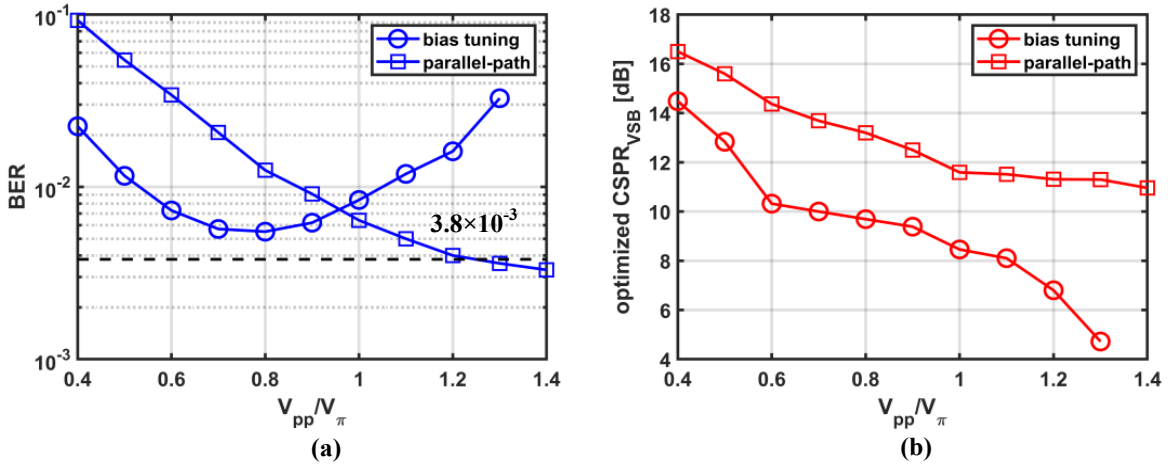

Fig. 5.10 (a) The achievable BERs at the optimum CSPR and (b) the optimum CSPR as functions of V_{pp}/V_{π} when using different CSPR control schemes in a VSB system.

We also note that as long as the maximum achievable V_{pp}/V_{π} is larger than 1.1, the best BER performance that can be achieved over the entire tunable range of V_{pp}/V_{π} by using the parallel path structure based scheme is lower than that of the bias tuning scheme. Based on our discussions in section 5.2.3, if we use the InP platform to implement the transmitter circuit, a $V_{pp}/V_{\pi} > 1.1$ is achievable, hence we should use the parallel path structure based CSPR control scheme to achieve better BER performance, but if we use the SiPh platform, neither of the two CSPR control methods and achieve a BER that is below the 6.7% overhead HD-FEC threshold.

5.2.6 Summary

Now we can answer the question that we asked at the end of section 5.2.1. Is the parallel path

structure based scheme better than the bias tuning scheme in a loss limited SSB/VSB system? It depends on the system parameters. If the system can only provide a relatively small V_{pp}/V_{π}, and the bias tuning scheme can achieve a sufficiently high ROP with this small V_{pp}/V_{π} at the optimum CSPR, then the bias tuning is better than the parallel path structure based scheme, because the device nonlinearity is not that severe, and the penalty caused by the additional optical loss at the transmitter will cancel or even outweigh the gain achieved by reducing the device nonlinearity when using the parallel path structure based scheme. On the other hand, if the bias tuning scheme cannot achieve the desired performance with a small V_{pp}/V_{π}, and there is still room to increase V_{pp}/V_{π}, then we should use the parallel path structure based scheme, because in the bias tuning scheme, increasing V_{pp}/V_{π} does not necessarily improve the transmission performance as it also enhances the device nonlinearity, while in the parallel path scheme, we can use a much larger V_{pp}/V_{π} to benefit from the increased ROP without worrying too much about the modulator's device nonlinearity.

Specifically, in this work, we compared these two CSPR control schemes in a 100 Gb/s loss limited IQ modulator based SSB system over 40 km and a 100 Gb/s loss limited VSB system over 40 km through numerical simulations. Our results show that, considering the system parameters specified in this section and assuming that the entire transmitter photonic circuit can be implemented on the InP platform, the parallel path structure based scheme can achieve better BER performance in both systems.

5.3 On power consumption of KK-family algorithms

5.3.1 Motivation

A key step in the receiver DSP of an SSB/VSB self-coherent system is to reconstruct the field information of the received signal from its amplitude information. In an IQ modulator based SSB system, if the IQ imbalance can be neglected, the received signal can be rigorously SSB. In Chapter 2, section 2.4.2.2, we have introduced the KK algorithm, the iter-KK algorithm and the ufKK algorithm, which can be used to reconstruct the field information of a rigorous SSB signal. In a VSB system however, since the optical filter generally has a limited edge gradient, the received signal usually has a quasi-SSB spectrum, and the under-filtered unwanted

sideband will cause penalties to the aforementioned three KK-family algorithms, which limits the system's BER performance. Therefore, in Chapter 4, section 4.3, we have proposed the FA-iter-KK algorithm, which can significantly improve the BER performance in a VSB system.

In this work, we are going to compare the power consumption of these four KK-family algorithms. We hope our results can provide some guidance on practical implementations of KK-family algorithms in loss limited SSB and VSB systems.

5.3.2 Fundamental building blocks of DSP algorithms

In this work, we estimate the power consumption of DSP algorithms based on their computational complexities following the method described in [112], which subdivides DSP operations into five categories: multiplications, additions, read-only memory (ROM) operations for look-up tables (LUTs), register operations and gate operations. The energy consumed per operation are summarized in Table 5.2. Note that [112] considered the 180 nm CMOS node, but in this work, we consider the 7 nm CMOS node, hence the energy consumption values used in this thesis are scaled based on the scaling rule presented in [113].

Table 5.2 Energy consumption per DSP operation

symbol	Quantity	Value(7nm)
$E_{op,M}$	Average energy per n_b-bit multiplier op.	193.15 fJ
$E_{op,A}$	Average energy per n_b-bit adder op.	24.15 fJ
$E_{op,RO}$	Average energy per n_b-input ROM read per bit	16.06 fJ
$E_{op,R}$	Average energy per register read and write	4.03 fJ
$E_{op,G}$	Average energy per gate op.	0.81 fJ

Value computed assuming n_b= 8.

Each complex addition is implemented as 2 real additions. Each complex multiplication can be implemented as either 1) 4 real multiplications and 2 real additions (Eq. 5.5) or 2) 3 real multiplications and 5 real additions (Eq. 5.6). In this work, we consider the second option, since according to Table 5.2, a multiplier is more energy consuming than 3 adders.

$$\begin{gathered} x = a + ib, y = c + id, \\ xy = (ac - bd) + i(bc + ad) \end{gathered} \tag{5.5}$$

$$\begin{gathered} x = a + ib, y = c + id, \\ k_1 = c(a + b), k_2 = a(d - c), k_3 = b(c + d) \\ xy = (k_1 - k_3) + i(k_1 + k_2) \end{gathered} \tag{5.6}$$

Also note that in Eq. 5.6, if $y = c + id$ is a constant value, $d - c$, and $c + d$ can be computed offline and prestored. Therefore, if one of the factors is a constant value, a complex multiplication can be implemented as 3 real multiplications and 3 real additions.

Typical DSP stacks of SSB/VSB self-coherent systems include both time-domain operations and frequency-domain operations, hence a large number of multipliers and adders will be contributed from the DFT/IDFT blocks. DFTs and IDFTs can be implemented using computationally efficient fast Fourier transform (FFT) algorithms. If the size of the DFT/IDFT equals to 2^n (where n is an integer), it can be implemented using the split-radix algorithm [114]. However, as we will shortly see in section 5.3.3, in this work, we assume that the digital resampling blocks are implemented in the frequency domain. As a result, we also need FFTs with the number of points $N \neq 2^n$.

An N-point FFT with $N \neq 2^n$ can be divided into a sub-FFT with N_1 points and a sub-FFT with N_2 points using the prime factor algorithm (PFA) [114], where we have $N = N_1 N_2$. If each sub-FFT requires $N_{op,Mi}$ real multiplications and $N_{op,Ai}$ real additions ($i = 1,2$), then the original N-point FFT would require $N_1 N_{op,M2} + N_2 N_{op,M1}$ real multiplications and $N_1 N_{op,A2} + N_2 N_{op,A1}$ real additions. For each sub-FFT, if the number of point equals to 2^n, then it can be implemented using the split-radix algorithm, otherwise we can apply the PFA again to divide this sub-FFT. We keep repeating this process until we end up with sub-FFTs with the number of points equals to either 2^n or a small prime number, and those small size FFTs can be implemented using Winograd's algorithm [115]. Table 5.3 lists the number of real multiplications and real additions required by FFTs with different sizes.

Table 5.3 Numbers of real multipliers and adders required per FFT block

# FFT points	# real multipliers	# real adders
2	0	4
3	4	12
5	10	34
7	16	72
9	20	84
11	40	168
$N = 2^n$	$N \log_2 N - 3N + 4$	$3N \log_2 N - 3N + 4$

If the inputs of the DFTs or the outputs of the IDFTs are real-valued signals, we can further

reduce the computational complexities of these blocks by implementing two N-point DFTs/IDFTs with real-valued inputs/outputs through a single N-point DFT/IDFT with a complex-valued input/output. Specifically, if we want to compute the DFTs of two real-valued signals $x_1[n]$, and $x[n]$, we can first compute the DFT of a complex-valued signal $y[n] = x_1[n] + ix_2[n]$. Suppose we have:

$$Y[k] = DFT\{y[n]\} = Y_r[k] + Y_i[k] \tag{5.7}$$

where $Y_r[k]$ and $Y_i[k]$ are the real and imaginary parts of the DFT of $y[n]$. Then the DFTs of $x_1[n]$ and $x_2[n]$ can be computed as follows:

$$\begin{cases} X_1[k] = DFT\{x_1[n]\} = \dfrac{Y_r[k] + Y_r[-k]}{2} + i\dfrac{Y_i[k] - Y_i[-k]}{2} \\ X_2[k] = DFT\{x_1[n]\} = \dfrac{Y_i[k] + Y_i[-k]}{2} - i\dfrac{Y_r[k] - Y_r[-k]}{2} \end{cases} \tag{5.8}$$

Note that the reversal operation and division by 2 only require register readings/writings[18].

Similarly, if we want to compute the IDFTs of two Hermitian-symmetric signals $X_1[k] = X_{1r}[k] + iX_{1i}[k]$ and $X_2[k] = X_{2r}[k] + iX_{2i}[k]$, i.e. the outputs of the IDFTs are two real-valued signals, we can first construct a complex signal

$$Y[k] = (X_{1r}[k] - X_{2i}[k]) + i(X_{2r}[k] + X_{1i}[k]) \tag{5.9}$$

Then the IDFTs of $X_1[k]$ and $X_2[k]$ are exactly the real part and the imaginary part of the IDFT of $Y[k]$, respectively, i.e.:

$$\begin{cases} IDFT\{X_1[k]\} = real\{IDFT\{Y[k]\}\} \\ IDFT\{X_2[k]\} = imag\{IDFT\{Y[k]\}\} \end{cases} \tag{5.10}$$

5.3.3 Frequency-domain digital resampling vs. time-domain digital resampling

Fig. 5.11(a) shows the schematic of the KK algorithm. A problem with the KK algorithm is that it includes a logarithm function, which broadens the spectrum [81]. To accommodate the broadened spectrum, generally we need digital upsampling and downsampling before and after the KK algorithm, as shown in Fig. 5.11(b).

To bypass digital resamplings, people have proposed the iter-KK [80] and the ufKK [82]

[18] Multiplication/Division by 2 can be implemented as 1-bit shifting [112].

algorithms, the schematics of which are shown in Fig. 5.12.

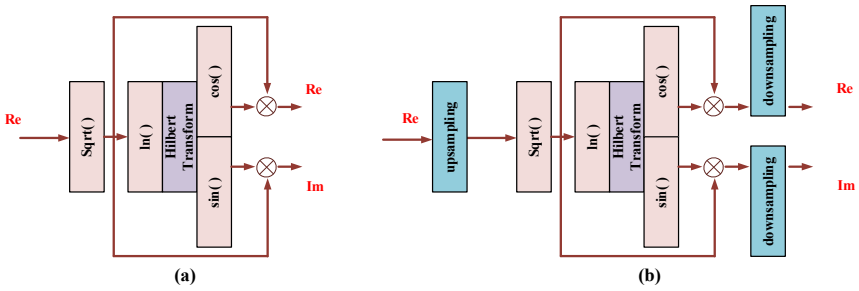

Fig. 5.11 Schematics of (a) the KK algorithm, and (b) the KK algorithm with digital resampling blocks.

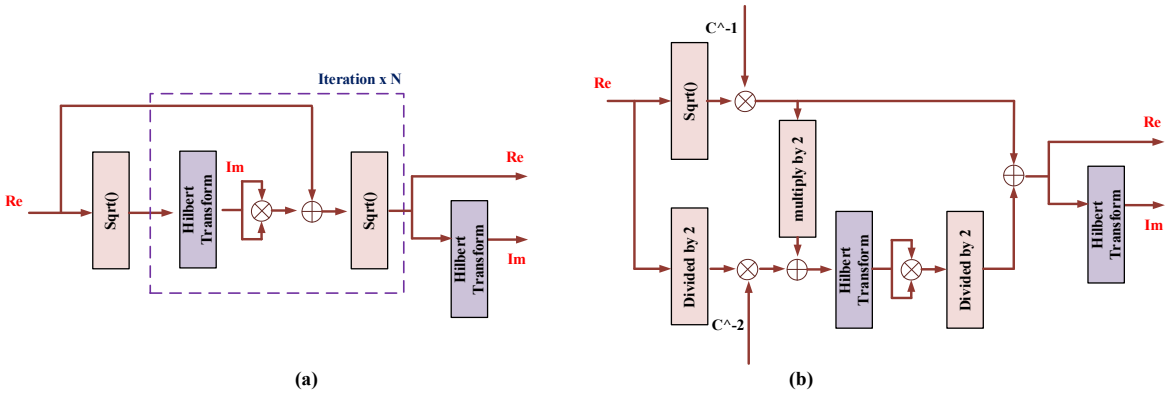

Fig. 5.12 Schematics of (a) the iter-KK algorithm, and (b) the ufKK algorithm. [Adapted] with permission from [38] © The Optical Society.

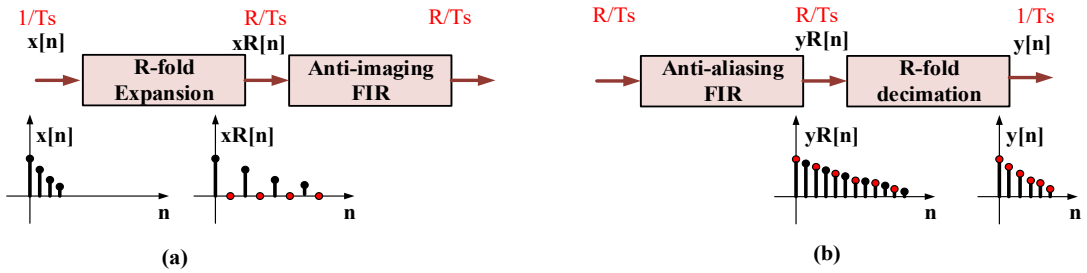

Fig. 5.13 Principles of time-domain implementations of (a) digital upsampling and (b) digital downsampling. [Adapted] with permission from [38] © The Optical Society.

Interestingly, both the iter-KK and the ufKK algorithms require at least one extra Hilbert transform compared to the KK algorithm[19]. But note that a Hilbert transform is just an FIR filter in the time domain [81]. On the other hand, if we use the KK algorithm, we cannot avoid the digital resampling blocks. If we implement the digital resampling blocks in the time domain,

[19] This is true if the iter-KK and the ufKK algorithms are implemented as Fig. 5.13. Later on, we will show that these two algorithms can be further simplified when we implement digital resampling in the frequency domain.

we will need more FIR filters, since a time-domain upsampling block contains an R-fold expansion followed by an anti-imaging filter, and a time-domain downsampling block contains an R-fold decimation preceded by an anti-aliasing filter, as shown in Fig. 5.13.

If we assume that both the Hilbert transform and the digital resampling are implemented in the time domain, then removing the resampling blocks by replacing the KK algorithm with the iter-KK algorithm or the ufKK algorithm is definitely worth doing. In [81], the authors compared the power consumption of the KK algorithm and the ufKK algorithm based on this assumption, and their results shows that the ufKK algorithm saves ~85% power compared to the KK algorithm. However, we have to point out that, the time-domain implementation of the digital resampling is not efficient, which could lead to an overestimation of its computational complexity and power consumption.

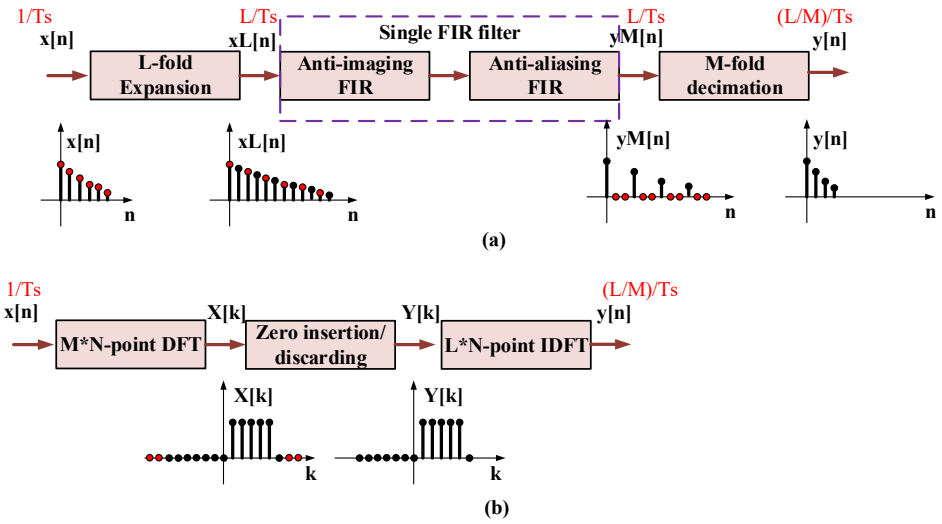

Fig. 5.14 Principles of (a) time-domain digital resampling and (b) frequency-domain digital resampling with rational resampling ratio. [Adapted] with permission from [38] © The Optical Society.

Fig. 5.14 compares the principles of time-domain and frequency-domain implementations of digital resampling in a more general case, where the resampling ratio is a rational value L/M (where L and M are integers). In the time domain, we need to first upsample the signal by a factor of L, then downsample it by a factor M. Although the anti-imaging and anti-aliasing filter can be merged into a single FIR filter, it needs to be running at L times the original sampling rate. Therefore, when using the time-domain implementation of digital resampling, it is preferred to use integer resampling ratios. On the other hand, in the frequency domain, in

order to achieve a resampling ratio of L/M, we just need to insert or discard a certain number of zeros to adjust the sampling rate, and make sure that the ratio of the IDFT size to the DFT size equals to L/M. Therefore, frequency-domain resampling allows us to further reduce the sampling rate by using non-integer resampling ratios at a lower cost.

We also note that expansion, decimation, zero insertion and zero discarding just require register readings and writings, which are more power efficient than multiplications and additions. Therefore, the power consumption of a digital resampling block will be mainly contributed from the FIR filters or the DFTs/IDFTs. Since the DFTs and the IDFTs can be implemented using computationally efficient FFT algorithms as we have discussed in section 5.3.2, frequency domain digital resampling could be more power-efficient.

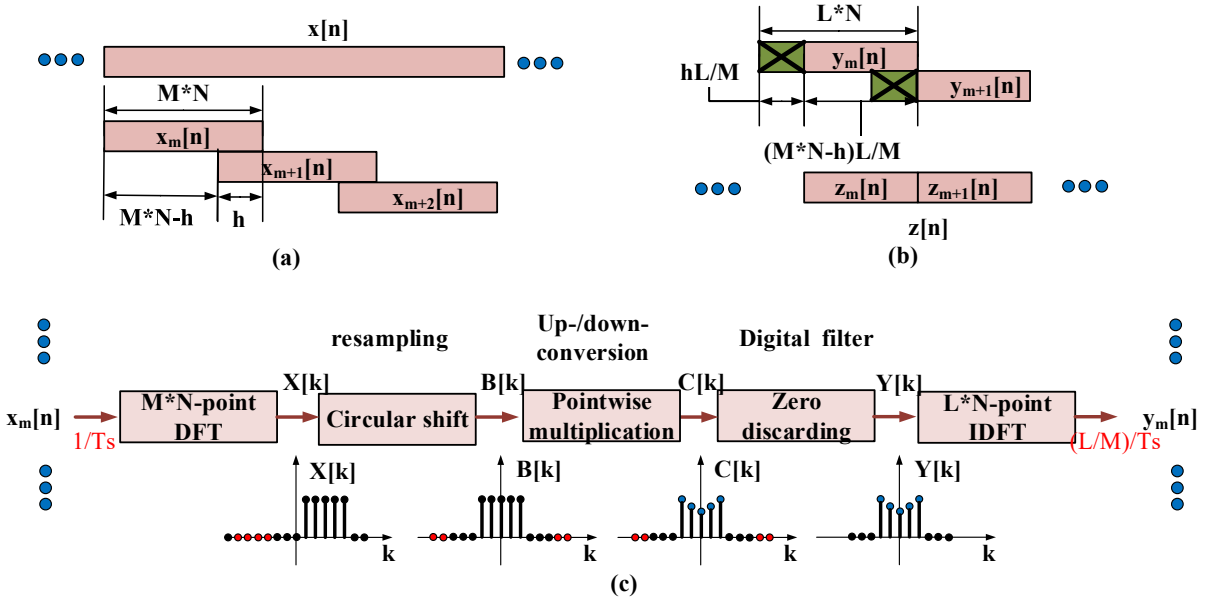

Fig. 5.15 Principle of frequency-domain digital resampling (with rational resampling ratio) merged with frequency down-conversion and a digital filter. (a) Slice the input sequence into overlapping sections, (b) concatenate the processed and shortened sections to form the output sequence, and (c) frequency-domain processing of each section.

In addition, remember that in the receiver DSP of an SSB/VSB self-coherent system, after reconstructing the field information using one of the KK-family algorithms, there is always a CD compensation or a generalized CD compensation (in the VSB case) block, which is often implemented as a frequency-domain digital filter using the overlap-and-save algorithm. Also, if we transmit a passband signal, we need to down-covert the signal back to the baseband for

further processing. A frequency down-conversion operation can be implemented as a circular shift in the frequency domain. Frequency-domain implementation of digital resampling allows us to merge the digital resampling block after the KK-family algorithm (if there is any), the frequency down-conversion block and the CD compensation/generalized CD compensation block into a single frequency-domain processing block. This way, we only need one DFT and one IDFT at the beginning and the end of this merged block, as we can see in Fig. 5.15.

Specifically, we can first slice the input sequence into overlapping sections with a section length of MN (where both M, N are integer numbers) and an overlapping sequence length of h as shown in Fig. 5.15(a). Then each section is processed with a frequency-domain processing block as shown in Fig. 5.15(c), and we will end up with several overlapping sections with a section length of LN (where both L, N are integer numbers) and an overlapping sequence length of hL/M. By carefully choosing the $L, M,$ and h, we can guarantee that hL/M is also an integer. After that, we discard the first hL/M points in each section and concatenate the remaining parts to form the output sequence as shown in Fig. 5.15(b). This process is equivalent to applying an FIR filter with $h + 1$ taps to the input sequence in the time domain and then resample the sequence by L/M.

As we have mentioned in section 5.3.2, if the inputs/outputs of two DFTs/IDFTs are real-valued signals, we can further reduce the computational complexities by implementing these two DFTs/IDFTs through a single DFT/IDFT of the same size with a complex-valued input/output. The output of the frequency-domain processing block shown in Fig. 5.15(c) is a complex-valued signal (a baseband QAM signal), hence we cannot do anything with the IDFT. The input of the DSP block shown in Fig. 5.15(c) is the output of the KK/iter-KK/ufKK algorithm. Remember that a KK-family algorithm reconstructs the complex-valued field information of a SSB signal, and the spectrum of a SSB signal does not overlap with the spectrum of its complex conjugate in the frequency domain. Therefore, if we only keep the real part of the reconstructed field information at the output of the KK-family algorithm, we can share the DFT between two parallel frequency-domain processing blocks (for two different input sections) based on Eqs. 5.7 and 5.8, and the complex-valued field information can be recovered by applying a digital

RSB filter to suppress half of the spectrum. Note that this digital RSB filter can be merged into the frequency-domain filter after the KK-family algorithm which is already there (e.g. the filter used to compensate for the CD). As a result, the schematic of the frequency-domain processing block shown in Fig. 5.15(c) can be turned into the form shown in Fig. 5.16. Compared to the schematic shown in Fig. 5.15(c), the schematic shown in Fig. 5.16 requires $4MN$ additional real adders for every two parallel processing blocks, but it saves a MN-point DFT, hence in this work, we will implement the frequency-domain processing blocks based on the schematic shown in Fig. 5.16.

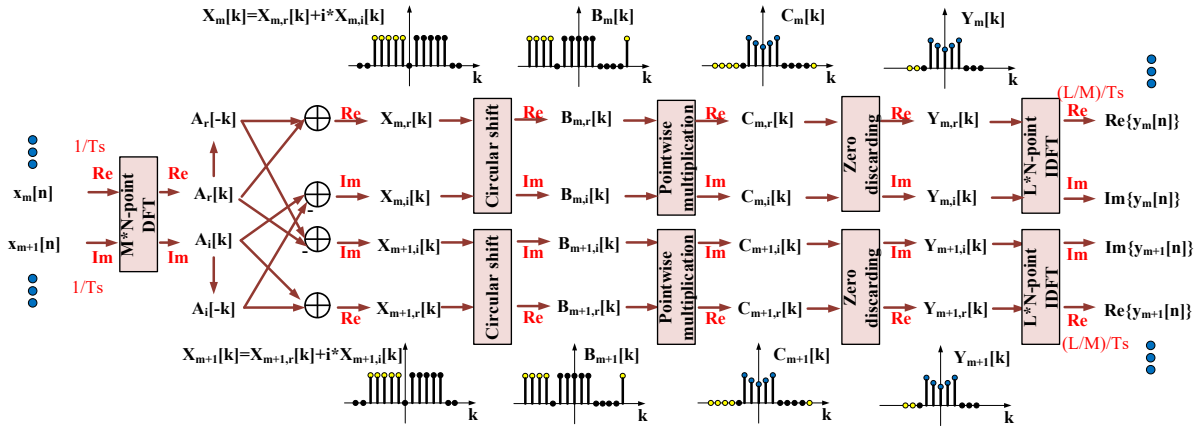

Fig. 5.16 An alternative implementation of the frequency-domain processing block after the KK-family algorithm, where the DFT is shared between two parallel processing blocks.

Similarly, at the transmitter side, when we transmit a passband signal, we need a digital resampling step, a frequency up-conversion operation, and a frequency-domain digital filter for each DAC channel (as we have mentioned in Chapter 3, section 3.2.2, the pulse shaping and the pre-emphasis can be implemented as a single filter), which can also be merged into a single frequency-domain processing block. Fig. 5.17(a) and Fig. 5.17(b) show the schematics of the transmitter-side frequency-domain processing blocks in an IQ modulator based SSB system and a VSB system, respectively.

In an IQ modulator based system, since we use two DAC channels, for each complex-valued input section $x_m[n]$, we need to generate two real-valued output sections $yi_m[n]$ and $yq_m[n]$, hence each processing block contains one DFT and one IDFT. Note that in Fig. 5.17(a), instead of directly applying a digital filter (through pointwise multiplications) to the spectrum

of a complex-valued frequency-upconverted SSB signal $C_m[k] + iD_m[k]$, we choose to apply two digital filters to $C_m[k]$ and $D_m[k]$ separately, since the two DAC channels and the two RF amplifiers of the in-phase path and quadrature path may have different frequency responses. On the other hand, in a VSB system, we only need one DAC channel, hence we only need to keep the in-phase component $yi_m[n]$. As a result, the IDFT can be shared between two parallel processing blocks based on Eqs. 5.9 and 5.10, i.e. every two frequency-domain processing blocks require two MN-point DFTs and only one LN-point IDFT.

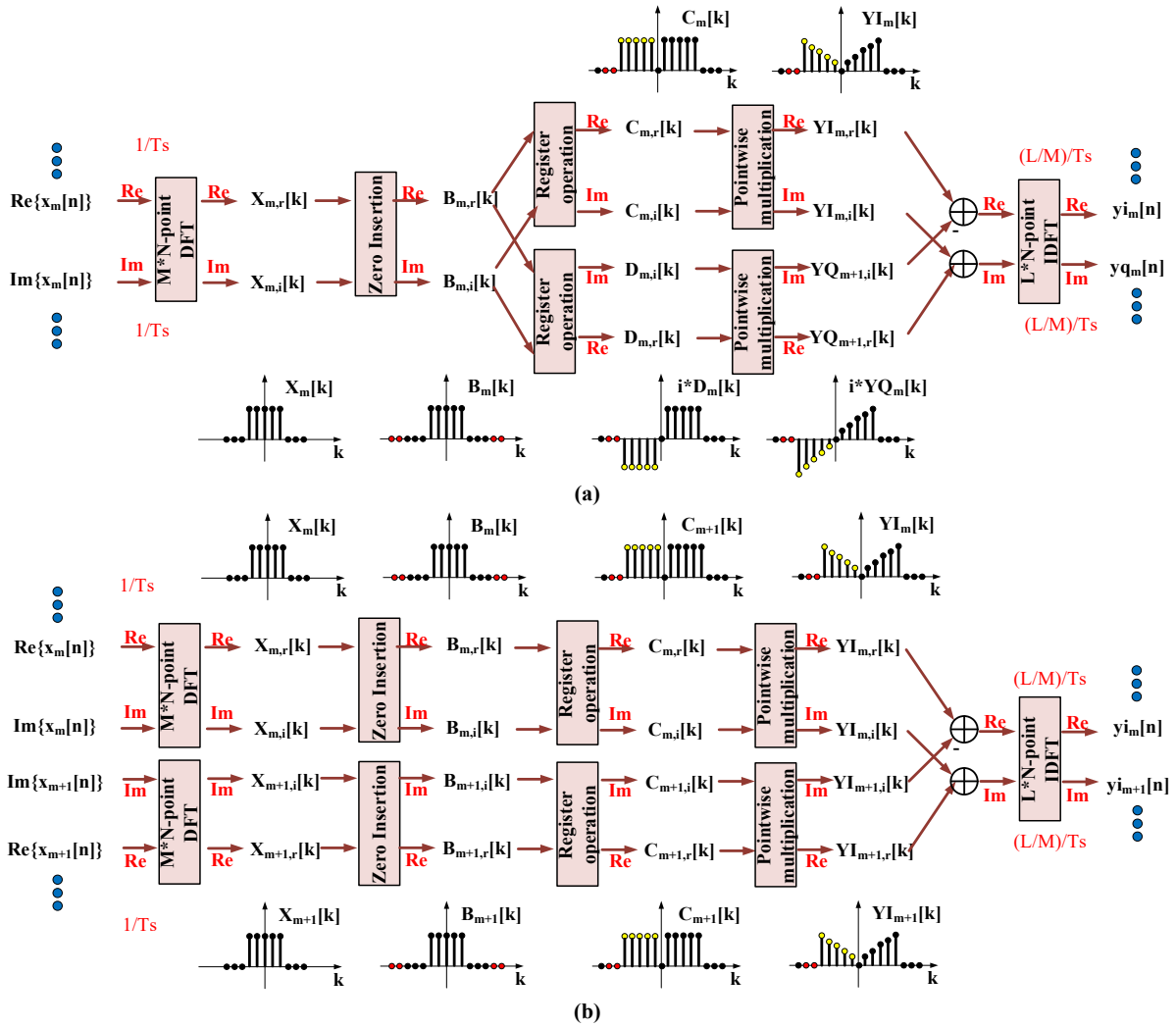

Fig. 5.17 Schematics of the frequency-domain processing blocks at the transmitters in (a) an IQ modulator based SSB self-coherent system and (b) a VSB self-coherent system.

5.3.4 Frequency-domain implementation of Hilbert transform

A common building block of the KK algorithm, the ufKK algorithm and the iter-KK algorithm is the Hilbert transform. In this work, we assume that the Hilbert transform is also implemented

as a digital filter in the frequency domain using the overlap-and-save algorithm as shown in Fig. 5.18.

The frequency response of the Hilbert transform is given by:

$$H_{hil}(j\omega_k) = \begin{cases} 0, k = 0 \\ -i, 1 \le k \le \dfrac{N}{2} - 1 \\ i, \dfrac{N}{2} \le k \le N - 1 \end{cases}, \quad \omega_k = \frac{2\pi k}{N}, 0 \le k \le N - 1 \qquad (5.11)$$

where N is the number of points used in the DFT and the IDFT. Note that pointwise multiplications with $H_{hil}(j\omega_k)$ do not really require multipliers, since multiplying a complex value by $\pm i$ only requires flipping the sign bit and switching the real and the imaginary components, which can be implemented as register operations.

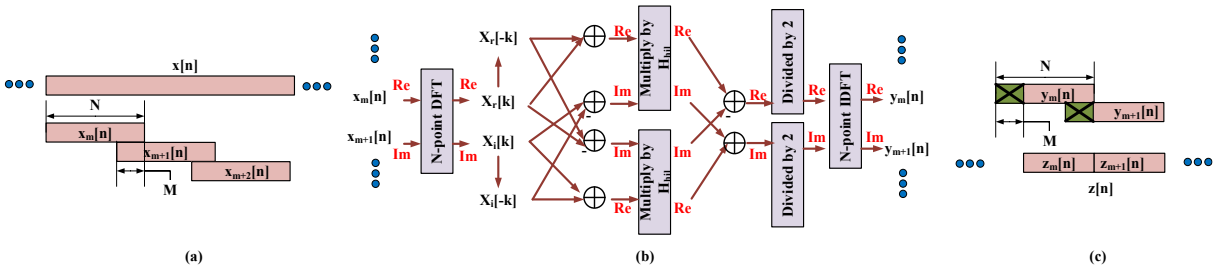

Fig. 5.18 Principle of frequency-domain implementation of Hilbert transform. (a) Slice the input sequence into overlapping sections, (b) frequency-domain processing of every two sections, and (c) concatenate the processed and shortened sections to form the output sequence.

Also note that both the input and the output of a Hilbert transform are real-valued sequences. Based on our discussions in section 5.3.2, we can share both the DFT and IDFT between two parallel processing blocks. When we share the DFT between two parallel blocks based on Eqs. 5.7 and 5.8, there is a factor 1/2 in Eq. 5.8. We omit this factor in Fig. 5.16 because it can be considered during the pointwise multiplication step (by scaling the frequency-domain filter). However, as we have just said, when we implement the Hilbert transform, the pointwise multiplications with $H_{hil}(j\omega_k)$ are achieved by flipping the sign bits and switching the real and imaginary components, hence this "division by 2" step needs to be implemented explicitly. Fortunately, division by 2 can be implemented as a 1-bit shift, which requires only register operations [112].

5.3.5 Power consumption of KK-family algorithms in a loss limited IQ modulator based SSB system

Now we can transform the schematics of the KK algorithm shown in Fig. 5.11 into the form shown in Fig. 5.19. Note that the digital resampling block before the KK algorithm in Fig. 5.11 is the first block of the receiver DSP stack in an SSB/VSB self-coherent system, hence instead of resampling the output of the ADC channel in the DSP, we can directly change the sampling rate of the ADC channel.

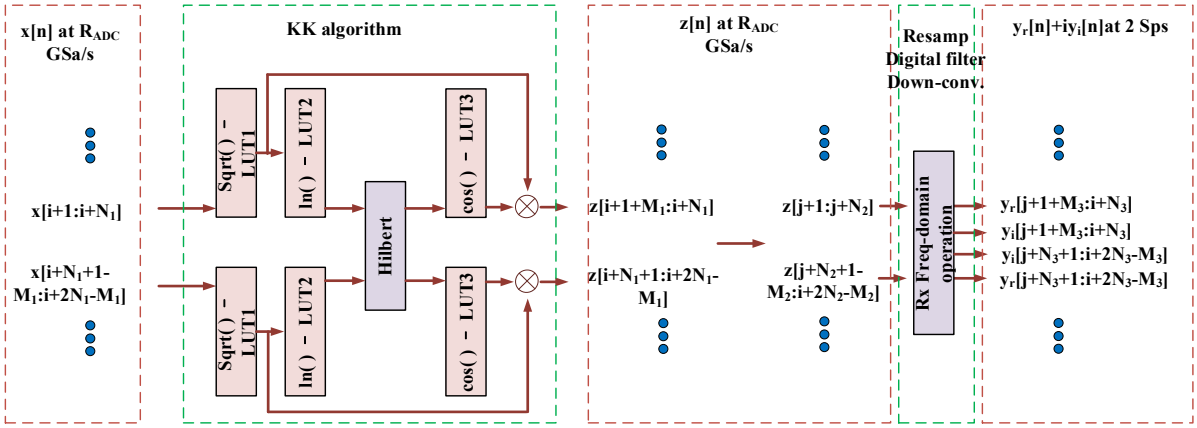

Fig. 5.19 Practical implementation of the KK algorithm and the following frequency-domain processing.

As we have mentioned in section 5.3.4, we just need to keep the real part of the output of the KK algorithm since we can apply a digital RSB filter to the real part of an SSB signal to retrieve its field information, hence the branch to generate the imaginary part of the SSB signal in Fig. 5.11 is removed. The square root operation, the logarithm function and the cosine function are implemented as LUTs. The Hilbert transform is implemented as Fig. 5.18, which is shared between two parallel DSP blocks as we have discussed in section 5.3.4. Then we use a receiver-side frequency-domain processing block as shown in Fig. 5.16 (where the DFT is shared between two parallel processing blocks) to down-convert the passband signal back to the baseband, apply frequency-domain filters, and resample the signal to 2 Sps for further processing (e.g. time-domain equalization).

Similarly, the schematics of the iter-KK algorithm and the ufKK algorithm shown in Fig. 5.12 can be changed into the forms shown in Fig. 5.20. The square root operations can be implemented as LUTs. Multiplications/divisions by 2 can be implemented as register

operations (1-bit shift). The Hilbert transforms at the outputs of the iter-KK algorithm and the ufKK algorithm shown in Fig. 5.12 are removed, since we only need to keep the real parts of the outputs of the KK-family algorithm, and then apply RSB filters in the following frequency-domain processing blocks. The remaining Hilbert transforms and the DFT in the frequency-domain processing block (Fig. 5.16) can be shared between two parallel processing blocks as in the KK algorithm case.

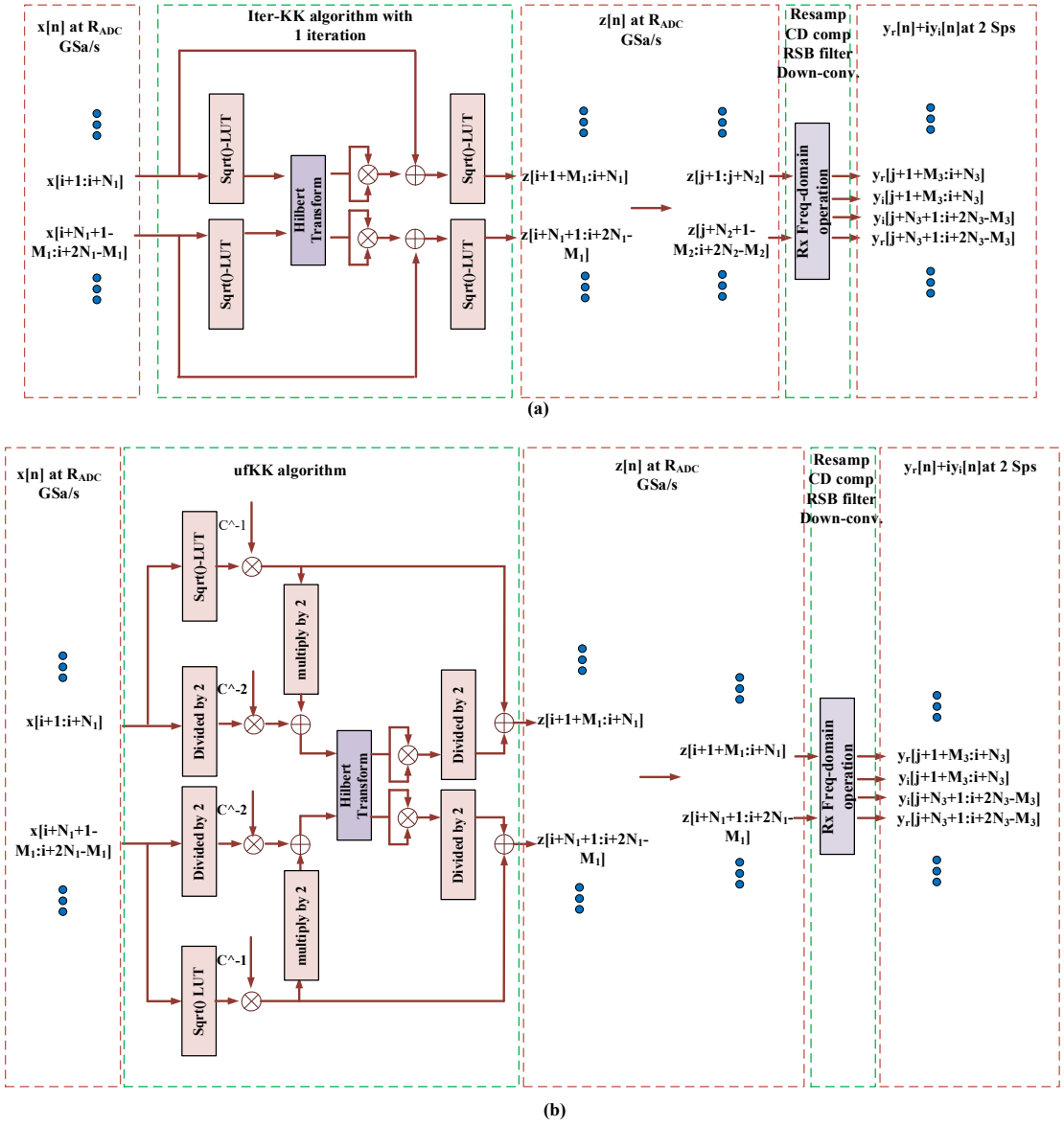

Fig. 5.20 Practical implementations of (a) the iter-KK algorithm with 1 iteration and the following frequency-domain processing, and (b) the ufKK algorithm and the following frequency-domain processing.

Note that the multipliers and the adders in the KK-family algorithms are mainly contributed from the DFTs and the IDFTs in the Hilbert transforms, and a N-iteration iter-KK algorithm

requires N Hilbert transforms. To minimize the number of multipliers and adders, in this work, we will only consider 1 iteration in the iter-KK algorithm. As we will shortly see, 1 iteration can already achieve decent transmission performance in a 100 Gb/s loss limited IQ modulator based SSB system over 40 km.

We reuse the link model of the loss limited IQ modulator based SSB system developed in section 5.2 to estimate the performance of the KK, the iter-KK with 1 iteration, and the ufKK algorithms. This time, we only consider the parallel path structure based CSPR control scheme. Note that the clipping ratio also affects the CSPR even if the bias point or the splitting ratio in the parallel path structure is fixed, hence in section 5.2, to simplify the problem, we fixed the clipping ratio at the DAC channels for all different combinations of V_{pp}/V_{π} ratios and CSPR values in both the bias tuning case and the parallel path structure case. In practice, for each V_{pp}/V_{π}, the CSPR and the clipping ratio can be optimized simultaneously to further improve the transmission performance. In this work, we fixed the V_{pp}/V_{π} ratio at 1.4, and we simultaneously optimize the splitting ratio in the parallel path structure and the clipping ratio at the DAC channels, which is why the BERs presented in this section are slightly better than the results shown in section 5.2. The ADC sampling rate is varied between 64 GSa/s and 96 GSa/s. The rest system parameters are the same as the ones shown in Table 5.1.

Based on our discussions in sections 5.3.3 to 5.3.5, for the power consumption analysis, the transmitter and receiver DSP stacks of an IQ modulator based SSB self-coherent system shown in Fig. 5.3 should be transformed into the forms shown in Fig. 5.21.

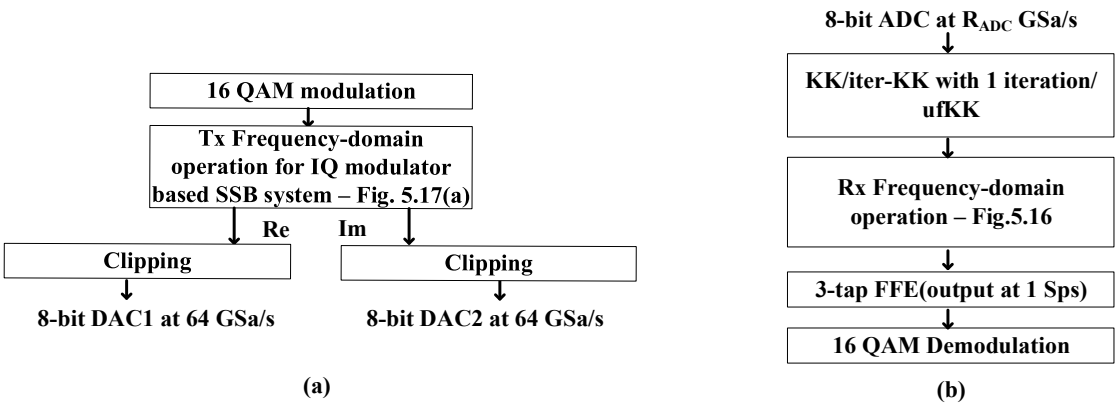

Fig. 5.21 (a) Transmitter and (b) receiver DSP stacks used in an IQ modulator based SSB system for the power consumption analysis.

The RC pulse shaping, the pre-emphasis, the transmitter-side digital resampling and the frequency up-conversion are merged into a single frequency-domain processing block shown in Fig. 5.17(a). The receiver-side digital resampling before the KK-family algorithm is replaced by directly changing the sampling rate of the ADC channel. The receiver-side digital resampling after the KK-family algorithm, the frequency-domain digital filter, and the frequency down-conversion are merged into a single frequency-domain processing block shown in Fig. 5.16.

Note that the frequency-domain filter can also be used to compensate for the ISIs caused by both the CD effect and the components' bandwidth limitations. The frequency-domain tap coefficients can be obtained as follows. We first turn-off the frequency-domain filter and use sufficient taps in the time-domain equalizer. The time-domain tap coefficients can be converged using the LMS algorithm. Then we take the DFT of the converged time-domain tap coefficients to obtain the frequency-domain tap coefficients. After that, we turn on the frequency-domain filter. The frequency-domain tap coefficients are stable, thus they can be computed offline and prestored in a practical system[20]. This approach allows us to minimize the number of taps used in the adaptive time-domain equalizer.

When we implement the Hilbert transforms, we always use 1024-point DFTs and IDFTs in each block. But when we implement the transmitter-side and receiver-side frequency-domain processing blocks, since we either insert or discard zeros in the frequency domain to adjust the sampling rate, we use $448R$-point DFTs/IDFTs for signals at $28R$ GSa/s. For example, if a frequency-domain processing block resamples a signal from 64 GSa/s to 56 GSa/s, then the size of the DFT is 1024 ($R = 16/7$), and the size of the IDFT is 896 ($R = 2$).

Frequency up-/down-conversion, or mixing, is the multiplication of an input signal by a complex sinusoid signal $\exp(j2\pi f_{mix}t)$ in the time domain, which is equivalent to shifting the

[20] Note that when we use this approach to determine the frequency-domain tap coefficients, we should switch the order of the pointwise multiplication and the zero-discarding steps in Fig. 5.16, since the time-domain filter is operating at the output sampling rate of the frequency-domain processing block. In this case, the "zero-discarding" step may discard non-zero frequency bins. But the spectral information in these discarded bins will not be used in the output sequence anyway (because originally they will be set to zeros before being discarded).

spectrum of the input signal in the frequency domain by the mixing frequency f_{mix}. But note that when we implement the up-/down-conversion together with a digital filter in the frequency domain using the overlap-and-save algorithm, there will be some constraints on f_{mix} [116]:

1) The precision of f_{mix} is limited by the resolution of DFT, since we can only shift the spectrum by an integer number of frequency bins.
2) The precision of f_{mix} is further limited by the fact that we don't use a complete buffer of output in the overlap-and-save algorithm. Suppose that we use $N-h$ samples out of N samples in each block (at the sampling rate of the output sequence), we must restrict f_{mix} to the subset of frequencies whose periods complete in those $N-h$ samples, otherwise phase discontinuities occur, i.e. we can only shift in multiples of N/h bins.

In this work, we consider an RC pulse shaped 28 Gbaud passband 16QAM signal with a roll-off factor of 0.1. Since we use a minimum sampling rate of 64 Gsa/s at the DAC and the ADC, f_{mix} has to be larger than or equal to $28*(1+0.1)/2 = 15.4\ GHz$, and should not be larger than $64/2-28*(1+0.1)/2 = 16.6\ GHz$. We consider an overlapping sequence length of $h=8K$ (where K is an integer and is variable) at 64 GSa/s, and remember that the size of the DFT/IDFT at 64 GSa/s is $N=1024$, thus we can only shift in multiples of $N/h = 1024/(8K) = 128/K$ bins. In this work, we choose to shift by 256 bins at 64 GSa/s, which corresponds to $f_{mix} = 16\ GHz$, and a guard band of $16-15.4 = 0.6\ GHz$.

To estimate the power consumption of KK-family algorithms related DSP blocks, we need to determine the following three parameters: 1) the sampling rate of the ADC channel R_{ADC}, 2) the length of the overlapping sequence used in the Hilbert transform h_1, and 3) the length of the overlapping sequence used in the frequency-domain processing block after the KK-family algorithm at the output sampling rate h_3, i.e. the overlapping sequence length used at the IDFT. Note that the overlapping sequence length used at the DFT h_2 is uniquely determined by h_3, since we have $h_2/h_3 = R_{in}/R_{out}$, where R_{in} and R_{out} are the sampling rates at the input and the output of the frequency-domain processing block, respectively, and we have $R_{in} = R_{ADC}$ and $R_{out} = 56$ GSa/s.

We use the link model shown in Fig. 5.2 to study the impacts of R_{ADC}, h_1 and h_3 on the

system performance, and the results are shown in Fig. 5.22. We first use sufficiently large h_1 and h_3 values and sweep R_{ADC}. To make a fair comparison between the power consumption of different KK-family algorithms, we need the different algorithms to achieve the same transmission performance. Therefore, in this work, we choose $R_{ADC} =$ 88 GSa/s for the KK algorithm, $R_{ADC} =$ 80 GSa/s for the ufKK algorithm and $R_{ADC} =$ 64 GSa/s for the iter-KK algorithm with 1 iteration. Next, we fix h_3 at 35 and sweep h_1. Interestingly, we find that changing h_1 does not significantly change the achievable BERs, and we can even use $h_1 = 0$ in all these three KK-family algorithms. Then we fix h_1 at 0 and sweep h_3. We observe that as long as h_3 exceeds 28, further increasing h_3 no longer significantly improve the BER performance, which indicates that $h_3 + 1 = 29$ taps in the time domain (at 2 Sps) is sufficient to mitigate the ISI in our system. We will use $h_3 = 28$ for all the three KK-family algorithms in the following analysis. Note that h_3 can only be changed in multiples of 7, because in this work we implement the frequency-down conversion as circular shift in the frequency domain, and we need to guarantee that the periods of f_{mix} complete in $N_3 - h_3$ samples, where N_3 is the IDFT size in frequency-domain processing block after the KK-family algorithm.

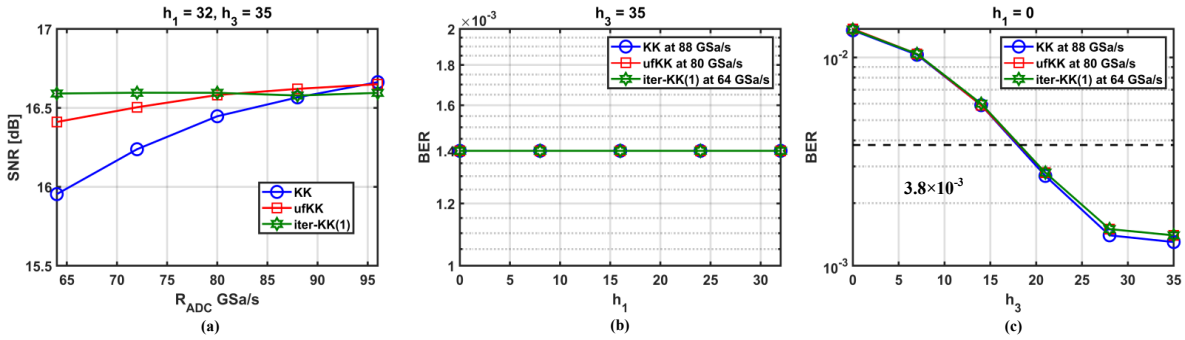

Fig. 5.22 (a) Effective SNRs as functions of the ADC sampling rate, (b) BERs as functions of the overlapping sequence length used in the Hilbert transform, and (c) BERs as functions of the overlapping sequence length used in the receiver-side frequency-domain processing block after the KK-family algorithm, when applying different KK-family algorithms in a 100 Gb/s 40 km IQ modulator based loss limited SSB self-coherent system.

Table 5.4 summarizes the important receiver-side (Rx) DSP parameters (for the KK-family algorithm related blocks only) used in an IQ modulator based SSB system considered in the power consumption analysis.

Now we can use the method described in [112] to estimate the power consumption of different

DSP blocks. Let's take the KK algorithm as an example to explain the procedure. The power consumed per symbol at the KK algorithm block (excluding the frequency-domain processing block after it) can be computed as:

$$P_{RxFreqProc} = \frac{R_{ADC} \sum_c E_{op,c} N_{op,c}}{N_1 - h_1} \tag{5.12}$$

where $E_{op,c}$ is the energy consumed per operation (values given in Table 5.3), $N_{op,c}$ is the number of operations per DSP block (with N_1 inputs and $N_1 - h_1$ outputs).

Table 5.4 Rx DSP parameters used in an IQ modulator based SSB system

symbol	description	KK	ufKK	Iter-KK w/ 1 iteration
R_{sig} [Gbaud]	Symbol rate of the signal	28	28	28
f_{clock} [MHz]	Frequency of the clock signal	500	500	500
R_{ADC} [GSa/s]	ADC sampling rate (the sampling rate at the input/output of the KK-family algorithm)	88	80	64
p_1	Degree of parallelization of Hilbert transform	176	160	128
h_1	Overlapping sequence length in Hilbert transform	0	0	0
N_1	DFT/IDFT size in Hilbert transform	1024	1024	1024
p_2	Degree of parallelization of the frequency-domain processing block after the KK-family algorithm	112	112	112
N_2	DFT size in frequency-domain processing block after the KK-family algorithm	1408	1280	1024
h_3	Overlapping sequence length at the IDFT of the frequency-domain processing block after the KK-family algorithm	28	28	28
N_3	IDFT size in frequency-domain processing block after the KK-family algorithm	896	896	896
R_{out} [GSa/s]	Sampling rate at the output of the frequency-domain processing block after the KK-family algorithm	56	56	56

Considering the schematic of the KK algorithm shown in Fig. 5.19 and the schematic of the Hilbert transform shown in Fig. 5.18(c), in each block, there are 1/2 N_1-point DFT, 1/2 N_1-point DFT (since they are shared by two parallel DSP blocks), $3N_1$ n_b-in n_b-out ROM readings for time-domain LUTs (in this analysis we assume $n_b = 8$), N_1 1-bit

readings/writings for sign bit flipping in the Hilbert transform, $2N_1$ n_b-bit readings and writings for division by 2 operation, and $3N_1$ additional real adders (since we share the DFT/IDFT based on Eqs. 5.7 to 5.10). Since FFT implementation can be fully parallel, each block also requires $n_b(N_1 - h_1)\lceil \log_2(p1) \rceil$ 1:2 demultiplexing operations and $n_b(N_1 - h_1)\lceil \log_2(p1) \rceil$ 2:1 multiplexing operations [112]. Each demultiplexing operation contains one gate operation, and each multiplexing operation contains two gate operations. In addition, there are $(4N_1 - h_1)$ n_b-bit register readings/writings per block for data storage and reversal operation.

Note that once we change the KK-family algorithms, we also change the R_{ADC} values, which then changes the power consumption of the ADC channel. Following the [112], in this work we assume that the power consumption of the ADC channel scales in proportional to its bit resolution and sampling rate, and we use a 60 GSa/s 7-bit 7 nm CMOS ADC [117] as our reference point to calculate the power consumption of the ADC channel used in this work.

Table 5.5 Power consumption of the ADC channel and the KK-family algorithm related DSP blocks

symbol	description	KK	ufKK	Iter-KK w/ 1 iteration
P_{ADC} [mW]	Power consumed by the ADC channel	507.9	461.7	369.4
$N_{M,KK}$	Number of real multipliers per symbol (on average) of the KK-family algorithm block	25.2	28.6	18.3
$N_{A,KK}$	Number of real adders per symbol (on average) of the KK-family algorithm	94.3	91.4	70.9
P_{KK} [mW]	Power consumed by the KK-family algorithm	178.8	181.8	125.4
$N_{M,RxFreq}$	Number of real multipliers per symbol (on average) of the frequency-domain processing block after the KK-family algorithm	28.9	26.8	24.7
$N_{A,RxFreq}$	Number of real adders per symbol (on average) of the frequency-domain processing block after the KK-family algorithm	122.4	108.8	98.4
P_{RxFreq} [mW]	Power consumed by the frequency-domain processing block after the KK-family algorithm	187.5	173.7	158.6
P_{sum} [mW]	Total power consumption of the ADC channel and the KK-related Rx DSP blocks	874.2	816.6	653.4

Table 5.5 summarizes the estimated power consumption of the ADC channel and the KK-related receiver-side DSP blocks of different KK-family algorithms. In this work, when we

change the KK-family algorithms, we only change the parameters listed in Table 5.4, such that the change of the system's total power consumption is solely contributed from the changes of the power consumption of the ADC channel and the KK-related receiver-side DSP blocks. In other words, to compare the power consumption of different KK-family algorithms, we only need to compare the power consumption of the ADC channel and the KK-related DSP blocks. We find that in a 100 Gb/s IQ modulator based loss limited SSB system over 40 km with the system parameters shown in Table 5.1 (with a $V_{pp}/V_{\pi} = 1.4$ and a CSPR of 10 dB) and the KK-family algorithm related DSP parameters shown in Table 5.4, assuming frequency-domain implementations of digital resampling and the Hilbert transforms, the KK algorithm is the most power-consuming option among all these three algorithms, since it requires larger R_{ADC} and h_3 than the rest two options. To achieve the same transmission performance, the ufKK algorithm and the iter-KK algorithm with 1 iteration require ~6.6% and ~25.5 % less power than the KK algorithm[21], respectively.

5.3.6 Power consumption of FA-iter-KK algorithm in a loss limited VSB system

Next, we repeat this analysis for the FA-iter-KK algorithm in a VSB system. Remember that in a VSB system, the received signal contains both RSB and LSB spectra, and the FA-iter-KK algorithm tries to recover $Re(s_1[n]) + Re(s_2[n])$ from the sampled photocurrent $I[n]$, where $s_1[n]$ is proportional to the optical field of the RSB spectrum, and $s_2[n]$ is proportional to the complex conjugate of the optical field of the LSB spectrum. Specifically, we have:

$$Re(s_1[n]) + Re(s_2[n]) = \sqrt{I[n] - \{Im(s_1[n]) - Im(s_2[n])\}^2} - C \qquad (5.13)$$

where C is the DC component of the $I[n]$. Eq. 5.13 allows us to estimate $Re(s_1[n]) + Re(s_2[n])$ from $Im(s_1[n]) - Im(s_2[n])$. If we know the frequency responses of the optical filter $H_F(j\omega_k)$ and the CD effect $H_{CD}(j\omega_k)$, we can also estimate $Im(s_1[n]) - Im(s_2[n])$ from $Re(s_1[n]) + Re(s_2[n])$ using:

[21] Considering the power consumption of the ADC channel and the KK related DSP blocks only, if we consider the total power consumption of the entire system, these percentages should be further decreased).

$$\begin{aligned} &Im(s_1[n]) - Im(s_2[n]) \\ &\quad = Im(IDFT\{DFT\{Re(s_1[n]) + Re(s_2[n])\}H_1(j\omega_k)\}) \\ &\quad - Im(IDFT\{DFT\{Re(s_1[n]) + Re(s_2[n])\}H_2(j\omega_k)\}) \end{aligned} \tag{5.14}$$

where $H_1(j\omega_k)$ and $H_2(j\omega_k)$ are given by:

$$\begin{cases} H_1(j\omega_k) = \dfrac{2H_{RSB}(j\omega_k)H_{CD}(j\omega_k)H_F(j\omega_k)}{H_{CD}(j\omega_k)H_F(j\omega_k) + H_{CD}^*(-j\omega_k)H_F^*(-j\omega_k)} \\ H_2(j\omega_k) = \dfrac{2H_{RSB}(j\omega_k)H_{CD}^*(-j\omega_k)H_F^*(-j\omega_k)}{H_{CD}(j\omega_k)H_F(j\omega_k) + H_{CD}^*(-j\omega_k)H_F^*(-j\omega_k)} \end{cases} \tag{5.15}$$

According to the properties of DFT, $DFT\{Im(s_i[n])\}, i = 1,2$ equals to the Hermitian odd component of $DFT\{s_i[n]\}, i = 1,2$, hence if we define:

$$F(j\omega_k) = \frac{1}{2}[-iH_1(j\omega_k) + iH_1^*(-j\omega_k) + iH_2(j\omega_k) - iH_2^*(-j\omega_k)] \tag{5.16}$$

Eq. 5.14 can be simplified to:

$$\begin{aligned} &Im(s_1[n]) - Im(s_2[n]) \\ &\quad = IDFT\{DFT\{Re(s_1[n]) + Re(s_2[n])\}F(j\omega_k)\} \end{aligned} \tag{5.17}$$

The main idea of the FA-iter-KK algorithm is to start by assuming $Im(s_1[n]) - Im(s_2[n]) = 0$, and then uses Eqs. 5.13 and 5.17 iteratively to approach good estimations of $Re(s_1[n]) + Re(s_2[n])$ and $Im(s_1[n]) - Im(s_2[n])$.

Eq. 5.17 can be implemented in the frequency domain using the overlap-and-save algorithm. Note that both $Re(s_1[n]) + Re(s_2[n])$ and $Im(s_1[n]) - Im(s_2[n])$ are real-valued signals, hence the DFT and the IDFT in Eq. 5.17 can be shared between two parallel DSP blocks. Eq. 5.13 should be implemented in the time domain. The square root operation can be implemented as an LUT. Note that if we properly design $F(j\omega_k)$ to remove the DC component, i.e. if we force the tap coefficient at DC to be zero, then the minus C operation in Eq. 5.13 does not need to be implemented explicitly using an additional adder. Similarly, since there is always a frequency-domain filter after the KK-family algorithm, we don't need to implement the minus C operation explicitly at the output of the FA-iter-KK algorithm either.

Fig. 5.23 shows how we can implement the FA-iter-KK algorithm and the following frequency-domain processing block in practice. In this work, we only consider the FA-iter-KK algorithm with 1 iteration to minimize the number of multipliers and adders used in the DFTs/IDFTs. As we will shortly see, 1 iteration can already achieve decent transmission performance in a 100 Gb/s loss limited VSB system over 40 km. By comparing Fig. 5.23 to Fig. 5.18 and Fig. 5.20(a),

we find that, schematic of the FA-iter-KK algorithm looks almost the same as that of the iter-KK algorithm with the same number of iterations. Both the FA-iter-KK algorithm with 1 iteration and the iter-KK algorithm with 1 iteration require $2N$ n_b-bit in n_b-bit out LUTs, 1/2 N-point DFT, 1/2 N-point IDFT, a frequency-domain filter, N extra real multipliers and $4N$ extra real adders per block. The only difference is that, the frequency-domain filter $H_{hil}(j\omega_k)$ in the iter-KK algorithm can be implemented using register operations, since it only includes multiplications with 0 and $\pm i$, but the frequency-domain filter $F(j\omega_k)$ in the FA-iter-KK algorithm has to be implemented using complex multipliers, and each complex multiplier includes 3 real multipliers and 3 real adders, since the tap coefficients of $F(j\omega_k)$ can be pre-computed using Eqs. 5.15 and 5.16.

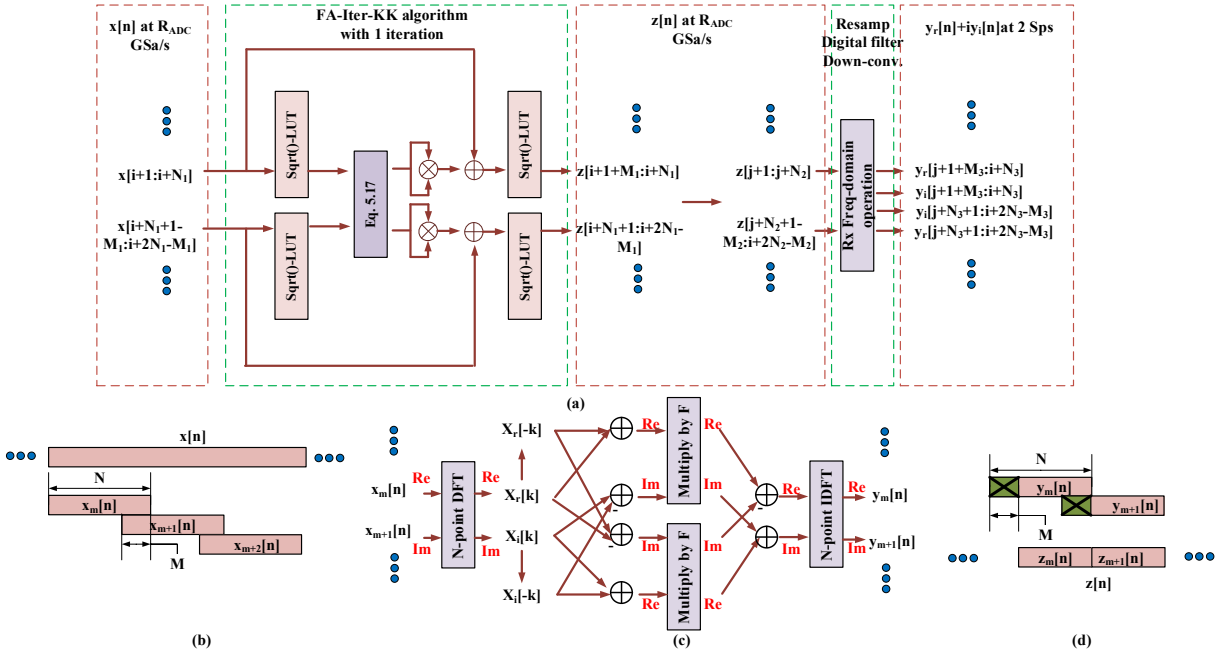

Fig. 5.23 (a) Practical implementations of the FA-iter-KK algorithm with 1 iteration and the following frequency-domain processing block, (b)-(d) principle of filter response aware frequency-domain processing in the FA-iter-KK algorithm, (b) slice the input sequence into overlapping sections, (c) frequency-domain processing of every two parallel sections, and (d) concatenate the processed and shortened sections to form the output sequence.

Based on our discussions above, the DSP stacks of a VSB self-coherent system depicted in Fig. 5.9 can be transformed into the forms shown in Fig. 5.24 for the power consumption analysis. In a VSB system, since we only use one DAC channel, the transmitter-side frequency domain processing block is implemented using the schematic shown in Fig. 5.17(b). The digital

resampling before the FA-iter-KK algorithm is replaced by directly adjusting the sampling rate of the ADC channel. The FA-iter-KK algorithm with 1 iteration is implemented based on the schematics shown in Fig. 5.23. For comparison, we also try the KK algorithm, the ufKK algorithm and the iter-KK algorithm with 1 iteration in the VSB system, and the schematics of these systems are the same as the ones used in the IQ modulator based SSB system described in section 5.3.5. No matter which KK-family algorithm we use, the receiver-side frequency-domain processing block after the KK-family algorithm is always implemented based on the schematic shown in Fig. 5.16. Similar to the IQ modulator based SSB system case, to obtain the frequency-domain filter tap coefficients, we first turn off the frequency-domain filter, and use sufficient taps in the time-domain filter. Next, we use the LMS algorithm to converge the time-domain tap coefficients, and then take the DFT to compute the frequency-domain tap coefficients. This way, the frequency-domain filter can compensate for most of the ISI in the system (e.g. the ISI caused by the CD, the CD induced power fading effect, and the components' bandwidth limitations). Once we turn on the frequency-domain filter, we can minimize the number of taps used in the adaptive time-domain equalizer.

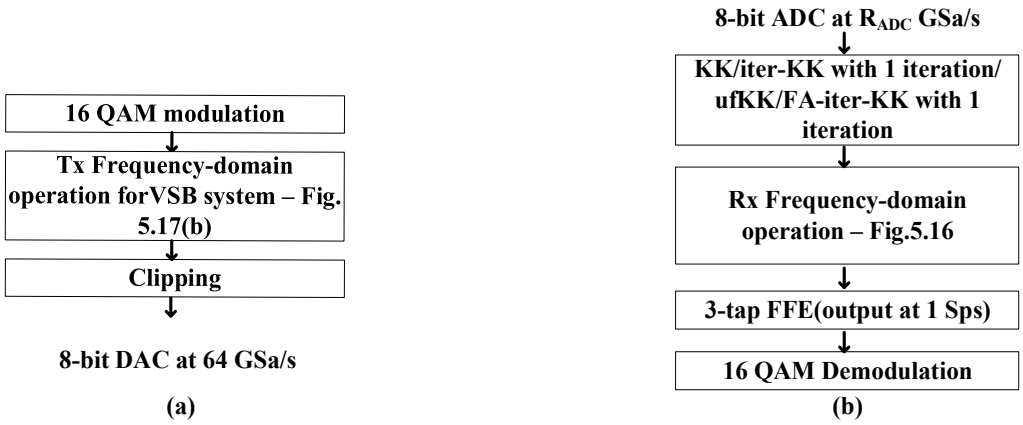

Fig. 5.24 (a) Transmitter and (b) receiver DSP stacks used in a VSB system for the power consumption analysis.

Then we use the link model presented in section 5.2 to study the impacts of DSP parameters on the transmission performance of a 100 Gb/s loss limited VSB system over 40 km. We consider an RC pulse shaped 28 Gbaud passband 16QAM signal with a roll-off factor of 0.1. The guard band is 0.6 GHz (the reason has been provided in section 5.3.5). Similar to the IQ

modulator based SSB system case, we only consider the parallel path structure based CSPR control scheme in the VSB system (Fig. 5.8). The V_{pp}/V_{π} ratio is fixed at 1.4, the splitting ratio in the parallel path structure and the clipping ratio at the DAC are simultaneously optimized. The frequency response of the optical filter is shown in Fig. 5.6, and the rest system parameters are shown in Table 5.1. The results are shown in Fig. 5.25.

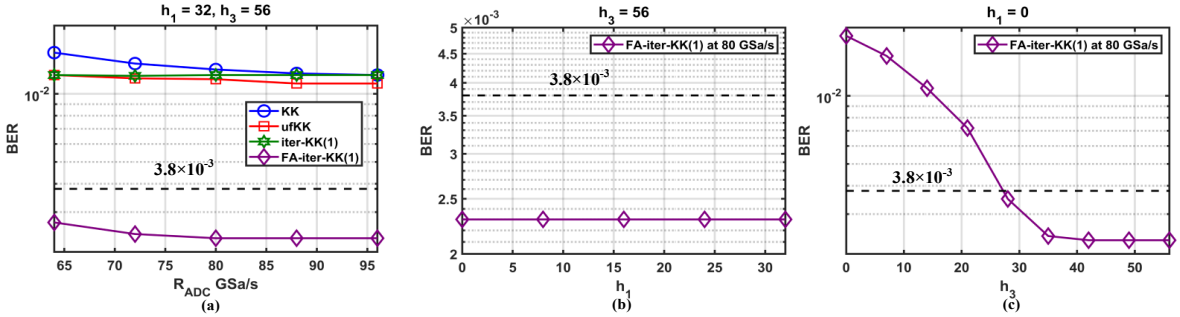

Fig. 5.25 (a) BERs as functions of the ADC sampling rate, when applying different KK-family algorithms in a 100 Gb/s 40 km loss limited VSB self-coherent system, (b) BER as a function of the overlapping sequence length used in the frequency-domain operation in the FA-iter-KK algorithm, and (c) BER as a function of the overlapping sequence length used in the receiver-side frequency-domain processing block after the FA-iter-KK algorithm, when applying the FA-iter-KK algorithm in a 100 Gb/s 40 km loss limited VSB self-coherent system.

Similar to section 5.3.5, here we focus on three parameters: 1) the sampling rate of the ADC channel R_{ADC}, 2) the length of the overlapping sequence used in frequency-domain processing bock inside the FA-iter-KK algorithm h_1 (or the length of the overlapping sequence used in the Hilbert transform in the KK/ufKK/iter-KK cases), and 3) the length of the overlapping sequence used in the frequency-domain processing block after the KK-family algorithm at the output sampling rate h_3, i.e. the overlapping sequence length used at the IDFT. We first use sufficiently large h_1 and h_3 values and sweep R_{ADC}. We find that in a VSB system, among all the four KK-family algorithms considered in this comparison, only the FA-iter-KK algorithm can achieve a BER that is below the HD-FEC threshold of 3.8×10^{-3}, and we observe that as long as R_{ADC} exceeds 80 GSa/s, further increasing R_{ADC} no longer improves the BER performance. Hence in this work, we use $R_{ADC} = 80$ GSa/s for the FA-iter-KK algorithm with 1 iteration in the VSB system. Then we sweep h_1 and h_3 in this case. We find that h_1 does not have a significant impact on the transmission performance, hence we can use $h_1 = 0$. We

also notice that, when h_3 exceeds 35, further increasing h_3 no longer significantly decreases the achievable BER, hence we use $h_3 = 35$ in the following analysis. The required h_3 value is higher than that of the IQ modulator based SSB system. In a VSB system, since the optical filter has a limited edge gradient (8 dB/10 GHz in this work), the CD effect will also lead to power fading (ripples in the spectrum) effect, hence the resulted ISI will span over more samples at 2 Sps (the output sampling rate of the frequency-domain processing block after the KK-family algorithm), and we need more time-domain taps to compensate for the ISI. Remember that a frequency-domain filter with an overlapping sequence length of h_3 is equivalent to a $h_3 + 1$-tap filter in the time domain.

Some readers may wonder that, according to Fig. 5.25(a), if we use $R_{ADC} = 64$ GSa/s, the BER is slightly worse, but it is still below the FEC threshold, and the power consumption of the FA-iter-KK algorithm can be reduced. Why don't we sacrifice the BER performance a bit to reduce the DSP power? Yes, we can always sacrifice the BER performance to reduce the power consumption of the system, but not necessarily the power consumption of the DSP. In this work, we simply push for the best BER performance by using aggressive DSP, and then we reduce the laser's output power to achieve a BER that is just below the FEC threshold. This way, we will reduce the power consumption of the laser since we can reduce the laser's driving current, and a better BER performance can be translated to a larger reduction in the laser's power consumption. This is actually a hidden assumption in section 5.3.5. Remember that in the IQ modulator based SSB system case, we choose the DSP parameters to make sure that the KK algorithm, the ufKK algorithm and the iter-KK algorithm with 1 iteration achieves the same transmission performance, but the achievable BERs are indeed way below the FEC threshold assuming the output power of the laser is 16 dBm. The hidden assumption is that we can always reduce the laser's output optical power (and hence its power consumption) to achieve BERs that are just below the threshold. But since all the algorithms achieve the same BER performance, the potential reduction of the power consumption of the laser should be the same for all the three algorithms, hence we can ignore that part when we compare the power consumption of different algorithms in section 5.3.5. As we will shortly see, in this work, when

we compare the power consumption of a VSB system to that of an IQ modulator based SSB system, we should no longer ignore the laser's power consumption, since the two systems may require different laser output power to achieve BERs that are just below the FEC threshold. Table 5.6 summarizes the receiver-side DSP parameters (for the KK-family algorithm related blocks only) used in a VSB system considered in the power consumption analysis.

Table 5.6 Rx DSP parameters used in a VSB system

symbol	description	FA-iter-KK w/ 1 iteration
R_{sig} [Gbaud]	Symbol rate of the signal	28
f_{clock} [MHz]	Frequency of the clock signal	500
R_{ADC} [GSa/s]	ADC sampling rate (the sampling rate at the input/output of the FA-iter-KK algorithm)	80
p_1	Degree of parallelization of the frequency-domain operation in the FA-iter-KK algorithm	160
h_1	Overlapping sequence length used in the FA-iter-KK algorithm	0
N_1	DFT/IDFT size in the FA-iter-KK algorithm	1024
p_2	Degree of parallelization of the frequency-domain processing block after the FA-iter-KK algorithm	112
N_2	DFT size in frequency-domain processing block after the FA-iter-KK algorithm	1280
h_3	Overlapping sequence length at the IDFT of the frequency-domain processing block after the FA-iter-KK algorithm	35
N_3	IDFT size in frequency-domain processing block after the FA-iter-KK algorithm	896
R_{out} [GSa/s]	Sampling rate at the output of the frequency-domain processing block after the FA-iter-KK algorithm	56

In a VSB system, to achieve a BER that is below the HD-FEC threshold with a 6.7% overhead, we have to use the FA-iter-KK algorithm. But remember that if we use an IQ modulator based SSB system with negligible IQ imbalance, we can generate a rigorous SSB signal, then we can use the iter-KK algorithm with 1 iteration (which is the most power-efficient algorithm according to section 5.3.5). It will be interesting to see how the power consumption of a VSB

loss limited system enabled by the FA-iter-KK algorithm with 1 iteration (with the receiver-side DSP parameters shown in Table 5.6) compares to that of an IQ modulator based SSB loss limited system enabled by the iter-KK algorithm with 1 iteration (with the receiver-side DSP parameters shown in Table 5.4).

In this comparison, we exclude the power consumption of the common components and common DSP blocks of the two systems, which include the power consumption of the thermoelectric cooler (TEC), the PD-TIA, the HD-FEC coding/decoding blocks, the 16QAM modulation/demodulation blocks, the time recovery blocks and the time-domain equalizers, since the power consumption of these parts should be the same in both systems. The remaining parts are: the power consumption of the lasers, the DAC channels, the drivers, the modulators, the transmitter-side frequency-domain processing blocks, the ADC channels, the KK-family algorithms and the receiver-side frequency-domain processing blocks after the KK-family algorithms.

Table 5.7 Parameters of the laser model

symbol	Description	value
γ_{las} [mW/mA]	Slope efficiency	0.137
I_{th} [mA]	Threshold current	40
$V_{LD,f}$ [V]	Forward voltage	2.7

As we have discussed previously, to make a fair comparison between the power consumption of two systems, we need the two systems to achieve the same transmission performance. In this work, we tune the laser's output optical power to achieve BERs that are just below 3.8×10^{-3} in both the VSB system and the IQ modulator based SSB system. We assume that the output power of the laser P_{opt} is related to the driving current I_{LD} through a simple linear model

$$P_{opt}[mW] = \gamma_{las}(I_{LD} - I_{th}) \tag{5.18}$$

where I_{th} is the threshold current of the laser. We use a commercial laser [119] as a reference point to calculate the slope efficiency γ_{las}, so that we can calculate I_{LD} from the required P_{opt} using Eq. 5.18. Then the optical output power dependent part of the laser diode's electrical power consumption (i.e. excluding the power consumption of the TEC) can be estimated as

$$P_{LD,elec} = I_{LD}V_{LD,f} \tag{5.19}$$

where $V_{LD,f}$ is the forward voltage of the laser diode. The parameters used in the laser model are summarized in Table 5.7.

Similar to the ADC case, we follow the model described in [112] to estimate the power consumption of the DAC channel. We assume that the power consumption of the DAC channel is proportional to its bit resolution and sampling rate, and we take a 60 GSa/s 8-bit 7 nm CMOS DAC [119] as a reference point to compute the values. The power consumption of the drivers and the modulators are estimated based on the datasheet of a commercially available DP coherent driver modulator [120] whose specifications are similar to the specifications of the drivers and the modulators considered in our models (Table 5.1).

The transmitter-side system and DSP parameters used in this comparison study are summarized in Table 5.8.

Table 5.8 Tx system parameters and DSP parameters used in different systems

symbol	description	VSB	SSB(IQ)
P_{opt} [dBm]	Output optical power of the laser required to achieve a BER that is just below the FEC threshold	15.5	14.5
n_{DAC}	Number of DAC channels	1	2
n_{dri}	Number of RF drivers	1	2
n_{MZM}	Number of MZMs	1	2
$R_{in,Tx}$ [GSa/s]	Sampling rate at the input of the Tx side frequency-domain processing block	56	56
p_0	Degree of parallelization of the Tx-side frequency-domain processing block	128	128
h_0	Overlapping sequence length in the DFT of the Tx-side frequency-domain processing block	14	14
N_1	DFT/IDFT size in the Tx-side frequency-domain processing block	1024	1024

The estimated power consumption results are shown in Table 5.9 where the power consumption of the common parts of the two systems have been excluded. We observe that the receiver of a VSB system consumes more power than that of an IQ modulator based SSB system, since the sampling rate of the ADC is higher, the overlapping sequence length used in the frequency-domain processing block after the KK-family algorithm is longer, and the frequency-domain filter inside the FA-iter-KK algorithm is more computationally complicated than the Hilbert

transform in the iter-KK algorithm. However, at the transmitter side, although a VSB system requires higher laser output power to achieve the same transmission performance as an IQ modulator based SSB system, which increases the power consumption of the laser, it removes one DAC channel, one RF amplifier and one MZM. In addition, the transmitter-side frequency-domain processing block is simpler than that of the IQ modulator based SSB system. As a result, the transmitter of the VSB system consumes less power than that of the IQ modulator based SSB system, and when we consider the total power consumption of the entire system, we find that the VSB system is more power efficient than the IQ modulator based SSB system.

Table 5.9 Comparison of power consumption of an IQ modulator based SSB system and a VSB system (Excluding common parts)

symbol	description	VSB	SSB(IQ)
$P_{LD,elec}$ [mW]	Power consumed by the laser diode (the output optical power dependent part)	807.3	663.4
P_{DAC} [mW]	Power consumed by the DAC channels	597.3	1194.7
$P_{driv\&mod}$ [mW]	Power consumed by the driver and the modulator	675	1350
P_{TxFreq}	Power consumed by the Tx-side frequency-domain processing block	149.0	187.8
P_{sum1} [W]	Total power consumption of the Tx-side hardware components and DSP blocks that are different between two systems	2.23	3.41
P_{ADC} [mW]	Power consumed by the ADC channel	461.7	369.4
P_{KK} [mW]	Power consumed by the KK-family algorithm	187.5	125.4
P_{RxFreq} [mW]	Power consumed by the frequency-domain processing block after the KK-family algorithm	174.3	158.6
P_{sum2} [W]	Total power consumption of the Rx-side hardware components and DSP blocks that are different between two systems	0.82	0.65
P_{sum} [W]	Total power consumption of the hardware components and DSP blocks that are different between two systems	3.05	4.06

But we should note that, up to now, we have assumed that the receiver DSP always knows the exact frequency response of the optical filter seen by the signal in our model, which is not necessarily true in a real system, because the center frequency of the laser may drift. The laser we considered in this analysis (the commercial laser we used as our reference point) has a

maximum output power of 100 mW (20 dBm) and a maximum wavelength drifting of 40 pm (in the C-band) over the entire operating temperature range [118], hence here we consider a maximum frequency drifting of $\Delta f = \pm 2.5$ GHz with respect to the target central frequency[22]. As a result, the filter response seen by the optical signal will be shifted by $-\Delta f$ as shown in Fig. 5.26(a). But remember that the frequency-domain filter tap coefficients of the FA-iter-KK algorithm and the frequency-domain processing block after the FA-iter-KK algorithm are pre-computed, hence in practice, there might be a mismatch between the $H_F(j\omega_k)$ considered in the DSP and the actual $H_F(j\omega_k)$ seen by the signal, which could degrade the transmission performance.

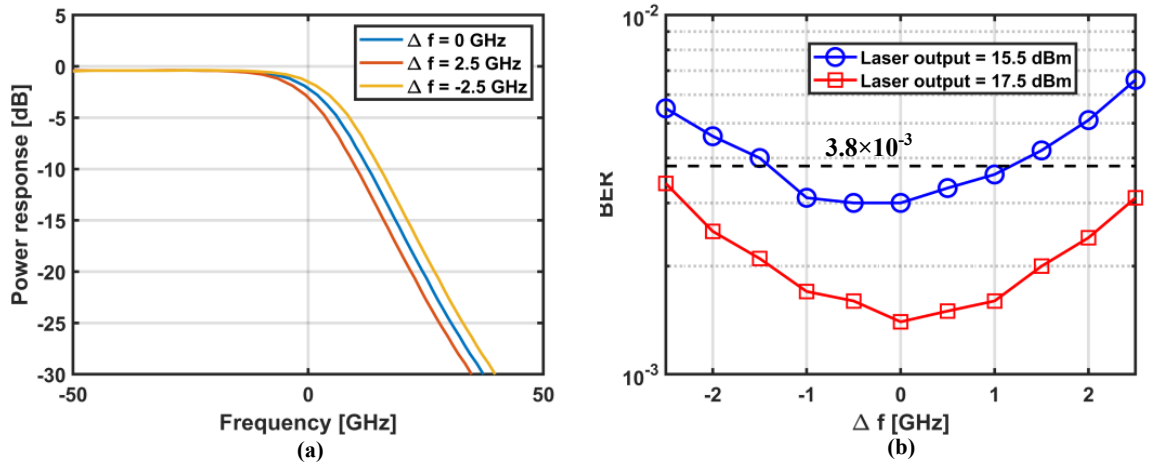

Fig. 5.26 Power response of the optical filter seen by the signal with different laser frequency offsets, and (b) BERs as functions of laser frequency offset with different laser output power.

Fig. 5.26(b) plots the BERs as functions of Δf when using 1) a 15.5 dBm laser and 2) a 17.5 dBm laser. In this study, we first set $\Delta f = 0$ Hz to optimize the frequency-domain tap coefficients in the receiver DSP. Then we fix the frequency-domain taps and vary Δf in the system to study its impact on the transmission performance. Fig. 5.26(b) shows that, to improve the system's tolerance to Δf, we need to increase the laser output power to leave more margin in the zero-frequency-offset case. As we can see from Fig. 5.26(b), once we increase the laser output power to 17.5 dBm, we can achieve a BER that is below the HD-FEC threshold of

[22] Note that the maximum frequency drifting of a typical laser for short-reach applications defined in the 400 ZR IA is $\pm$ 1.8 GHz [4], which is smaller than the value used here.

3.8×10^{-3} over the entire range of $\Delta f \in [-2.5,2.5]$ GHz.

Since we need to increase the laser's output power in a VSB system to improve the system's tolerance to laser frequency drifting, the results shown in Table 5.9 need to be updated. The updated results are shown in Table 5.10.

Table 5.10 shows that, although we need to further increase the laser's output power in a VSB system when we consider the potential mismatch between the $H_F(j\omega_k)$ used in the DSP and the $H_F(j\omega_k)$ seen by the signal due the frequency drifting of the laser, the VSB system enabled by the FA-iter-KK algorithm with 1 iteration can still be more power efficient than the IQ modulator based SSB system enabled by the iter-KK algorithm with 1 iteration.

Table 5.10 Comparison of power consumption of an IQ modulator based SSB system and a VSB system considering the laser frequency drifting (Excluding common parts)

symbol	description	VSB	SSB(IQ)
$P_{LD,elec}$ [mW]	Power consumed by the laser diode (the output optical power dependent part)	1216.6	663.4
P_{DAC} [mW]	Power consumed by the DAC channels	597.3	1194.7
$P_{driv\&mod}$ [mW]	Power consumed by the driver and the modulator	675	1350
P_{TxFreq}	Power consumed by the Tx-side frequency-domain processing block	149.0	187.8
P_{sum1} [W]	Total power consumption of the Tx-side hardware components and DSP blocks that are different between two systems	2.64	3.41
P_{ADC} [mW]	Power consumed by the ADC channel	461.7	369.4
P_{KK} [mW]	Power consumed by the KK-family algorithm	187.5	125.4
P_{RxFreq} [mW]	Power consumed by the frequency-domain processing block after the KK-family algorithm	174.3	158.6
P_{sum2} [W]	Total power consumption of the Rx-side hardware components and DSP blocks that are different between two systems	0.82	0.65
P_{sum} [W]	Total power consumption of the hardware components and DSP blocks that are different between two systems	3.46	4.06

5.3.7 Summary and discussions

In this work, we estimate and compare the power consumption of the KK algorithm, the ufKK algorithm, the iter-KK algorithm with 1 iteration, and the FA-iter-KK algorithm with 1 iteration

in loss limited SSB and VSB self-coherent systems, based on the assumption that the Hilbert transform and the digital resampling are implemented in the frequency domain. Considering the parameters of this study, we find that in a 100 Gb/s IQ modulator based SSB loss limited system over 40 km, the iter-KK algorithm with 1 iteration is the most power-efficient option to achieve a BER that is below the 6.7% overhead HD-FEC threshold of 3.8×10^{-3}, and in a 100 Gb/s VSB loss limited system over 40 km, the FA-iter-KK algorithm with 1 iteration is the only option that can achieve a BER that is below the aforementioned HD-FEC threshold. We further compare the power consumption of a VSB loss limited system enabled by the FA-iter-KK algorithm with 1 iteration and an IQ modulator based SSB loss limited system enabled by the iter-KK algorithm with 1 iteration. We find that although the VSB system needs a higher optical power margin to tolerate the potential drifting of the laser's center frequency, it can still be more power efficient than the IQ modulator based SSB system. But we should note that, the results presented here are highly dependent on the modelling parameters. The conclusions may change if the parameters used in our models are changed. The take-home messages of this work are:

1) Once we implement the KK-family algorithms in the frequency domain, the fact that KK-family algorithms require higher sampling rate does not significantly increase the power consumption of the receiver DSP. The resampling block before the KK-family algorithm can be replaced by directly changing the sampling rate of the ADC channel, and the resampling block after the KK-family algorithm can be merged into the CD compensation block which cannot be omitted anyway.
2) When we compare the power consumption of IQ modulator based SSB systems processed with different KK-family algorithms, we have limited our discussions to the power consumption of the DSP blocks, which are estimated based on their computational complexities using the same methods, hence it is fair to say that the iter-KK algorithm with 1 iteration is less power consuming than the KK algorithm and the ufKK algorithm.
3) The FA-iter-KK algorithm looks complicated at first glance, but when we implement it in the frequency domain, we find that it has almost the same computational complexity as the

original iter-KK algorithm with the same number of iterations when operating at the same sampling rate. The only difference is that in the iter-KK algorithm, the implementation of the Hilbert transform can be further simplified since it only includes multiplications by 0 and $\pm i$.

4) Compared to the IQ modulator based SSB system, the VSB system generally achieves worse performance when using the same laser's output power and the same DSP parameters, hence to achieve the same performance, we need to increase the laser's output power and use more aggressive DSPs. But it also saves one DAC channel and one RF amplifier. Considering the parameters of this study, we find that the VSB system can be more power efficient than the IQ modulator based SSB system. However, if there exist DACs and RF amplifiers with similar performance as the ones used in our analysis but has significantly lower power consumption, if the slope efficiency of the laser is much higher than the value used in our model, or if we have to use an optical filter with a higher insertion loss, the IQ modulator based SSB system may be more power efficient than the VSB system.
5) More importantly, this work introduces a general method to compare the power consumption of the hardware components and DSP algorithms required to achieve certain transmission performance in loss limited SSB and VSB self-coherent systems. If the system/DSP parameters change, we simply need to redo the analysis using the same method with new parameters. Specifically, we can first use the link models developed in section 5.2 to determine the system parameters and DSP parameters to achieve certain BERs, and then use the power consumption models described in section 5.3 to estimate the power consumption of hardware components and DSP algorithms. In this work, we choose the system/DSP parameters based on our lab experience and our knowledge of the state-of-the-art components.

We hope this work shines a light on practical implementations of KK-family algorithms in loss limited SSB and VSB systems.

Chapter 6 Conclusion

6.1 Summary of presented work

In this thesis, we explored the potentials and the limits of O-band IM/DD systems and C-band SSB/VSB self-coherent detection systems for data center networking applications.

In Chapter 3, we demonstrated two methods to improve the transmission performance of the current O-band CWDM4 IM/DD solutions. Firstly, in section 3.2, we proposed to replace a portion of the FFE based pre-emphasis with either transmitter-side THP or receiver-side FFE aided with post-filter + MLSE, so that we can increase the AC power of the received signal without significantly increasing the equalization enhanced noise. We experimentally demonstrated 600 Gb/s net rate PAM4 transmission over 2-10 km with a commercialized CWDM4 TOSA using this method. Secondly, in section 3.3, we showed that by combining a symbol-wise wavelength interleaver with a pair of 4D-PAM4-TCM encoder and decoder, we can improve the robustness of an O-band CWDM4 IM/DD system against the inter-channel performance differences caused by inter-channel component differences and the CD-chirp interactions, which allows us to extend the reach of the system. We experimentally proved that the proposed wavelength-interleaved 4D-PAM4-TCM scheme outperforms the conventional time-domain encoded 4D-PAM4-TCM scheme and the traditional PAM4 scheme in a 400 Gb/s PAM4 system over 0-20 km using a commercialized CWDM4 TOSA.

Another approach to extend the reach of an IM/DD system is to upgrade it to an SSB/VSB self-coherent system. Since an SSB/VSB self-coherent system enables CD compensation in the DSP, it can be operated in the C-band. In Chapter 4, we studied the possibility of using single-wavelength amplified VSB self-coherent systems in typical inter-data center connections over 40-80 km. In section 4.2, we showed that to extend the reach of a 100 Gb/s DAC-less PAM4 transmitter based C-band IM/DD system to 80 km, we simply need to insert an optical filter between the modulator and the PD, and upgrade the receiver DSP. We also comprehensively studied the impacts of the linear and nonlinear impairments on the transmission performance of this VSB-PAM4 system and their mitigation methods. A problem of the VSB system is that

an optical filter generally has a limited edge gradient, thus the received signal is usually not strictly SSB, but the existing field reconstruction algorithms (e.g. the KK algorithm) are designed for rigorous SSB signals. To solve this problem, in section 4.3, we proposed an FA-iter-KK algorithm which uses the frequency response of the optical filter to facilitate the field reconstruction process. We experimentally proved that the FA-iter-KK algorithm outperforms the conventional field reconstruction algorithms in a 100 Gb/s DAC-less-VSB-PAM4 system over 40-80 km, and we further showed through simulation that this algorithm has the potential to reduce the filter edge gradient requirement in a VSB system. Another important feature of an SSB/VSB system is that, the CSPR generally needs to be optimized for different system parameters. In section 4.4, we demonstrated a SiPh transmitter circuit which enables on-chip CSPR control in a VSB system. This so-called parallel path structure based CSPR control scheme decouples the control of the CSPR and the control of the modulator's bias point, hence it allows us to always bias the modulator at the null point and minimize the device nonlinearity introduced by the modulator.

As we have mentioned in Chapter 1, section 1.2, the future of the C-band SSB/VSB self-coherent system lies in 100 Gb/s per wavelength unamplified loss limited links over 40 km. In Chapter 5, we built parameterized numerical models to estimate the transmission performance and the power consumption of the loss limited IQ modulator based SSB systems and the loss limited VSB systems. Specifically, we addressed the following two questions: 1) Which CSPR control scheme should we use in a loss limited SSB/VSB self-coherent system? and 2) Which field reconstruction algorithm should we use in a loss limited SSB/VSB self-coherent system? We found that although the parallel path structure based CSPR control scheme increases the optical loss at the transmitter, it reduces the device nonlinearity introduced by the modulator. Hence if the system can achieve a relatively large V_{pp}/V_{π} ratio (e.g. V_{pp}/V_{π}>1), the parallel path structure based CSPR control scheme can still achieve better transmission performance than directly tuning the bias point of the modulator even in a loss limited system. As for the field reconstruction algorithms, we found that in an IQ modulator based rigorous SSB system, among all the four KK-family algorithms considered in this study, the iter-KK algorithm with

1 iteration is the most power efficient option. In a VSB system however, if we are targeting a BER that is below the 6.7% overhead HD-FEC threshold after transmission over 40 km, we can only use the FA-iter-KK algorithm. We further revealed that, although the VSB system requires higher laser power and more complicated receiver DSP than the IQ modulator based SSB system, its transmitter DSP is simpler, and it removes one DAC channel, one RF amplifier and one MZM. Consequently, it is possible that the total system power consumption of a VSB system enabled by the FA-iter-KK algorithm with 1 iteration is less than that of an IQ modulator enabled by the iter-KK algorithm with 1 iteration. More importantly, in Chapter 5, we put forward a general method to estimate and compare the transmission performance and the system power consumption of SSB/VSB loss limited systems with different system parameters. We believe this work shines a light on practical implementations of SSB and VSB self-coherent systems.

6.2 Future work

Remember that in Chapter 3 we have introduced two distinct methods to improve the transmission performance of an O-band CWDM4 IM/DD system, i.e. the FTN method to increase the bit rate, and the wavelength-interleaved 4D-PAM4-TCM scheme to improve the system's tolerance to inter-channel performance discrepancies and increase the reach.

A natural next step is to combine these two methods in the same system, so that we can increase both the capacity and the reach without prior knowledge of the components and the link. The major challenge is to combine the THP or the MLSE with the 4D-TCM encoder/decoder, since implementing a symbol-level wavelength interleaver is rather straightforward. Note that both the MLSE and the TCM require Viterbi decoding at the receiver. If we use hard-decision Viterbi decoding, we could not directly concatenate the MLSE and the TCM decoder, since the soft information required by the TCM decoder is lost after the MLSE stage. One promising direction is to use a modified Viterbi decoder that employs a super-trellis to achieve equalization and TCM decoding simultaneously [121]. Such super-trellis can be constructed by combining the TCM encoder states with the channel states induced by post filter. Another direction is to use the soft-decision output Viterbi algorithm [122]. On the other hand, combing

the THP with the 4D-TCM is much simpler. One can simply implement the THP after the TCM encoder at the transmitter, and apply modulo operation at the receiver after the FFE and before the TCM decoder. But remember that THP suffers from data flipping problem (please refer to Chapter 2, section 2.3.3.3), and due to the operation principle of the Viterbi decoder, if we combine the THP and the TCM, data flipping will not only affect the decision at the current time interval, but also affect the decisions in the future. To solve this problem, we need to slightly modify the Viterbi decoder by extending the constellation in the subset slicer [66],[123].

In Chapter 4, section 4.3, we have proposed an FA-iter-KK algorithm which improves the accuracy of field reconstruction process in a VSB system. Remember that in Chapter 2, section 2.4.1, we mentioned that a twin SSB system can be regarded as two parallel VSB systems that are multiplexed together in a smart way [73]-[75]. In a twin SSB system, an IQ modulator is used to generate the combination of the RSB of a real-valued signal A and the LSB of another real-valued signal B, then after transmission, the light is divided into two branches and detected by two VSB receivers. Specifically, one VSB receiver will detect the (quasi-)RSB spectrum, and the other VSB receiver will detect the (quasi-)LSB spectrum. The residual unwanted sideband due to the limited edge gradients of the optical filters will also degrade the performance of a twin SSB system if we use the conventional KK-family algorithms to reconstruct the complex-valued field information. Therefore, an attractive short-term research topic is to modify the FA-iter-KK algorithm for a twin-SSB system. Note that in a VSB system, the RSB signal and the complex conjugate of the LSB signal are related through a linear filter, which is uniquely determined by the filter response and the CD effect, but in a twin SSB system, the RSB and the LSB spectra contain independent information. Hence most likely we need to jointly process the two photocurrents from the two VSB receivers in each iteration to simultaneously estimate the field information of signal A and signal B. It will also be interesting to see how the computational complexity of this joint processing block compares to that of two independent FA-iter-KK blocks.

Remember that in Chapter 2, section 2.4.2.3, we mentioned that the residual unwanted sideband will lead to power fading effect in a VSB system. If we use receiver-side equalization to

compensate for the power fading effect, the frequency-domain dips in the channel's magnitude response will lead to equalization enhanced noise. Moreover, the depths of the frequency-domain dips depend on the power difference between the LSB components and the RSB components, hence in a VSB system, the power fading effect in the low frequency regime is generally more severe than the power fading effect in the high frequency regime. Consequently, it could be beneficial to load different SEs to different frequency regimes through bit/entropy loading [124],[125] especially when the filter edge gradient is small. Note that the FA-iter-KK algorithm we proposed in Chapter 4 relaxes the requirement for the filter's edge gradient in a VSB system, and in Fig. 2.24 we showed that as we reduce the edge gradient of the filter, the power fading effect also becomes more severe. Therefore, another promising future work about the VSB self-coherent system is to customize the modulation format for different optical filter designs and transmission distances to maximize the capacity.

Finally, in Chapter 5, we have described a general method to estimate the transmission performance and the power consumption of a loss limited SSB/VSB self-coherent system. An appealing next step is to extend our models to cover other system configurations, such as the loss limited O-band IM/DD system and the loss limited C-band DP coherent system, so that we can compare different system configurations in terms of the power consumption required to achieve the certain transmission performance (e.g. certain bitrate with certain BER at certain transmission distance). This activity will be of great interest to the community, since it may eventually answer the questions:

1) Where is the border between the "IM/DD realm" and the "coherent realm"?
2) Can the SSB/VSB self-coherent system really beat the IM/DD system and/or the coherent system in terms of energy consumed per bit? If yes, in which form and in which application scenario (e.g. at which speed and which distance)?

Reference

[1] "Data Center Interconnect Essentials-Connecting Data centers" *DCI Essentials Ebook*, Ciena Corp., 2019. [Online]. Available: https://www.ciena.com/insights/ebooks/data center-interconnect-essentials.html.

[2] K. Zhong *et al.*, "Digital Signal Processing for Short-Reach Optical Communications: A Review of Current Technologies and Future Trends," in *IEEE J. Lightw. Technol.*, vol. 36, no. 2, pp. 377-400, 2018.

[3] "Optoelectronics & Photonics", *2021 Optoelectronics & Photonics Portfolio*, MACOM, 2021. [Online]. Available: https://www.macom.com/Optoelectronics.

[4] "Implementation Agreement 400 ZR", *OIF-400ZR-01.0*, OIF, 2020. [Online]. Available: https://www.oiforum.com/technical-work/hot-topics/400zr-2/.

[5] J. Houghson, "Understanding Data Center Interconnect: Inter-Data Center", Neophotonics.com. Available: https://www.neophotonics.com/what-is-inter-data-center-interconnect-dci/.(accessed Mar. 21, 2021).

[6] "400G-FR4 Technical Specification", *400G-FR4 Technical Specification Rev 2.0*, 100G Lambda MSA Group, 2018. [Online]. Available: https://100glambda.com/specifications/download/2-specifications/7-400g-fr4-technical-spec-d2p0.

[7] *Datasheet of Corning SMF 28 ultra optical filter*, Corning, 2014. [Online]. Available: https://www.corning.com/media/worldwide/coc/documents/Fiber/SMF-28%20Ultra.pdf.

[8] "Characteristics of a single-mode optical fibre and cable", *ITU-T Recommendation G.652,* Telecommuncation standardization sector of ITU, 2016. [Online]. Available: file:///G:/Zotero_Storage/storage/K4M5PB7S/en.html.

[9] A. Samani et *al*., "A low-voltage 35-GHz silicon photonic modulator enabled 112-Gb/s transmission system," in *IEEE Photon. J.*, vol. 7, no. 3, pp. 1–13, 2015.

[10] W. Wang *et al.*, "Advanced digital signal processing for reach extension and

performance enhancement of 112 Gb/s and beyond direct detected DML-based transmission," in *IEEE J. Lightw. Technol.*, vol. 37, no. 1, pp. 163-169, 2019.

[11] C. Xie *et al.*, "Single-VCSEL 100-Gb/s short-reach system using discrete multi-tone modulation and direct detection," in *Proc. Opt. Fiber Commun.*, Los Angeles, CA, USA, 2015, Paper Tu2H.2.

[12] L Sun *et al.*, "Multiband Three-dimensional carrierless amplitude phase modulation for short reach optical communications," in *IEEE J. Lightw. Technol.*, vol. 34, no. 13, pp. 3103–3109, 2016.

[13] K. Zhong *et al.*, "Experimental study of PAM-4, CAP-16, and DMT for 100 Gb/s short reach optical transmission systems," in *Opt. Express*, vol. 23, no. 2, pp. 1176–1189, 2015.

[14] "IEEE Standard for Ethernet Amendment 10: Media Access Control Parameters, Physical Layers, and Management Parameters for 200 Gb/s and 400 Gb/s Operation", *IEEE 802.3bs*, IEEE, 2017. [Online]. Available: https://ieeexplore.ieee.org/document/8207825.

[15] "400G-LR4-10 Technical Specification", *400G-LR4-10 Technical Specification Draft 1.0*, 100G Lambda MSA Group, 2020. [Online]. Available: https://100glambda.com/specifications/download/2-specifications/10-400g-lr4-10-technical-spec-rev1-0.

[16] "100G-LR1-20, 100G-ER1-30, 100G-ER1-40 Technical Specifications", *100G-LR1-20, 100G-ER1-30, 100G-ER1-40 Technical Specifications Rev. 1.0*, 100G Lambda MSA Group, 2020. [Online]. Available: https://100glambda.com/specifications/download/2-specifications/11-100g-lr1-20-er1-technical-specs-rev-1p0.

[17] "IEEE Standard for Ethernet-Amendment 11: Physical Layers and Management Parameters for 100 Gb/s and 400 Gb/s Operation over Single-Mode Fiber at 100 Gb/s per Wavelength", *IEEE 802.3cu-2021*, IEEE, 2021. [Online]. Available: https://standards.ieee.org/standard/802_3cu-2021.html.

[18] G. P. Agrawal, *Nonlinear fiber optics*, 5th ed, Boston, MA, USA: Academic Press, 2013.

[19] "IEEE Standard for Ethernet-Amendment 4: Physical Layers and Management Parameters for 50 Gb/s, 200Gb/s and 400 Gb/s Operation over Single-Mode Fiber", *IEEE 802.3cn-2019*, IEEE, 2019. [Online]. Available: https://ieeexplore.ieee.org/document/8937109.

[20] Z. Li *et al.*, "SSBI Mitigation and the Kramers–Kronig Scheme in Single-Sideband Direct-Detection Transmission With Receiver-Based Electronic Dispersion Compensation," in *IEEE J. Lightw. Technol.*, vol. 35, no. 10, pp. 1887-1893, 2017.

[21] X. Chen *et al.*, "218-Gb/s single-wavelength, single-polarization, single-photodiode transmission over 125-km of standard singlemode fiber using Kramers-Kronig detection," in in *2017 Opt. Fiber Commun. Conf. and Exhib. (OFC)*, Los Angeles, CA, USA, 2017, paper Th5B.6.

[22] X. Li *et al.*, "Demonstration of C-Band Amplifier-Free 100 Gb/s/ Direct-Detection Links Beyond 40-km SMF Using a High-Power SSB Transmitter," in *IEEE J. Lightw. Technol.*, vol. 38, no. 22, pp. 6170-6177, 2020.

[23] M. Zhu *et al.*, "56-Gb/s Optical SSB PAM-4 Transmission over 800-km SSMF Using DDMZM Transmitter and Simplified Direct Detection Kramers-Kronig Receiver," in *2018 Opt. Fiber Commun. Conf.*, San Diego, CA, USA, 2018, paper M2C.5.

[24] M. Zhu *et al.*, "Optical single side-band Nyquist PAM-4 transmission using dual-drive MZM modulation and direct detection," in *Opt. Express*, vol. 26, no. 6, pp. 6629-6638, 2018.

[25] Z. Wan *et al.*, "64-Gb/s SSB-PAM4 Transmission Over 120-km Dispersion-Uncompensated SSMF With Blind Nonlinear Equalization, Adaptive Noise-Whitening Postfilter and MLSD," in *IEEE J. Lightwav. Technol.*, vol. 35, no. 23, pp. 5193-5200, 2017.

[26] S. An *et al.*, "FTN SSB 16-QAM Signal Transmission and Direct Detection Based on Tomlinson-Harashima Precoding With Computed Coefficients," in *IEEE J. Lightw.*

Technol., vol. 39, no. 7, pp. 2059-2066, 2021.

[27] N. Kaneda *et al.*, "Nonlinear equalizer for 112-Gb/s SSB-PAM4 in 80-km dispersion uncompensated link," in *2017 Opt. Fiber Commun. Conf. and Exhib. (OFC)*, Los Angeles, CA, USA, 2017, paper Tu2D.5.

[28] J. Li *et al.*, "VSB Modified Duobinary PAM4 Signal Transmission in an IM/DD System With Mitigated Image Interference," in *IEEE Photon. Technol. Lett.*, vol. 32, no. 7, pp. 363-366, 2020.

[29] H. Chen *et al.*, "Comparison of VSB PAM4 and OOK Signal in an EML-Based 80-km Transmission System," in *IEEE Photon. Technol. Lett.*, vol. 29, no. 23, pp. 2063-2066, 2017.

[30] N. Diamantopoulos *et al.*, "56-Gb/s VSB-PAM-4 over 80-km Using 1550-nm EA-DFB Laser and Reduced-Complexity Nonlinear Equalization," in *2017 Eur. Conf. on Opt. Commun. (ECOC)*, Gothenburg, Sweden, 2017, pp. 1-3.

[31] J. Zhang *et al.*, "100 Gbit/s VSB-PAM-n IM/DD transmission system based on 10 GHz DML with optical filtering and joint nonlinear equalization," in *Opt. Express*, vol. 27, no. 5, pp. 6098-6105, 2019.

[32] Z. Xing *et al.*, "Experimental Demonstration of 600 Gb/s Net Rate PAM4 Transmissions Over 2 km and 10 km with a 4-λ CWDM TOSA," in *IEEE J. Lightw. Technol.*, vol. 38, no. 11, pp. 2968-2975, 2020.

[33] Z. Xing *et al.*, "600G PAM4 transmission using a 4-lambda CWDM TOSA based on controlled-ISI pulse shaping and Tomlinson-Harashima precoding," in *45th Eur. Conf. on Opt. Commun. (ECOC 2019)*, Dublin, Ireland, 2019, paper Tu.3.D.1.

[34] Z. Xing *et al.*, "Wavelength-Interleaved 4D-PAM4-TCM in a 4-λ × 100 Gb/s CWDM System," in *IEEE Photon. Technol. Lett.*, vol. 32, no. 13, pp. 755-758, 2020.

[35] Z. Xing *et al.*, "100 Gb/s PAM4 transmission system for datacenter interconnects using a SiP ME-MZM based DAC-less transmitter and a VSB self-coherent receiver," in *Opt. Express*, vol. 26, no. 18, pp. 23969-23979, 2018.

[36] Z. Xing *et al.*, "Filter Response Aware Iterative KK Algorithm for VSB systems," in

46th Eur. Conf. on Opt. Commun. (ECOC), Brussels, Belgium, 2020, paper Th2D.8.

[37] Z. Xing *et al.*, "SiPh Self-coherent Transmitter Circuit with on-chip CSPR Control Capability based on a Tunable Power Splitter," in *2019 Opt. Fiber Commun. Conf.* (OFC), San Diego, CA, USA, 2019, paper Tu2H.3.

[38] Z. Xing *et al.*, "On computational complexities of KK algorithms with frequency-domain digital resampling", in *Adv. Photon. Congr. (IPR, NP, NOMA, PVLE, PSC, NETWORKS, SPPcom, SOF)*, Montreal, Canada, 2020, paper SPTu1I.6.

[39] E. Agrell *et al.*, "Information-Theoretic Tools for Optical Communications Engineers," in *2018 IEEE Photon. Conf. (IPC)*, Reston, VA, USA, 2018, pp. 1-5.

[40] K. Roberts *et al.*, "Beyond 100Gb/s: Capacity, flexibility, and network optimization," in *J. Opt. Commun. Netw.*, vol. 9, no. 4, pp. C12–C24, 2017.

[41] H. Sun *et al.*, "Real-time measurements of a 40 Gb/s coherent system," in *Opt. Express.*, vol. 16, no. 2, pp. 873–879, 2008.

[42] "Interfaces for the Optical Transport Network", *ITU-T Recommendation G.709/Y.1331.*, Telecommuncation standardization sector of ITU, 2020. [Online]. Available: https://www.itu.int/rec/T-REC-G.709-202006-I/en.

[43] P. Littlewood *et al*., "Optical Transport Networking – Master the ins and outs of OTN", *Experts guide on OTN Ebook*, Ciena Corp., 2015. [Online]. Available: https://www.ciena.com/insights/ebooks/Expert-Series-Experts-Guide-to-OTN-Utilities-Edition.html.

[44] P. Dong *et al.*, "High-speed low-voltage single-drive push-pull silicon Mach-Zehnder modulators," in *Opt. Express*, vol. 20, no. 6, pp. 6163-6169, 2012.

[45] M. Chagnon, "Optical Communications for Short Reach," in *IEEE J. Lightw. Technol.*, vol. 37, no. 8, pp. 1779-1797, 2019.

[46] L. A. Neto *et al.*, "Simple estimation of fiber dispersion and laser chirp parameters using the downhill simplex fitting algorithm," in *IEEE J. Lightw. Technol.*, vol. 31, no. 2, pp. 334–342, 2013.

[47] W. Shieh *et al.*, "Equalization-enhanced phase noise for coherent-detection systems

using electronic digital signal processing," in *Opt. Express*, vol. 16, no. 20, pp. 15718-15727, 2008.

[48] J. R. O'Callaghan *et al.*, "Refractive index contributions to phase shifting in InP based 30 GHz bandwidth n-i-n Mach-Zehnder Modulators," in *IPRM 2011 - 23rd Int. Conf. on Indium Phosphide and Related Mater.*, Berlin, Germany, 2011, pp. 1-4.

[49] L. Chrostowski *et al.*, *Silicon Photonics Design: From Device to Systems*, Cambridge, MA, USA: Cambridge University Press, 2015.

[50] G. P. Agrawal, *Fiber Optics Communication Systems* 4th ed, Hoboken, NJ, USA: Wiley, 2010.

[51] J. G. Proakis and M. Salehi, *Digital Communications,* 5th ed. New York, NY, USA: McGrawHill, 2008.

[52] N. Benvento and G. Cherubini, *Algorithms for Communication Systems and their Applications,* Chichester England: Wiley, 2002.

[53] Y. Gao *et al.*, "Direct-Detection Optical OFDM Transmission System With Pre-Emphasis Technique," in *IEEE J. Lightw. Technol.*, vol. 29, no. 14, pp. 2138-2145, 2011.

[54] J. Zhang *et al.*, "EML-based IM/DD 400G (4×112.5-Gbit/s) PAM-4 over 80 km SSMF based on linear pre-equalization and nonlinear LUT pre-distortion for inter-DCI applications," in *2017 Opt. Fiber Commun. Conf. and Exhib. (OFC)*, Los Angeles, CA, USA, 2017, paper W4I.4.

[55] J. Fan *et al.*, "MLSE equalizer with channel shortening for faster-than-Nyquist signaling," in *IEEE Photon. Technol. Lett.*, vol. 30, no. 9, pp. 793–796, 2018.

[56] K. Zhong *et al.*, "Experimental demonstration of 500 Gbit/s short reach transmission employing PAM4 signal and direct detection with 25Gbps device," in *2015 Opt. Fiber Commun. (OFC)*, Los Angeles, CA, USA, 2015, Paper Th3A.3.

[57] M. Tomlinson, "New automatic equaliser employing modulo arithmetic," in *Electron. Lett.*, vol. 7, nos. 5–6, pp. 138–139, 1971.

[58] H. Harashima and H. Miyakawa, "Matched-transmission technique for channels with

intersymbol interference," in *IEEE Trans. Commun.*, vol. TCOMM-20, no. 4, pp. 774–780, 1972.

[59] R. D. Wesel and J. M. Cioffi, "Achievable rates for Tomlinson–Harashima precoding," in *IEEE Trans. Inf. Theory.*, vol. 44, no. 2, pp. 824–831, 1998.

[60] M. Xiang *et al.*, "Single-lane 145 Gbit/s IM/DD transmission with faster-than-Nyquist PAM4 signaling," in *IEEE Photon. Technol. Lett.*, vol. 30, no. 13, pp. 1238–1241, 2018.

[61] Q. Hu *et al.*, "Up to 94 GBd THP PAM-4 transmission with 33 GHz bandwidth limitation," in *44th Eur. Conf. Exhib. Opt. Commun. (ECOC)*, Rome, Italy, 2018, pp. 1–3.

[62] Q. Hu *et al*., "IM/DD Beyond Bandwidth Limitation for Data Center Optical Interconnects," in *IEEE J. Light. Technol.*, vol. 37, no. 19, pp. 4940-4946, 2019.

[63] J. Li *et al.*, "Approaching Nyquist Limit in WDM Systems by Low-Complexity Receiver-Side Duobinary Shaping," in *IEEE J. Lightw. Technol.*, vol. 30, no. 11, pp. 1664-1676, 2012.

[64] G. Ungerboeck, "Channel coding with multilevel/phase signals," in *IEEE Trans. Inf. Theory*, vol. 28, no. 1, pp. 55-67, 1982.

[65] C. Prodaniuc *et al.*, "Performance comparison between 4D trellis coded modulation and PAM-4 for low-cost 400 gbps WDM optical networks," in *IEEE J. Lightw. Technol.*, vol. 34, no. 22, pp. 5308–5316, 2016.

[66] M. Xiang *et al.*, "Experimental study of performance enhanced IM/DD transmissions combining 4D trellis coded modulation with precoding," in *Opt. Express*, vol. 26, no. 25, pp. 32522–32531, 2018.

[67] N. Stojanovic *et al.*, "4D PAM-7 trellis coded modulation for data centers," *IEEE Photon. Technol. Lett.*, vol. 31, no. 5, pp. 369–372, 2019.

[68] F. Gardner, "A BPSK/QPSK Timing-Error Detector for Sampled Receivers," in *IEEE Trans. Commun.*, vol. 34, no. 5, pp. 423-429, 1986.

[69] D. Godard, "Passband Timing Recovery in an All-Digital Modem Receiver," in *IEEE*

Trans. Commun., vol. 26, no. 5, pp. 517-523, 1978.

[70] S. J. Lee, "A new non-data-aided feedforward symbol timing estimator using two samples per symbol," in *IEEE Commun. Lett.*, vol. 6, no. 5, pp. 205-207, 2002.

[71] N. Stojanovic *et al.*, "Feed-forward and feedback timing recovery for Nyquist and faster than Nyquist systems," in *2014 Opt. Fiber Commun. Conf.*, San Francisco, CA, USA, 2014, paper Th3E.3.

[72] K. Kikuchi, "Fundamentals of Coherent Optical Fiber Communications," in *IEEE J. Lightw. Technol.*, vol. 34, no. 1, pp. 157-179, 2016.

[73] L. Zhang *et al.*, "Transmission of 112-Gb/s+ DMT over 80-km SMF enabled by twin-SSB technique at 1550nm," in *2015 Eur. Conf. on Opt. Commun. (ECOC)*, Valencia, Spain, 2015, pp. 1-3.

[74] Y. Zhu *et al.*, "Beyond 200G Direct Detection Transmission With Nyquist Asymmetric Twin-SSB Signal at C-Band," in *IEEE J. Lightwave Technol*., vol. 35, no. 17, pp. 3629-3636, 2017.

[75] S. Fan *et al.*, "264 Gb/s Twin-SSB-KK Direct Detection Transmission Enabled by MIMO Processing," in *2018 Optic. Fiber Commun. Conf. (OFC)*, San Diego, CA, USA, 2018, paper W4E.5.

[76] T. M. Hoang *et al.*, "Single wavelength 480 Gb/s direct detection over 80km SSMF enabled by Stokes vector Kramers Kronig transceiver," in *Opt. Express*, vol. 25, no. 26, pp. 33534-33542, 2017.

[77] D. Che *et al.*, "Single-Channel 480-Gb/s Direct Detection of POL-MUX IQ Signal Using Single-Sideband Stokes Vector Receiver," in *2018 Opt. Fiber Commun. Conf. (OFC)*, San Diego, CA, USA, 2018, paper Tu2C.7.

[78] D. Che *et al.*, "Maximizing the spectral efficiency of Stokes vector receiver with optical field recovery," in *Opt. Express*, vol. 26, no. 22, pp. 28976-28981, 2018.

[79] Y. Zhu *et al.*, "Direct detection of polarization multiplexed single sideband signals with orthogonal offset carriers," in *Opt. Express*, vol. 26, no. 12, pp. 15887-15898, 2018.

[80] A. Mecozzi *et al*., “Kramers–Kronig coherent receiver,” in *Optica*, vol. 3, no. 11, pp. 1220-1227, 2016.

[81] T. Bo *et al.*, “Toward practical Kramers-Kronig receiver: resampling, performance, and implementation,” in IEEE J. Lightw. Technol., vol. 37, no. 2, pp. 461-469, 2019.

[82] T. Bo *et al.*, “Kramers-Kronig receiver operable without digital upsampling,” in Opt. Express, vol. 26, no. 11, pp. 13810-13818, 2018.

[83] M. Zhu *et al.*, “Influence of EEPN and P2A noise with CD pre- and post-compensation in optical SSB transmission and Kramers-Kronig receiver system,” in *Opt. Express*, vol. 27, no. 14, pp. 19664-19674, 2019.

[84] Q. Zhuge *et al.*, “Spectral efficiency-adaptive optical transmission using time domain hybrid QAM for agile optical networks,” in *IEEE J. Lightw. Technol.*, vol. 31, no. 15, pp. 2621–2628, 2013.

[85] J. Cho and P. J. Winzer, “Probabilistic Constellation Shaping for Optical Fiber Communications,” in *IEEE J. Lightw. Technol.*, vol. 37, no. 6, pp. 1590- 1607, 2019.

[86] A. Aimone *et al.*, “DAC-free Ultra-Low-Power Dual-Polarization 64-QAM Transmission with InP IQ Segmented MZM Module,” in *2016 Opt. Fiber Commun. Conf. (OFC) Post deadline Papers*, Anaheim, CA, USA, 2016, paper Th5C.6.

[87] M. Mazzini *et al.*, “25GBaud PAM-4 Error Free Transmission over both Single Mode Fiber and Multimode Fiber in a QSFP form factor based on Silicon Photonics,” in *2015 Opt. Fiber Commun. Conf. (OFC) Post deadline Papers*, Los Angles, CA, USA, 2015, paper Th5B.3.

[88] K. Sekine *et al.*, “40 Gbit/s, 16-ary (4 bit/symbol) optical modulation/demodulation scheme,” in *Electron. Lett.*, vol. 41, no.7, pp. 430-432, 2005.

[89] T. Sakamoto *et al.*, “Coherent synthesis of optical multilevel signals by electrooptic digital-to-analog conversion using multi parallel modulator,” in *IEEE J. Sel. Top. Quantum Electron.*, vol. 16, no. 5, pp. 1140-1149, 2010.

[90] M. Mazzini *et al.*, “25GBaud PAM-4 Error Free Transmission over both Single Mode Fiber and Multimode Fiber in a QSFP form factor based on Silicon Photonics,” in

2015 Opt. Fiber Commun. Conf. (OFC) Post deadline Papers, Los Angles, CA, USA, 2015, paper Th5B.3.

[91] D. Patel *et al.*, “Silicon photonic segmented modulator-based electro-optic DAC for 100 Gb/s PAM-4 generation,” in *IEEE Photonics Technol. Lett.*, vol. 27, no. 23, pp. 2433–2436, 2015.

[92] R. Li *et al.*, “Silicon photonic ring-assisted MZI for 50 Gb/s DAC-less and DSP-free PAM-4 transmission,” in *IEEE Photonics Technol. Lett.*, vol. 29, no. 12, pp. 1046–1049, 2017.

[93] R. Li *et al.*, “Silicon photonic dual-drive MIM based 56 Gb/s DAC-less and DSP-free PAM-4 transmission,” in *Opt. Express*, vol. 26, no. 5, pp. 5395-5407, 2018.

[94] A. Samani *et al.*, “A silicon photonic PAM-4 modulator based on dual-parallel Mach-Zehnder interferometers,” in *IEEE Photonics J.*, vol. 8, no.1, pp. 7800610, 2016.

[95] R. Dubé-Demers *et al.*, “Low-power DAC-less PAM-4 transmitter using a cascaded microring modulator,” in *Opt. Lett.*, vol. 41, no. 22, pp. 5369–5372, 2016.

[96] M. H. Eiselt *et al.*, “Direct Detection Solutions for 100G and Beyond,” in *2017 Opt. Fiber Commun. Conf. (OFC)*, Los Angeles, CA, USA, 2017, paper Tu3I.3.

[97] A. Samani *et al.*, "Experimental parametric study of 128 Gb/s PAM-4 transmission system using a multi-electrode silicon photonic Mach Zehnder modulator," in *Opt. Express*, vol. 25, no. 12, pp. 13252-13262, 2017.

[98] G. P. Agrawal, *Lightwave Technology: Components and Devices*, Hoboken, NJ, USA: Wiley, 2004.

[99] Y. Zhang *et al.*, “A compact and low loss Y-junction for submicron silicon waveguide,” in *Opt. Express*, vol. 21, no. 1, pp. 1310-1316, 2013.

[100] Z. Lu *et al.*, “Comparison of photonic 2×2 3-dB couplers for 220 nm silicon-on-insulator platforms,” in *2015 IEEE 12th Int. Conf. on Group IV Photon. (GFP)*, Vancouver, BC, Canada, 2015, pp. 57-58.

[101] J. Ozaki *et al.*, “Ultra-Low Power Dissipation (<2.4 W) Coherent InP Modulator Module with CMOS Driver IC,” in *2018 Eur. Conf. Opt. Commun. (ECOC)*, Rome,

Italy, 2018, pp. 1-3.

[102] Y. Ueda *et al.*, "Compact InP spot-size converter with vertically tapered core layer formed by micro-loading effect," in *Electron. Lett.*, vol. 53, no. 12, pp. 797-799, 2017.

[103] "The road to a multi-billion euro market in integrated photonics", *JePPIX roadmap*, JePPIX, 2018. [Online]. Available: https://www.jeppix.eu/knowledge/roadmap/latest-edition/.

[104] *Datasheet of OFS LC fiber connector*, Furukawa, 2017. [Online]. Available: https://www.ofsoptics.com/wp-content/uploads/LC-Connector-Family-116-web-3.pdf.

[105] *Datasheet of MACOM PT-28 E PIN-TIA*, MACOM, 2017. [Online]. Available (on request): https://www.macom.com/support/contact-us/product-inquiry-form?category=165&partNumber=MARP-PT28E&datasheet=true.

[106] E. El-Fiky *et al.*, "400 Gb/s O-band silicon photonic transmitter for intra-datacenter optical interconnects," in *Opt. Express*, vol. 27, no. 7, pp. 10258-10268, 2019.

[107] Y. Ogiso *et al.*, "Over 67 GHz Bandwidth and 1.5 V Vπ InP-Based Optical IQ Modulator With n-i-p-n Heterostructure," in *IEEE J. Lightw. Technol.*, vol. 35, no. 8, pp. 1450-1455, 2017.

[108] G. Letal *et al.*, "Low loss InP C-band IQ modulator with 40GHz bandwidth and 1.5V Vπ," in *2015 Opt. Fiber Commun. Conf. and Exhib.(OFC)*, Los Angeles, CA, USA, 2015, paper Th4E.3.

[109] E. Rouvalis, "Indium Phosphide Based IQ-Modulators for Coherent Pluggable Optical Transceivers," in 2015 *IEEE Compound Semiconductor Integrated Circuit Symposium (CSICS)*, New Orleans, LA, USA, 2015, pp. 1-4.

[110] J. Zhou *et al.*, "High Baud Rate All-Silicon Photonics Carrier Depletion Modulators," in *IEEE J. Lightw. Technol.*, vol. 38, no. 2, pp. 272-281, 2020.

[111] *Datasheet of a Lumentum 100 GHz spacing filter add/drop module*, Lumemtum, 2015. [Online]. Available: https://resource.lumentum.com/s3fs-public/technical-library-items/fadm100_ds_cms_ae_030906.pdf.

[112] B. S. G. Pillai *et al.*, "End-to-End Energy Modeling and Analysis of Long-Haul

Coherent Transmission Systems," in *IEEE J. Lightw. Technol.*, vol. 32, no. 18, pp. 3093-3111, 2014.

[113] A. Stillmaker *et al.*, "Scaling equations for the accurate prediction of CMOS device performance from 180 nm to 7 nm," in *Integration*, vol. 58, pp. 74–81, 2017.

[114] P. Duhamel *et al.*, "Fast Fourier transforms: a tutorial review and a state of the art," in *Signal Process.*, vol. 19, pp. 259–299, 1990.

[115] S. Winograd, "On computing the discrete Fourier transform," in *Math. Computation*, vol. 32, no.1, pp. 175–199, Jan. 1978.

[116] M. Borgerding, "Turning overlap-save into a multiband mixing, downsampling filter bank," in *IEEE Signal Process. Mag.*, vol. 23, no. 2, pp. 158-161, 2006.

[117] M. LaCroix *et al.*, "6.2 A 60Gb/s PAM-4 ADC-DSP Transceiver in 7nm CMOS with SNR-Based Adaptive Power Scaling Achieving 6.9pJ/b at 32dB Loss," in *2019 IEEE Int. Solid-State Circuits Conf. - (ISSCC)*, San Francisco, CA, USA, 2019, pp. 114-116.

[118] *Data sheet of Emcore 1782 DWDM High Power CW Source Laser*, Emcore, 2021. [Online]. Available: https://emcore.com/wp-content/uploads/2016/03/1782.pdf.

[119] Y. Greshishchev *et al.*, "A 60 GS/s 8-b DAC with > 29.5dB SINAD up to Nyquist frequency in 7nm FinFET CMOS," in *2019 IEEE BiCMOS and Compound semiconductor Integr. Circuits and Technol. Symp. (BCICTS)*, Nashville, TN, USA, 2019, pp. 1-4.

[120] *Datasheet of a Neophotonics coherent driver modulator module HB-CDM – 64 GBaud Class 40*, Neophotonics, 2020. [Online]. Available: https://www.neophotonics.com/products/64-gbaud-coherent-driver-modulator/.

[121] P. R. Chevillat and E. Eleftheriou, "Decoding of trellis-encoded signals in the presence of intersymbol interference and noise," in *IEEE Trans. Commun.*, vol. 37, no. 7, pp. 669-676, 1989.

[122] J. Hagenauer and P. Hoeher, "A Viterbi algorithm with soft-decision outputs and its applications," in *1989 IEEE Global Telecommun. Conf. and Exhib. 'Commun. Technol. for the 1990s and Beyond'*, Dallas, TX, USA, 1989, vol.3, pp. 1680-1686.

[123] A. K. Aman *et al.*, “Combined trellis coding and DFE through Tomlinson precoding,” in IEEE J. Sel. Areas Commun., vol. 9, no. 6, pp. 876-884, 1991.

[124] M. Xiang *et al.*, “Multi-subcarrier flexible bit-loading enabled capacity improvement in meshed optical networks with cascaded ROADMs,” in *Opt. Express*, vol. 25, no. 21, pp. 25046-25058, 2017.

[125] D. Che and W. Shieh, “Approaching the Capacity of Colored-SNR Optical Channels by Multicarrier Entropy Loading,” in IEEE J. Lightw. Technol., vol. 36, no. 1, pp. 68-78, 2018.